RADIATIVE TRANSFER IN THE VICINITY OF ACCRETING NEUTRON STARS

POLARIZED EMISSION IN STRONG MAGNETIC FIELDS

STRAHLUNGSTRANSPORT IN DER NÄHE VON AKKRETIERENDEN NEUTRONENSTERNEN

POLARISIERTE EMISSION IN STARKEN MAGNETFELDERN

DER NATURWISSENSCHAFTLICHEN FAKULTÄT
DER
FRIEDRICH-ALEXANDER-UNIVERSITÄT
ERLANGEN-NÜRNBERG
ZUR
ERLANGUNG DES DOKTORGRADES
DR. RER. NAT.

VORGELEGT VON

EKATERINA SOKOLOVA-LAPA

AUS KALININGRAD

ALS DISSERTATION GENEHMIGT
VON DER NATURWISSENSCHAFTLICHEN FAKULTÄT
DER FRIEDRICH-ALEXANDER-UNIVERSITÄT ERLANGEN-NÜRNBERG

TAG DER MÜNDLICHEN PRÜFUNG:	19. Juli 2023
VORSITZENDER DES PROMOTIONSORGANS:	Prof. Dr. Wolfgang Achtziger
GUTACHTER:	Prof. Dr. Jörn Wilms
GUTACHTER:	Prof. Dr. Anna L. Watts
GUTACHTER:	Prof. Dr. Aya Bamba

TO MY MOTHER AND SISTER
AND TO THE MEMORY OF MY FATHER

"...and struggled with recalcitrant passage of 'The Ring'.
At this point I require to know how much later the moon gets
up each night when nearing full, and how to stew a rabbit!"
— J. R. R. Tolkien

from a letter to Christopher Tolkien
"The Letters of J. R. R. Tolkien", edited by H. Carpenter and C. Tolkien

ABSTRACT

Accreting neutron stars in binary systems with a massive companion exhibit a variety of observational phenomena, such as a complex shape of the spectra and pulse profiles and a low polarization signal, which challenge theoretical modeling. In shaping the emission spectra from the magnetic poles, Compton scattering plays a crucial role. In the presence of a strong magnetic field, $\sim 10^{12}$ G, this process is highly anisotropic and resonant due to electron quantization. The latter leads to the formation of absorption line-like features in the spectra, which are known as cyclotron lines. The radiation in strong magnetic fields is polarized due to the presence of real and virtual charges and is typically described in terms of two polarization modes of photons. Together, these effects make modeling of the emission properties a complex task.

A new generation of X-ray missions with high energy resolution put into question the statement that the continuum from these objects is well described by a power law due to the more commonly observed complexity of the spectra at intermediate energies, ~8–20 keV. Often, additional broad Gaussian-line-like components in absorption or emission (sometimes referred to as "10-keV" feature) or two-component Comptonization models are required to describe the spectra. The origin of these components is not well understood. An even bigger challenge was provided by observations of accreting neutron stars at low mass-accretion rates, where spectra of the well-known sources showed a dramatic transition to the two-hump shapes. The latest indication of our poor understanding of the details of the emission formation came from the measured degree of polarization, which is much lower than was expected.

The last few decades of modeling efforts focused on the separated treatment of the line-less Comptonized continua in the accretion channel and the cyclotron lines, which often uses a phenomenological power-law spectrum as an input. In addition, the physical models for the continuum commonly adopt polarization- and angular-averaged treatment. They generally result in smooth spectra without irregularities, except for the imprinted cyclotron lines. In this work, I bring the focus onto joint simulations of the continuum and the cyclotron lines that include the effects of anisotropy and polarization. I developed a radiative transfer code that allows treating energy and angular redistribution during resonant Compton scattering and takes into account polarization effects in a strongly magnetized medium. I investigate the spectral formation and angular distribution of the emission for various parameters of the medium and various assumptions about the mechanism responsible for the polarization of the radiation field. Finally, I present a model for low-luminosity accretion, which combines radiative transfer, calculation of the temperature and density profiles in the neutron star atmosphere, and relativistic ray tracing from the rotating neutron star to obtain phase-dependent spectra and pulse profiles.

The main message of this study is that polarization and redistribution effects play a crucial role in the formation of the spectra and emission profiles of accreting highly magnetized neutron stars. I show that the complexity of the continuum at intermediate energies naturally follows from the contribution of different polarization modes. Another effect altering the spectral shape is the redistribution of photons in the large proximity to the cyclotron resonance due to the presence of the hot plasma. It leads to the formation of the broad red wing of the cyclotron line at energies significantly below the line core. I argue that the often required "10-keV" feature could result from one or both of these effects. In addition, I show that the spectra are altered by the effect of vacuum polarization, in contradiction to the common assumption that for magnetic fields $\sim 10^{12}$ G it only affects the polarization signal. I demonstrate that this effect can introduce additional complexity in the soft and intermediate energies and result in suppression of the high-energy continua and the cyclotron lines. Aside from that, I show that emission profiles from a highly magnetized slab have complex energy-dependent shapes that rarely resemble similarity with the typically assumed pencil beam.

This study emphasizes the role of the detailed radiative transfer calculation and serves as a foundation for more complex modeling, which should include the dynamic effects in the accretion channel and more careful treatment of the cyclotron line and its harmonics. For the low-luminosity model that includes relativistic ray tracing, I present a method based on fitting phase-averaged and phase-dependent spectra, which allows accessing such fundamental parameters as the strength of the magnetic field at the poles, their location, and the inclination of the observer's line of sight to the rotational axis of the neutron star. The obtained geometry can serve as an independent check of the recent results obtained by polarimetric measurements.

ZUSAMMENFASSUNG

Akkretierende Neutronensterne in einem Doppelsternsystem mit einem massereichen Begleiter zeigen eine Vielzahl von beobachtbaren Phänomenen wie komplexe Emissionsspektren und Pulsprofile und eine niedrige Polarisations der beobachteten Strahlung. All das ist eine Herausforderung für theoretische Modelle. Das Emissionsspektrum wird hauptsächlich durch Compton-Streuung erzeugt. Innerhalb eines starken Magnetfelds, $\sim 10^{12}$ G, ist dieser Prozess stark anisotropisch und resonant durch die Quantisierung der Electronenzustände. Letzteres führt zu linienartigen Absorptionsmerkmalen im Spektrum, welche Zyklotronlinien genannt werden. Die Strahlung innerhalb des starken Magnetfelds wird durch die echten und virtuellen Ladungen polarisiert und wird typischerweise durch zwei Polarisationsmoden beschrieben. All das erschwert das modellieren der Eigenschaften der Strahlung.

Die neueste Generation der Röntgenmission für hochaufgelöste Spektroskopie stellen die übliche Beschreibung der beobachteten Spektren mit einem Potenzgesetz in Frage. Aufgrund der Komplexität im Bereich mittlerer Energien, $\sim$8–20 keV, werden häufig breite Gaussähnliche Linien in emission oder absorption (oft als "10-keV"-Feature bezeichnet), oder Comptonisationsmodelle mit zwei Komponenten verwendet. Der Ursprung dieser Komponenten ist noch nicht gut verstanden. Eine noch größere Herausforderung stellen Beobachtungen von akkretierenden Neutronensternen mit niedriger Massenakkretionsrate dar. Hier sind signifikante Veränderungen der Spektren zu einer Zwei-Höcker-Form zu beobachten. Der letzte Hinweis, dass unser Verständnis übern den Ursprung der Strahlung unzureichend ist, kam durch die Beobachtung eines sehr niedrigen Polarisationsgrades.

In den letzten Jahrzehnten lag der Fokus darauf, das Compton-Kontinuum und die Zyklotronlinen getrennt voneinander zu beschreiben. Letztere verwendeten häufig phänomenologische Modelle, wie Potenzgesetze, als Grundlage. Die Kontinuumsmodelle hingegen wurden meist winkel- und polarisationsunabhänging beschrieben. Das führte zu sehr einfachen Spektren, mit Ausnahme der Zyklotronlinien. In dieser Arbeit stelle ich kombinierte Simulationen des Kontinuums und der Zyklotronlinen vor, die sowohl die Winkel- als auch die Polarisationsabhängigkeit berücksichtigen. Dafür verwende ich einen von mir entwickelten Code, um das Problem des Strahlungstransports durch Comptonstreuung zu lösen. Der Code berücksichtigt sowohl die Polarisation der Strahlung als auch deren Richtungsabhängigkeit in einem stark magnetisiertem Medium. Damit untersuche ich die Entstehung der Strahlung und die Richtungsabhängigkeit der Emission für verschiedene Parameter des Mediums und verschiedene Annahmen über das Verhalten der Polarisation. Am Ende beschreibe ich ein Modell für die Emission von Neutronensternen in einem Zustand niedriger Massenakkretion. Kombiniert mit einem relativistischen Strahlungstransportcode Code für rotierende Neutronensterne, beschreibe ich so die phasenaufgelösten Spektren und Pulsprofile.

Die Kernaussage dieser Arbeit ist, dass Polarisations- und Verteilungseffekte eine wichtige Rolle bei der Entstehung der Strahlung von hoch magnetisierten Neutronensternen spielen. Ich zeige, dass die Komplexität des Kontinuums bei mittleren Energien durch den Beitrag verschiedener Polarisationsrichtungen gegeben ist. Zusätzlich zeige ich, wie sich die

Form des Spektrums durch die Umverteilung der Photonenenergien nahe der Zyklotronresonanz innerhalb des heißen Mediums verhält. Das führt zu einem breiten roten Ausläufer der Zyklotronlinie bei Energien die weit unterhalb des Linienzentrums sind. Ich argumentiere, dass das "10-keV"-Feature von einem oder beiden dieser Effekt verursacht wird. Zusätzlich zeige ich, wie die Spektren durch die Vakuumpolarisation verändert werden, was im Wiederspruch zur üblichen Annahme steht, dass für Magnetfelder $\sim 10^{12}$ G nur das Polarisationssignal verändert wird. Ich zeige, dass dieser Effekt zusätzliche Beiträge zur Komplexität des Spektrums bei niedrigen und mittleren Energien liefert und das Kontinuum und Zyklotronlinien bei hohen Energien abschwächt. Ich zeige auch, dass die Emission einer hoch magnetisierten Scheibe sehr komplexe energieabhängige Formen erzeugt, die selten mit der Annahme eines "fan-beams" zu erklären sind.

Diese Arbeit unterstreicht wie wichtig es ist, das Problem des Strahlungstransport im Detail zu lösen und legt die Grundlage für präzisere Berechnungen. Für das Modell für niedrige Akkretionsraten präsentiere ich einen Fitansatz um zu zeigen, dass damit grundsätzlich Systemparameter zugänglich sind, wie die Stärke des Magnetfelds, die Orientierung der Magnetpole und die Inklination des Neutronensterns zum Beobachter. Diese Ergebnisse erlauben einen unabhängigen Test der Parameter wie sie durch Polarisationsmessungen erhalten wurden.

CONTENTS

1

OUTLINE

This thesis is focused on the problem of radiation propagation in the vicinity of accreting neutron stars. Neutron stars are compact objects formed in the final stage of the evolution of massive stars. They are supported by neutron degeneracy pressure, which allows containing a mass of the order of the sun in a spherical shape with a radius of only $\sim$10 km. The violent phenomena that accompany the formation of neutron stars and the extreme state of their interiors result in high gravitational and magnetic fields and fast rotation of these objects. Together, it gives rise to peculiar phenomena.

The high magnetic field severely affects the behavior of matter, vacuum, and radiation. The medium in the vicinity of neutron stars is birefringent due to the effects of the magnetoactive plasma and polarized vacuum. High-energy radiation propagating through this medium is typically described in the formalism of two normal waves, which exhibit complex polarization properties. In addition, the quantization of charged particles in the strong magnetic field onto Landau levels, introduces resonant phenomena in their interaction with photons. Propagation of photons is thus strongly affected by the presence of the quantized real and virtual charges, which makes radiative transfer modeling a challenging task.

Due to the high gravitational field of a neutron star, the accretion of matter onto its surface produces a large energy release and results in strong X-ray radiation (Zel'dovich 1964; Salpeter 1964). Accretion phenomena typically occur in binary systems, where a neutron star has a non-degenerate companion. Accretion by isolated neutron stars from the interstellar medium is also possible, but has not been unambiguously observed to this date, likely due to the much lower luminosity of this event. The strong magnetic field affects matter not only at the quantum level but at larger scales as well. When the accretion flow penetrates inside the magnetosphere of a magnetized neutron star, $B \gtrsim 10^{11}$ G, it is channeled at the magnetic poles by the field lines. The kinetic energy of the flow, falling with a high velocity (a noticeable fraction of the speed of light) is mainly converted to radiation near the surface of the neutron star and is emitted predominantly in X-rays. Due to the rotation of the neutron star, it results in coherent pulsations seen by a remote observer.

Accretion phenomena introduce another layer of complexity for modeling photon propagation in the vicinity of a neutron star. Deceleration of the accretion flow, which proceeds via different processes depending on the mass-accretion rate, inevitably results in heating of the plasma to temperatures $\gtrsim 5$ keV ($\sim 5 \times 10^7$ K) and, in extreme cases, can approach $\sim$50 keV. Such high temperatures make Compton scattering the most important mechanism for the formation of the spectrum, which generally can be described as a power law with a high-energy cutoff. In the presence of electron quantization, Compton scattering becomes a resonant process with complex redistribution in energy and angular space and dependent on the photon polarization. It is also responsible for the formation of absorption-line-like features in the spectra, known as cyclotron lines or Cyclotron Resonant Scattering Features (CRSFs).

In this thesis, I focus on accreting neutron stars (accreting X-ray pulsars) in High-Mass X-ray Binaries (HMXBs), where the donor is a massive early-type (O/B) star. Neutron stars in these systems typically have magnetic fields of $\sim 10^{12}$-10^{13} G. Intensive mass supply via the stellar wind or the Roche Lobe overflow can result in such a powerful radiation flux produced near the neutron star surface, that the radiation pressure starts playing the main role in the deceleration of the falling flow. This denotes the formation of an extended radiative shock which gradually brakes the matter and forms a hydrostatic structure known as accretion column (Basko & Sunyaev 1976). The X-ray radiation is then expected to be emitted from the column walls. At lower mass-accretion rates, the collective plasma effects and Coulomb collisions are likely to play a crucial role in plasma stopping. In this case, the braking happens near the surface of the neutron star and X-rays are emitted by heated polar caps.

It is fair to say that the interest in radiative transfer simulations in accretion columns and polar caps was largely sparked by the discovery of a cyclotron line in the spectrum of Her X-1 by Trümper et al. (1977). Figure 1.1 shows the X-ray spectrum of Her X-1 with noticeable excess at $\sim$55 keV, which was interpreted by Truemper et al. (1978) as a cyclotron line *in emission*. The following discussion of whether the line is in emission or in absorption, corresponding to a dip at lower energies, $\sim$45 keV, showed, however, that this not an obvious matter (see a detailed history of this discussion described in Staubert et al. 2019). The answer was searched in multiple simulations which aimed for the consistent treatment of the cyclotron resonance and the continuum to access this fundamental information about the spectral formation (e.g., Yahel 1979; Kirk & Meszaros 1980; Nagel 1980). Finally, with the introduced detailed treatment of resonant magnetic Comptonization, the answer converged to an *absorption* line for the expected conditions of the emission region (Nagel 1981a; Meszaros & Nagel 1985a,b), which by now became common knowledge (Staubert et al. 2019).

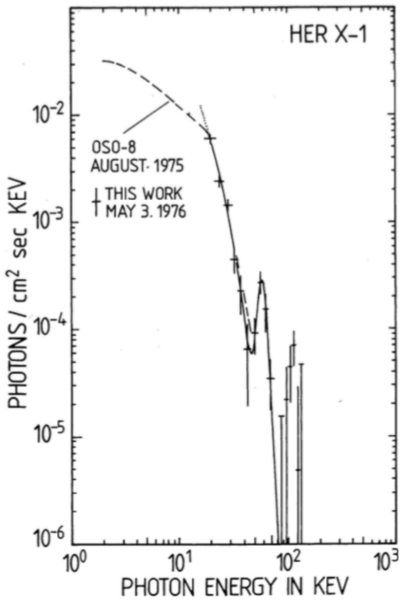

Figure 1.1: Spectrum of Her X-1 obtained with a balloon observation, with the first detection of the cyclotron line. Figure 2 from Truemper et al. (1978) © AAS. Reproduced with permission.

The later works are largely split into detailed simulations of cyclotron lines and their harmonics on top of the assumed phenomenological continuum (see, e.g., Araya & Harding 1999; Schönherr et al. 2007a; Nishimura 2008; Schwarm et al. 2017a,b) and the line-less continuum calculations from extended accretion columns with bulk and thermal (non-resonant) Comptonization (see, e.g., Becker & Wolff 2007; West et al. 2017a,b), often related to the determination of the hydrodynamic structure of the column (Postnov et al. 2015; Gornostaev 2021). The continuum simulations are typically performed for angle- and polarization-averaged cases and result in an overall smooth continuum shape, unless an additional source of photons is introduced directly. This, however, contradicts the observations, as the spectra more often exhibit noticeable excess or lack of photons at intermediate energies around 8–20 keV, which can be described by additional broad line-like components in emission or absorption. Accessing the information about the possible origination of this complexity of the observed continua is one of the objectives of this thesis.

Another, yet unsolved, problem introduced by observations is the complexity of many of the observed pulse profiles from accreting X-ray pulsars (see, e.g., Naik & Jaisawal 2015; Kretschmar et al. 2021). It could result from a complex geometry of the magnetic field, which is more challenging to justify than in the case of isolated neutron stars or lower magnetic fields as the accretion flow is expected to couple with the field far away from the neutron star, where the dipolar component is likely to dominate. Another possible explanation is a compound pattern of the beam from the emission region, which is expected due to the anisotropy imposed by the magnetic field (Nagel 1981b). Based on the properties of photon polarization modes, it is often assumed that a fan-like beam is emitted from the column walls and a simple directed outwards pencil-like emission profile results from the polar cap. In reality, however, their combination is often required to reproduce pulse profiles (see, e.g., Iwakiri et al. 2019), and the origin of these contributions is not well understood.

I argue that both problems – complex shapes of the spectra and of pulse profiles – can (and have to) be addressed by the polarized radiative transfer that takes into account detailed photon energy and angular redistribution during magnetic Compton scattering in a hot, magnetoactive plasma. Except for a pure plasma effect on the wave propagation in the presence of a strong magnetic field, the vacuum polarization from the virtual charges has to be taken into account. It is often stated that vacuum polarization only alters the spectrum formation at magnetar-like magnetic fields, $\sim 10^{14}$ G and for the fields typical of accreting X-ray pulsars only introduces a modification of the polarization signal in the magnetosphere (Ho & Lai 2004; van Adelsberg & Lai 2006). This effect was investigated for the fields $\sim 10^{12}$ G for cold atmospheres without Compton scattering (see, e.g., Pavlov & Shibanov 1979; Kaminker et al. 1982), but was not studied in detail for hot Comptonizing media. Lately, this effect was brought back into the discussion for accretion-powered X-ray pulsars in High-Mass X-ray Binaries due to the observed unexpectedly-low degree of polarization (Doroshenko et al. 2022), which was not yet followed by modeling. In this work, I include this effect for some of the presented models and illustrate its importance for accretion-powered X-ray pulsars in High-Mass X-ray Binaries.

The puzzles provided by modern observations thus strongly suggest stepping back and continuing the investigation of fine effects, such as redistribution and vacuum polarization in a strong magnetic field, from the point where they were left a few decades ago. This objective drives the research presented in this thesis. In Chapter 2, I provide an introduction to neutron stars, accretion phenomena, and the evolutionary scenario that leads to the formation of High-Mass X-ray Binaries and review observational manifestations of various neutron star populations via electromagnetic radiation. In Chapter 3, I focus on High-Mass X-ray Binaries and describe the current state of the theoretical spectral modeling and the questions posed by observation in detail, such as the complexity of the spectral shapes and pulse profiles. In Chapter 4, I outline the concept of the radiative transfer modeling by bringing together the general form of the radiative transfer equation, a description of the electromagnetic wave propagation in the magnetized plasma, the influence of vacuum polarization, and the complex nature of the opacity due to the magnetic resonant Compton scattering and free-free processes. There, I also describe the radiative transfer code `FINRAD` which was developed within the frame of this research. I then present the first results of the radiative transfer simulations for different conditions of the magnetized medium, including inhomogeneous atmospheres in Chapter 5. There, I show the effect of vacuum polarization on the spectral formation and address anisotropic emission profiles obtained in the simulations. Finally, in Chapter 6, I consider accretion at low mass-accretion rates, which occurs in quiescence of High-Mass X-ray Binaries with Be stars, where a simplified geometry of the emission region allows for a straightforward combination of radiative transfer calculation with modeling of the atmospheric structure and relativistic ray tracing. This combined model can be used for the phase-resolved spectral data analysis to access fundamental parameters of a neutron star, such as the strength of the magnetic field at the poles, the inclination of the dipolar axis and the degree of its distortion, and also the viewing angle to the observer with respect to the rotational axis of the neutron star. Chapter 7 concludes this study and offers perspectives for further research.

Part I

INTRODUCTION TO NEUTRON STARS AND ACCRETION PHENOMENA

2

NEUTRON STARS

"I am convinced, once more, that neutron stars are much smarter than we are."
Kent S. Wood

Neutron stars are marvelous objects representing the densest form of baryon matter which can be directly observed. While thermal pressure insures equilibrium of regular stars, neutron stars are supported by pressure of degenerate neutrons. The concept of a "gigantic nucleus" formed when nuclei come in close contact was proposed by Landau (1932), following by the discovery of neutron by Chadwick (1932, see historical investigation by Yakovlev et al. 2013). By then, the existence of objects supported by a degenerate electron gas – white dwarfs – was established (Fowler 1926; Milne 1930a). Chandrasekhar (1931) and Landau (1932) independently addressed a question of what happens when the mass of a white dwarf exceeds a certain limit (Lipunov 1992). Both works implied the possibility of existence of more "highly collapsed" (Chandrasekhar 1931) configuration than white dwarfs. The mass limit of $\sim 1.46\,M_\odot$, known as the Chandrasekhar limit, denotes the upper limit on the white dwarf's mass (Chandrasekhar 1939, the value is dependent on the number of leptons per baryon and is given here for equal composition). Baade & Zwicky (1934) related supernova events to the formation of a neutron star. Later, Oppenheimer & Volkoff (1939) studied equilibrium solutions for masses composed of neutrons, referring to the previous result of Landau (1932) for a cold degenerate Fermi gas and bringing the equation of state into focus.

The discussion around neutron stars remained theoretical until the discovery of periodic pulses with a period $P \approx 1.3\,\mathrm{s}$ from the "Cambridge Pulsar" CP1919 (known now as PSR B1919+21, see Bell & Hewish 1967; Hewish et al. 1968, for the original discussion). It was clear that such short periods could originate only from a compact source, a white dwarf or a neutron star (Hewish et al. 1968). A subsequent discovery of a pulsar in the Crab Nebula (Staelin & Reifenstein 1968) with much shorter period of $\sim$0.03 s (Comella et al. 1969) required a greater compactness of an object and, as a result, higher density, ruling out the possibility of a white dwarf.

It is somehow ironic that the first discovered neutron stars were isolated ones. A few years before their discovery, Zel'dovich (1964) and Salpeter (1964) discussed that accretion onto a compact object produces a large energy release. Although the bright X-ray source Sco X-1 was already known at this time (Giacconi et al. 1962), it was only later realized by Shklovskii (1967) that this object represents a binary system with a neutron star and a massive non-degenerate companion. The early-predicted isolated accreting neutron stars (Salpeter 1964) remain undiscovered to this date.

Neutron stars are often called the remnants of stellar evolution. However, they are phenomenologicaly rich objects on their own and are the subjects of their own evolution. In this chapter, I will set the stage for the thesis, introducing neutron stars and the related observational phenomena. In Section 2.1 I describe some aspects of neutron star formation and general characteristics of these object. The evolution of their characteristics is discussed in Section 2.2. Section 2.3 describes the origin of neutron stars in binary systems and the accretion that occurs in close binaries. I present a variety of observational manifestations of neutron stars in Section 2.4 and provide some final remarks in Section 2.5.

2.1 FORMATION AND GENERAL PROPERTIES

Neutron stars are degenerate objects, in which a mass of $\sim 1.4\,M_{\odot}$ is confined to a sphere-like volume of only ~ 10 km. The extreme conditions of their interior and environment – high gravitational and magnetic fields, high densities, and fast rotation – present multiple challenges for modern physics. Many of these challenges, one way or another, fall to a lot of observational and theoretical astrophysics. To provide a better understanding of the puzzling observational phenomena and directions of theoretical modeling discussed in this thesis, I, first, present the main properties of neutron stars. Section 2.1.1 describes the general details of the neutron star formation. Section 2.1.2 discusses the process of the cooling of a newly born neutron star. In Section 2.1.3, I provide major information on the structure and composition of the neutron star interiors. Finally, the origin of the extra-strong magnetic fields and the fast rotation is discussed in Section 2.1.4.

2.1.1 *Formation*

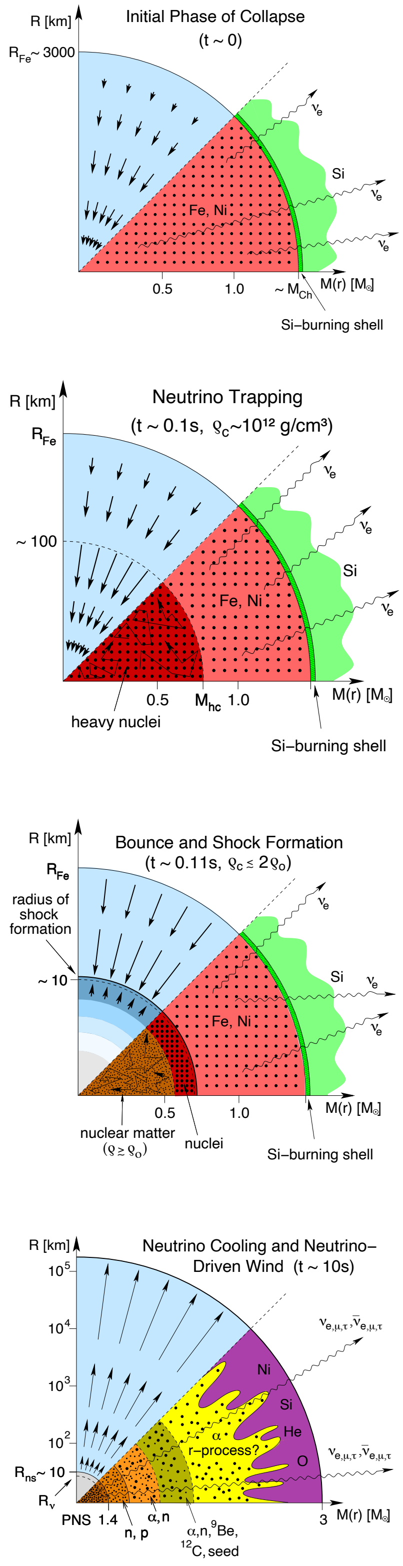

Figure 2.1: Schematic depiction of the selected major stages of the core-collapse supernova event. Selected panels from Figure 1 of Janka et al. (2007). Reprinted from Janka et al. (2007), with permission from Elsevier.

Neutron stars are formed during the gravitational collapse of massive stars, $M \gtrsim 8\,M_{\odot}$, where $M_{\odot}$ is the solar mass, which proceed after they exhaust their nuclear fuel. Iron production is the final energetically favorable reaction of nucleosynthesis which can take place in the interior of a massive star (Hoyle 1954; Burbidge et al. 1957). After the iron core is formed, its mass still can be increased by nuclear burning in the silicon shell around it (the book of Kippenhahn et al. 2013, is recommended for the detailed information about the physics of the stellar interior, including shell burning processes). When the mass of the core exceeds the Chandrasekhar limit, the pressure of the degenerate electron gas can no longer resist the gravitational force, leading to the beginning of the collapse.

Early stages of the collapse are characterized by the decrease of the electron density in the interior due to electron capture and photodisintegration due to the γ-rays produced by the rapidly contracting core. This stage is very sensitive to the number of electrons per nucleon (Bethe 1990). The reduction of the electron density and the energy release by the produced neutrinos accelerate the collapse. As the density of the core increases up to $\sim 10^{12}\,\mathrm{g\,cm^{-3}}$, neutrinos become trapped in the matter as their transport is affected by neutral currents enabling elastic scattering off complex nuclei (Freedman 1974; Tubbs & Schramm 1975, and references therein). Finally, when nuclear densities are reached in the central part, $\sim 10^{14}\,\mathrm{g\,cm^{-3}}$, the nuclear pressure stops the collapse of the inner core. As the outer parts of the core still continue a supersonic fall, they rebound off the inner core, which results in the shock wave propagating outwards and denoted the beginning of the supernova explosion. A compact object, a proto-neutron star, forms at the center, while the shock wave rapidly looses its energy mainly to the dissociation of heavy nuclei while traveling through the outer core (Janka et al. 2007). For tens of seconds, the proto-neutron star is opaque for neutrinos, which heat up the interiors by down-scatterings propagating outward. This heat results in neutrino-pair production and enhanced neutrino flux. In turn, heating by neutrinos creates a low-density hot region below the shock and drives it further outwards. This mechanism of shock energization seems to drive the explosion of the outer shells of the collapsing star (Colgate 1989) and is known as *delayed neutrino-heating mechanism* (Janka et al. 2007). Figure 2.1 shows a few principal stages of the core-collapse supernova. The detailed reviews by Janka et al. (2007) and Bethe (1990) are recommended for more information on the theory of core-collapse supernova explosions.

A further collapse of the proto-neutron star to a black-hole is possible in case of the fall-back accretion or if its mass after initial cooling (on the scales of a neutrino diffusion time) starts to exceed the limit, which was reduced by the loss of leptons. This is a possible scenario for SN 1987A, when the $\sim$10 s-neutrino signal confirmed the core collapse, but no evidence of a neutron star was found 'since (Lattimer & Prakash 2004).

2.1.2 *Cooling of a Young Neutron Star*

A hot proto-neutron star with a temperature of $\sim 10^{11}$ K passes a few major cooling stages. For the first $\sim$10–100 years a young neutron star experiences thermal relaxation, which corresponds to the crust thermal evolution and heat transport by electron conduction to the center (Lattimer & Prakash 2004). This stage is followed by the neutrino cooling stage with a duration $\lesssim 10^5$ yr (Yakovlev et al. 2004). Nuclear reactions that produce neutrinos result in cooling due to rapid neutrino escape and are generally known as *URCA* processes (first introduced by Gamow & Schoenberg 1941). The *direct URCA* (DURCA)

$$\begin{aligned} n &\rightarrow p + e^- + \bar{\nu}_e \\ p &\rightarrow n + e^+ + \nu_e \end{aligned} \tag{2.1}$$

is the most efficient process, but requires high proton abundances to fulfill the simultaneous conservation of momentum and energy and thought to be unlikely for a neutron star interior. It, however, can play a significant role at high densities above the nuclear one, – the conditions, which are fulfilled in the core of a neutron star – and is also onset in the exotic phases of matter: pion or kaon condensate, quark matter, and in the presence of hyperons (Lattimer & Swesty 1991; Yakovlev et al. 2004).

At less extreme conditions, the modified URCA processes (MURCA) are expected to govern neutrino cooling. They require the presence of an additional nucleon to fulfill the momentum conservation,

$$\begin{aligned} n + (n,p) &\rightarrow p + (n,p) + e^- + \bar{\nu}_e \\ p + (n,p) &\rightarrow n + (n,p) + e^+ + \nu_e. \end{aligned} \tag{2.2}$$

The dominance of the modified URCA processes is known as the *"standard cooling scenario"* versus the *"enhanced cooling scenario"* which involves the direct URCA processes (Pethick 1992; Page et al. 2004).

One needs to take into account, however, that after a young neutron star cooled down to the temperatures of 10^9–10^{10} K (which is expected to happen on a scale of a few days after the birth; Potekhin et al. 2015), neutrons (and protons) in its interior become superfluid, which provides an additional mechanism for neutrino emission via breaking and formation of nucleonic Cooper pairs (Flowers et al. 1976). Based on this, Page et al. (2004) suggested a new *"minimal cooling scenario"* extending the standard paradigm with modified URCA to include the effects of superfluidity and superconductivity. It requires, however, the absence of any fast direct

It is known from Gamow's autobiography that the name "URCA" processes suppose to reflect the name of Cassino da Urca in Rio de Janeiro, where Gamow and Schoenberg met, and the rapid disappearance of money from the gambler's pockets, similar to the thermal energy from the stellar interior. This name and its derivatives, however, somehow sound more ironic for a Russian-speaking person. First of all, "urca" (or "urka") is a very well-known old slang name for gangsters actively used in the early Soviet times. It is interesting to note that Gamow himself used this word in a non-capitalized manner, but of course it is impossible to prove whether he aimed for this play on words too. Furthermore, "Murca" (or "Murka") is the name of the heroine of an old song which has also a well-known (thanks to the Soviet cinematography) "gangster"-version, where Murca is a nickname of a woman who infiltrates undercover an urka's gang and turns them to the police. Finally, "durca"/"durka" is a slang name for a mental hospital. I hope the reader will forgive me for this lyrical digression. Gamow is not the only one who enjoys jokes.

URCA processes. The neutrino emission in the minimal cooling scenario depends on the stellar mass, the composition of the envelope, superfluid properties of the interiors, and the equation of state (EOS). It is expected that the Cooper-pair neutrino emission proceed in the core and the inner crust (Yakovlev & Pethick 2004) and can be efficient for neutron stars of ages 10^2–10^5 yr (the conditions are discussed in Page et al. 2009). More details on neutrino emission from neutron stars can be found in the comprehensive review by Yakovlev et al. (2001).

After the stage dominated by neutrino emission, the cooling of a neutron star is determined by the heat transfer from the core to the surface and the thermal photon emission with typical temperatures of 10^5–10^6 K. The minimal cooling scenario followed by the photon thermal emission seems to be compatible with observations of neutron stars with magnetic field $B \lesssim 10^{13}$ G (see, e.g., Page et al. 2009). For highly magnetized neutron stars, however, their magnetic field plays an important role in their thermal evolution, resulting in brighter X-ray emission from the surface (Viganò et al. 2013). Some aspects of the coupled magneto-thermal evolution will be discussed in Section 2.2.2.

2.1.3 *Internal Structure and Composition*

The strong gravitational field is responsible for the extreme stratification of the neutron star interiors. The structure of a neutron star is usually divided on to the following qualitatively different regions: the inner and outer core, the mantel, the inter and outer crust, the ocean and the atmosphere (Potekhin et al. 2015; Haensel et al. 2007). Figure 2.2 illustrates the principal regions of a neutron star.

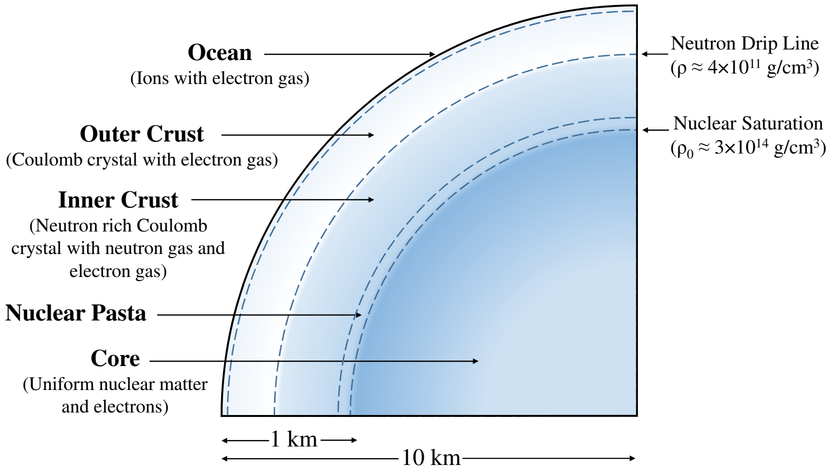

Figure 2.2: Schematic structure of a neutron star. Figure 2 from Caplan & Horowitz (2017). Reproduced with permission from Caplan & Horowitz (2017). Copyright (2017) by the American Physical Society.

Atmosphere and Ocean

The *atmosphere* is the thinnest part of the neutron star – the outermost layer of the plasma extending down to a density $\rho \sim 10^6\,\mathrm{g\,cm^{-3}}$. Its thickness can vary from a few millimeters to a few centimeters, depending on the local temperature and the strength on the magnetic field, and can turn into a condensed surface in case of the cold plasma in a very strong magnetic field (see Zavlin & Pavlov 2002, and referenced therein). At the bottom of the atmosphere, the atoms are already fully ionized due to the high density. The atmosphere is responsible for shaping the spectrum of the thermal radiation and can provide an important information about the parameters of the neutron star. In Chapter 6 of this thesis I present the extreme case of accreting magnetized atmospheres, whose spectra differ significantly from black-body radiation. The *ocean* is characterized by the non-ideal Coulomb liquid formed by ions due to the further increasing ion density and has a total extension of tens of meters. It is crucial for the heat transport between the surface and deeper interiors. Both, the atmosphere and the ocean, are able to support convective processes.

The atmosphere and the ocean together are sometimes referred to as the "envelope" (Meisel et al. 2018). On the other hand, the reference to the outer crust as to the "outer envelope" is also met in the literature (Haensel et al. 2007).

Crust

At a density of a few $10^7\,\mathrm{g\,cm^{-3}}$ the ocean solidifies as ions form a Coulomb crystal, while the electrons stay in the form of degenerate gas. This transition corresponds to the *outer crust*, which extends for a few hundred meters with increasing Fermi energy of electrons. It increases the rate of electron capture and makes nuclei in the lattice neutron-rich (Haensel et al. 2007). A density of $\rho \sim 10^{11}$–$10^{12}\,\mathrm{g\,cm^{-3}}$ corresponds to the neutron drip line denoting the critical proton-to-neutron ratio. At this point nuclei start becoming unbound and allow neutrons to drip from the lattice, forming the neutron gas. The *inner crust* thus represents the mix of the neutron-rich Coulomb crystal, the degenerate electron gas and neutron gas, which soon becomes degenerate as well. At the bottom of the inner crust nuclei exist in the form of nuclei clusters. These clusters can be distorted into complex shapes due to competing nuclear attraction and Coulomb forces (Meisel et al. 2018). This state of matter is known as the *nuclear pasta*. The existence of this exotic nuclei is conditional and does not occur in all models (depending on the assumed effective nucleon-nucleon force Douchin & Haensel 2000). The properties of the solid crust make it important for the evolution of the neutron star, affecting heat transport from the hot core and building the stresses. The most inner layer of the crust, which is also sometimes referred to as the *mantel* and accounts for most of its mass, plays a crucial role. The extensive review by Meisel et al. (2018) is recommended for more information on the outer layers of a neutron star: the crust and the ocean.

"It [the crust] contains matter at subnuclear density, and therefore there is no excuse for the theoretical physicists, at least in principle: the interactions are known, and many-body theory techniques are available"
Chamel & Haensel (2008)

Core

Finally, at densities $\sim 10^{14}\,\mathrm{g\,cm^{-3}}$, approaching the nuclear density, the transition to the liquid *outer core* occurs. For neutron stars with masses $\lesssim 1.5\,M_\odot$, the outer core is the only core, extending down to the center. It consists of neutrons, protons, electrons, and muons. The electrons and the muons are in a form of an ideal Fermi gas (Haensel et al. 2007). The strong interactions force nucleons to pair, which results in superconductivity and superfluiditiy. Protons are expected to acquire superconductive properties as they create Cooper pairs organized in flux tubes. Neutrons are likely to form a superfluid. The arrays of quantized vortices appear in the superfluid due to the rotation of the neutron star. Closer to the upper boundary of the outer core, these vortices can pin to the nuclei of the inner crust, leading to interesting dynamic effects due to the momentum transfer. This, for example, can explain such phenomenon as "glitching", which will be discussed in Section 2.4.1.1.

For massive neutron stars, $M_{\mathrm{NS}} \gtrsim 1.5\,M_\odot$, the formation of the *inner core* is expected, where the density can be an order of magnitude grater than the nuclear density. The state of matter in these extreme conditions is yet not well understood. Generally, exotic forms of matter, such as hyperons, pion and kaon condensate, and the phase transition to quark matter are discussed (Haensel et al. 2007). Currently, it is unclear whether the transition between the outer and the inner core is homogeneous or not (Lattimer 2021).

Equation of State

The equation of state connecting the pressure, P, the temperature, T, and the density, ρ, in the interior of a neutron star is crucial for understanding its composition in detail. For the high-density matter, the equation of state is currently unknown and remains one of the greatest challenges in the field. There are many suggested equations of state developed for the core, the crust, and unified ones that treat the core and the crust continuously (a smaller number is developed for the crust due to its non-uniformity; Zdunik et al. 2017, and references therein). The equation of state determines macroscopic parameters, such as the mass, M_{NS}, and the radius, R_{NS}, which can be deduced from the astrophysical observations. It is expected that the obtained M_{NS}-R_{NS} can be inverted to determine the equation of state (Özel & Psaltis 2009). A few general directions are currently explored to access the information about the equation of state of the neutron star interiors, such as gravitational wave observations and X-ray timing techniques (see the comprehensive review by Watts et al. 2016). Determining the fundamental characteristics of neutron stars is one of the main objectives of the Neutron Star Interior Composition Explorer (*NICER*), covering the soft X-rays. Some advances with the obtained insights with *NICER* can be found, for example, in Raaijmakers et al. (2021), Bogdanov et al. (2021), Kojo et al. (2022), and Lattimer (2021).

The knowledge of the equation of state of the nuclear matter at a very high density is also related to the problem of determination of the maximum neutron star mass (Kalogera & Baym 1996). The latter allows distinguishing between neutron stars and stellar-mass black holes when the mass is primary information about the compact object. As was mentioned before, Oppenheimer & Volkoff (1939) were the first to address this problem obtaining low maximum limits of $\sim 0.7\,M_{\odot}$ for the equation of state of a cold Fermi gas. Later, Rhoades & Ruffini (1974) showed that the maximum mass of a neutron star corresponds to the equation of state which maximizes the sound speed, that is, makes it equal to the speed of light, and found the limit of $\sim 3.2\,M_{\odot}$. Within the same framework, using more modern equations of state, Kalogera & Baym (1996) obtained the value of $2.9\,M_{\odot}$. The recent discovery of the coalescence of the $\sim 23\,M_{\odot}$ black hole with a $\sim 2.6\,M_{\odot}$ compact object (GW190814; Abbott et al. 2020), motivated the further investigation of this problem. Godzieba et al. (2021) showed that the possibility of a secondary neutron star in GW190814 cannot be ruled out and argued that the measurements of the neutron star radii by The Laser Interferometer Gravitational-Wave Observatory (LIGO)/Virgo and *NICER* will allow constraining the equation of state.

2.1.4 *Magnetic Fields and Rotation*

Neutron stars possess the strongest known magnetic fields, which typically varies within $B \sim 10^{8}$–10^{15} G. The upper limit, $B \sim 10^{14}$–10^{15} G, corresponds to the class of neutron stars known as *magnetars* (see Kaspi & Beloborodov 2017, and references therein), while the lowest fields, 10^{8}–10^{9} G are obtained for *millisecond pulsars* (Harding 2022). The magnetic field is strongly dependent on the neutron star's age, accretion history, and formation channel. The problem of the formation of strong magnetic fields echoes the origin of the rapid rotation, thus I consider them together in this section. The rotational periods of neutron stars vary from $P{\sim}10^{-3}$ s (millisecond pulsars) up to $P{\sim}10^{4}$ s known for some X-ray pulsars with massive companions (Wang 2013). Here, I mainly focus on the origin of the magnetic fields and the spin of neutron stars. I will discuss some aspects of the magnetic and rotational evolution in Section 2.2 and address various populations of neutron stars, including their characteristic magnetic field and spin periods, in Section 2.4. the magnetic field origin.

One of the classically discussed channels for the origin of strong magnetic fields and large rotational velocities is the *fossil* scenario. Its main idea is that the angular momentum and the total magnetic flux are conserved during the collapse of the progenitor. The pre-collapsed core of the massive star rotates much more rapidly than the envelope, to the degree that even additional mechanisms of the angular momentum transfer are investigated to prevent the critical rotation of the core (see the detailed review of this problem in Langer 2012). The conservation of a large part of the core's angular momentum is possible during the supernova explosion, which can explain the rapid rotation of young neutron stars of 10^{-2}–10^{-1} s. At the same time, the strongest magnetic fields from O and B stars are expected to reach ${\sim}10^{3}$–10^{4} G (Walder et al. 2012). If the total magnetic flux is conserved during the supernova event, the magnetic field can be greatly amplified due to the much smaller radius of a neutron star. This scenario is, however, unrealistic as the neutron star is formed from a dense core of the progenitor, which corresponds to only a small percent of the total cross section. As was shown by Spruit (2008), this would correspond to the maximum field of the neutron star of ${\sim}10^{14}$ G.

The rotational period of the famous Crab pulsar, whose age is well known, ${\sim}10^{3}$ yr, is ${\sim}33$ ms (Comella et al. 1969).

An immediate problem arises as this field value is insufficient to account for the strongest fields known for some magnetars. Another less obvious obstacle for the fossil hypothesis was noted by Spruit (2008): if the strong long-scale magnetic field is present in the progenitor at all stages of its evolution, including the latest supergiant ones, it provides an efficient coupling of the core and the envelope. In turn, it would prevent the existence of the vastly different rotational velocities of the core and the envelope due to magnetic torque. This scenario was proposed by Spruit & Phinney (1998) and results in sufficient deceleration of the core. While it helps to solve the problem of the core reaching critical rotation, it results in much smaller rotational periods of newly born neutron stars of ${\sim}100$ s. Spruit (2008) concluded that the angular momentum and the strong magnetic field cannot both be fossil. It is possible that magnetic fields of the regular neutron stars, $B \sim 10^{12}$ G have a fossil nature, while their spin is the result of a kick during the birth process due to, for example, the regular motion of the progenitor star in the Galaxy (Spruit & Phinney 1998).

Makarenko et al. (2021) also recently illustrated with population synthesis that the fossil field hypothesis does not allow to simultaneously reproduce the populations of the regular pulsars and the magnetars.

Another mechanism for the formation of the strong fields of neutron stars was proposed by Duncan & Thompson (1992) and Thompson & Duncan (1993). It is based on the convective nature of the (proto-)neutron star interiors during the first tens of seconds after its formation. The magnetic field in the rotating, conductive, and convective neutron star can be amplified by the dynamo effect. Thompson & Duncan (1993) noted that the amplification in this case is likely to happen at a cost of the convection. They showed that this mechanism can result in fields of ${\sim}10^{14}$–10^{15} G, but generally requires fast rotation of the newly-born neutron star, $P \lesssim 30$ ms.

There is evidence for young neutron stars with the fields varying in the range 10^{11}–10^{15} G. While it is mainly the dipolar component of the field that can be measured with the standard methods (see Section 2.4), the field configuration, especially of the newly born neutron stars, can be very complex, including multipolar, toroidal, and stochastic components. The region where the magnetic field is anchored in the neutron star is also a complicated question, not yet fully understood. It depends on the superconductivity of the core, whether the magnetic field can be present there or is expelled to the crust. An excellent review by Igoshev et al. (2021b) is recommended for more details on these topics.

2.2 MAGNETO-ROTATIONAL AND THERMAL EVOLUTION

In Section 2.1, I described the general properties of a neutron star and the way of acquiring these properties during the core collapse and supernova explosion. It leaves us with a relatively young ($\gtrsim 10^3$ yr) neutron star moving through the interstellar medium or in a binary orbit with a companion, in case the progenitor was a member of a binary system and the binary survived the supernova explosion. In this section, I will describe how fundamental characteristics of a neutron star, such as the magnetic field strength, rotational period, and the surface temperature distribution evolve with time. The rotational period and the magnetic field to a high degree define how a neutron star can interact with the surrounding plasma. Under the influence of the gravitational field, the plasma will attempt to accrete onto the neutron star. It can be stopped by the nearly static magnetic field, its rotation, or the strong wind of relativistic particles ejected from the surface. Section 2.2.1 describes the most fundamental types of these interactions, based on the principle ability of the plasma to reach the magnetosphere and the accompanying conditions. The interactions change due to the evolution of the rotational period of a neutron star. In Section 2.2.2, I discuss the possible ways for the magnetic field evolution, which for non-accreting neutron stars is strongly connected to the surface temperature distribution.

2.2.1 *Magneto-Rotational Evolution*

The strong gravitational field of a neutron star allows for the gravitational capturing of the surrounding plasma. Due to its conductivity, the surrounding plasma in this case experiences not only gravitational, but also electromagnetic interaction with the magnetic field of the neutron star. In this complex setup, whether the captured plasma can reach the surface of a neutron star or whether will it be repelled by the magnetic field or magneto-dipole radiation depends on multiple factors. Moreover, the interaction with the neutron star magnetic field can occur even before the plasma experiences a significant gravitational focusing. The rotational period of the neutron star, P, its magnetic field strength, B, and the potential mass-accretion rate, $\dot{M}$, are the most basic parameters, defining the interaction properties. I outline the characteristic scales based on these parameters, with respect to which plasma can be stopped by the magnetic field of the neutron star. Section 2.2.1.1 presents a classification based on the type of interaction of the neutron star with the surrounding medium in Section 2.2.1.2. This classification is known as the *magneto-rotational evolution* (Lipunov 1992), although its stages do not necessarily follow a continuous sequence for real objects. I provide some final remarks on the classification in Section 2.2.1.3.

2.2.1.1 *Stopping Radius*

In this section, I outline the characteristic scales for plasma stopping by the rotating field of the neutron star. Here, I generally follow the classical description by Lipunov (1992), which, in turn, is based on the works of Shvartsman (1970), Shvartsman (1971b), Illarionov & Sunyaev (1975), Lipunov (1982), Kornilov & Lipunov (1983), and Lipunov (1987).

In a first and very simplified approximation, a neutron star can be treated as a gravitating magnetic dipole with the radius R_{NS}, mass M_{NS}, and magnetic dipolar momentum

$$\mu = \frac{BR_{\mathrm{NS}}^3}{2}, \tag{2.3}$$

where B is a surface magnetic field strength at the poles of the neutron star, rotating with the period $P = 2\pi\Omega^{-1}$. The surrounding medium is defined via its density , ρ, the sound speed, c_{s}, and the relative velocity with respect to the neutron star, v_∞, which together provide the possible mass-accretion rate through the continuity equation (see, e.g., Lipunov 1987)

$$\dot{M}_{\mathrm{c}} = \sigma_G \rho (v_\infty^2 + c_{\mathrm{s}}^2)^{1/2}, \tag{2.4}$$

where σ_G is the cross section of the gravitational interaction. This cross section depends on the *gravitational capture radius*

$$R_{\mathrm{G}} = \frac{2GM_{\mathrm{NS}}}{c_{\mathrm{s}}^2 + v_\infty^2} \approx 3.7 \times 10^{10} \left(\frac{v}{10^8\,\mathrm{cm\,s^{-1}}} \right)^{-2} \mathrm{cm}. \tag{2.5}$$

The estimate is done for the canonical[1] neutron star and v combines the contribution from the relative motion and the speed of sound in the plasma. Crossing this radius towards the neutron star, the matter starts experiencing a significant gravitational focusing.

The absolute value of the magnetic field strength absolute value is distributed on the surface of a magnetic dipole with the radius R_{NS} as

$$B_d = \frac{\mu}{R_{\mathrm{NS}}}(1 + 3\sin\theta)^{1/2},$$

where θ is the latitude (see, e.g., Lipunov 1992).

This ratio is known as the Mach number

$$\mathfrak{M} = \frac{v_\infty}{c_{\mathrm{s}}},$$

widely used in the physics of shocks.

A few other characteristic radii, whose ratio to a high degree determines the problem, need to be introduced as well. In the case of the misaligned magnetic and rotational axes, the dipole emits electromagnetic waves at the rotational frequency. A distance

$$R_l = \frac{c}{\Omega} \approx 4.8 \times 10^9 \left(\frac{P}{1\,\mathrm{s}} \right) \mathrm{cm} \tag{2.6}$$

from the center of the dipole is known as the *light cylinder radius* (Pacini 1968; Goldreich & Julian 1969). At this distance, the electromagnetic field stops being static and the rotational velocity of the dipole's magnetic lines reaches the speed of light c. At distances $R > R_l$, the field has to be represented by an electromagnetic wave that is propagating away from the neutron star. The power radiated away by the dipole inclined at an angle α to the rotation axis is (Pacini 1968)

$$P_{\mathrm{rad}} = \frac{2}{3c^3} B^2 R_{\mathrm{NS}}^6 \sin^2\alpha \left(\frac{2\pi}{P} \right)^4. \tag{2.7}$$

In this way, the neutron star loses the rotational kinetic energy and spins down with the rate $\dot{P} > 0$. The energy ejected by a pulsar is transferred to the surrounding medium by the relativistic pulsar wind (see more on this topic in Section 2.4.1.1). The wind transfers momentum to the plasma, hindering accretion.

---

[1] The canonical parameters for a neutron star are $M_{\mathrm{NS}} = 1.4\,M_\odot$, $R_{\mathrm{NS}} = 10\,\mathrm{km}$. They are used for estimates throughout this thesis unless it is specified otherwise.

The surrounding matter will be halted at the *stopping radius*, R_{stop}, whose location depends on the balance of the ram pressure of the accreted plasma, P_{acc}, and the electromagnetic pressure, P_{mag}, imposed by the rotating magnetized neutron star (Lipunov 1987)

$$P_{\text{mag}}(R_{\text{stop}}) = P_{\text{acc}}(R_{\text{stop}}). \tag{2.8}$$

Depending on whether R_{stop} occurs inside or outside of R_l, it is determined by different processes. When R_{stop} lays outside of R_l, a pulsar wind of relativistic particles and magneto-dipolar waves that hold the matter away from the neutron star, creating a cavity. Due to the functional dependencies of P_{mag} and P_{acc} on the distance R from the center of the neutron star, the stable cavity is only possible if $R_{\text{stop}} < R_{\text{G}}$ (Lipunov 1992), meaning that the matter is stopped only after it was gravitationally captured. The stopping radius, in this case, is called *Shwartsman radius*, R_{Sh}, after Victoriy Shwartsman, who first considered this regime of interaction between a pulsar and the surrounding medium (Shvartsman 1970). The convenient expression is given, for example, by Khokhriakova & Popov (2022, see their Equation 5).

If the plasma is stopped inside R_l, magnetic pressure is defined by the dipole magnetic field, $P_{\text{mag}} \propto B^2 \propto \mu^2 R^{-6}$. In this case, R_{stop} obtained from Equation 2.8 is called the *Alfvén radius*, R_{A}, named after Hannes Olof Gösta Alfvén. Its expression depends on whether the stopping occurs before or after the gravitational capture of the matter, and can be written as (see, e.g., Lipunov 1992)

$$R_{\text{A}} = \begin{cases} \left(\dfrac{2\mu^2 G^2 M_{\text{NS}}^2}{\dot{M} v_\infty^5}\right)^{1/6}, & \text{for } R_{\text{A}} > R_{\text{G}}, \\ \left(\dfrac{\mu^2}{2\dot{M}\sqrt{2GM_{\text{NS}}}}\right)^{2/7}. & \text{for } R_{\text{A}} \leq R_{\text{G}}, \end{cases} \tag{2.9}$$

Here the first situation corresponds, for example, to the interaction of the Earth's magnetic field with the solar wind, while the second one is more typical for neutron stars in wind-fed High-Mass X-ray Binaries (see Section 2.4.2.1). The latter expression was derived by Davidson & Ostriker (1973) and Lamb et al. (1973) for the radially free-falling flow of a matter. The Alfvén radius denotes the characteristic size of the magnetosphere and sometimes is directly referred to as the *magnetospheric radius*. I follow this tradition, with the note that in reality, R_{A} is not described exactly by Equation 2.9. The expression may differ if one, for example, takes the orbital motion of the plasma into account (see, e.g., Equation 17 of Lamb et al. 1973). Campana et al. (2018) showed that for a number of X-ray sources the value of $0.5R_{\text{A}}$, where R_{A} is given by Equation 2.9, provides a good description for the magnetospheric radius. So far, the picture of the neutron star interaction with the surrounding plasma in the case $R_{\text{stop}} < R_l$ did not include stellar rotation. However, at the Alfvén radius $R = R_{\text{A}}$, the matter encounters the rotating magnetic field of the neutron star, which will attempt to bring it into the corotation. The distance at which the Keplerian velocity of the matter is equal to the neutron star rotational velocity is called the *corotation radius*

$$R_{\text{c}} = \left(\frac{GM}{\Omega^2}\right)^{1/3} \approx 1.7 \times 10^8 \left(\frac{P}{1\,\text{s}}\right)^{2/3} \text{cm}. \tag{2.10}$$

2.2.1.2 *Magneto-Rotational Classification*

The characteristic radii introduced in the previous section, R_{G}, R_{l}, R_{A}, R_{Sh}, and R_{C}, represent the basis for classifying the stages of the magneto-rotational evolution of a neutron star. The most general stages are *ejector*,

$$R_{\text{stop}} = \begin{cases} R_{\text{Sh}}, & \textit{for } R_{\text{stop}} > R_{\text{l}}, \\ R_{\text{A}}, & \textit{for } R_{\text{stop}} \leq R_{\text{l}}. \end{cases}$$

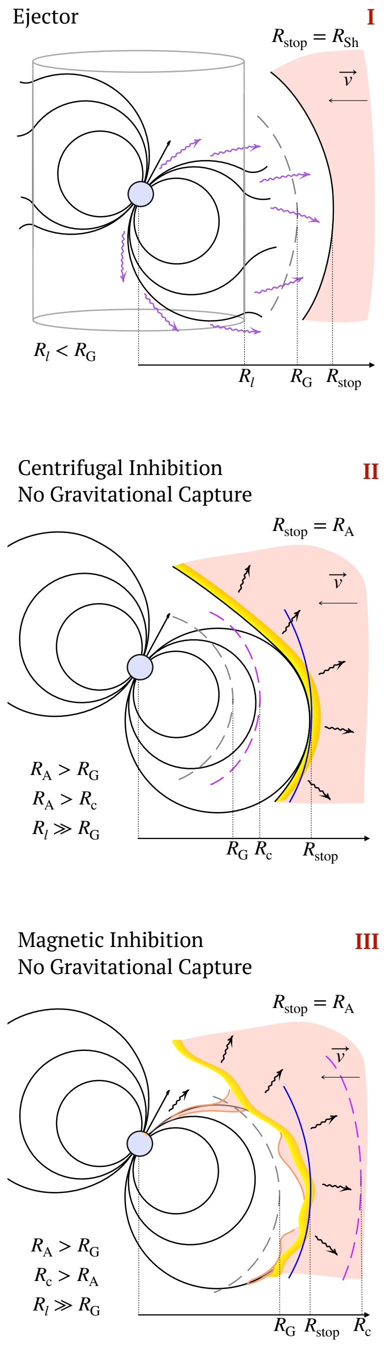

Figure 2.3: Stages of neutron star magneto-rotational evolution (part 1), from top to bottom: *ejector (case I)*, *centrifugal inhibition (case II, supersonic propeller)*, *without gravitational capture of the matter*, and *magnetic inhibition (case III, subsonic propeller)*, *without gravitational capture*. A detailed description of stages is given in the text.

propeller, and *accretor*. A newly born neutron star starts its life as an ejector with a powerful pulsar wind, which stops the surrounding plasma outside the light cylinder. Losing angular momentum to the ejection, the pulsar spins down sufficiently to allow the plasma inside R_L, which stops the ejection mechanism. The following intermediate stages are characterized by the loss of angular momentum to the plasma, interacting with the rotating magnetosphere. Finally, if a sufficient spin-down is achieved by this mechanism, the neutron star may become an accretor. The accretion can result in the spin-up of the neutron star due to the transferred angular momentum. The classification and the nomenclature of the intermediate evolutionary stages is notably inconsistent in the literature, sometimes even contradictory. In the following, I base the classification mainly on the group of works by Illarionov & Sunyaev (1975), Davies et al. (1979), Davies & Pringle (1981), Stella et al. (1986), Lipunov (1992), Harding & Leventhal (1992), Toropina et al. (2001), Ikhsanov (2001) Rutledge (2001), Toropina et al. (2003), Toropina et al. (2006), Bozzo et al. (2008), and Wang (2016), commenting, when possible, on inconsistencies between the used definitions. While the ejector and accretor have a less ambiguous definition, the term "propeller", which is meant to describe an intermediate stage of evolution, is used in a variety of ways. It was introduced by Illarionov & Sunyaev (1975) to describe the inhibition of accretion by a centrifugal barrier, created by the rapidly rotating magnetic field. They considered the situation when the matter is first captured by the gravitational field and then stopped at the magnetospheric boundary ($R_\mathrm{A} < R_\mathrm{G}$), rotating at the super-Keplerian velocity ($R_\mathrm{A} > R_\mathrm{C}$). Often, the condition $R_\mathrm{A} > R_\mathrm{C}$ is used as a definition of the propeller stage (see, e.g., Toropina et al. 2006; Lipunov 1992; Harding & Leventhal 1992). However, a much broader definition exists, based on the spin-down torques acting on the magnetosphere from the accretion flow, which play the main role in the change of angular momentum of the neutron star (see, e.g., Mori & Ruderman 2003; Davies et al. 1979). In this case, the condition $R_\mathrm{A}\Omega > c_\mathrm{s}(R_\mathrm{A})$ leads to a supersonic collision of the matter with the magnetosphere and the *supersonic propeller* regime, while $R_\mathrm{A}\Omega \leq c_\mathrm{s}(R_\mathrm{A})$ denotes the *subsonic propeller* (Davies & Pringle 1981). The latter corresponds to the condition $R_\mathrm{C} > R_\mathrm{A}$ (Ikhsanov 2001), which directly contradicts the first definition. Here I follow rather the first approach, defining the propeller as a regime, in which the plasma meets the centrifugal barrier in the vicinity of the rotating neutron star and is dragged (or repelled) away from the gravitational center[2]. This situation is called the *centrifugal inhibition* of accretion, as opposed to the *magnetic inhibition*. The latter acts when the neutron star has slowed down sufficiently to allow the plasma settling on to the magnetosphere, $R_\mathrm{C} > R_\mathrm{A}$ (Wang 2016). However, the magnetic field still halts the accretion in the absence of instabilities that transport matter across the magnetic field. This situation serves the definition of magnetic inhibition (Toropina et al. 2003). Centrifugal inhibition and magnetic inhibition are used in the literature to distinguish between some of the intermediate evolutionary regimes (see, e.g. Wang 2016; Bozzo et al. 2008). However, they suffer the most inconsistencies in usage, which is discussed below.

In the following, I will briefly describe various principal stages of the magneto-rotational evolution, making another attempt at the coherent classification. The corresponding sketches in Figure 2.3 (cases I–III) and

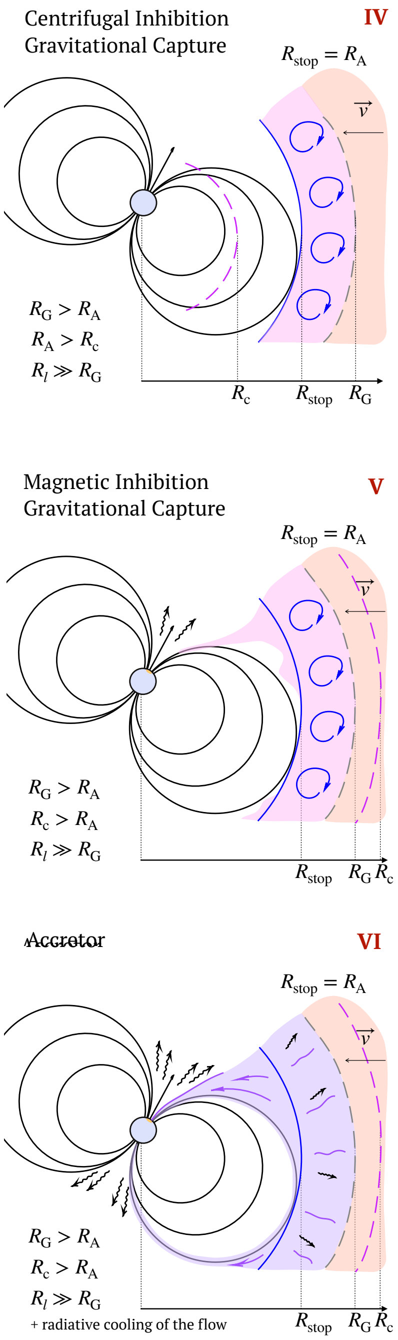

Figure 2.4: Stages of neutron star magneto-rotational evolution (part 2), from top to bottom: *centrifugal inhibition (case IV, supersonic propeller), with gravitational capture of the matter*, *magnetic inhibition (case V, subsonic propeller), with gravitational capture*, and *accretor (case VI)*. A detailed description of stages is given in the text.

---

[2] This definition would correspond to the supersonic propeller being classified as a propeller. However, not a subsonic propeller.

Figure 2.4 (cases IV–VI) accompany the description below.

Ejector (case I)

As was mentioned before, a neutron star is expected to be born as an ejector, with the ability to stop the surrounding plasma at distances greatly exceeding the light cylinder radius greatly exceeding ($R_l \ll R_{\rm stop}$, $R_{\rm stop} = R_{\rm Sh}$). A young pulsar with the strong dipolar field and fast rotational velocity is called an *ejector* due to the fast wind of the relativistic particles and the magneto-dipole waves radiated away along the open field lines. The energy losses powering the relativistic wind do not depend on the properties of the surrounding matter, but on the magnetic field and the rotational period of the neutron star $\dot{E} \propto \mu^2 P^{-4}$ (Davies & Pringle 1981). Typical examples of a neutron star at the ejector stage include radio and γ-ray pulsars (Section 2.4.1.1), including young pulsars in High-Mass X-ray Binaries (Section 2.4.2.4), as well as old neutron stars in close binaries with a low-mass companion, spun up by long historical episodes of accretion (Section 2.4.2.3).

Centrifugal Inhibition (Propeller), No Gravitational Capture (case II)

In case a neutron star spun down sufficiently so that the matter can penetrate inside the light cylinder, $R_{\rm l} > R_{\rm stop}$, the pulsar ejection mechanism is highly suppressed by the dense environment. Typically, at this stage the rotational period of the neutron star is still short, so the rotation of the outer magnetospheric boundary is super-Keplerian, $R_{\rm A} > R_{\rm C}$. The rapidly rotating magnetic field drags the surrounding plasma, frozen into the field, expelling it in the outflow and preventing the accretion. This process transfers the angular momentum to the plasma from the rotating neutron star, spinning it down. In case the magnetospheric radius is larger than the gravitational capture radius, $R_{\rm A} > R_{\rm G}$, the matter does not experience significant focusing by the gravitational field at $R_{\rm A}$. This regime – a propeller without gravitational capture – was studied by of Harding & Leventhal (1992), Toropina et al. (2006), Toropina et al. (2008), Mori & Ruderman (2003). It corresponds to the *supersonic propeller*. As was suggested by Harding & Leventhal (1992) and confirmed in the simulations of Toropina et al. (2006, 2008), in this case a bow shock is formed in front of the neutron star. At the same time, the propeller-generated outflow is pushed into the direction of the tail in a conical shock. (see Figure 2.5 and Toropina et al. 2006). The radiation of a dim bow shock is emitted in X-rays (Bozzo et al. 2008). The propeller regime without gravitational focusing is usually studied in the context of evolved high-velocity magnetars (see Section 2.4.1.3), whose strong magnetic field allow for the condition $R_{\rm A} > R_{\rm G}$. The observability of objects under such conditions, as well as their principal existence, is still uncertain. As an example, it would require an evolved old magnetar with still strong magnetic field $B \sim 10^{15}$ G and very long periods of $P \gtrsim 100$ s. Such high fields of old magnetars might contradict our current understanding of the strong magnetic field evolution, which expects to decay in on shorter time scales.

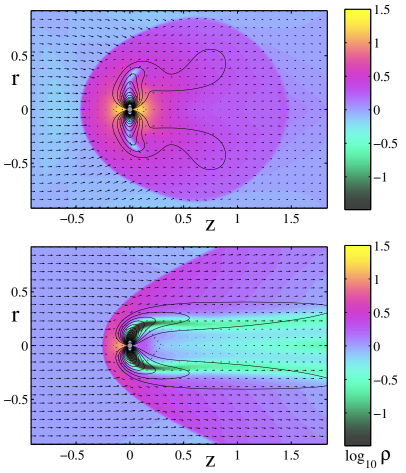

Figure 2.5: Flow of matter surrounding a neutron star with the strong, magnetar-like magnetic field in the propeller regime ($R_{\rm C} < R_{\rm A}$), with $R_{\rm A} > R_{\rm G}$ (no gravitational capturing above $R_{\rm A}$) for Mach numbers. *Top*: $\mathfrak{M} = 1$, *bottom*: $\mathfrak{M} = 3$. The spatial scales are given in $R_{\rm G}$. Figure 1 from Toropina et al. (2006).

Magnetic Inhibition (Georotator), No Gravitational Capture (case III)

If the spin-down rate at the propeller stage at $R_{\rm A} > R_{\rm G}$ is sufficient, a neutron star can extend its corotation radius outside of the Alfvén surface. In this case, the surrounding medium does not encounter a centrifugal barrier at the magnetospheric boundary. Potentially, it can be accumulated at the Alfvén surface and penetrate inside the magnetosphere. However, there are two principal effects limiting the possibility of accretion in this case. First, without gravitational focusing, the cross section of the interaction is greatly reduced. Secondly, even in the absence of fast rotation, the magnetic field can halt the plasma, not letting it inside the magnetosphere. Such magnetic inhibition can be overcome if the plasma develops a sufficient cool-down mechanism, after which the direct accretion begins (Ikhsanov 2007). However, in this state of magnetic inhibition, the leakage of the matter inside the magnetosphere is possible via the Kelvin-Helmholtz instability (Harding & Leventhal 1992), direct accretion onto the polar caps, or Bohm diffusion (see Toropina et al. 2003, and references therein). This regime of the magnetic inhibition in the absence of fast rotation and gravitational focusing is also termed in the literature as *magnetic plow* (Toropina et al. 2001) and *georotator* (see, e.g., Lipunov 1992). The magnetosphere again represents an obstacle to the flow of matter and a bow shock forms. The simulations by Toropina et al. (2001) showed that the magnetic lines are stretched downwind into the magnetotail, where some energy release is possible due to reconnection (see Figure 2.6). Harding & Leventhal (1992) suggested that accretion of the matter in this case can happen at rates increasing with higher velocities, $\dot{M} \propto v^{1/3}$ (so-called *magnetic accretion*; Rutledge 2001). Toropina et al. (2001) showed that although no matter is accumulated at the shock, a small amount of the incoming flux can be accreted at the upwind pole at rates, substantially higher than for the regular accretion in a gravitational field (Bondi-Hoyle-Lyttleton accretion, see Section 2.3.4.1). The total energy release, including the radiation of the bow shock and reconnection in the magnetotail is, however, extremely low, $L \sim 10^{21}$–$10^{24}\,\mathrm{erg\,s^{-1}}$. The problem discussed in case II and related to the existence of the old neutron stars with substantially low rotational periods, but still magnetar-like magnetic fields, $B \sim 10^{14}\,\mathrm{G}$, is even more acute for this case.

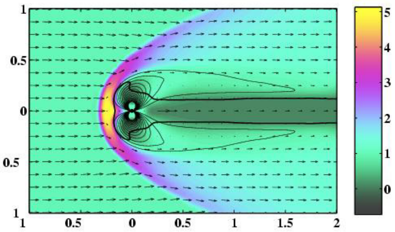

Figure 2.6: Flow of matter around a magnetize, $B = 10^{14}\,\mathrm{G}$, neutron star in the regime of the magnetic plow (magnetic inhibition, $R_\mathrm{C} > R_\mathrm{A}$), with $R_\mathrm{A} > R_\mathrm{G}$ (no gravitational capturing above R_A) for $\mathfrak{M} = v/c_\mathrm{s} = 3$. A solid thick black line indicates the stretched downwind Alfvén surface. Figure 8 from Toropina et al. (2001) © AAS. Reproduced with permission.

Centrifugal Inhibition (Propeller), Gravitational Capture (case IV)

If the magnetic field of the neutron star is not high enough for $R_\mathrm{A} > R_\mathrm{G}$ to hold, the star can pass similar stages of the centrifugal and magnetic inhibition as discussed above on the way of its spin-down, but with the effect of gravitational focusing. The situation given by $R_\mathrm{G} > R_\mathrm{A} > R_\mathrm{c}$, represents a classical propeller case, considered in the context of (moderately) magnetized neutron stars accreting in the binary system (Davidson & Ostriker 1973; Illarionov & Sunyaev 1975). This regime was studied intensively in theoretical works and numerical simulations (see, e.g., Davies et al. 1979; Davies & Pringle 1981; Romanova et al. 2003). It is also known as the *supersonic propeller*, same as for the case of centrifugal inhibition without gravitational focusing. When the radial flow falls onto a neutron star at $R < R_\mathrm{G}$, the matter accumulates in a quasi-static envelope as it cannot penetrate under the centrifugal barrier. As a result of the interaction with the envelope, the neutron star spins down, losing the rotational energy. The energy is mainly transferred to the envelope. The heated surrounding shell is convective, that is, the energy transport outwards happens not by radiative losses, but by large-scale circulatory motions (Davies & Pringle 1981). Simulations by Romanova et al. (2003) showed the existence of a propagating outward shock wave, separating the free fall zone and the inner region. The authors demonstrated the formation of the convective shell in the inner region due to a supersonic equatorial outflow of the matter, repelled by the magnetic field and reflected from the shock wave (see Figure 2.7). Romanova et al. found that a very small fraction of the infalling flow, $\dot{M}/\dot{M}_\mathrm{c} \propto P$, can be accreted to the surface of the neutron star, depending on the rotational period. The propeller

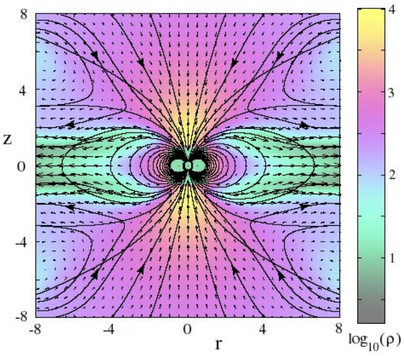

Figure 2.7: Matter flow around gravitating propeller ($R_\mathrm{G} > R_\mathrm{A}$). Contours with arrows show the streamlines of the flow. Figure 6 from Romanova et al. (2003) © AAS. Reproduced with permission.

regime with gravitational capturing is well known and observed for a number of transient X-ray pulsars, such as V 0332+53 and 4U 0115+63. See Stella et al. (1986), Tsygankov et al. (2016), and Campana et al. (2018) for more details.

Magnetic Inhibition, Gravitational Capture (case V)

When a sufficient spin-down is achieved at the propeller stage, the corotation radius moves above the magnetosphere, $R_\mathrm{c} > R_\mathrm{A}$. Until the quasi-static envelope around the magnetosphere, which was developed during the propeller stage, cools down significantly, $T \leq 0.3T_\mathrm{ff}(R_\mathrm{A})$, where T_ff is a free-fall temperature (Elsner & Lamb 1976), the accretion of the plasma onto the surface will be limited. The power lost to the friction between the slowly rotating magnetosphere at the base of the envelope still can serve as an energy deposition for the plasma. However, it is not the centrifugal barrier that limits the matter penetration inside the magnetosphere, but the magnetic field itself. This regime was addressed by Davies et al. (1979), Davies & Pringle (1981) as a *subsonic propeller*. Here I would like to note, for the sake of consistency, that according to this classification, the regime of magnetic inhibition without gravitational capture (case II) can be addressed with the same term. Ikhsanov (2001) found that in the regime of magnetic inhibition, the plasma can penetrate the magnetosphere via diffusion and magnetic reconnection, resulting in sufficient mass-accretion rates onto the poles so the source would be observed as a low-luminosity persistent X-ray pulsar ($L \sim 10^{33}\,\mathrm{erg\,s^{-1}}$). In this case, torques due to accretion can even dominate over the spin-down torques. Simulations by Toropina et al. (2003) showed, similar to the previous propeller case, the formation of the shock wave propagating outwards. However, a fully subsonic spherical flow is established between the shock and the magnetosphere (see Figure 2.8). Toropina et al. also showed that a fraction of the captured plasma penetrates the Alfvén surface and is accreted in two conical flows onto magnetic poles with the rate scaling as $\dot{M}/\dot{M}_\mathrm{c} \propto (R_\mathrm{NS}/R_\mathrm{A})^5$. On the other hand, Shakura et al. (2013a) suggested that plasma can also penetrate through the equatorial region at small rates, determined by the ratio of the free-fall time t_ff to the characteristic plasma cooling time t_cool as $\dot{M}/\dot{M}_\mathrm{c} \approx (t_\mathrm{ff}(R_\mathrm{A})/t_\mathrm{cool}(R_\mathrm{A}))^{1/3}$, translating into luminosities $L \lesssim 10^{36}\,\mathrm{erg\,s^{-1}}$ Shakura et al. (2015). The cooling time depends on the dominated cooling process of the shell, such as bremsstrahlung or inverse Compton scattering. After a sufficiently low temperature is reached by the envelope, the convective motions stop and open the avenue for the direct stable accretion. This regime can be realized in moderate and low-luminosity sources, such as High-Mass X-ray Binaries Vela X-1, GX 302−1, and Supergiant Fast X-ray Transients (Shakura et al. 2015). The low-rate accretion onto the poles described by Ikhsanov (2001) could operate in the quiescent state of Be X-ray Binaries, such as GX 304−1 and A 0535+262 (see also Stella et al. 1986).

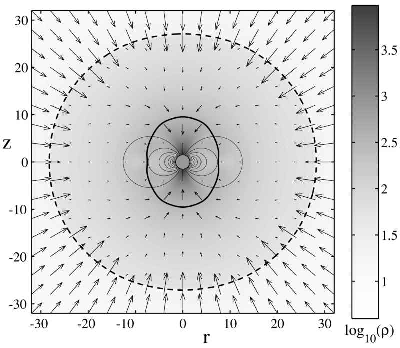

Figure 2.8: Matter flow around a neutron star in magnetic inhibition with gravitational capturing (case V, $R_\mathrm{G} > R_\mathrm{A}$, $R_\mathrm{C} > R_\mathrm{A}$, warm envelope around the magnetosphere). A solid thick black line indicates the Alfvén surface. Figure 2 from Toropina et al. (2003) © AAS. Reproduced with permission.

Accretor (VI)

After efficient cooling (usually, Compton cooling) develops in the envelope plasma around the magnetosphere, a lower temperature is established in the absence of convection. This allows the onset of Rayleigh-Taylor instability of the magnetospheric boundary that is expected to be an efficient mechanism for plasma penetration inside the magnetosphere (Elsner & Lamb 1976). The plasma enters the magnetosphere at high mass accretion rate $\dot{M} \sim \dot{M}_\mathrm{c}$ and is channeled by the field lines onto the magnetic poles, where it decelerates to the rest. Some details on possible deceleration mechanisms are given in Chapter 3. The resulting luminosity is then determined by the mass-accretion rate and the gravitational field of the neutron star, $L \propto G\dot{M}$ (see more detail in Section 2.3). Toropina et al. (2012) simulated direct accretion onto magnetized neutron stars, $B \sim 10^{12}$ G, moving through the medium. They found that such a regime is characterized by enhanced accretion onto a downstream pole, which deforms the magnetic field, pushing it outwards and provoking oscillations (see Figure 2.9). These oscillations are translated to a change of $\dot{M}$. The average value of the mass-accretion rate for one of the main cases was $\dot{M} \approx 0.45\dot{M}_\mathrm{c}$. Accretion onto a neutron star from the wind of a binary companion is also extensively studied with numerical simulations, demonstrating the deviation of $\dot{M}$ from $\dot{M}_\mathrm{c}$ (see, e.g., Bozzo et al. 2016) and its variability (El Mellah et al. 2018). The accreted matter inserts torques onto the magnetosphere and transfers the angular momentum to the neutron star (Postnov et al. 2014, see also their expressions for torques at different accretion regimes). A noticeable spin-up due to the transferred momentum is possible.

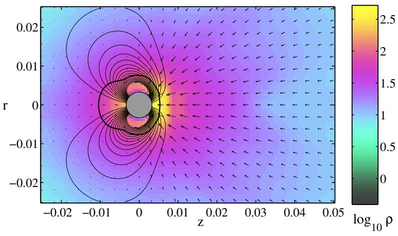

Figure 2.9: Matter flow around an accreting magnetized ($B = 10^{12}$ G) neutron star. A think black line shows the Alfvén surface ($R_\mathrm{G} \gg R_\mathrm{A}$, $R_\mathrm{c} \gg R_\mathrm{A}$). Figure 4 from Toropina et al. (2012).

2.2.1.3 *Final Remarks on the Classification*

In this way, the main evolutionary path of a neutron star is characterized by a series of spin-down phases, before it can accrete and gain angular momentum. The discussed stages II–III and IV–V rather represent alternative paths, corresponding to high ($B \sim 10^{14}$ G) and moderate ($B \sim 10^{11}$–10^{12} G) magnetic field values, respectively. Transitions between these paths are also possible: for example, from the propeller in case II to the propeller in case IV or magnetic inhibition in case V, if a significant field decay is in play. Moreover, some stages on the way from *ejector* to *accretor* are conditional. The path I→IV→V→VI can instead be I→V→VI or I→IV→VI, or even I→IV↔V→VI, depending on the conditions met. Possible hints for the transitions between the magnetic inhibition and direct accretion (IV↔V) are known for Supergiant Fast X-ray Transients and Be X-ray Binaries, denoting the quiescence/outburst behavior. More exotic rapid jumps between the ejector and the accretor stage are observed in transitional Millisecond Pulsars (Dubus 2015).

The picture outlined above is still greatly simplified and lacks some other possible evolutionary stages. For example, taking into account the magnetic field of the matter flow itself, allows one to investigate different accretion regime. In this case the gravitationally captured magnetized flow is decelerated well above the magnetospheric radius by its own amplified magnetic field. After that, accretion in the settling regime can occur. This regime was studied by Shvartsman (1971a), Bisnovatyi-Kogan & Ruzmaikin (1976), and Igumenshchev et al. (2003) and is suggested to explain observational properties of Be X-ray Binary SXP 1062 (Ikhsanov 2012).

Davidson & Ostriker (1973) suggested that accreting neutron stars are expected to have rotational periods, close to the equilibrium value, which should correspond to $R_\mathrm{A} \approx R_\mathrm{c}$. Later, Davies et al. (1979) and Davies & Pringle (1981) noted that due to various evolutionary paths, which can lead to the stable accretion and different types of the spin-down torques at these stages, the equilibrium value needs to be defined by taking into account the spin-down history of a pulsar. The second difficulty with the condition given by Davidson & Ostriker (1973), is that, as one can see from the numerical magneto-hydrodynamic simulations, in reality, the Alfvén radius is not simply defined by Equation 2.9. The Alfvén surface may have a complicated shape.

I would like to note once again that the term *magnetic inhibition* was understood in the literature in different ways, leading to the inconsistent classification between different work. Thus, Bozzo et al. (2008) suggested that the propeller in case II needs to be considered as magnetic, but not centrifugal inhibition, which was later adopted by Kretschmar et al. (2019). Here I argue, however, that magnetic inhibition was evoked in earlier works to specify the stopping power of the magnetic field itself, even in the absence of rotation (Toropina et al. 2003). Moreover, it was specified in works, such as Stella et al. (1986), Wang (2016) that the magnetic inhibition acts when $R_c > R_A$ and the centrifugal barrier is unimportant during the plasma-magnetosphere interaction.

2.2.2 *Magneto-Thermal Evolution*

The assumption used in the previous sections is that the magnetic field of the neutron star does not change on the timescales of the considered processes. Although in many cases it is a valid approximation, in general, this might not be true. The evolution of the neutron star magnetic field can be complex, non-linear, and highly dependent on the initial field structure and strength. On the long timescales, the field of a neutron star tends to decay, providing an additional heating of the neutron star interiors via Joule effect (Miralles et al. 1998). It increases the temperature of the magnetic poles due to anisotropic heat transfer and thus enhances the pulsed thermal emission in X-rays. In the case of the magnetic poles being heated by the bombardment of the atmospheric particles, the developed thermal gradient across the caps, misaligned with the radial density one, can result in the significant local magnetic field enchantment due to the Biermann battery effect (see De Grandis et al. 2020, and Figure 2.10). The evolution of the magnetic field is inevitably coupled with the thermal evolution, also because of the magnetic field influence on the thermal conductivity and cooling of the crust (Potekhin et al. 2015).

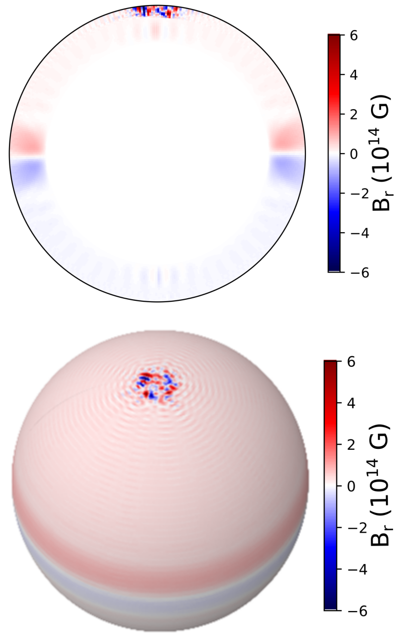

Figure 2.10: Radial component of the magnetic field for a neutron star with the large-scale quasi-dipolar magnetic field, $B \approx 10^{12}$ G, during the outer heating by the magnetospheric particles bombardment. The small magnetic structure with the values up to $\sim$a few 10^{14} G is developed due to the Biermann battery effect. Figure 13 from De Grandis et al. (2020) © AAS. Reproduced with permission.

As was mentioned in Section 2.1.4, the magnetic field in principle can exist in the crust and the core of a neutron star. A crust-confined magnetic field is easier to treat theoretically and was assumed in the majority of the models related to the magnetic field structure and evolution (see, e.g., Viganò et al. 2013; Lander & Gourgouliatos 2019; Gourgouliatos et al. 2016). Electrons are the only free charge carriers in the solid lattice of the neutron star crust. In this case, Ohmic dissipation and the Hall effect are the main drivers of the field evolution. This process is usually described by the so-called *Hall-MHD induction equation*, derived from Faraday's and Ohm's laws (see, e.g., Igoshev et al. 2021b)

$$\frac{\partial \mathbf{B}}{\partial t} = c\nabla \times \left(\frac{1}{4\pi e n_e}(\nabla \times \mathbf{B}) \times \mathbf{B} + \frac{c}{4\pi\sigma}\nabla \times \mathbf{B} \right), \tag{2.11}$$

where e is the elementary charge, n_e is the electron number density, and σ is the electrical conductivity. Here, two terms on the right-hand side correspond to the Hall effect and Ohmic dissipation, respectively. The Ohmic term describes the gradual linear field decay on the long timescales. The more complex Hall evolution, although based on the non-dissipative effect, involves turbulence-like processes, which redistribute the magnetic energy from large to small scales (forward cascade) and vice versa (inverse cascade) (Igoshev et al. 2021a). The forward cascade is responsible for the field decay, while the inverse one can lead to field enhancement. However, the Hall term is important mainly for high magnetic fields $B \gtrsim 10^{14}$ G. As noted by Igoshev et al., Equation 2.11

describes the evolution of the total field within the neutron star, which is much larger than the observable part extended outwards.

In case the magnetic field confined to the core is considered, the description of the evolution becomes less trivial. The outer part of the core is a multicomponent superfluid, where electrons, protons, and neutrons move in a different way. As I mentioned in Section 2.1.3, the magnetic field is quantized in flux tubes due to the superconductivity of the core. The interaction of these tubes with the other components of the fluid is not well understood and may have a significant influence on the magnetic field evolution (Glampedakis et al. 2011, and references therein). The recent detailed numerical simulations by Viganò et al. (2021) included, for the first time, both crustal magnetic field evolution and the ambipolar diffusion in the outer core, lacking, however, the effects of superfluidity.

Accretion of matter from the surrounding medium can also significantly affect the field decay. The suppression of the magnetic field by the intense accretion was proposed to explain the discovery of young weakly magnetized neutron stars near the geometrical centers of the associated supernova remnants (see Section 2.4.1.4). Chevalier (1989) suggested that a short episode of the high-rate accretion onto a newly born ($\sim$10 days) neutron star can occur when the reverse shock after the supernova event reaches the center of the explosion (fall-back). The neutron star in these conditions can accrete up to $\sim 0.1\,M_\odot$ of matter, the pressure of which near the surface exceeds the magnetic field pressure. In this case, the field stays "hidden" in the crust, until it diffuses back to the surface. PSR 1734$-$3333, a pulsar with possibly rapidly growing magnetic field, might be one example of the field recovery after the fall-back (Gao et al. 2017).

Another example of the field decay due to the accretion are Millisecond Pulsars, which are mainly old neutron stars with low fields, $B \sim 10^8$–10^{10} G, spun up by long episodes of stable accretion in a binary system (Section 2.4.2.3). However, for younger ($\sim 10^6$ yr) neutron stars in High-Mass X-ray Binaries, there seems to be no significant field decay (Ye et al. 2019). This is likely related to the fact that Millisecond Pulsars accrete a greater amount of matter over their lifetime, $\sim$0.1–0.8 $M_\odot$ versus $\sim 10^{-3}\,M_\odot$ for High-Mass X-ray Binaries (see Igoshev et al. 2021b, and references therein). An empirical law, suggested by Shibazaki et al. (1989),

$$B = \frac{B_0}{1 + \dot{M}t/m_\mathrm{B}}, \tag{2.12}$$

where B_0 is the initial field strength and $m_\mathrm{B} \approx 10^{-4}\,M_\odot$ is the field decay constant, describes well the evolution of the magnetic field decay under the accretion (see also the alternative expression given by Equation 17 of Aguilera et al. 2008).

Standard cooling theories, which consider cooling by direct or modified URCA processes and do not take the magnetic field into account, predict that on a scale of hundreds of years, neutron star's interiors become isothermal and the cooling occurs via thermal emission from the entire surface, together with neutrino emission (see, e.g., Yakovlev & Pethick 2004). However, observations of isolated X-ray bright neutron stars show the existence of the periodically pulsating thermal emission component, hinting at the non-homogeneous temperature distribution across the surface. This inhomogeneity could be created, for example, by previous episode of accretion, by the bombardment of the poles with the streaming charged particles in the magnetosphere, or by the internal heating provided by the magnetic field decay. The magnetic field also affects the thermal conductivity of the neutron star crust, by imposing

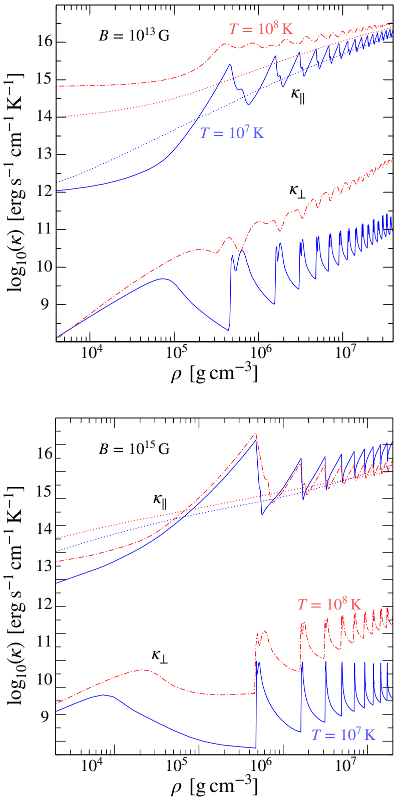

Figure 2.11: Electron thermal conductivity of a plasma in high magnetic fields for perpendicular (upper) and parallel (lower) to the magnetic field transport. Dash-dotted red lines correspond to the electron temperature $T = 10^7$ keV, solid blue lines to the $T = 10^8$ keV. Dotted lines show the non-magnetic case. *Top:* $B = 10^{13}$ G, *bottom:* $B = 10^{15}$ G. Figure 9 from Potekhin et al. (2015). Reproduced with permission from Springer Nature.

the quantization of electrons onto Landau levels. This results from the dependency of the thermal conductivity on the opacity $\varkappa$ (Potekhin et al. 2015),

$$\kappa = \frac{16\sigma_{\rm SB} T^3}{3\rho\varkappa}, \tag{2.13}$$

where $\sigma_{\rm SB}$ is the Stefan-Boltzmann constant and ρ is the density of the medium. As will be shown in detail in Chapter 4, the electron opacities in the strong magnetic field are highly anisotropic and have a resonance nature due to transitions between Landau levels. Figure 2.11 illustrates how the dependency of the thermal conductivity on the density of the plasma changes in the high magnetic field, compared to the non-magnetic case. Very high magnetic fields ($B \gtrsim 10^{14}$ G) are also capable of modifying the neutrino emission, by influencing URCA processes, synchrotron neutron radiation, and pair annihilation. Recent reviews by Potekhin et al. (2015) and Potekhin et al. (2020) are recommended for more details on the current studies of neutron stars cooling and heat transport.

To model a combined magneto-thermal evolution, one needs to couple the induction equation (for example, as given by Equation 2.11 for the crust-confined field) and the heat transport equation. Multiple simulations on the base of this approach are discussed in the work of Pons & Viganò (2019, which is also provides a comprehensive review on the magnetic, thermal, and rotational evolution of non-accreting neutron stars). Detailed modeling of the magneto-rotational evolution by Viganò et al. (2013) showed that the observed phenomenological diversity of such isolated neutron stars as Magnetars, Rotation-Powered Pulsars with high magnetic fields, and The Magnificent Seven (see Section 2.4.1) can be explained by varying only the initial magnetic field, mass, and ocean composition within their model. Three-dimensional simulations by De Grandis et al. (2020) presented the evolution of hot spots produced by the magnetic energy deposition or the external heating of the polar regions on the surface of a neutron star. The modeling showed that the spots can have a complex shape and drift, following the magnetic field lines. Figure 2.12 shows an example of the evolution of the cooling hot spot after its external heating[3].

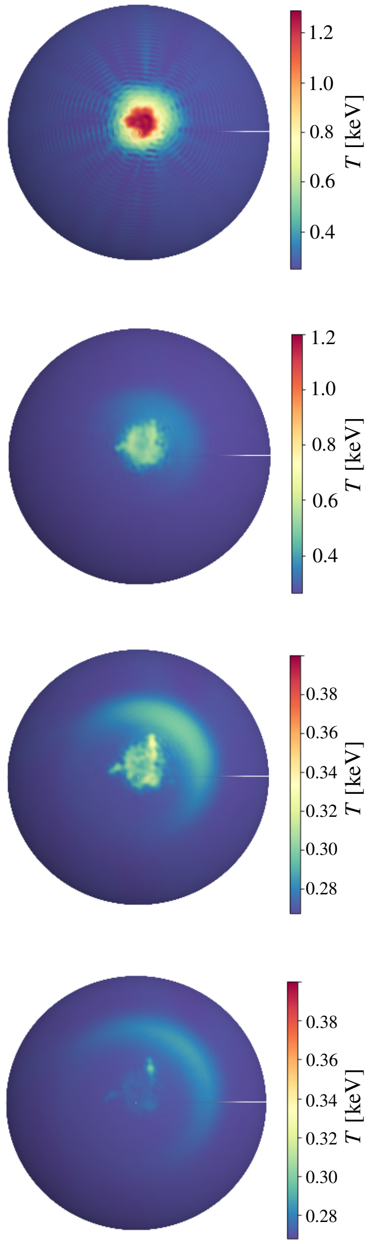

Figure 2.12: Cooling of a polar spot on the surface of a neutron star with a dipole-like large-scale field $B \simeq 10^{12}$ G, after the heat injection from above. The snapshots are give with 300 yr, starting from the time when the heating stopped. The first snapshot corresponds to the magnetic field distribution presented in Figure 2.10. Figure 12 from De Grandis et al. (2020) © AAS. Reproduced with permission.

2.3 MASS EXCHANGE IN CLOSE BINARIES

A significant number of massive stars are born in binary systems (up to 100%, see, e.g., Mason et al. 2009, with a lower limit placed at ∼21%, Mahy et al. 2013), which implies that a high number of neutron stars originates from binaries. Two stellar objects, being gravitationally bound, are considered a "close" system if the conditions for the mass transfer between the components occur during their lifetime. Tutukov & Yungelson (1973) and van den Heuvel & De Loore (1973) described the possible evolutionary scenario for the formation of a binary pulsar system. This scenario starts from two massive early-type stars, followed by the individual evolution of the components, modified by the presence of the mass exchange. Over the past decades, this scenario was accepted as the "standard" one (Postnov & Yungelson 2014). Binary systems that consist of a neutron star and a massive early-type (O/B) star are the intermediate stage of this evolutionary path and the main focus of the present work.

---

[3] This heating could be produced by the backflow of the particle streaming in the magnetosphere, or by the episode of accretion

In this section, I will address the potential of a binary system (Section 2.3.1) and how it changes due to the orbital motion (Section 2.3.2). Then, I will briefly describe a standard evolutionary scenario, which contains a High-Mass X-ray Binary as one of the intermediate stages (Section 2.3.3). After that, I will address accretion which can proceed in a binary system (Section 2.3.4).

2.3.1 *Roche Potential*

The opened avenue for the mass transfer in close binaries can significantly affect the evolutionary paths of the components. This is crucial for the understanding of many observational phenomena, both among regular stellar binaries (see, e.g., Pustylnik 1998, for the Algol paradox) and among the systems with a compact companion. The interaction between the binary companions is determined by gravitational and centrifugal forces. For a circular orbit and synchronized rotation, the total potential is well approximated by the Roche potential. In a cartesian co-rotating reference frame with the origin defined by the position of the more massive ("primary") star, the x-axis along the line connecting the center of the companions, and z-axis perpendicular to the orbital plane, the Roche potential can be written as (see, e.g., Postnov & Yungelson 2014)

$$\Phi = -\frac{GM_1}{|\vec{r}_1|} - \frac{GM_2}{|\vec{r}_2|} - \frac{1}{2}\Omega_{\rm orb}^2 \left((x-\mu a)^2 + y^2\right), \tag{2.14}$$

where $\Omega_{\rm orb} = 2\pi/P_{\rm orb}$, $a = |\vec{r}_1 - \vec{r}_2|$ is the binary separation, and $\mu = M_2/(M_1 + M_2)$ is the reduced mass. Figure 2.13 shows an example of the three-dimensional Roche potential, together with the two-dimensional slice through the orbital plane of a binary system ($z = 0$) with equipotential lines. The Lagrangian points indicate the intersections of the equipotential lines. The L_1 point is the most important for the evolution of a binary system as it introduces the possibility of mass and angular momentum transfer. This saddle point denotes the minimum energy for the particle to be bound to the binary system, but not to any of the individual masses M_1 and M_2. The *critical lobe* or *Roche lobe(s)* is defined as the equipotential contour containing the L_1 point. In case one of the components in a binary system is close to filling its critical lobe (known as "Roche lobe overflow"), it can loose the matter through L_1. This matter will be accreted onto a binary companion, likely via formation of an accretion disk due to the high angular momentum brought by the accreted plasma. In this situation, the shape of the stellar surface itself is defined by the shape of the Roche potential.

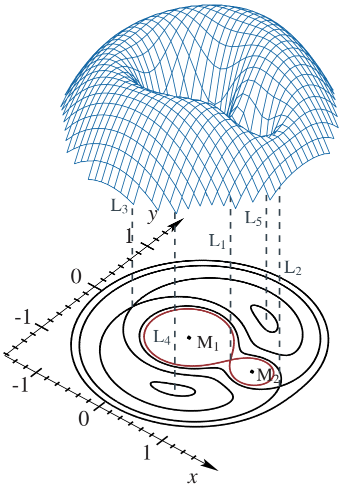

Figure 2.13: Roche potential (blue surface) for masses M_1 and M_2, shown with the equatorial cross section, corresponding to the orbital plane. The red line indicated the critical lobe with the L1 point. This illustration is reproduced based on the work of Bissinger (2016), with the usage of their script.

2.3.2 *Orbital Motion*

So far, the treatment of the binary system was limited to a circular orbit, when components keep the same distance to each other at all phases of orbital motion. In this case, the Roche potential stays the same at all orbital phases, fully defined by the mass ratio $q = M_1/M_2$ and the binary separation a. This situation does not represent a general case, especially for binary systems with neutron stars, whose formation was likely accompanied by a kick and can result in highly-eccentric orbits (Lai et al. 2001, and references therein). The motion of two gravitationally bound point-like masses M_1 and M_2 is described by Keplerian laws. Due to the condensed nature of stellar objects and typically non-relativistic orbital velocities, this problem is well treated by Newtonian theory.[4]

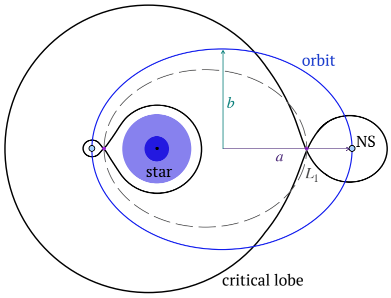

Figure 2.14: Sketch of the Roche (critical) lobes in the periastron and apoastron of a binary system with a neutron star. Based on Figure 2 of Okazaki & Negueruela (2001).

This task is known to be equivalent to the problem of the reduced mass μ_m motion in the external gravitational field. The solution of this problem which gives the parameters for the elliptical motion of a mass M_1 around M_2, with M_2 located in one of the focus points of the ellipse. In this way, we generally treat a motion of a neutron star in a binary system as a motion in an elliptical orbit with the eccentricity e and orbital period P_orb around the non-degenerate companion. The (maximum) binary separation is now redefined via the semimajor axis of the ellipse a. For more information on the orbital motion and orbital parameters, the reader is referred to the thorough introduction by Bissinger (2016). However, it is important to note that due to the typical non-zero eccentricity, the separation of the two components can significantly change during the orbital revolution. This leads to a change of the Roche potential. Figure 2.14 illustrates the situation, where near the apoastron (maximum separation) the Roche lobes of the companions are much larger than in the periastron (minimum separation). This may result in Roche lobe overflow for the regular star at the periastron passage, provoking sporadic accretion onto the neutron star (see, e.g., Okazaki & Negueruela 2001).

2.3.3 *Standard Evolutionary Scenario for HMXBs*

As was mentioned before, the possibility of such accretion events is an important modification of the stellar evolution in a binary system. Here I briefly outline the main stages of the standard evolutionary scenario that involves the core-collapse supernova explosion and passes the stage of the High-Mass X-ray Binary with a neutron star, leading to the possible formation of a binary pulsar. In this description, I mainly follow the work of Postnov & Yungelson (2014), which is recommended for more detailed description.

The standard evolutionary scenario starts with a detached binary of early-type stars. After the primary star burns out hydrogen in the central part of its core and leaves the main sequence, it expands, filling its Roche lobe. The Roche lobe overflow[5] allows for the mass transfer from the evolved primary to the secondary star. This results in the loss of a hydrogen envelope by the primary, which becomes a helium Wolf–Rayet, and the spin-up of the secondary (rapidly rotating Be star, see Section 2.4.2.1). After the massive Wolf–Rayet star ends its life in a core-collapse supernova explosion, the system, becomes a neutron star binary if it survives the supernova kick. A young neutron star can halts the plasma of the companion's wind by the ejector mechanism (see Section 2.2.1), until it spins down significantly. During this (short) phase, the system can be observed as a Gamma-ray Binary (Section 2.4.2.4), where γ-ray emission is produced in the shock of colliding pulsar and stellar winds.

The subsequent stage of the system evolution is a High-Mass X-ray Binary, when the neutron star can accrete from the companion, producing bright, often pulsating, X-ray emission. It is important to note that accretion at this stage can proceed not only via Roche lobe overflow but also via the powerful stellar wind emitted by the O/B star (see Section 2.3.4.1 for more details on wind accretion). When the secondary star evolves

---

[4] This, however, does not apply to the relativistic systems, which consist of two compact objects and can be brought into contact within a Hubble time (Benacquista & Downing 2013), such as binary pulsars.

[5] The interaction of binary components at this stage is also possible via a common envelope (see, e.g., Postnov & Yungelson 2014).

into a supergiant, it expands and includes the neutron star into a common envelope. Two possible consequent scenarios are the formation of the Wolf–Rayet/neutron star binary inside the expanding envelope or the merging of the neutron star with a helium core (the hypothetical Thorne–Żytkow object; Thorne & Zytkow 1977). The Wolf–Rayet/neutron star binary evolves when the Wolf–Rayet star undergoes a supernova explosion. If the system survives the second supernova event, it becomes a binary pulsar (Double Neutron Star, DNS), whose evolution is mainly defined by the emission of gravitational waves, leading to a neutron star merger.

2.3.4 *Accretion*

Now I focus on the intermediate stage of this evolutionary scenario, a High-Mass X-ray Binary, that allows for a mass transfer from the non-degenerate companion to the neutron star. The way the mass is transferred mainly depends on its velocity, angular momentum, and the proximity of the binary components. Accretion onto a neutron star is a powerful source of X-ray radiation. The potential energy release can be expressed in terms of *accretion luminosity*, which is given by the potential energy acquired by the accreted matter $\dot{M}$ in the gravitational field

$$L_{\mathrm{acc}} = \frac{GM_{\mathrm{NS}}\dot{M}}{R_{\mathrm{NS}}}, \tag{2.15}$$

where G is the gravitational constant. In general, for accreting neutron stars, Equation 2.15 provides a good estimate for the energy release at a given $\dot{M}$. The mass-accretion rate here is to be understood as the rate of the matter supply passing the magnetospheric boundary. Section 2.3.4.1 and Section 2.3.4.3 illustrate that it may significantly differ from the rate, given by the mass loss of a donor star. However, the accretion process near the surface of the neutron star can be accompanied by energy losses, for example, to the deep heating of the non-equilibrium crust (see, e.g., Haensel & Zdunik 2008) and particle acceleration in shock regions (Blandford & Eichler 1987). In this way, L_{acc} can be understood as an upper limit on the luminosity, emitted by the accreting neutron star at a given $\dot{M}$.

It is important to note that there is also a principal limit to the mass-accretion rate, provided by the interaction of the emitted radiation and accreted matter. The classical *Eddington luminosity*

$$L_{\mathrm{Edd}} = 4\pi\frac{GM_{\mathrm{NS}}cm_{\mathrm{p}}}{\sigma_{\mathrm{Th}}} \approx 1.3\times10^{38}\left(\frac{M}{M_{\odot}}\right)\,\mathrm{erg\,s^{-1}}, \tag{2.16}$$

where σ_{Th} is the Thomson scattering cross section, m_{p} is a proton mass, describes the situation when the radiation field is capable of stopping the spherical accretion of pure hydrogen plasma by elastic electron scattering (see, e.g., Frank et al. 2002). Equation 2.16 provides only a crude estimate for the limiting luminosity L_{crit}, that may differ significantly due to more complex chemical composition of the plasma, other dominant types of photon-electron interactions, and geometrical factors. It also can be greatly increased by the instability of the acoustic waves induced by the strong radiation field, which reduces the effective opacity (Shaviv 1998). Due to the high anisotropy introduced by the strong magnetic field to the photon-electron interactions and flow geometry, the limiting luminosity in case of accretion onto a magnetized neutron star also differs from Equation 2.16. This case is considered in more detail in Chapter 3. Such examples help to understand the so-called super Eddington accretion that is observed, for example, in Ultraluminous X-ray sources (see Section 2.4.2.5).

In the following sections, I will review the main accretion mechanisms onto magnetized neutron stars that are usually discussed in the context of close binary systems. Here I limit the description to the penetration of the matter inside the magnetosphere. The details on the final stopping near the surface of the neutron star are reviewed in Chapter 3. The ratio of the speed of sound in the accretion flow $c_{\rm s}$ to the relative velocity of the neutron star v_∞ (with respect to the medium) determines the accretion regime if the angular momentum of the matter is negligible (Lipunov 1992). Section 2.3.4.1 describes the accretion from the wind of a normal companion, distinguishing the case of the spherical ($c_{\rm s} \gg v_\infty$) and cylindrical accretion ($v_\infty \gtrsim c_{\rm s}$). Section 2.3.4.2 illustrates the situation, when the angular momentum of the plasma cannot be ignored, and the matter is transferred via the disk accretion. In Section 2.3.4.3, I discuss a subsonic regime of the spherical accretion, which can occur in the case of the low luminosity of a source.

2.3.4.1 *Supersonic Wind Accretion*

The supersonic accretion onto a point mass, moving through a homogeneous gas, is known as Bondi-Hoyle-Lyttleton accretion. It was first studied in the works of Hoyle & Lyttleton (1941) and Bondi & Hoyle (1944) for the steady speed of a star moving through an isothermal gas with $v_\infty \gtrsim c_{\rm s}$ This regime is also known as *cylindrical accretion* (see, e.g., Lipunov 1992) or "Hoyle–Lyttleton" accretion. This regime closely describes the case of a neutron moving in an orbit through the stellar wind of its stellar component. The interaction of the gas with the magnetic field of the neutron star occurs below $R_{\rm G}$, and $R_{\rm c} > R_{\rm A}$. Simultaneously, the photon flux from the neutron star is high enough to provide sufficient radiative cooling of the shell above the magnetospheric radius. Such then, it represents a classical case of accretor (see Figure 2.4, case VI). Due to the supersonic motion of the neutron star, a bow shock is formed. The material within the cylinder with a radius $\sim R_{\rm G}$ can lose enough energy passing through the tail of the shock, forming an accretion wake (Davidson & Ostriker 1973). Figure 2.15 depicts the cylindrical accretion in a supergiant neutron star binary. Bondi (1952) considered the case when the gas pressure cannot be neglected, $c_{\rm s} > v_\infty$, that describes *spherically symmetric ("Bondi-Hoyle") accretion*. In general, when neither $c_{\rm s}$ nor v_∞ can be neglected, the mass-accretion rate onto a neutron star is given by

$$\dot{M}_{\rm BHL} = \frac{4\pi G^2 M^2 \rho_\infty}{(v_\infty^2 + c_{\rm s}^2)^{3/2}}, \tag{2.17}$$

where ρ_∞ is the density of the gas at the capture radius (see, however, the discussion in Shima et al. 1985, about the factor of 2 in the numerator, missing in the original work of Bondi). For more details, see the review by Edgar (2004). Passing through the shock, the motion of the flow rapidly becomes supersonic and the final deceleration of the falling plasma happens closer to the neutron star via, for example, collisionless or radiative shocks (see Chapter 3).

In real systems, the orbital motion, the influence of the rotating neutron star on the flow, and the clumpy structure of the stellar wind affect the possible accretion rate $\dot{M}$, which is not given simply by Equation 2.17. These complex tasks cannot be treated analytically and require numerical simulations (see, e.g., computations by Bozzo et al. 2016; El Mellah et al.

For cylindrical accretion the gravitational capture radius is sometimes referred to as the "Hoyle–Lyttleton" radius (Edgar 2004),

$$R_{\rm HL} = \frac{2GM}{v_\infty^2},$$

while for the spherical accretion it is also known as the "Bondi radius" (see, e.g., Russell et al. 2015)

$$R_{\rm B} = \frac{2GM}{c_{\rm s}^2}.$$

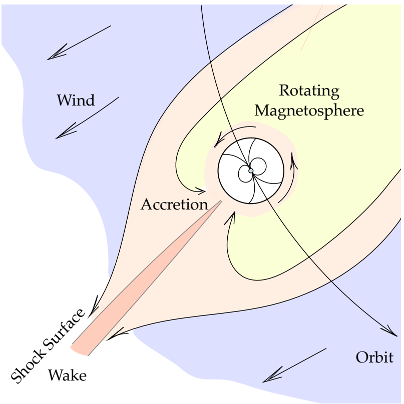

Figure 2.15: Schematic illustration of wind accretion. Based on Figure 3 of Davidson & Ostriker (1973).

2018). It was shown that the orbital effects in a wind-accreting system can even result in the formation of the disk-like structure around a neutron star, which can significantly change the picture of accretion (El Mellah et al. 2019).

2.3.4.2 *Disk Accretion*

When the accretion flow has high angular momentum, direct accretion is not possible, and the matter first forms the accretion disk around a neutron star. This accretion regime was already mentioned by Prendergast & Burbidge (1968) and Shvartsman (1971a) and later developed in detail by Pringle & Rees (1972), Lamb et al. (1973), and Ghosh & Lamb (1978). In this case, t is expected that the flow forms a nearly-Keplerian disk, spiraling towards the gravitational center. At the same time, the viscous transport of the angular momentum is directed outwards (Pringle & Rees 1972).

Here, I mainly follow Ghosh & Lamb (1978) to Describe the general picture of the magnetic field interaction with the disk. This regime differs significantly from the spherical accretion, as one cannot assume that the magnetic field of the neutron star is globally screened from the plasma. Instead, the field lines thread the disk and become distorted by the moving flow. Far away from the neutron star, the flow dynamics is governed by the viscous stresses and in principle can be described by the Shakura & Sunyaev (1973) model for thin accretion disks. Approaching the neutron star, the flow experiences the growing influence of the magnetic stresses, which happens in the so-called transition region. Finally, after the plasma passes the inner boundary layer of the transition region, its motion becomes determined by the magnetic field. In the boundary layer, the field is screened by a factor of ~ 10, and the flow starts to corotate with the magnetosphere. Ghosh & Lamb (1978) suggests that the inner radius of this layer is of order $\sim 0.4 R_\mathrm{A}$. Figure 2.16 illustrates the described picture of the disk accretion. The magnetic field lines twisted by the disk flows induce the torque on the neutron star, which can be either positive or negative at the same $\dot{M}$, depending on its angular velocity. It leads to the spin-up or spin-down of the neutron star.

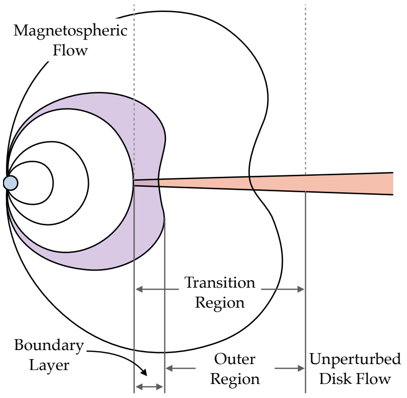

Figure 2.16: Schematic illustration of disk accretion with indicated principal regions. Based on Figure 1 of Ghosh & Lamb (1978).

This simplified picture sketches the major physical processes that come into play. It is, however, not applicable in the case of the super-Eddington accretion, where the disk transitions into the radiation-dominated state. The radiation disks are expected to become geometrically thick and accompanied by powerful outflows (see, e.g., Chashkina et al. 2019).

2.3.4.3 *Subsonic Wind Accretion*

The accretion regimes described in the two previous sections correspond, in general, to the case of an accretor (see Figure 2.4, VI) discussed in Section 2.2.1. It assumes that the emission from the neutron star is sufficient so the flow develops efficient Compton cooling, which requires high enough mass-accretion rates and results in high luminosity. At lower mass-accretion rates, $\dot{M} \lesssim 10^{16}\,\mathrm{g\,s^{-1}}$, however, radiative cooling may be insufficient, and the warm shell will be accumulated above the magnetosphere. This case was also described in Section 2.2.1 denoting the magnetic inhibition (or "subsonic propeller", see Figure 2.4, V). As was mentioned there, the shell is characterized by the large-scale convective motions. These motions govern the removal of the angular momentum from the neutron star (Shakura et al. 2013a). The penetration of the plasma inside the magnetosphere is possible at low mass-accretion rates, where its motion proceeds in a subsonic settling regime.

This regime, known as "quasi-spherical settling accretion", was proposed by Shakura et al. (2012) for slowly rotating magnetized neutron stars and further developed in Shakura et al. (2013a,b). The character of the accretion is unstable as the magnetic field can be locked in the shell in the form of loops. These can cause the reconnection and opening the magnetic case causing a rapid penetration of the plasma inside the magnetosphere, which results in a flare (Shakura et al. 2014; Popov et al. 2015).

The model suggests that the emission from the poles can cool the magnetospheric cusp region, but more significant plasma entry to the magnetosphere is expected via instabilities in the equatorial zone (Shakura et al. 2013a). As was mentioned in Section 2.2.1, the mass-accretion rate in this case is governed by the ratio of the free-fall, $t_{\rm ff}$, and the radiative cooling time, $t_{\rm cool}$, which is determined by bremsstrahlung, and is expected to be much lower than $\dot{M}_{\rm BHL}$ (Shakura et al. 2015),

$$\dot{M} = \left(\frac{t_{\rm ff}}{t_{\rm cool}}\right)^{1/3} \dot{M}_{\rm BHL}. \tag{2.18}$$

2.4 OBSERVATIONAL MANIFESTATIONS

This section attempts to bring together the shreds of evidence collected from the observations of neutron stars in different energy bands over the past $\sim$50 years. Inevitably, the focus is shifted to the X-ray observations, reflecting the impressive variety of the different phenomena we can observe at these energies (due to, for example, corresponding characteristic plasma temperatures of 0.1–10 keV), as well as the personal bias of the author.

The observed populations of neutron stars are classified based on the source that powers their emission and the specifics of their spin evolution (Harding 2013), which is highly influenced by the environment of a neutron star (see Section 2.2.1). One can identify such major power sources for the emission of neutron stars as rotational energy, magnetic field decay, internal heat, and accretion (Mereghetti 2011). The internal heat may itself originate from the magnetic field decay. As a result of this diversity, neutron stars show an impressive variety of observational manifestations, including bursting, flaring, and – the most common – pulsations due to the misalignment of their rotation and magnetic axes or due to a complex temperature distribution over the surface (see Section 2.2.1).

The common way to present the variety of the observed galactic neutron stars is the so-called P-$\dot{P}$ diagram, where different populations evolve, sharing common spin values and spin evolution. Figure 2.17 shows the most distinct populations of neutron stars in our Galaxy. The importance of the measured P-$\dot{P}$ values for pulsars can be understood if one, in a very simplistic approach, invokes again a rotating magnetic dipole approximation for a neutron star (Section 2.2.1). The energy emitted by the rotating magnetic dipole can then be expressed in terms of the *spin-down luminosity*

$$L_{\rm sd} = 4\pi^2 I \frac{\dot{P}}{P^3}, \tag{2.19}$$

where $I = 2M_{\rm NS}R_{\rm NS}^2/5 \approx 10^{45}\,{\rm g\,cm^2}$ is the moment of inertia of a sphere with canonical neutron star parameters. Depending on the spin period, the emitted radiation may appear as pulsations from the radio to γ-rays.

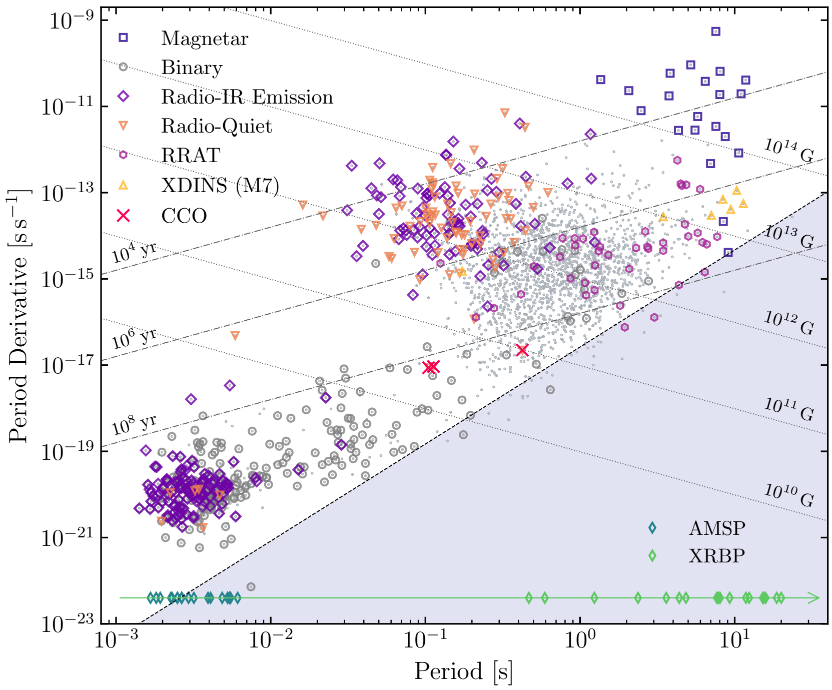

Figure 2.17: P-$\dot{P}$ diagram for the Galactic pulsar population. Data are taken from the Australia Telescope National Facility (ATNF) pulsar catalog (Manchester et al. 2005), with the help of `psrqpy` package (including the basis of the script for the plot; Pitkin 2018).

In most cases, $L_{\rm sd}$ does not match the directly observed luminosity from a pulsar. Even keeping in mind the approximate nature of Equation 2.19, discrepancies can reach orders of magnitude. In the case of a young pulsar in a nebula, the radiation from the neutron star can be significantly absorbed by the surrounding material and re-emitted at other wavelengths. However, in the case of an additional energy reservoir other than rotational power, the observed luminosity might be higher than the expected spin-down value. Such reservoirs can be the thermal energy of a cooling neutron star or the magnetic stress in the crust.

Assuming that the power of the magnetic dipole emission is equal to the loss rate of rotational energy, the minimum surface magnetic field strength (Condon & Ransom 2016)

$$B > \left(\frac{3c^3 I}{8\pi^2 R_{\rm NS}^6}\right)^{1/2} (P\dot{P})^{1/2} \approx 3.2\times 10^{19} \left(\frac{P\dot{P}}{\rm s}\right)^{1/2} {\rm G} \tag{2.20}$$

and the characteristic age of a pulsar

$$\tau_{\rm c} = \frac{P}{2\dot{P}} \tag{2.21}$$

can be estimated. Based on Equation 2.20 and Equation 2.21, isolines for the magnetic field and the characteristic age can be shown on the P-$\dot{P}$ diagram. One should note that the characteristic age is defined by Equation 2.21 under the assumption that the initial period of a pulsar $P_0 \ll P$. If the latter condition is not applicable, such age estimates will be highly incorrect. One of the prominent examples are Central Compact Objects – young neutron stars located inside the supernova remnants (red crosses in Figure 2.17). They are likely to be born with P_0 close to their current measure values, and thus their $\tau_c \sim 10^8$ yr is much higher than their real age $\sim 10^2$–10^3 yr.

In the situation when the evolution of the spin period is strongly influenced by the effects beyond the rotational energy losses, such as accretion, the location of a pulsar on the P-$\dot{P}$ diagram can be highly misleading. For this reason, accreting millisecond pulsars (AMSPs) and accretion-powered X-ray binary pulsars (XRBPs) are shown in Figure 2.17 only along the x-axis, to illustrate their characteristic spin periods.

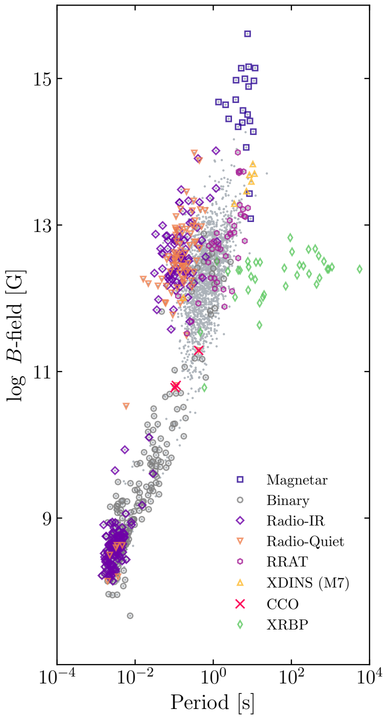

Figure 2.18: Different populations of the galactic neutron stars in the magnetic field–spin period diagram. For all populations but XRBPs, the magnetic field is estimated using Equation 2.20. Only XRBPs with detected cyclotron lines are plotted, with magnetic fields given by Equation 2.22. Cyclotron line energies are taken from Staubert et al. (2019, Table A.1).

Cyclotron lines are another source of information on the surface magnetic field value that provides a sanity check for the estimates based on magnetic dipolar losses. Cyclotron lines are sometimes observed in the spectra of isolated and accreting neutron stars at soft and hard X-rays. As was already mentioned, the motion of charged particles in strong magnetic fields is quantized perpendicular to the field lines onto Landau levels (Landau 1930). The quantization results in a resonant nature of the interactions between charged particles and photons, such as emission, absorption, and scattering. The resonant Compton scattering in the magnetized plasma in the vicinity of a neutron star leads to the formation of absorption line-like features – cyclotron lines – in the X-ray spectra. As the distance between the Landau levels depends on the neutron star's magnetic field, it can be estimated from the energy of the cyclotron line (the so-called "12-B-12 rule")

$$B \simeq \frac{1}{(1+z)} \left(\frac{E_{\rm cyc}}{11.6\,\rm keV} \right) \times 10^{12}\,\rm G, \tag{2.22}$$

where $E_{\rm cyc}$ is the observed line centroid energy in keV and z is the gravitational redshift. I will focus more on the physics of the line formation in Chapter 4 and Chapter 6. Typical magnetic fields of various neutron star populations are shown in Figure 2.18.

In the following, I will describe the major properties of the observed populations of the galactic neutron stars. In Section 2.4.1, I will focus on isolated neutron stars, such as Rotation-Powered Pulsars (RPPs), Central Compact Objects (CCOs) in supernova remnants, X-ray Dim Isolated Neutron Stars (XDINSs), and Magnetars. Section 2.4.2 brings together different types of neutron stars in binary systems. Such systems include High- and Low-Mass X-ray Binaries (LMXBs), Millisecond Pulsars (MSPs), Gamma-ray Binaries (GRBs), and Ultraluminous X-ray Sources (ULXs). I will discuss the possible evolutionary link between the different neutron star populations in Section 2.4.3.

2.4.1 *Emission from Isolated Neutron Stars*

Here and afterward, I use the term "Isolated Neutron Star" for all types of physically isolated neutron stars, that is, without a binary component. Sometimes (see, e.g., Harding 2013) this term is specifically applied to the X-ray dim isolated neutron stars, which, in the author's opinion, may be confusing. The emission from isolated neutron stars is observed from radio to γ-rays, being caused mainly by such mechanisms as the magneto-rotational energy losses, relaxation of magnetic stresses (crustquakes), and surface cooling. The reader will see in Section 2.4.2, that some of these mechanisms are also important for certain classes of neutron stars in binary systems.

The radio emission is observed from the majority of the detected pulsars. The exact mechanism that consistently explains all observational properties of the radio emission is still debated, but a common understanding involves the coherent curvature radiation from the particles accelerated by the strong electromagnetic field generated during the rotation of a magnetized neutron star. The (non-coherent) curvature and synchrotron radiation of the relativistic particles contributes to the X-rays and γ-rays. Crusius-Waetzel & Lesch (2002) suggested that anisotropic synchrotron emission can also explain the observed spectral shapes of pulsars between the infrared and soft X-rays. The contribution to the optical and ultraviolet energy bands can also come from the tail of the thermal emission peaking at soft X-rays.

Isolated neutron stars are relatively bright X-ray sources. In general, the X-ray emission from these objects consists of three major components of a distinct nature. The soft near-thermal part is associated with a surface and/or atmospheric emission of a cooling neutron star. The temperature distribution on the surface is non-uniform and highly coupled with the individual magnetic field configuration and evolution (Igoshev et al. 2021b). The pulsations of this component are often associated with the hotter and larger emission regions of the size $\sim$km on the neutron star surface. Sometimes, a more homogeneous temperature distribution results in no detectable pulsations (see, for example, the lack of pulsations for one of the X-ray Dim Isolated Neutron Stars, RX J1605.3+3249, Malacaria et al. 2019). A second thermal component is sometimes distinguished in the spectra of isolated neutron stars and is commonly interpreted as the emission of the magnetic poles, which are additionally heated by the streaming backflow of the relativistic particles generated in the magnetosphere (Zavlin 2007, "backflow current heating"). This component has a slightly higher temperature than the direct surface emission. The power-law-like non-thermal emission at harder X-rays is produced by synchrotron emission and inverse Compton processes in the magnetosphere. The non-thermal component is expected to dominate in X-ray spectra of young pulsars. At ages $\sim 10^5$–10^6 yrs, the most pronounced contribution to the soft X-rays can come from the thermal surface emission (Becker 2009). For older neutron stars, the surface temperature becomes too low, and the soft X-ray emission mainly originates from the heated polar hot spots. Figure 2.19 demonstrate the possible contribution of the thermal and non-thermal components to the total X-ray flux.

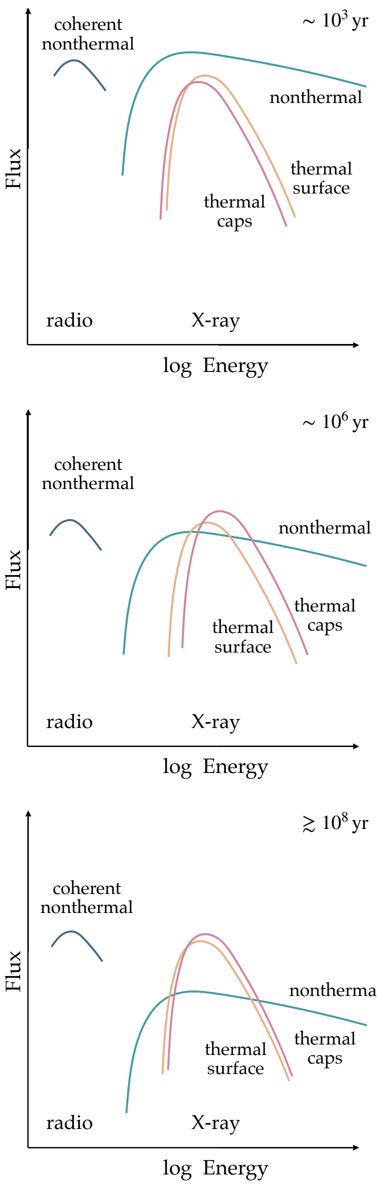

Figure 2.19: Sketch of typical emission components for isolated neutron stars and their approximate relative contribution to the flux at different ages. Based on Figure 1 of Zavlin (2007).

In the following, I will briefly describe the main subclasses of isolated neutron stars, with their typical observational properties and suggested models to interpret them.

2.4.1.1 *Rotation-Powered Pulsars*

Isolated neutron stars have been known by their radio emission from the very first day of pulsar's astronomy (Hewish et al. 1968). Although it soon was understood that such emission should be produced by relativistic particles in the vicinity of rapidly rotated neutron stars, the exact mechanism remains a subject of discussion. Charged particles in the vicinity of a neutron star, being whether extracted from the surface, whether created by pair production (for magnetic fields $> B_\mathrm{c}$), are streaming along the open magnetic lines, involved with them to the rotation, forming a corotating magnetosphere extending up to the light cylinder (Goldreich & Julian 1969). The accelerated particles, moving along the field lines, emit curvature and synchrotron radiation. Two different classes of models predict particle acceleration near the magnetic poles (so-called "inner gap", see, e.g., Ruderman & Sutherland 1975; Gil et al. 2003) and in the outer magnetosphere ("outer gap", see, e.g., Cheng et al. 1986). Figure 2.20 provides a schematic depiction of a radio pulsar.

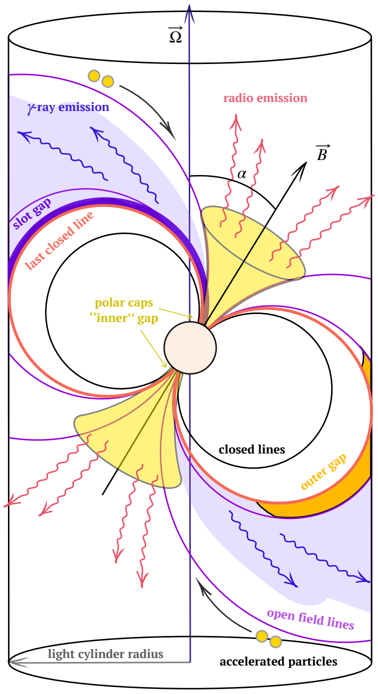

Figure 2.20: Sketch of the rotation-powered pulsar's magnetosphere.

The pulsar's radio emission has a high linear and significant circular polarization, and high brightness temperatures of $T_\mathrm{b} \gtrsim 10^{26}$ K (see, e.g., Cordes 1979), which require the coherent mechanism of emission. This means that the radio emission is mainly produced not by individual particles streaming along the magnetic field lines, but by plasma bunches and should involve collective plasma effects. Gangadhara et al. (2021) showed that an enhanced coherent emission and polarization state could be produced as a result of the resonance between the radio and plasma waves. Other models involve, for example, growing plasma instabilities in the magnetosphere (Ruderman & Sutherland 1975).

As was previously mentioned, incoherent emission by individual particles streaming in the magnetosphere along the field lines contributes to the higher energy bands. The γ-emission that carries most of the spin-down power of a typical pulsar, is produced by the curvature emission of the highly relativistic particles accelerated to $\sim$10 TeV and likely originates from the high altitudes in the pulsar's magnetosphere (see Harding 2013, and references therein). Crusius-Waetzel & Lesch (2002) showed that the cooling of the power-law distributed relativistic particles in the outer gap by the curvature radiation losses can reproduce the observed γ-ray spectra and luminosity. In this case, the latter scales according to $L_\gamma \propto BP^{-5/3}$.

Although the pulse profiles are a unique signature of a pulsar and show a variety of individual behavior, the general shape of the cumulative radio pulse profile can be described as a single-peaked Gaussian, with occasional sub-peaks (see, e.g., Stappers et al. 2011; Pilia et al. 2016). For the majority of pulsars observed with *Fermi*, the γ-ray pulse profiles show two peaks, with separation of $\gtrsim 0.2$ of the rotation phase (Abdo et al. 2011, 2013). For the pulsars observed at X-rays, the thermal components and the nonthermal power-law can show different alignments with γ-ray peaks. It is often the case that the peaks of thermal components from the surface cooling and/or from backflow heated polar caps are not in phase with γ-ray ones (see, e.g., Lin et al. 2010), while the maxima in a pulse profile of a nonthermal component are sometimes aligned with γ-ray peaks. Figure 2.21 shows radio, X-ray, and γ-ray pulse profiles for a young rotation-powered pulsar PSR J0205+6449.

Interestingly, thermal emission from the caps and the surface also does not seem to show any common phase alignment. Thus, De Luca et al. (2005) showed with *XMM-Newton* EPIC observations that even such similar pulsars as famous *Three Musketeers* – Geminga, PSR B0656+14, and PSR B1055−52, middle-aged neutron stars, whose X-ray emission shows three distinct components (cooling surface, heated polar caps, and nonthermal) – exhibit different dependencies of the relative position of the peaks of two thermal components. This fact suggests that the temperature distribution across the surface is more complex than the one predicted by the simplistic model of a cooling neutron star with dipolar magnetic field. The latter is supported by more complex modeling, (see, e.g., Pons & Geppert 2007, with the heated equatorial belt in addition to polar caps).

For a large number of pulsars, only radio or only high-energy emission is detected, which might be a geometrical effect (observer's inclination and beaming), see Ravi et al. (2010) – radio and gamma beams have comparable beaming factors. Radio-beam is wider (gamma-like) for high-

$L_{\rm sd}$ (young, millisecond pulsars), half of that for low-$L_{\rm sd}$. It seems to be consistent with the origination of the radio emission higher in the magnetosphere. Sometimes radio and gamma profiles are aligned and very similar (see, e.g., MSP PSR J0034−0534, Abdo et al. 2010), supporting the co-location of regions for radio and gamma emission. A study of the radio-loud and radio-quite pulsars with detected γ-emission by Hui et al. (2017) showed that the observed differences between these two populations, such as large γ-ray spectral curvature of the radio-quiet pulsars and the magnetic field strengths at the light cylinder $B_{\rm LC}$ (with a similar distribution of the surface values B), can be explained simply by geometrical effects (such as narrowness of the radio beams expected for the pulsars with larger rotational periods) and the rotational periods, which tend to be generally smaller for the radio-loud pulsar, in the assumption that the emission originates from the outer gap.

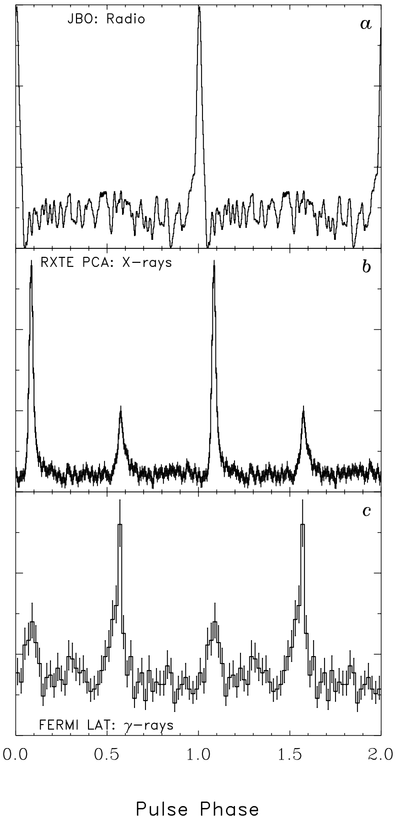

Figure 2.21: Pulse profiles of a young ($\lesssim 10^4$ yr) rotation-powered pulsar PSR J0205+6449 in different energy band: radio (a, 1.4 GHz), X-ray (b, $\sim$2–20 keV), and γ-ray (c, $>$100 MeV). Figure 3 from Kuiper et al. (2010). Credit: Kuiper et al. (2010), reproduced with permission © ESO.

In addition to all the peculiar properties that have been already discussed in this section, the rotation-powered pulsars also show timing anomalies in their behavior. One of the most interesting examples are *glitches* – sudden increases of the rotational period appearing against the background of the smooth and stable spin-down, followed by relaxation period (see, e.g., Espinoza et al. 2011). Glitches are rare events appearing on short time scales ($\sim$1 min Dodson et al. 2002), however, the relaxation times vary from hours to years (Lyne et al. 2000). The most common explanation for these events is a rapid exchange of angular momentum between superfluid neutrons of the inner crust with the solid outer crust. The rotational lag of a superfluid with respect to the solid component is caused by its quantum vortices are strongly attracted to the nuclear clusters of the outer crust that prevents spin-down. When the lag becomes too large, the recoupling of these components results in the rapid angular momentum transfer to the outer crust and an observed glitch. (for more details see Haskell et al. 2020; Haskell & Sedrakian 2018; Khomenko & Haskell 2018, and references therein)

Another irregularity is the so-called *nulling* phenomenon observed in more than $\sim$200 pulsars (Wang et al. 2020) as an absence of pulsations or their decrease in energy by a factor of ten or more on scales of a few rotational periods (Backer 1970). Sometimes nulling is followed by mode-changing, an abrupt switch of the cumulative pulse profile between different (commonly two) stable states. Interestingly, even the spin-down rate can decrease during the nulling state, which might hint that the presence of a pulsar wind significantly influences the pulsar braking mechanism (Kramer et al. 2006). Nulling can possibly result from the large-scale global changes in the current density distribution in the magnetosphere (Wang et al. 2007; Timokhin 2010). This phenomenon is more characteristic for slowly rotating older ($\tau_{\rm c} \gtrsim 5$ Myr) pulsars, although a recent study by Wang et al. (2020) points out that it might be more closely related to the rotational period than to the (characteristic) age of a pulsar. The extreme form of pulse nulling is likely observed in Rotating Radio Transients (RRATs), sources, that only show a sporadically detectable emission, followed by a long state of quiescence (McLaughlin et al. 2006). Rotating Radio Transients have characteristic ages similar to the pulsars showing a typical nulling behavior (see Figure 2.17). It is interesting to note that this type of object naturally occurs within the model proposing the changing current densities in the magnetosphere as a cause of nulling (Timokhin 2010). However, the origin of quiescence of Rotating Radio Transients and their surface magnetic field strength remains a matter of debate (see, e.g., Gençali & Ertan 2021; Shapiro-Albert et al. 2018).

2.4.1.2 *X-ray Dim Isolated Neutron Stars*

The *ROSAT* mission revealed that not all isolated neutron stars produce radio emission, presenting, among others, a discovery of seven radio-quite (and X-ray dim) sources (Walter et al. 1996; Zampieri et al. 2001). This group of sources is known to date as X-ray Dim Isolated Neutron Stars, or *The Magnificent Seven* (M7). Their magnificence lays in the fact that their emission showed a nearly perfect Planckian soft X-ray emission with black-body temperatures ranging from 40 to 100 eV and low luminosities of $L{\sim}10^{30}$–$10^{32}\,\mathrm{erg\,s^{-1}}$ (see the review by Turolla 2009, and references therein). The members of the Magnificent Seven are presented in Table 2.1. Six of them show pulsations with periods in the order of seconds, and only RX J1605.3+3249 has no detection of pulsations (Malacaria et al. 2019; Pires et al. 2019). The Magnificent Seven are classified as middle-aged neutron stars with ages $\sim 10^6$ yr, which is consistent with their detected periods, assuming the spin down from tenths of milliseconds due to magnetodipole emission (Page et al. 2006). Such loss rates also require high field values at the magnetic poles, $B = 6.4 \times 10^{19} (P\dot{P})^{1/2} \sim 10^{13}$ G (Haberl 2007).

Table 2.1: Members of the Magnificent Seven.

THE MAGNIFICENT SEVEN
RX J1856.5−3754
RX J0720.4−3125
RX J0806.4−4123
RX J0420.0−5022
RX J1308.6+2127
RX J1605.3+3249
RX J2143.0+0654

From early observations, the main deviation of the spectra from the thermal black-body emission seemed to be due to some interstellar attenuation (low though, as the result of the proximity of the sources) and a number of the absorption line-like features that are sometimes interpreted as proton cyclotron lines, giving a consistent result with the magnetic field estimates from timing studies. Alternative explanations included H/He transitions in high magnetic fields and inhomogeneous surface temperature distribution. Such a near-thermal spectral shape was understood as a simple cooling of a neutron star in the absence of the magnetospheric and accretion activities, making these sources excellent candidates for the fundamental studies of neutron star parameters (Turolla 2009; Haberl 2007).

However, as often happens, later observations have brought perfection into question. A deep observation with *XMM-Newton* revealed a more complex shape for RX J1605.3+3249 (Pires et al. 2019; Malacaria et al. 2019), consistent rather with the emission from a partially ionized atmosphere (Ho et al. 2007) than with direct cooling of the neutron star surface. It was followed by the discovery of a hard X-ray excess in the spectra of RX J1856.5−3754 and RX J0420.0−5022, the origination of which seems to be independent of the surface thermal emission (Dessert et al. 2020), in the archival *XMM-Newton* and *Chandra* data. Together with excess above the expected Rayleigh-Jeans tail in the optical and UV bands, it strongly hints at a nonthermal power-law-like component that can also be explained within the model of the emission from the highly magnetized atmosphere. Recently, three members of the Magnificent Seven, RX J0720.4−3125, RX J2143.0+0654, and RX J1605.3+3249, were observed by eROSITA. These high-resolution observations also question the historically accepted cooling model, revealing a more complex spectral shape and equally spaced multiple absorption features for all three sources, supporting the interpretation of them as cyclotron lines (Pires et al. 2022).

2.4.1.3 *Magnetars*

Magnetars are the group of neutron stars that host the strongest magnetic fields observed in the Universe, usually of orders 10^{14}–10^{15} G. These enormous magnetic fields used to serve as a definition for magnetars, however the discovery of "low-field" magnetars such as SGR 0418+5729 ($B \lesssim 7.5 \times 10^{12}$ G, Rea et al. 2010) and Swift J1822.3−1606 ($B \sim 2.7 \times 10^{13}$ G, Rea et al. 2012), as well as the detection of a magnetar-like activity from the regular rotation-powered pulsars (see, e.g., PSR J1119−6127, Younes et al. 2016), stimulated reconsideration of this term. In our current understanding, magnetars are neutron stars whose emission is mainly powered by the decay of the magnetic field, with sporadical bursting activity, fed by the relaxation of the built-up magnetic stresses. These are typically young neutron stars, often directly associated with the supernova remnants, with unusually long periods (see Figure 2.17) of about a few seconds and rather large $\dot{P} \sim 10^{-11}\,\mathrm{s\,s^{-1}}$, showing highly variable emission, mainly in X-rays and γ-rays.

"Excellent talk. Minus point for defining magnetars as 'stress-powered' neutron stars"
Anna L. Watts to Sam Lander, PHAROS 2022

Historically, magnetars were manifested as two separated classes of objects that were thought to be unrelated to each other: soft gamma repeaters (SGRs) and anomalous X-ray pulsars (AXPs). Soft gamma repeaters established themselves as transient sources, exhibiting short (∼a few tenth of seconds duration) *burst*, that can be repeated within a few days, but sometimes are found to be years apart. A few soft gamma repeaters showed a *giant flare* – a short, less than a second, enormous rise of the flux, with total luminosities of $\sim 10^{44}$–$10^{47}\,\mathrm{erg\,s^{-1}}$ in the soft-γ-ray and X-ray energy bands, followed by a decline of several minutes, with detectable pulsations (see, e.g., Cline et al. 1980, for the first detection of a giant flare and Figure 2.22 for an example). Anomalous X-ray pulsars, on the other hand, were known as relatively bright pulsating X-ray sources. Despite their similarities with traditional accretion-powered X-ray pulsars (except for their unusually soft X-ray spectra), they showed no hint of an accretion disk or a companion star. The evidence accumulated over the years, such as soft-γ-ray bursts from anomalous X-ray pulsars and the quiescence emission from soft-γ-ray repeaters, showed clearly that both groups represent the same objects, making this classification obsolete. The reader is recommended to find out more about the thorny path of the history of magnetars from the excellent reviews of Kaspi & Beloborodov (2017) and Harding (2013).

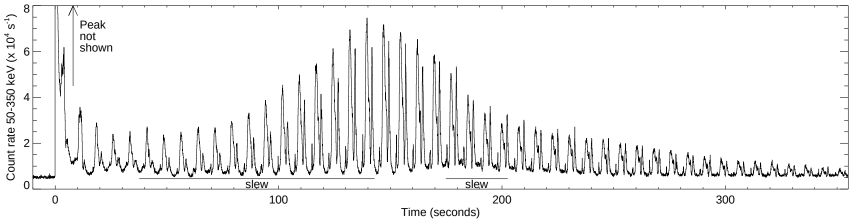

Figure 2.22: Light curve of a giant flare and its "tail" from SGR 1806–20 during the 2005 superburst. Figure 1 from Palmer et al. (2005). Reproduced with permission from Springer Nature.

The quiescent emission from magnetars typically consists of a soft thermal component and a nonthermal tail, with turnover at ∼10 keV and total X-ray luminosities $L_X \sim 10^{31}$–$10^{35}\,\mathrm{erg\,s^{-1}}$, which is a few orders of magnitude higher than the estimated spin-down luminosity (see Equation 2.19). The soft X-ray pulse profiles in quiescence are rather broad, more often single-peaked, and have a broad distribution of the pulsed fraction (Hu et al. 2019). Magnetar outbursts are characterized by a significant increase of the X-ray luminosity ($L_X \sim 10^{36}\,\mathrm{erg\,s^{-1}}$) lasting from weeks to several months, usually accompanied by the complication of the pulse profile's shape and spectral hardening, as well as possible (sometimes multiple) short bursts and glitches. Interestingly, magnetars with lower quiescent luminosities seem to be usually accompanied by the larger luminosity enhancement (Pons & Rea 2012).

Some magnetars show activity in the radio band as well, however, from the currently known ∼30 magnetars, only five seem to have pulsations in the radio band (Olausen & Kaspi 2014). The radio emission is usually associated with outbursts and show rather different properties than the emission of radio pulsars, including high variability (see, e.g., Chu et al. 2021). A comprehensive review on the observational properties of magnetars is given by Rea & Esposito (2011).

The birth of a magnetar is likely accompanied by the formation of a strong toroidal component of the magnetic field (Braithwaite 2009). After the formation of a solid crust, the multi-fluid composition of the outer layers of a neutron star allows for the evolution of the internal magnetic field that is frozen to the electron fluid, slowly drifting with respect to neutrons and ions (see Kaspi & Beloborodov 2017, also for more information on the possible drift mechanisms). Such drift of the magnetic field lines results in building up magnetic stress that can lead to a release of the elastic and magnetic energy, accompanied by a *crustquake* or plastic flow, which can be associated with smaller stresses in the outermost part of the crust (Lander et al. 2015). A crustquake can result in a possible large-scale restructuring of the crustal and magnetospheric fields, leading to bursting activity. Such restructuring of the magnetic field can explain the spectral and pulse profile changes during the magnetar's outbursts (Pons & Perna 2011; Pons & Rea 2012). Propagation of a thermoplastic wave through the crust can result in unpinning of the quantum vortices of a superfluid component, leading to a glitch.

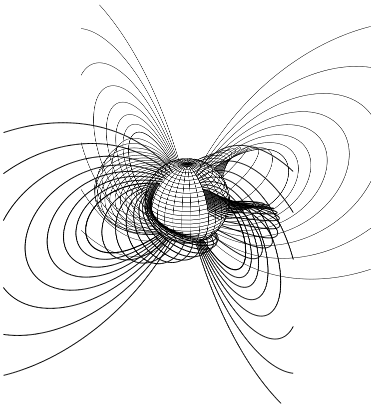

Figure 2.23: Simulation of the twisted magnetosphere of a magnetar. Figure 1 (right panel) from Akgün et al. (2017).

The high quiescent luminosity of active magnetars hints at the involvement of a strong heating mechanism involved. The source of heat remains a subject of discussion, involving such proposed mechanisms as ambipolar diffusion in the liquid core, mechanical heating due to the crust deformation by magnetic stresses, ohmic dissipations that can be accompanied by the magnetic energy transport by the Hall drift, and the bombardment of the magnetic poles of a magnetar by charged particles accelerated in the magnetosphere (for more details, see Beloborodov & Li 2016, and references therein). Here it is important to note that currents in the dynamic magnetospheres of magnetars are rather different from the charges that can move only along the open field lines in the magnetosphere of a regular rotation-powered pulsar. The crustal displacement in magnetars can lead to a twist of the external field, which is anchored to the crust (see Figure 2.23). Such non-potential twisted fields require a current flow along the closed field lines as well (Beloborodov 2009). The observed hard spectra of magnetars in quiescence can then be explained by the resonant Compton scattering of X-rays emitted from the surface off the charged particles streaming in the magnetosphere (Baring & Harding 2007). However, I would like to note that the recent calculations by González-Caniulef et al. (2019) of an atmosphere that is bombarded by relativistic particles, predict the existence of a strongly overheated outer layer. As I will show in Chapter 6, resonant Compton scattering *inside* such inhomogeneous atmospheres can by itself produce a high-energy excess in X-ray emission. A comprehensive review by Turolla et al. (2015) is recommended for more detailed information on the theoretical interpretation of magnetar properties.

2.4.1.4 *Central Compact Objects*

The term "Central Compact Objects in supernova remnants" is reserved for X-ray bright radio-quite isolated neutron stars found near a geometrical center of supernova remnants. Central Compact Objects show no signs of magnetospheric activity that for regular rotation-powered pulsars results in a broad-band nonthermal emission component. They have no apparent emission in the radio, infrared, and optical bands (see, e.g., Mignani et al. 2019) and no pulsar wind nebula surround them, while their X-ray emission is typically thermal and non-variable and thought to emerge from the cooling atmosphere of a neutron star. Sometimes, absorption features exist that some authors interpreted as cyclotron lines (Bignami et al. 2003).

To date, ten central compact objects are known, and only three of them show pulsations: J1852+0040 in Kes 79, J0822−4300 in Puppis A (Figure 2.24), and 1E 1207.4−5209 in PKS 1209−51/52, with rotational periods of ∼0.1–0.1 s. The measured low spin-down rates ($\dot{P} \sim 10^{-17}\,\mathrm{s\,s^{-1}}$) for these sources gave the community more questions than answers. Considering the relatively high rotational periods, central compact objects are placed in the middle part of the P-$\dot{P}$ diagram (see red crosses in Figure 2.17), implying high characteristic ages and low surface magnetic fields. While the characteristic age estimated based on Equation 2.21 ($\tau_c \sim 10^8$ yr) are clearly wrong (as they seemed to be born with periods close to the current ones), which was verified by sufficiently precise estimates of the corresponding supernova remnant ages (∼10^3–10^4 yr) (see, e.g., Lovchinsky et al. 2011), the magnetic fields seem to be in agreement with values of $B \sim 10^{11}$ G inferred from the observed electron cyclotron lines in the soft X-ray spectra and a lack of nonthermal emission. The latter, though, is still extreme for typical parameters of central compact objects. The estimated spin-down luminosity L_{sd} is about an order of magnitude lower than the one observed in X-rays.

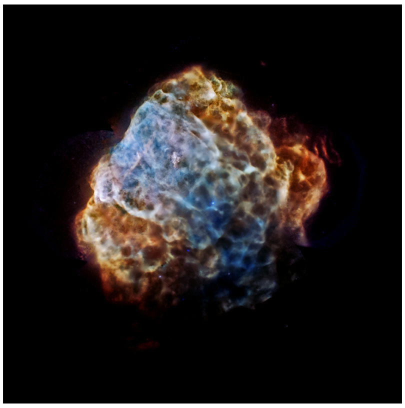

Figure 2.24: X-ray image of Puppis A remnant. Credit: NASA/CXC/SAO.

A number of scenarios were proposed to explain why these young neutron stars ended up with such unusually low magnetic fields, including a failed dynamo mechanism due to the slow rotation of the collapsing progenitor, a strong magnetar-like crustal field, accompanied by a weak outer dipolar component, and a "buried field" due to the accretion of the fall-back supernova material (see De Luca 2017, and references therein). A fall-back and hidden crustal field scenario could explain the unusually contrasted surface thermal map (as required, for example, by emission from J1852+0040 with a high, ∼64%, pulsed fraction; Halpern & Gotthelf 2010). It is still unclear why all but three sources of this group shows no pulsation (see discussion by Doroshenko et al. 2018).

Figure 2.25: X-ray image of the supernova remnant Cassiopeia A. Credit: NASA/CXC/SAO.

The thermal black-body-like spectra of Central Compact Objects are sometimes well described with two emission components from the hydrogen highly magnetized atmosphere, where the low-energy electron cyclotron line can be produced (Ho 2013). Spectra of the non-pulsating sources of this group, like Cas A (Figure 2.25), can be well described with models of an atmosphere composed of carbon (Ho & Heinke 2009). However, the same model gives emission regions comparable to the neutron star surface and is likely incompatible with such strong pulsations as observed for J1852+0040.

Aside from all spectral and timing puzzles related to the central compact objects, they and their host supernova remnants are an ideal target to study remnant kinematics, which, together with a carefully measured proper motion of a neutron star can give the exact origin of the supernova explosion (Mayer & Becker 2021).

2.4.2 *Neutron Stars in Binaries*

The proximity of a non-degenerate component can substantially change the evolution of the main characteristics of a neutron star and its observational manifestations. The accretion onto a magnetized neutron star results in the transfer of angular momentum from the donor, and accretion torques significantly influence the evolution of the rotational period of the pulsar, opening an avenue for its spin-up. Millisecond Pulsars – old neutron stars spun up by the episodes of accretion – are a striking example of how efficient this process can be. Accretion of matter onto a surface in such a strong gravitational field leads to an enormous energy release, which is why accreting X-ray pulsars are among the brightest X-ray sources. Depending on the type of the companion, the dynamic of the interaction in neutron star binaries can differ substantially, providing a wide ranges of mass accretion rates, $\dot{M} \sim 10^{12}$–$10^{19}\,\mathrm{g\,s^{-1}}$. The timing and spectral behavior of the system are highly dependent on the mass accretion rate, orbital period and rotational period of the neutron star, and the strength of its magnetic field.

The age of the neutron star and the type of the non-degenerate companion, determine to a high degree main observational properties of the binary system. The stellar winds from the donor that set the properties of the plasma surrounding the neutron star differ in velocity, structure, and even in the mechanisms of their origination for stars of different spectral types (see, e.g., the review on stellar winds by Owocki 2013). If a young neutron star has not yet spun down enough to pass its ejector phase, a strong pulsar wind keeps the plasma of a stellar wind away from the light cylinder. In this case, the interaction of the two components of the binary is limited to the collision of relativistic particles of the pulsar wind with the plasma flowing out of the donor companion. In the case of strong fast winds of OB-type stars, this interaction produces bright gamma-ray emission (Dubus et al. 2017). After the neutron star spun down significantly, and the plasma can penetrate under the light cylinder, the further evolution of the rotational period is determined by the balance of spin-down and the spin-up torques (see Section 2.2.1), eventually reaching some quasi-equilibrium value. Corbet (1984) noted that the orbital separation of components and the type of a donor star might have the most decisive influence on equilibrium spin value. He introduced the so-called *Corbet Diagram*, which is a powerful instrument to study the connection between the spin period P of a neutron star and the orbital period P_{orb} of a binary system. Figure 2.26 shows an example of a Corbet Diagram for some types of accreting binary systems. Some populations, such as Be X-ray Binaries (BeXRBs), show a more obvious correlation between P and P_{orb} than the others. Nevertheless, different classes of binaries are clearly visually separated on the diagram.

In the following, I will describe the main populations of neutron star binaries that include Low-Mass X-ray Binaries with typically old neutron stars that have been spun up by accretion, younger High-Mass X-ray binaries with strongly magnetized neutron stars and supergiant companions, more exotic Symbiotic X-ray Binaries with an M-type giant donor star, and systems, whose compact objects are still subjects of debate in a number of cases, such as Gamma-ray Binaries and Ultraluminous

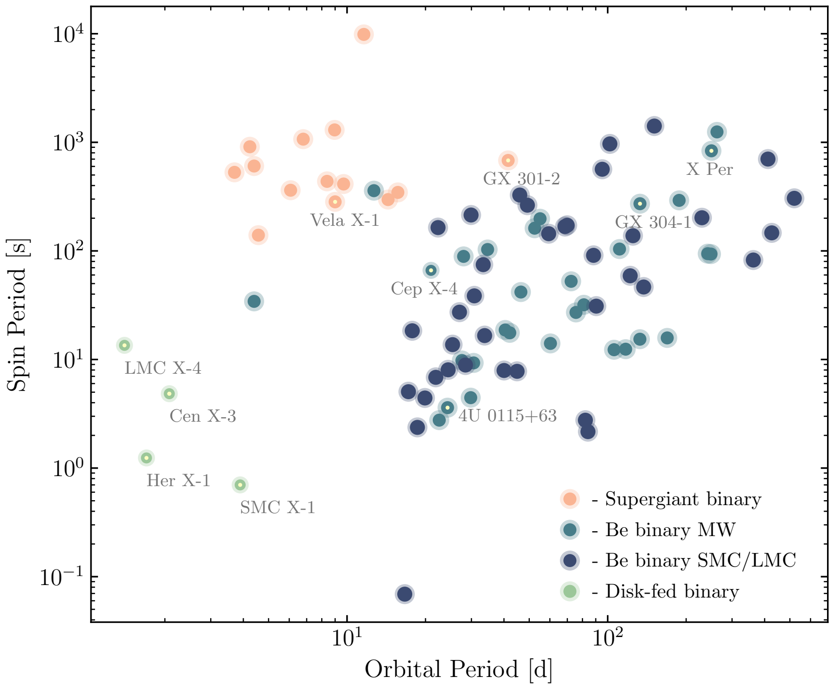

Figure 2.26: Corbet diagram for known High-Mass X-ray Binaries in the Milky Way (MW), Large Magellanic Clouds (LMC), and Small Magellanic Clouds (SMC). Some sources mentioned in the text are marked explicitly and their names are given. I thank Robin H. D. Corbet who provided the data for this figure, as well as Arthur Avakyan and Marvin Neumann who also kindly provided the early version of the catalogue of the Galactic High-Mass X-ray Binaries, XRBcats, which is now published in (Neumann et al. 2023).

X-ray sources. In general, binary systems can also contain a black hole instead of a neutron star. The discussion of the black hole binaries (which are much less numerous than the ones with neutron stars, Walter et al. 2015) is outside of the scope of the present work (see, e.g., Grinberg 2014, for more information on the topic), and thus for simplicity, I avoid writing, for example, "High-Mass X-ray Binaries with neutron stars", always meaning High-Mass X-ray binaries with neutron stars. Binaries with black holes are more difficult to create due to a dramatic mass loss of massive companions that are supposed to become a black hole (see, e.g., Langer et al. 2003, and references therein).

2.4.2.1 *High-Mass X-ray Binaries*

High-Mass X-ray Binaries consist of a strongly magnetized neutron star orbiting a massive star, typically a young OB-type supergiant or a Be-star. In such systems, favorable conditions arise for accretion onto a neutron star due to the intense stellar winds of the early-type donor. Interestingly, to our current knowledge, all three main mechanisms of accretion discussed in Section 2.3.4 might act in such systems. High-Mass X-ray Binaries are internally subdivided into the Supergiant X-ray Binaries (SGXBs), where a neutron star accretes from the wind of an OB-supergiant, and Be X-ray Binaries (BeXRBs) containing a neutron star and a Be star with extended excretion disk. Both groups include persistent and transient subclasses. Supergiant Fast X-ray Transients (SFXTs) are transient supergiant X-ray binaries, which exhibit stable low X-ray emission in quiescence with rare, short (with a duration of a few days) outbursts that sometimes can be associated with periastron passages (Sidoli 2017). The observed X-ray luminosity ranges from $L_X \sim 10^{32}\,\mathrm{erg\,s^{-1}}$ in quiescence of some transient Supergiant X-ray Binaries up to the $L_X \sim 10^{39}\,\mathrm{erg\,s^{-1}}$ in the brightest outbursts of Be X-ray binaries.

Neutron stars in High-Mass X-ray Binaries are typically middle-aged ($\gtrsim 10^5$ yr), although recently for a few of these systems, which are associated with supernova remnants, significantly lower upper limits on the age were obtained, less than 10^5 yr (see, e.g., Gvaramadze et al. 2019), with the youngest ones being only a few thousand years old (Heinz et al. 2013; Maitra et al. 2019). It is not yet fully clear how such young neutron stars can enter the stable accretion stage so quickly. Khokhriakova & Popov (2022) showed that an episode of a fallback of the ejecta onto a newly born neutron star can allow it to avoid the ejector phase and start an early accretion from a donor star.

The spin periods of neutron stars in classical (meaning: persistent) Supergiant X-ray binaries are generally long, $P{\sim}100$–1000 s, while the orbital periods of this systems tend to be only ~10 days (Corbet et al. 2017). Figure 2.26 shows no obvious correlation of P-P_{orb} within this group. These wind-fed systems typically have low eccentricity, which, combined with their relatively small orbital periods, results in a very small spatial separation between the components. The orbital period distribution of Be X-ray Binaries spans from a few to a few hundred days. As was first shown by Corbet (1984), there is a positive correlation between the spin of a neutron star and the orbital periods of the system (see Figure 2.26). He suggested that in this case a longer separation of the components translates to the lower average density of the plasma surrounding the neutron star. In its turn, this results in spin-down until the equilibrium state is reached. Such a correlation conveniently allows for the estimates of P_{orb} from the known spin period (see, e.g., Equation 1 of Vinciguerra et al. 2020), however the large scatter in a growing sample of the systems weakened the correlation (see results of Haberl & Sturm 2016, for a study of the Corbet diagram of the Be X-ray Binaries in the Small Megallanic Cloud). The latter can mean that more complex models are needed to uniquely match P and P_{orb}. However, Knigge et al. (2011) noted that it is possible that the spin distribution is rather bimodal, with the distinct gap at ~40 s. Their suggested interperation states that neutron stars in two different populations are produces by two different types of supernovae. An alternative explanation by Cheng et al. (2014) includes different accretion modes, with one population more often experiencing giant outbursts, that result in longer spin-up episodes with higher mass-accretion rates.

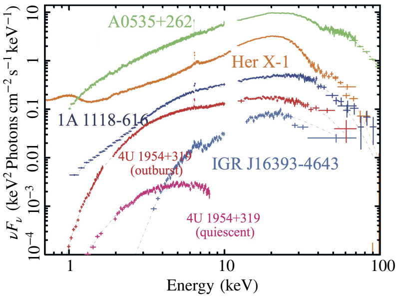

Figure 2.27: Typical spectra of HMXBs. The spectra of the symbiotic X-ray binary 4U 1954+319 are shown for the comparison. Figure 14 (top right panel) from Enoto et al. (2014) © AAS. Reproduced with permission.

Neutron stars in High-Mass X-ray Binaries possess strong magnetic fields, $B \sim 10^{12}$–10^{13} G. Such high values of the magnetic field imply large magnetospheric radii, $R_{\mathrm{m}} \sim 100\,R_{\mathrm{NS}}$ (see Section 2.2.1), at which accreted matter couples with the magnetic field of a neutron star and then being channeled onto the poles. The accretion in the presence of strong magnetic fields and high mass-accretion rates makes neutron stars in High-Mass X-ray binaries the brightest X-ray pulsars, with a wide variety of observed pulse profiles. The magnetic fields for these sources are mainly inferred from cyclotron lines, which are currently observed in spectra of about 40 systems (Staubert et al. 2019). Sometimes, multiple harmonics are detected (see, e.g., Nagase et al. 1991; Heindl et al. 2000, for 4U 0115+634), as well as unharmonically spaced lines (as, for example, in GX 302−1; Fürst et al. 2018). Spectra of High-Mass X-ray binaries at high mass-accretion rates at first approximation are fairly well characterized by the power-law with a high exponential cutoff (see, e.g., Müller et al. 2013). The primary mechanism shaping the spectra is thermal or bulk Comptonization of soft photons emitted from the polar caps, heated and thickened by accretion ("thermal mounds") in the warm magnetized plasma of the accretion channel (see, e.g., Becker et al. 2012). The soft X-rays are often heavily absorbed by the plasma, surrounding the magnetosphere, as well as in the Galactic medium (Kretschmar et al. 2019). However, in many cases, there is a necessity of additional empirical components to describe the spectra, such as the well-known "10-keV" feature – a broad Gaussian-like component that can appear in emission or in absorption. The detailed discussion about this feature is given Section 3.1.1. It hints at a more complex continuum formation that involves polarization of the emitted radiation, inhomogeneity of the plasma in the accretion channel, and cyclotron processes. These topics are discussed in greater details in Chapter 3, Chapter 5, and Chapter 6. Figure 2.27 shows typical spectra of the selected High-Mass X-ray Binaries.

Supergiant X-ray Binaries

Despite all the similarities between the subclasses of High-Mass X-ray Binaries that were already discussed, there are also striking differences in their manifestation. Permanent Supergiant X-ray Binaries, where a neutron star is in relatively close orbit with a blue supergiant continuously accretes from a fast stellar wind are the most classical representatives of the population. The wind of the supergiant is affected by the strong gravitation field of the neutron and its X-ray emission. The orbital motion of a neutron star through the plasma of the wind is accompanied by a detached bow shock and a trailing accretion and photoionization wakes (Kretschmar et al. 2019; Manousakis et al. 2012). The strong line-driven wind of blue supergiants is itself subject of instabilities that lead to the formation of the higher density "clumps" in the flow (see El Mellah et al. 2018, and references therein). El Mellah et al. showed that the presence of the clumps in the wind causes the Bondi-Hoyle-Lyttleton accretion (see Section 2.3.4.1) to be much less efficient due to specifics of the angular momentum transfer. These overall complex structure of the plasma flow (see Figure 2.28) leads to variable absorption and mass-accretion rate onto a neutron star and translates into observed aperiodic short-term variability (Grinberg et al. 2017). For more information on stellar winds from supergiant stars and the accretion phenomena in Supergiant X-ray Binaries, interested readers are referred to a comprehensive review by Martínez-Núñez et al. (2017).

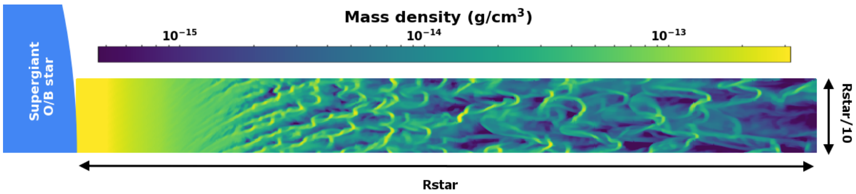

Figure 2.28: Color map of the wind density structure around the OB-supergiant. Figure 1 from El Mellah et al. (2018).

Supergiant Fast X-ray Transients

INTEGRAL's 9-year Galactic survey established Supergiant Fast X-ray Transients as a subclass of Supergiant X-ray Binaries (Walter et al. 2015). Despite similarities with persistent Supergiant X-ray Binaries, such as values of orbital periods and the type of a donor star, they show much more dramatic variability in X-ray flux. These sources show a much lower persistent luminosity, $L_X \lesssim 10^{34}\,\mathrm{erg\,s^{-1}}$, that characterizes their quiescent state. Most of the time Supergiant Fast X-ray Transients are in quiescence, showing only rare sporadic outbursts with a duration of about a day and short (∼thousands of seconds) flares reaching the X-ray luminosities of $\sim 10^{36}$–$10^{37}\,\mathrm{erg\,s^{-1}}$ (see Sidoli 2017, and references therein). More often, outbursts happen near the periastron (Sidoli et al. 2017). Pradhan et al. (2018) showed that the accretion environment around neutron stars in Supergiant Fast X-ray Transients is much less dense than in Supergiant X-ray Binaries. This might be due to the higher orbital motion of the neutron star that might hint to more eccentric orbits (Maccarone et al. 2014) or faster stellar winds for the systems with near-circular orbits (Giménez-García et al. 2016). In this way, the environment provides a much lower mass-accretion rate onto the neutron star, and the accretion might proceed in quasi-spherical subsonic mode (see Section 2.3.4.3). This model for Supergiant Fast X-ray Transients was proposed by Shakura et al. (2014) and explains the brightest flares by invoking sporadic magnetic reconnection due to capturing the magnetized plasma, which can enhance the subsequent penetration of the matter into the magnetosphere.

Disk-Fed Systems

A severely underpopulated subclass of High-Mass X-ray Binaries are Roche-lobe overflow powered systems: Cen X-3, SMC X-1, and LMC X-4. In these systems, due to the close orbits (∼a few days) and the size of a supergiant component, the (semi-)stable accretion occurs similar to Low-Mass X-ray Binaries via the inner Lagrangian point and the formation of a stable accretion disk around a neutron star, resulting in high X-ray luminosity $\sim 10^{37}\,\mathrm{erg\,s^{-1}}$ (see, e.g., Thalhammer et al. 2021). It is possible that the wind transfer also plays a role in this system. The switch of the accretion modes between the disk and the wind accretion suggested by Paul et al. (2005) for Cen X-3, but was not confirmed (Müller et al. 2011). The Roche-lobe overflow systems have short spin periods (∼1-10 s, compared to the other High-Mass X-ray Binaries, and populate the lower left corner of the Corbet diagram (Figure 2.26).

Be X-ray Binaries

Be X-ray Binaries are another example of a strong transient behavior in High-Mass X-ray Binaries. A Be companion in these systems is a late-type O, or an early type B non-supergiant star that forms an excretion disk expanding from the equator, possibly due to the fast rotation. Okazaki & Negueruela (2001) showed that for Be stars in Be X-ray Binaries, the circumstellar disk is truncated by the interaction with a neutron star, with the radius of truncation dependent on the eccentricity of the orbit. The truncation makes a disk smaller and denser than disks of isolated Be stars (Reig & Roche 1999). Be X-ray Binaries manifest themselves through the bursting activity in two different ways: Type I outburst, associated with the periastron passage, reaching $L_X \sim 10^{36}\,\mathrm{erg\,s^{-1}}$, and less frequent Type II (giant) outbursts, with $L_X \gtrsim 10^{37}\,\mathrm{erg\,s^{-1}}$. The possibility for a system to undergo Type I or Type II outbursts seems to be tightly related to the truncation radius of the excretion disk, which translates to the eccentricity of the system (Okazaki & Negueruela 2001). At the same time, the trigger mechanism for Type II outbursts might be associated with the passage of the neutron star through the warped disk of the Be star (Okazaki et al. 2013). A few Be X-ray Binaries were early established as persistent sources with the low, stable emission $L_X \sim 10^{34}$–$10^{35}\,\mathrm{erg\,s^{-1}}$ (Reig & Roche 1999). X Persei is one of the most well-known among them, with the puzzling excess in high-energy emission (see, e.g., Doroshenko et al. 2012). This behavior is not unexpected, as it was early understood that the low-rate accretion is possible in the regime of magnetic inhibition (see Section 2.2.1) in Be X-ray Binaries (Stella et al. 1986; Nelson et al. 1993). Evidence of the low-luminosity pulsed emission were also known from observations of their quiescent states (see, e.g., Reig & Zezas 2018; Tsygankov et al. 2017). However, the low level of flux mainly allowed accessing soft X-rays, from which it was not clear whether the low-rate accretion or the cooling of the hot spots after the previous accretion event is observed. A clear indication of the present accretion was obtained for the nearby sources, GX 304−1 and A 0535+262, by the high-energy access in the spectra, together with their transition from power-law-like at high luminosity state, to the two-component X Per-like shape at low luminosities (Tsygankov et al. 2019b,c). The hard spectra in quiescence, together with still present pulsations, hint that the accretion at low mass-accretion rates happens in these systems. Modeling of the spectra and pulse profiles of Be X-ray Binaries in quiescence is one of the main objectives of this work, which I discuss in detail in Chapter 6.

2.4.2.2 *Low-Mass X-ray Binaries*

Low-Mass X-ray Binaries are close systems consisting of a neutron star in an orbit with a low-mass companion star ($\lesssim 1\,M_\odot$), typically a main-sequence star or a red giant, although a few systems with brown and white dwarfs are known. The accretion usually occurs via Roche-lobe overflow, when a donor fills its Roche lobe, and the matter can reach a neutron star via the inner Lagrangian point. Typically, these are old systems with weakly magnetized ($B \lesssim 10^{10}\,\mathrm{G}$) neutron stars and orbital periods of a few hours for the main-sequence components and days-week for a supergiant one (Bahramian & Degenaar 2022, and references therein). The orbital periods tend to noticeably decay in these systems due to the loss of angular momentum to accretion and other processes (see, e.g., Tavani 1991; Ponti et al. 2017). On the other hand, the momentum transfer can spin up a neutron star to a very short period of a few milliseconds. This effect – spinning up of a neutron star due to the disk accretion in Low-Mass X-ray Binaries – is known as the *recycling scenario*. This scenario explains the origin of Millisecond Pulsars (MSPs, see the following section) in binary systems (see comprehensive review by Bhattacharya & van den Heuvel 1991).

Accreting Millisecond X-ray Pulsars (AMXP) are a subclass of Low-Mass X-ray Binaries that shows rapid X-ray pulsations due to the accretion of the matter channeled onto the magnetic poles, similar to disk-fed High-Mass X-ray Binaries. However, neutron stars in Accreting Millisecond X-ray Pulsars have much lower magnetic fields, $B \sim 10^8$–$10^9\,\mathrm{G}$. Due to the correspondingly smaller radius of the magnetosphere than for classical High-Mass X-ray Binaries with strongly magnetized neutron stars, an accretion disk may extend much closer to the neutron star in Accreting Millisecond X-ray Pulsars and play a more significant role in reprocessing of X-ray radiation. These are transient sources with various outburst duration (from days to a few years), relatively low outburst X-ray luminosities, $L_X \sim 10^{36}\,\mathrm{erg\,s^{-1}}$, no pulsations detected in quiescence, and short orbital periods of ∼1 day (see Patruno & Watts 2021, and references therein). A few objects, the so-called "transitional Millisecond Pulsars" (tMSPs) show the switch between the stage of the accreting

X-ray pulsar in Low-Mass X-ray Binaries, with no radio pulsation and the regular Millisecond Radio Pulsar state: PSR J1023+0038, XSS J12270−485, and IGR J18245−2452 in M28 (see Bahramian & Degenaar 2022, and references therein). It reinforces confidence in the recycling scenario.

However, for reasons that are not yet clear, not all X-ray pulsars in Low-Mass X-ray Binaries belong to Accreting Millisecond X-ray Pulsars. There are four known systems accreting from the Roche-lobe overflow that exhibit X-ray pulsations with $P \sim 0.1$–$1\,\mathrm{s}$ and significantly higher magnetic fields of neutron stars $B \sim 10^{10}$–$10^{12}\,\mathrm{G}$. Three of these systems have a low-mass donor companion (2A 1822−371, 4U 1626−67, GRO 1744−28), and one system is the famous Her X-1, which has an A/F donor companion of $\sim 2\,M_\odot$ (HZ Herculis discovered by C. Hoffmeister, the former member (1915–1918) of the Dr. Karl Remeis Observatory; Hoffmeister 1936; Ahnert et al. 1941). These systems seem to follow an evolutionary scenario substantially different from Accreting Millisecond X-ray Pulsars, and which might not be unique for all of these sources, representing a heterogeneous group with a large spread of orbital periods, as well as masses and types of donors.

Technically, Her X-1 belongs to Intermediate-Mass X-ray binaries (IMXBs), with the mass of a companion $1\,M_\odot \lesssim M \lesssim 10\,M_\odot$ - rare sources, possible progenitors of LMXBs.

In addition to the 15 currently known Accreting Millisecond X-ray Pulsars and four slowly-rotating X-ray pulsars in Low-Mass X-ray Binaries, there are three systems showing X-ray pulsations among the Symbiotic X-ray Binaries (SyXBs). These are systems that differ from others Low-Mass X-ray Binaries by the lack of the Roche-lobe overflow. Instead, neutron stars in Symbiotic X-ray binaries mainly accrete the matter from the slow stellar wind of a late-type (K/M) giant. For a few systems, including the only persistent source within the group, GX 1+4, long orbital ($P_\mathrm{orb} \gtrsim 1000\,\mathrm{days}$) and spin periods ($P \gtrsim 100\,\mathrm{s}$) were measured (Yungelson et al. 2019). Symbiotic X-ray binaries are in general transient sources, with an overall faint X-ray emission $L_X \sim 10^{32}$–$10^{36}\,\mathrm{erg\,s^{-1}}$ and high variability during short outbursts.

The number of known systems with pulsations is relatively small compared to the whole population of Low-Mass X-ray Binaries. The reasons for that are not yet well understood, although several explanations were suggested. The interested reader is referred to the recent review by Bahramian & Degenaar (2022) for more details. In this case, the question arises: how can we be sure that all non-pulsating Low-Mass X-ray Binaries are not the black hole binaries? The answer lies in the more common activity for the majority of Low-Mass X-ray Binaries: the thermonuclear (Type I) bursts. They indicate the unstable burning of accreted H and He on the surface of a neutron star. These bursts are characterized by a sudden rise of the X-ray intensity and the duration of about thousands of seconds (Galloway et al. 2008). Some sources also exhibit Type II outbursts related to the sporadic accretion phenomena. These bursts lack the spectral softening during the decay, which usually indicates cooling for Type I outbursts (Lewin et al. 1993).

Most Low-Mass X-ray Binaries are transient sources, typically showing a softer spectrum at higher luminosity and a harder one at the lower state. The X-ray spectrum mainly consists of a soft thermal component and a hard Comptonized component (see, e.g., Güngör et al. 2017).

2.4.2.3 *Millisecond Pulsars*

As was discussed in Section 2.4.1, typical pulsars are born with relatively short rotational periods and spin down over time, with fast spin-down rates corresponding to their young age (see Figure 2.17). The exact birth periods are not known but are estimated as more than tens of milliseconds (see Harding 2013, and references therein). The lower limit corresponds to such young known pulsars as, for example, Crab with $P \approx 33\,\mathrm{ms}$ and Vela with $P \approx 89\,\mathrm{ms}$. However, to date also more than 250 Rotation-Powered Pulsars with spin periods of only $\sim$ a few milliseconds are known (Manchester 2017). Shortly after the discovery of the first Millisecond Pulsars (Backer et al. 1982), a *recycling scenario* was independently suggested by Radhakrishnan & Srinivasan (1982), Alpar et al. (1982), and Fabian et al. (1983), stating that Millisecond Pulsars are descendants of Low-Mass X-ray Binaries, being old pulsars span up by the historical episodes of disk accretion. After the accretion is ceased, a previously accreting neutron star can renew a regular pulsar activity. A high number ($\sim 70\%$) of Millisecond Pulsars with confirmed binary companion, an extremely low number ($\sim$1%) of the normal Rotational-Powered Pulsars in binary systems, and the existence of transient Millisecond Pulsars that show the episodes of accretion from their low-mass companion, support the recycling scenario (see, e.g., Manchester 2017). The suggested explanations for the existence of Millisecond Pulsars without a binary companion include its ablation by a strong wind of the pulsar and, for systems in the globular clusters, spontaneous stellar interactions (see Lorimer 2008, and references therein).

In general, an individual scenario of the companion ablation does not seem to be so unrealistic if one has a look at the "spider" systems among Millisecond Pulsars: *Black Widows* and *Redbacks*. Spiders are tight systems with low-mass non-degenerate companions that are severely affected by the pulsar wind. A companion star typically has a mass of $\lesssim 0.1\,M_\odot$ in Black Widows and 0.1–$0.4\,M_\odot$ in Redbacks. Pulsars in spiders exhibit long eclipses on the radio light curve, created by the material evaporated from a companion. Chen et al. (2013) showed that these systems could be created in the evolutionary scenario from Cataclismic-Variable-like Low-Mass X-ray Binaries and that the final separation by the companion mass (Black Widow/Redback) can happen due to a difference in pulsar's beaming that transaltes to the irradiation power.

Millisecond Pulsars show a similar spectral energy distribution as regular Rotation-Powered Pulsars, with a minor differences, such as steeper spectra of coherent radio emission with wider pulse profiles, thermal X-ray spectra of higher temperature, and harder γ-ray emission not detected above $\sim$10 GeV (Harding 2022). Millisecond Pulsars show very stable low-rate spin down, with very rare glitches. They also have the lowest timing noise among the populations of pulsars and their timing stability over a decade times scale is comparable to terrestrial atomic clocks (see Lorimer 2008, and references therein).

2.4.2.4 *Gamma-Ray Binaries*

Gamma-ray Binaries are an intriguing, small population of fewer than ten confirmed members (Adams et al. 2021), recently established (over the last $\sim$20 years) by the advances of such γ-ray missions as the ground-based arrays of Cherenkov detectors (H.E.S.S., MAGIC, VERITAS) and space observatories (EGRET, *AGILE*, *Fermi*). Gamma-ray Binaries are defined as systems composed of a compact object and an early-type OB/Be star, whose spectral energy distribution shows a broad non-thermal emission peaking at energies above $\sim$1 MeV (Dubus et al. 2017). The nature of the compact object is not always clear, and for a long time compact objects only in two systems, PSR B1259$-$63/LS 2883 and PSR J2032+4127/MT91 213, were undoubtedly identified as neutron stars due to their detected radio and γ-pulsations (see Adams et al. 2021, and references therein). The recent detection of transient radio pulsations from LS I+61°303 and a series of magnetar-like bursts make a strong argument that this binary also contains a highly magnetized neutron star (Weng et al. 2022). In this way, the nature of a compact object remains uncertain only in about a half of the Gamma-ray Binaries population. However, some additional clues, such as the low mass of the compact companion and the combined spectral energy distribution, suggest the existence of neutron stars in the yet uncertain systems. The *pulsar scenario* was therefore proposed for them as well (see, e.g., Tokayer et al. 2021, for HESS J0632+057).

The pulsar scenario assumes that a compact object in Gamma-ray Binaries is a young Rotation-Powered Pulsar, ejecting the wind of relativistic particles. The collision of the pulsar wind with the dense plasma of an early-star wind creates a shock structure similar to a pulsar wind nebulae (see Section 2.4.1.1), but much closer to the pulsar than in the case of an isolated neutron star (see, e.g., Zdziarski et al. 2010). The γ-ray emission is then produced in the shock between the colliding winds[6] by the efficient mechanism, which nature is not yet well understood, converting a substantial amount of the pulsar's spin-down power into the nonthermal emission (Dubus 2015, and references therein). This scenario makes Gamma-ray Binaries potential short-lived predecessors of High-Mass X-ray Binaries, with the transition, determined by the sufficient spin-down of the pulsar to allow accretion to begin. The scenario is supported by the fact that the rotational periods for all pulsars that were confirmed as compact companions in Gamma-ray Binaries, span from a few tenths to a few hundreds milliseconds, which is typical for the young neutron stars (see, e.g., Abeysekara et al. 2018; Weng et al. 2022).

The orbital periods of currently known Gamma-ray Binaries show significant scatter from ~4 days for the most compact LS 5039 up to ~50 years for PSR J2032+4127. The γ-ray emission is often modulated on the orbital period (Dubus 2015). Thus, for the long-period PSR J2032+4127 the monitoring campaign for its periastron passage in November 2017 revealed a TeV emission peaking at periastron (Abeysekara et al. 2018) and high variability in radio and X-ray (Ng et al. 2019).

Dubus (2015) has pointed out that the current class of Gamma-ray Binaries should be more precisely called High-Mass Gamma-ray Binaries, as a few sources with low-mass companion also exhibit the high-energy γ-ray emission. These are systems with Millisecond Pulsars, some of them are known as Black Widows, Redbacks, and transitional Millisecond Pulsars (see Section 2.4.2.3). However, the community currently continues using the term "Gamma-ray Binaries" mainly for the systems with massive star companions.

2.4.2.5 *Ultraluminous X-ray Sources*

Ultraluminous X-ray Sources have been known for about forty years. They were first discovered as extra-galactic sources of extremely high X-ray luminosities ($L_X > 10^{39}\,\mathrm{erg\,s^{-1}}$) during the *Einstein* observatory survey (Long & van Speybroeck 1983). Many hints, such as a correlation of a number of Ultraluminous X-ray Sources with the star formation rate indicate that they most likely have a stellar origin and represent a rare state of High-Mass X-ray Binaries that accrete at super-Eddington

---

[6] Although the emission in these systems is powered by colliding winds, they do not belong to the class of objects officially carrying the name "colliding winds binaries", which are binary systems consisting of two non-degenerate supergiant OB-stars and emitting γ-rays as well.

rates (see, e.g., King et al. 2001). However, a few of the most luminous sources, $L_X > 10^{41}\,\mathrm{erg\,s^{-1}}$, are still among Intermediate Mass Black Holes candidates (see Marchant et al. 2017, and references therein). While the community, in general, recognized the majority of Ultraluminous X-ray Sources as the extreme condition of a binary system, the nature of the accretor remained unclear (Kaaret et al. 2017). Figure 2.29 shows optical (top panel) and X-ray (bottom panel) images of a galaxy with an Ultraluminous X-ray Source.

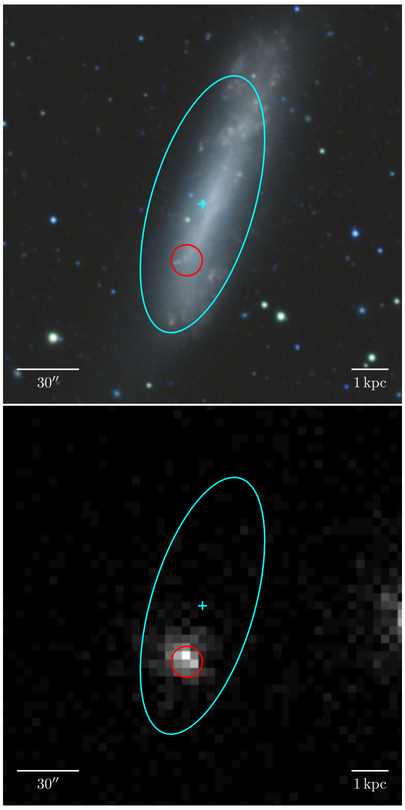

Figure 2.29: ULX candidate from eRASS1 survey by SRG/eROSITA. Top panel shows optical data from DESI, bottom panel is given by eROSITA. The region corresponding to the ULX is marked by the red circle. Courtesy of Philipp Weber.

The first detection of pulsations in the observation of M82 X-2 by Nuclear Spectroscopic Telescope Array (*NuSTAR*) established that at least some of the Ultraluminous X-ray Sources harbor a neutron star as a compact object (Bachetti et al. 2014). This event was followed by the discovery of seven more Pulsating Ultraluminous X-ray Sources (PULXs, or Ultraluminous X-ray pulsars, ULXPs) (see, e.g., Fürst et al. 2016; Israel et al. 2017a,b; Carpano et al. 2018), including the first galactic Ultraluminous X-ray Source, Swift J0243.6+6124 (Wilson-Hodge et al. 2018). Seven currently known Pulsating Ultraluminous X-ray Sources with determined P and $P_{\rm orb}$ are shown in Table 2.2. All these sources show the high spin-up rates, with the extreme examples of NGC 300 ULX1, that has been spun up from $\sim$125 s to $\sim$19 s in less than four years of observations (Vasilopoulos et al. 2018). The typical pulse profiles are simple broad sinusoidal-like (see, e.g., Fürst et al. 2016). A few Pulsating Ultraluminous X-ray Sources show rather stable super-Eddington accretion, while the others have a transient nature, likely being in an eccentric orbit with a Be star (King & Lasota 2019).

Table 2.2: PULXs with known rotational and orbital periods. Data are taken from (King & Lasota 2019) (see their Table 1 for more information), but the rotational period of rapidly spinning up NGC 300 ULX1 is updated according to the recent data (Vasilopoulos et al. 2019).

source	p [s]	$p_{\rm orb}$ [d]
M82 X-2	1.37	2.51(?)
NGC 5907 X-1	1.13	5.3
NGC 7793 P13	0.42	63.9
NGC 300 ULX1	$\sim$16	> 8
SMC X-3	$\sim$7.7	45.04
NGC 2403 ULX	$\sim$18	60-100(*?*)
Swift J0243.6+6124	9.86	28.3

The discovery of neutron stars in Ultraluminous X-ray Sources was followed by an active discussion of the possible cause that distinguishes Pulsating Ultraluminous X-ray Sources from the regular High-Mass X-ray Binaries. The idea that these systems can host a magnetar was suggested and supported by parts of the community (see, e.g., Tong 2015; Eksi et al. 2015), with rapidly developing efforts for modeling the magnetar-like magnetic fields (Mushtukov et al. 2015a). However, no magnetar-like activity was so far observed from any of Ultraluminous X-ray Sources. Occasionally used term the "low-field magnetar" hardly helps to understand the phenomenon in the absence of typical magnetars manifestations[7]. The current stage of our understanding is that Pulsating Ultraluminous X-ray Sources host highly magnetized neutron stars, but their magnetic fields are not necessarily required to reach magnetar-like values if geometrical effects (beaming) are taken into account (see, e.g., Erkut et al. 2020). Moreover, recent interpretations of typical for Ultraluminous X-ray Sources two-component spectrum with a curvature at $\sim$6 keV based on the high-quality *XMM-Newton* and *NuSTAR* data, favor the scenario of a super-critically accreting neutron star. Such then, Ultraluminous X-ray Sources are a high-luminosity tail of High-Mass X-ray Binaries in a "slightly unusual state" (King & Lasota 2019). Let me note, that there are potential high-field objects, $B \sim 10^{13}$ G, among the canonical High-Mass X-ray Binaries, such as X Persei and GRO J1008−57. In addition, recently a cyclotron line was detected in the spectrum of the galactic ULX Swift J0243.6+6124 at 130 keV, implying the magnetic field of $\sim 10^{13}$ G (Kong et al. 2022b). In light of this, it is yet to be answered why some systems develop the ultra-luminous condition, while others don't.

A rapidly increasing number of known Ultraluminous X-ray Sources (see the recent catalog by Walton et al. 2022, which includes 1843 ULX

---

[7] Here I am tempted to note that there are arguments against the existence of magnetars in binary systems, which will be presented in Section 2.4.3

candidates) gives hope for more detailed populational studies, unveiling some of remaining questions.

2.4.3 *Evolutionary connections*

The discussed rich variety of neutron stars observational manifestations leaves the question: Are there internal connections between different populations? Can their diverse properties be understood in a consistent way? This section is aimed to conclude the observational findings and to place some possible links between the different groups of neutron stars.

Among different classes of isolated neutron stars, a number of evolutionary connections is suspected. Moreover, some connections are necessary to solve the *birthrate problem*. If the different classes of isolated neutron stars (RPPs, RRATs, XDINs, magnetars, and CCOs) are treated as separated populations with individual birthrates, the sum of their estimated birthrates exceeds the core-collapse supernova rate in the Galaxy (Keane & Kramer 2008; Turolla et al. 2015). The evolutionary link would reduce the estimated total birthrate, providing a solution to this problem. The search for the evolutionary connections between different populations led to the idea that the observed properties of neutron stars might be determined by the limited number of parameters, such as magnetic field, mass, and rotational period at their birth (Turolla et al. 2015). In this way, the great diversity of observed properties can be explained by the combination of these parameters and their evolution during the neutron star life. This effort is know as *Grand Unification of Neutron Stars* (Kaspi 2010). The test of this idea is only possible via population synthesis (Popov & Prokhorov 2007), together with proper magneto-thermal evolutionary models (see Section 2.2.2) and increased sample size.

From the observed rates of core-collapse supernova events in nearby spiral galaxies, the total number of neutron stars in the Milky Way can be estimated as $\sim 10^9$ (Treves et al. 2000). This is a much greater number than the ~ 3000 neutron stars observed to this date, most of them manifesting themselves as radio pulsars (based on the ATNF catalog; Manchester et al. 2005). The common explanation for such a divergence between these numbers is that after an age of $\sim 10^7$ yr the supplies of rotational and internal energy are expected to fade, limiting the pulsar active stage of a neutron star to a small fraction of its total lifetime. The characteristic age of many isolated neutron stars lies in the range 10^4–10^7 yr (Rigoselli et al. 2021). With time, the thermal emission from the surface and polar caps is weakened as well, and accretion becomes the only way of detecting an isolated neutron star traveling through the interstellar medium. However, no matter early predictions (Salpeter 1964; Ostriker et al. 1970; Shvartsman 1971c), isolated accreting neutron stars have never been observed to this date. Even in the case of significant spin down, which would allow to overcome the centrifugal barrier, the accretion onto an isolated neutron star is expected to proceed in the quasi-spherical settling regime (see Section 2.3.4.3) due to magnetic inhibition. Popov et al. (2015) showed that the expected X-ray luminosity of such sources is only $L_X \sim 10^{27}\,\mathrm{erg\,s^{-1}}$, which reduces the possibility of their detection, even with the sensitivity of SRG/eROSITA, to only a few sources within ~ 30 pc. They note that the situation can be improved if one considers short flares expected from the accreting isolated neutron stars due to magnetic reconnection, which can enhance the emission up to $L_X \sim 10^{31}\,\mathrm{erg\,s^{-1}}$ during a few hours. The possible detection of these hypothetically existent nearby neutron stars is difficult to interpret and differentiate from the background.

A young neutron star, being born with a certain magnetic field strength, is expected to follow the corresponding isoline from left to right on the P-$\dot{P}$ diagram (see Figure 2.30). During this time, one can observe it as a radio and/or γ-ray pulsar, depending on geometrical effects. Passing the *death line*, the ejector mechanism switches off, and the neutron star enters a so-called *graveyard* or *death valley* (blue region in Figure 2.30). About 10^8 neutron stars in the Galaxy are too old to be detected as radio/γ-ray pulsars (Popov et al. 2006), and their thermal emission is too faint to be detected in X-rays. As were discussed in Section 2.4.2.3, there are ways to bring a pulsar back from the graveyard, by angular momentum transfer in a close binary system. In this way, Millisecond Pulsars are "resurrected" by their binary companion and spun up to the shortest observed periods.

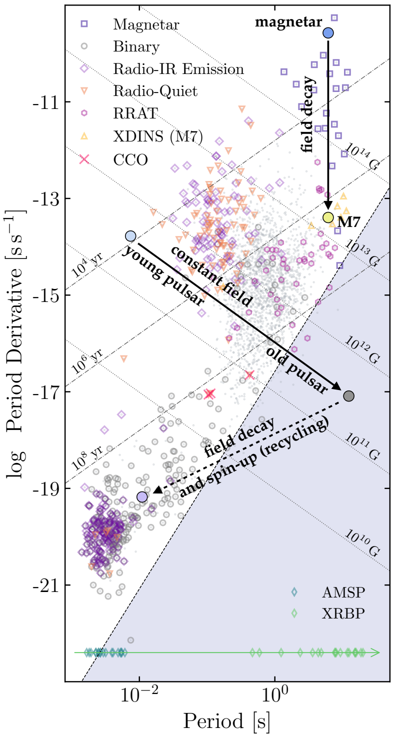

Figure 2.30: Same as in Figure 2.17, but with examples of possible evolutionary tracks. Partly based on Figure 2 (right panel) of Pires (2018)

Isolater Neutron Stars

However, pulsars can follow much more complicated paths due to the increase and decay of the magnetic field (Igoshev et al. 2021b). In this way, a fast decay expected for the strong fields of magnetars, allows them to move almost vertically down on the P-$\dot{P}$ diagram during part of their life time (see Figure 2.30) The field decay is expected to slow down at $B \lesssim 10^{14}$ G, which can lead to a significant spin-down (Igoshev et al. 2021b, and references therein). High magnetic fields estimated for X-ray Dim Isolated Neutron Stars and some Rotating Radio Transients, $\sim 10^{13}$ G, as well as their location on the P-$\dot{P}$ diagram, led to the idea that both populations might be related to the magnetars evolution. For X-ray Dim Isolated Neutron Stars this is also supported by their radio-silence and unusually high for their age thermal luminosities (Pires et al. 2014). Burke-Spolaor (2013) noted that on the P-$\dot{P}$ diagram, Rotating Radio Transients seem to create a bridge, connecting regular Rotation-Powered Pulsars with magnetars and X-ray Dim Isolated Neutron Stars. McLaughlin et al. (2006) suggested that Rotating Radio Transients can be evolutionary connected with magnetars. The unusual glitches, followed by the rapid spin-down, as well as high magnetic field of the RRAT PSR J1819−1458, $B \sim 5 \times 10^{13}$ G, can potentially be a hint that the source is an evolved magnetar (Lyne et al. 2009). However, as noted by Popov et al. (2006), the birthrate of both populations, Rotating Radio Transients and X-ray Dim Isolated Neutron Stars is much higher than the formation rate of magnetars. Although only seven X-ray Dim Isolated Neutron Stars are known so far, these objects are also extremely difficult to observe due to their faint X-ray emission. Such then, we see only the most nearby sources, when the actual population is much larger. Popov et al. (2006) pointed out that the birth rates of X-ray Dim Isolated Neutron Stars and Rotating Radio Transients are rather comparable and it could be that these two populations have evolutionary connection. Detailed simulations of the coupled magnetic and thermal evolution, which include the Hall term, show that the diversity of magnetats, Rotation-Powered Pulsars, and X-ray Dim Isolated Neutron Stars can be accounted for by varying only the magnetic field strength, mass of the neutron star, and the envelope composition (Viganò et al. 2013). As was mentioned before, Central Compact Objects are likely entering this picture as normal (or high-field) young pulsars, that experienced an episode of the intense fall-back accretion (see, e.g., Popov 2016).

An alternative scenario to explain the observational properties of isolated neutron stars is sometimes considered in the literature, though not being widely supported by the community. It suggests that all objects such as magnetars, X-ray Dim Isolated Neutron Stars, Rotating Radio Transients, Central Compact Objects and radio-quite pulsars, experienced fall-back accretion, followed by the formation of a fall-back disk (Alpar 2001). Within this model, the X-ray emission from these sources is powered by accretion from the disk at different mass-accretion rates. Gençali & Ertan (2021) suggested that Rotating Radio Transients are much less magnetized due to the torques imposed by the magnetosphere-disk interaction, and should be placed beneath the death line. They show only sporadic bursts, which might be triggered by the disk-field interactions. Due to the magnetic torques between the disk and the magnetospheres, magnetars and X-ray Dim Isolated Neutron Stars also within this model have much lower magnetic fields, 10^{12}–10^{13} G and 10^{11}–10^{12} G, respectively. A serious criticism, though, was raised by Doroshenko et al. (2020b) who argued against the accretion-powered origin of magnetars emission. They noted that aperiodic variability, typical for all accretion-powered sources, is not found in observations of magnetars. Another problem with this scenario is a lack of explanations for the giant flares. Moreover, the old ages suggested by the model for X-ray Dim Isolated Neutron Stars, which place them below the death line, contradict the kinematic age estimates.

High-Mass Binary Systems

As was discussed before, it is likely that the majority of neutron stars, including isolated ones, originate from massive binary systems (see Section 2.3, and references therein). A typical evolution of such systems has been already discussed in Section 2.3. A young neutron star paired with OB or Be companion, can pass the ejector stage being observed as a bright Gamma-Ray Binary due to colliding winds. Later, when matter penetration to the neutron star surface becomes possible, these systems can be observed as Supergiant X-ray Binaries or Supergiant Fast X-ray Transients for OB companions[8] and as Be X-ray Binaries for Be companion.

It was suggested by Popov & Prokhorov (2006), that the consequent evolution of a binary systems might serve as a natural channel for the formation of magnetars. The observed solitarity of magnetars led to the idea that the special evolution results in their formation and to the disruption of the binary progenitor. Simultaneously, no particularly large kick velocities are known for magnetars. However, as was early suggested by Thompson & Duncan (1993), the formation of very high, magnetar-like magnetic fields involves the dynamo mechanism and requires a fast rotation of the progenitor (see Section 2.1.4). As the core of a massive stars rapidly looses its angular momentum at the red supergiant stage, a mechanism enhancing the rotation is required to create a rapidly rotating neutron star progenitor (Popov 2016). The efficient momentum transfer most naturally happens in a binary system. Rapidly rotating Be stars formed in binary systems due to the accretion via the Roche lobe overflow, are one of the possible candidates. In this way, Be X-ray Binaries might be the cradles of magnetars. The second supernova explosion, accomponied by the magnetar formation, likely disrupts the system. If the system was not unbound, a newly born magnetar is left with the degenerous companion. Popov & Prokhorov (2006) showed that only ∼1% of neutron stars

---

[8] Whether the system is observed as Supergiant X-ray Binaries or Supergiant Fast X-ray Transients likely depends on the conditions established during the stellar wind interactions with the magnetosphere.

formed from the rapidly rotated progenitor stays in a binary, with the component likely being a black hole. They also suggested an alternative way to enhance the rotation of a neutron star progenitor is a coalescence of components, which naturally results in a single object. Popov (2016) noted that there are some evidences of the magnetar's formation from binary systems. Such is the case of CXOU J1647−45, studied by Clark et al. (2014). For this source, the former possible primary component was identified as a runaway star. Magnetars show no excessive proper motions, only $\sim$200 km s^{-1}, lower than the average value for the regular Rotation-Powered Pulsars (Kaspi & Beloborodov 2017).

In the rare case when the system survived the second supernova explosion and the second neutron star was born, it can be observed as a *binary pulsar*. These systems consist of a regular pulsar (secondary) and a recycled pulsar with a period of tens of ms and weak magnetic field ($\sim 10^{10}$ G). The first binary pulsar, PSR B1913+16, was discovered by Hulse & Taylor (1975) with a pulse period of 59 ms. A detailed explanation of the formation channel for this system was presented by Srinivasan & van den Heuvel (1982). They noted the old, spun-up neutron star in this system is expected to be detectable longer than the young one, which enters the "graveyard" earlier due to the higher magnetic field value and the spin-down rate. Taylor & Weisberg (1982) demonstrated that the rate of orbital period decay obtained from the long-term observations of such systems provides an excellent test for general relativity. The reviews by Lorimer (2008) and van den Heuvel (2017) are recommended for more information on binary pulsars.

Low-Mass Binary Systems

The evolutionary path of neutron star binaries with a low-mass companion is also well understood (see, e.g., Postnov & Yungelson 2014). It is expected to pass the late stage of Low-Mass X-ray Binaries, when the secondary fills its Roche lobe and accretion becomes possible. The spin-up of the old neutron stars can result in the activation of its ejector mechanism again, leading to the observed Millisecond Pulsars, which was already discussed in detail in Section 2.4.2.3.

2.5 CONCLUSIONS

In this chapter, I discussed the general characteristic of neutron stars (Section 2.1) and their evolution (Section 2.2), the origin of neutron stars in binary systems (with a strong focus on High-Mass X-ray Binaries) and accretion phenomena that can occur there (Section 2.3). Finally, I reviewed the variety of observational manifestations of neutron stars by their electromagnetic radiation, concentrating to a high degree on X-rays (Section 2.4).

The main purpose of this possibly excessive overview is to set a proper stage for the discussion of accretion-powered X-ray pulsars in High-Mass X-ray Binaries, which are the objects studied in this thesis. It is, however, insufficient to see these objects without a broader context. Many phenomena observed in accretion-powered X-ray pulsars, such as the evolution of rotational periods and the change of accretion regimes, have the same origin as in the other types of neutron star populations. For example, similar conditions can occur in the atmospheres of the High-Mass X-ray Binaries accreting in quiescence, Accreting Millisecond Pulsars, and magnetars with polar caps bombarded by particle streams. Thus, the model for the X-ray emission from accretion-heated atmospheres of neutron stars in

High-Mass X-ray Binaries which I present in Chapter 6 to describe the first case can be related to the other classes of objects.

It becomes clearer that modeling emission from neutron stars require treatment of extreme conditions. The presence of accretion flows makes this task more challenging due to the warm Comptonizing plasma and its dynamics, affected by the strong magnetic field. It calls for the detailed radiative transfer simulations in the optically thick plasma with non-trivial opacity and redistribution during scattering in the strong magnetic fields, accompanied by accounting for the strong gravity, to describe the observed phenomena. In the following chapters, I will describe the physics of accreting X-ray pulsars and radiative transfer modeling in greater detail.

3

ACCRETION COLUMNS AND POLAR CAPS OF ACCRETING X-RAY PULSARS

"Sometimes I wonder, whether these accretion columns even exist."
Konstantin Postnov

The general physics of the capture of matter by a neutron star and the interaction of plasma with the magnetic field at the magnetospheric boundary was discussed in detail in the previous chapter (see Section 2.2.1). Here, I consider the case of neutron stars in High-Mass X-ray Binaries in more detail and assume that the conditions for a plasma to be coupled with the magnetic field near the magnetospheric radius, R_m have developed. The main physical processes of interest are then related to the deceleration of the plasma near the surface and the photon production and energization in the accretion channel. As was mentioned in Section 2.1, there is observational evidence for more complex configurations of magnetic fields than a pure non-distorted dipole, including the off-centered dipole and quadri-dipolar models. For field strengths of $B \sim 10^{12}$–$10^{13}\,\mathrm{G}$ and mass-accretion rates of $\dot{M} \sim 10^{14}$–$10^{18}\,\mathrm{g\,s^{-1}}$ considered here, the magnetic field is capable of stopping the matter far away from the surface, at a distance of $R_\mathrm{m} \sim 100$–$1000\,R_\mathrm{NS}$. As the quadruple component decreases much faster with the distance from the surface (see, e.g., Pétri 2020), it is expected that the (possibly off-centered) dipolar field dominates the flow dynamics in this case.

The gravitationally captured matter is then channeled by the magnetic field lines, which results in the confinement of accretion flows and the X-ray emission to the two small regions at the magnetic poles of the neutron star. It is often assumed that during accretion from a disk due to the coupling of the plasma to the magnetic field lines at the transition region, the accretion funnel is hollow (Ghosh et al. 1977), while wind accretion results in the filled channel (Basko & Sunyaev 1976; Mushtukov et al. 2015b, also Burnard et al. 1991, and references therein). As a result, the imprint of the flow onto the neutron star surface can be either circular or ring shaped. Obviously, the real picture can be significantly more complex than these two simplified cases. The penetration of the plasma into the magnetosphere will depend on the size of the threading region and the inclination of the magnetic axis to the disk plane. Moreover, in the case of an off-centered dipole, azimuthal symmetry of the funnel cannot be expected (Gornostaev 2021). As a result, the accretion channel can be open on one side, leaving a crescent-like imprint on the surface. In the case of a hollow channel and relatively high mass-supply rates, magnetohydrodynamic instabilities can also develop. They cause leakage of the plasma on the outer and inner rim, widening and filling in the ring (Mukherjee et al. 2013). The radial size of the imprint can be estimated as $r_0 {\sim} R_\mathrm{NS}\sqrt{R_\mathrm{NS}/R_\mathrm{m}} {\sim}$ a few hundred meters, via the opening angle of the dipolar field lines (see, however, discussion in, e.g., Davidson 1973). This value depends on the magnetic field and the mass-accretion rate. Caution is advised as additional factors, such as the spreading of the material around the channel, can affect the size of the spot. The uncertainty of the size of the polar region can greatly complicate the determination of the plasma density inside the channel, which is crucial for understanding the deceleration regime and the emission production.

It is usually assumed that the matter falls onto the poles along the field lines at velocities close to the parabolic (free-fall) one $v_\mathrm{ff} = \sqrt{2GM_\mathrm{NS}/R_\mathrm{NS}}$, which for such a high gravitational field has a relativistic value of $\sim 0.6c$. The deceleration of the supersonic flow occurs close to the neutron star surface resulting in the production of broadband X-ray emission. The main mechanism responsible for the plasma stopping will vary depending on the mass-accretion rate. The pressure of the increased X-ray emission from the poles can become sufficiently high to launch a radiation-dominated shock wave, when the conditions are developed for a large and stable mass supply, typical for outbursts in Be X-ray Binaries. This shock significantly decelerates the plasma at some distance above the surface (Davidson 1973; Basko & Sunyaev 1976). This phenomenon is associated with the *critical luminosity* that denotes the onset of the radiation-dominated shock and formation of an accretion column as a hydrodynamic emitting structure. Below the extended shock wave, the matter settles in the denser region where it decelerates to rest mainly via Coulomb collisions. This quasi-static region is often referred to as the "accretion mound", the "thermal mound", or the "sinking zone" (Basko & Sunyaev 1976; Postnov et al. 2015; West et al. 2017a). Lower mass-accretion rates are associated with a lower photon flux from the vicinity of the neutron star. If the radiative pressure is not sufficient to break the flow, the possibility of collisionless gas-mediated shocks (Shapiro & Salpeter 1975; Langer & Rappaport 1982) or stopping via Coulomb collisions in the extended neutron star atmosphere (Zel'dovich & Shakura 1969) have to be considered.

The emission in the denser, lower part of the accretion channel is produced mainly via bremsstrahlung. It is then shaped by Compton scattering in its outer, more tenuous regions. Depending on the electron temperature, flow velocity, and the stopping mechanism, *thermal* or *bulk* Comptonization shapes the spectrum. The processes mentioned above are strongly affected by the presence of the strong magnetic field near the surface. They depend on the polarization of photons and acquire much stronger anisotropy and energy dependency compared to the non-magnetoactive environment (see Section 4.4 for more detail). As was mentioned in Chapter 2, the quantization of electrons in strong magnetic fields leads to the formation of cyclotron lines on top of the Comptonized continuum. Polarization of photons, introduced by the effects of magnetized plasma and polarized vacuum, is usually treated in terms of two polarization modes: ordinary and extraordinary. The polarization vector of ordinary photons oscillates mainly in the plane of the magnetic field vector and the direction of propagation. For so-called extraordinary photons, the polarization vector oscillates mainly perpendicularly to this plane. Such behavior naturally results in different interactions with electrons, whose motion perpendicular to the magnetic field is limited to the Landau levels. An in-depth treatment of the polarization modes (which is a non-trivial topic on its own) and the corresponding dependencies of the cross sections are left for an in-depth discussion in Chapter 4. Here, however, the important point is that the behavior of the polarization vectors results in different beam patterns of the flux for each of the two polarization modes. It is common to describe the emission profile of the extraordinary mode as a "fan beam" and the ordinary mode as a "pencil beam" (see, e.g., Basko & Sunyaev 1975; Postnov et al. 2015). These terms are often used only to indicate whether the emission originates from the top of an accretion column or a hot spot (pencil beam), or column walls (fan beam), without specifying the relation to the polarization modes (see, e.g., Klein & Arons 1989; Becker et al. 2012).

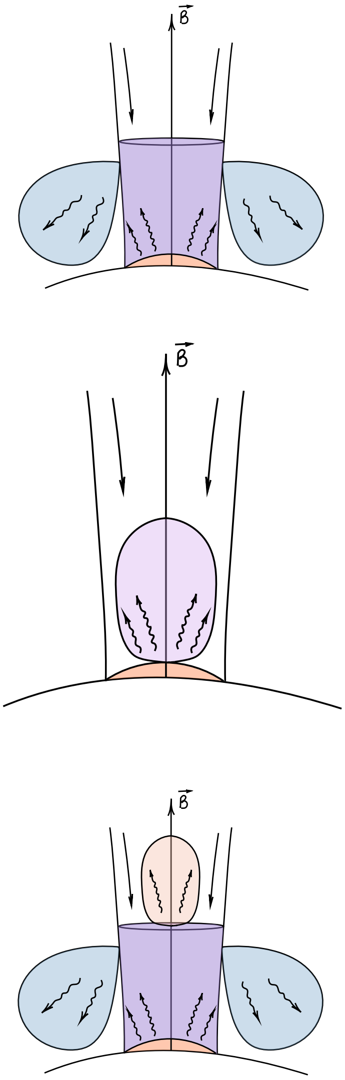

Figure 3.1: Schematic illustration of the principal beam shapes discussed in the literature: fan (top), pencil (middle), and fan+pencil (bottom).

The two principal geometries of the emission region are a column-like structure extended above the surface and a heated and thickened by accretion polar cap (a hot spot). These geometries are often associated with different types of emission profiles dominating the flux. A fan beam is typically expected from the accretion column walls, while a pencil beam is expected from the top of the column or from the polar cap (Becker et al. 2012; Cappallo et al. 2017). Figure 3.1 presents schematic depictions of the commonly discussed beam patterns. In the case of the accretion column, when the radiation shock plays a major role in plasma deceleration, the beaming should be significantly affected by the velocity of the falling particles. Interacting with hot down-falling electrons, photons are redirected more towards the surface of the neutron star (Lyubarskii & Syunyaev 1982). Consequently, in the rest-frame of the neutron star, the beam shapes can be significantly deformed (see, e.g., Falkner 2018; Kylafis et al. 2021, for examples of beaming in a moving plasma) and the top of the shock is locked by advection. Such beaming is expected to result in illumination of the neutron star atmosphere around the column by the produced radiation. The re-emission of the reprocessed radiation by the heated atmosphere is known as "reflection" and can potentially contribute to the total spectrum (Poutanen et al. 2013; Postnov et al. 2015). To understand the influence of the reflected radiation, it is crucial to know the height dependency of the column emission. If the main contribution is coming from near the base of the column, only a relatively small ring around it will be illuminated (see an example of such a ring in the model by Leahy 2005). However, in the case of a high energy density photon flux is emitted significantly above the surface and lower latitudes of the neutron star surface can be irradiated. The direct emission of the reprocessed column radiation by the neutron star atmosphere is unaffected by the dynamic effects of the accretion flow.

The confinement of the emission to the polar regions on the surface of a neutron star gives rise to the observed periodic variations of the flux if the line of sight and the dipolar axis of the neutron star are misaligned with its rotational axis. These coherent pulsations averaged over a significant part of the light curve, result in pulse profiles. Often, their complexity far exceeds the profiles of rotation-powered pulsars and accreting millisecond pulsars. These are other important signatures of the sources. Figure 3.2 shows an example of the pulse profile.

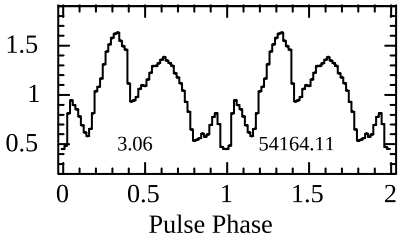

Figure 3.2: Pulse profiles of EXO 2030+375 by *RXTE*/PCA. Figure 1 (left bottom panel) of Epili et al. (2017).

Having outlined the major concept of accreting X-ray pulsars in High-Mass X-ray Binaries, in this chapter I discuss more detailed observational evidence and present some theoretical advances in their interpretation. To a high degree, I focus on spectroscopic phenomena. Section 3.1 describes the general tendencies and peculiarities observed in X-ray spectra and pulse profiles. In Section 3.2, the currently accepted picture and the ongoing discussion of physical interpretation of the observed phenomena are presented. Final remarks and an outlook are given in Section 3.3.

3.1 OBSERVATIONAL PROPERTIES

Following the focus of the present work, I will limit the discussion to such observational characteristics of accreting X-ray pulsars as continua (Section 3.1.1), cyclotron lines (Section 3.1.2), pulse profiles (Section 3.1.3), and the polarization signal (Section 3.1.4). Some peculiar timing phenomena, such as quasi-periodic oscillations and aperiodic variabilities, as well as spin-up and spin-down events, are outside the scope of this review. The same is applied to the complex phenomena of photoabsorption and fluorescence in the circumstellar material further away from the surface of the neutron star (see Ballhausen 2021, for the overview on the topic).

3.1.1 *Spectra*

In general, broadband X-ray spectra of accreting highly magnetized neutron stars are fairly well characterized by a power law with a photon index of $\sim$1 and a high-energy exponential cutoff of $\sim$10–30 keV (Falkner 2018; Walter et al. 2015). The observed Comptonized continuum are often described by phenomenological models. One of the most commonly used is the `XSPEC` model `cutoffpl`

$$\texttt{cutoffpl(E)} = KE^{-\Gamma} \exp(-E/E_{\text{fold}}), \tag{3.1}$$

where Γ is the photon index, E_{fold} is the folding energy, determining the continuum roll-over, and K is the normalization constant that gives the overall level of the flux. Another common choice is a power law with the Fermi-Dirac-like cutoff (Tanaka 1986),

$$\texttt{fdcut(E)} = KE^{-\Gamma} \frac{1}{1 + \exp(-(E - E_{\text{cut}})/E_{\text{fold}})}, \tag{3.2}$$

with the cutoff energy E_{cut}. Finally, Mihara (1995) suggested a combination of a positive and negative power law with exponential cutoff

$$\texttt{NPEX(E)} = (K_1 E^{-\Gamma_1} + K_2 E^{-\Gamma_2}) \exp(-E/kT), \tag{3.3}$$

where T is the temperature of the emitting plasma.

As the spectrum is expected to originate from a warm plasma with Compton scattering as a dominant process, sometimes physical models for thermal Comptonization, as, for example, `comptt` (Titarchuk 1994), are used. It is important to note, however, that this model was developed for the classical case of non-magnetic Comptonization. The spectra shaped by Comptonization in a highly magnetized plasma can differ substantially due to polarization and anisotropy effects, even for the ordinary mode and in the absence of the cyclotron resonance in the selected energy range (see, e.g., Comptonized spectra by Ceccobello et al. 2014). The difference is even stronger when accounting for the contribution of the extraordinary mode to the total continuum (Lyubarskii 1988). This problem is addressed in the present study as well. More recent physical models developed by Becker & Wolff (2007), Wolff et al. (2016, `B&W`), Farinelli et al. (2012), Farinelli et al. (2016, `compmag`), specifically for the accretion column emission, are based on the analytical and numerical solution of the spatially one-dimensional Kompaneets-like equation (see Chapter 4 for more details), with angle-, polarization-, and energy-averaged cross sections for Compton scattering. They include the treatment of the thermal and bulk Comptonization based on pre-defined or arbitrary velocity profiles for the plasma inside the accretion channel. These models are also available for the community, but are rarely used due to the complexity of the parameter space, the sometimes ambiguous interpretations of the parameters, and such issues as the lack of the internal energy conservation, which is left for the user to resolve (a possible strategy is described in Thalhammer et al. 2021).

The recent decades of collected observations by broadband X-ray telescopes with finer energy resolution and higher sensitivity revealed many cases of a more complex continuum structure than the traditionally assumed power law with high-energy cutoff. To describe the spectra in a statistically satisfying way, it is often required to include an additional component at intermediate X-rays. Adding a broad Gaussian line with centroid energy around 8–30 keV, also known as the “10-keV” feature, became a common approach to improve the fit. Examples of this component (not always named directly as the “10-keV” feature), used as an additional *emission* feature, include, but are not limited to, some observations of 4U 0115+63 (Ferrigno et al. 2009; Liu et al. 2020; Bissinger né Kühnel et al. 2020), Cep X-4 (Vybornov et al. 2017; Schwarm et al. 2017b), Cen X-3 (Thalhammer et al. 2021), EXO 2030+375 (Klochkov et al. 2007), and A 0535+262 (Ballhausen et al. 2017). In *absorption* a “10-keV” feature was used to describe the spectra of GX 304−1 (Rothschild et al. 2017), Vela X-1 (Fürst et al. 2014b; Diez et al. 2022), 4U 1901+03 (Reig & Milonaki 2016), 4U 1907+09 (Coburn et al. 2002). Figure 3.3 shows an example of this feature. Coburn et al. (2002) argued that some sources, such as Her X-1, 4U 1538+52, and GX 301−2, show a wiggle or a bump in the residuals at $\sim$10 keV in data from different satellites (*RXTE*, *Ginga*, *BeppoSAX*) when a power-law-like continuum with high-energy cutoff is used. However, no systematic studies for the new generation of X-ray satellites (such as *INTEGRAL* or *NuSTAR*) are available in the literature (see, however, related notes in Doroshenko et al. 2020a). It is unclear whether such wiggles should be attributed to the same effect as, for example, the strong, broad feature required in some phases of 4U 0115+63 (Ferrigno et al. 2009). Sometimes, a clear correlation of the centroid energy of the component with the flux level is even observed, both in absorption (Reig & Milonaki 2016) and emission (Berger et al., in prep.). For some sources, the “10-keV” feature can be satisfactorily used in absorption and emission with different parameters (Vybornov et al. 2017). Malacaria et al. (2015) noted that the fit of a cutoff/power-law model to some phase-resolved spectra of GX 304−1 by *INTEGRAL* could be improved by an additional high-energy ($\sim$20–30 keV) Gaussian component. Both absorption and emission components with different centroid energies were appropriate.

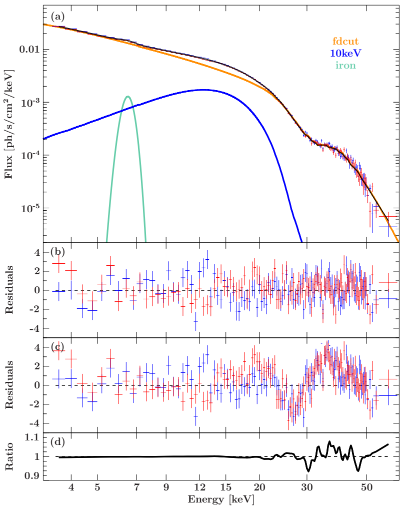

Figure 3.3: Unfolded spectrum of Cep X-4 taken by *NuSTAR* during its 2014 outburst (L_X is a few 10^{36} erg s^{-1}). The best-fit model includes the “10-keV” feature (in blue). Figure 6 of Schwarm et al. (2017b).

I took the liberty of including similar instances of this feature from the literature, even if it is not always explicitly called the “10-keV feature”.

It is evident that the “10-keV” feature in emission is often required not only for the classical power law with exponential cutoff, but for `NPEX` and `comptt` models as well (see, e.g., Liu et al. 2020). Farinelli et al. (2016) modeled phase-averaged spectra of 4U 0115+63 and Cen X-3 with `compmag` without additional features, compensating for their absence with intense cyclotron emission. It is unclear, however, whether this strong contribution has a physical justification. Moreover, the application of this model to the *NuSTAR* observation of A 0535+262 still requires a strong additional emission feature on top of the `compmag` continuum (Ballhausen et al. 2017). Similarly, the `BW` model can require contribution of the “10-keV” feature (see, e.g., Thalhammer et al. 2021; Ferrigno et al. 2009, for Cen X-3 and 4U 0115+63, respectively). As was noted by some authors (Malacaria et al. 2015; Vybornov et al. 2017; Staubert et al. 2019), the necessity of such features is likely to reflect our current poor understanding of the spectral formation in the accretion channel.

In the case of an absorption feature the criteria to distinguish between a cyclotron line around 10 keV and a continuum component are unclear. Some argue that the usage of such features can be avoided by choosing two-component continuum models. Thus, Doroshenko et al. (2020a) showed that the cyclotron line at $\sim$12.5 keV claimed in the spectrum of KS 1947+300 by Fürst et al. (2014a) can be described by a continuum model which consists of two thermally Comptonized components (`comptt`) of different temperatures. Doroshenko et al. (2020a) speculated that two components originate in the accretion column and from the irradiated region around it. A similar discussion accompanied the discovery of a dip in the spectrum of X Per. There, a cyclotron line was reported by Coburn et al. (2001) at ∼30 keV and later interpreted by Doroshenko et al. (2012) as a dip between two `comptt` components. In this case, the latter authors interpreted the contribution as the thermally Comptonized direct emission of the polar cap and the emission component Comptonized by the bulk motion of the flow above the neutron star surface. It is interesting to note that accounting for the concave curvature of the spectra was also one of the main objectives of designing the `NPEX` model (Makishima et al. 1999). There are though enough observational arguments hinting that the claims of single cyclotron lines at energies ∼10 keV should be taken with a grain of salt. At the same time, a physical justification for the usage of two components describing non-magnetic thermal Comptonization to characterize spectra of accreting highly-magnetized neutron stars remains highly ambiguous and unconvincing. Such combined models can be considered to obtain the qualitative description of the spectra. However, their physical meaning is doubtfully going beyond the phenomenological combination of the negative and positive power laws.

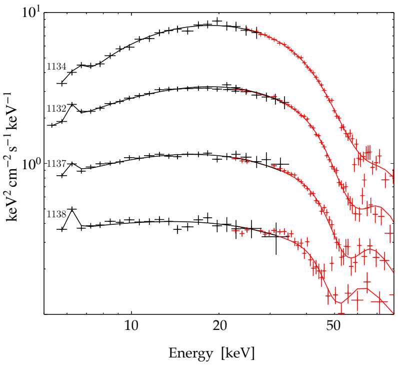

Figure 3.4: Phase-averaged spectrum of GX 304−1 at different luminosity levels. Figure 7 of Malacaria et al. (2015), reproduced with permission © ESO.

Accreting X-ray pulsars in High-Mass X-ray Binaries cover a large range of observed luminosities, from $\sim 10^{32}\,\mathrm{erg\,s^{-1}}$ up to $\sim 10^{38}\,\mathrm{erg\,s^{-1}}$. Two sources, Swift J0243.6+6124 and SMC X-3 manifest themselves as not only regular pulsars, but pulsating ULXs, reaching luminosities close to $\sim 10^{40}\,\mathrm{erg\,s^{-1}}$. The latter regime, however, lays outside the scope of the present work. The dependency of spectral parameters on luminosity is observed for many accreting X-ray pulsars. Figure 3.4 shows the hardening of the GX 304−1 spectrum with increasing luminosity. An anticorrelation of the folding energy, E_{fold}, with luminosity was also found (Malacaria et al. 2015). The source is considered to be *subcritical*, meaning that the luminosity never exceeds the critical value, corresponding to the onset of the radiation-dominated regime (see Section 3.2.1 for more details). A similar trend of gradual hardening (characterized by the smaller photon index Γ) and decreasing E_{fold} was observed for A 0535+262 during its 2020 giant outburst (Kong et al. 2021). Interestingly, this trend was present below, as well as above, the critical luminosity, $\sim 7 \times 10^{37}\,\mathrm{erg\,s^{-1}}$, which was deduced from the change in the cyclotron line behavior (see Section 3.1.2), up to the peak of the outburst. Postnov et al. (2015) showed that for a number of sources, the hardness of the spectra flattens with luminosity. Some of them (e.g., 4U 0115+63, V 0332+63) even show the turnover which can be associated with the critical luminosity and the launch of a radiation-dominated shock above the surface of the neutron star. Postnov et al. (2015) suggested that the flattening of the hardness ratio was related to the increasing role of the surface irradiation at higher luminosities.

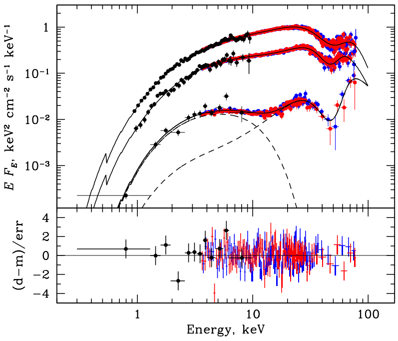

Figure 3.5: Spectra of A 0535+262 at different luminosity states. The lowest spectrum is taken in quiescence, with $L_{\mathrm{X}} \sim 7 \times 10^{34}\,\mathrm{erg\,s^{-1}}$. Figure 1 of Tsygankov et al. (2019b).

The other extreme of High-Mass X-ray Binary activity, is the quiescent behavior of Be X-ray Binaries. Evidence of the presence of the present accretion in quiescence, such as coherent pulsations, time-variability, and deviation of the soft continuum from the thermal spectrum, has been seen for a few decades (see Tsygankov et al. 2017, and references therein). These clues, to some degree, contradict the common expectation of the onset of the propeller effect due to a low mass-accretion rate (Section 2.2.1). It was early proposed, however, that Be X-ray Binaries with slowly rotating neutron stars likely do not enter the propeller regime and experience the accreting quiescent state instead (Stella et al. 1986). Recently, broadband spectra were obtained with *NuSTAR* for a few sources in quiescence. Among them are A 0535+262 (Tsygankov et al. 2019b), GX 304−1 (Tsygankov et al. 2019c), and GRO J1008−57 (Lutovinov et al. 2021). The spectra show not only hard high-energy emission but also a dramatic transition to a two-hump structure (see Figure 3.5). The components peak at ∼5 keV and ∼30 keV, with a deep dip appearing between them. Similarities of the flux level and spectral shape between these sources and X Per that the accretion regime may be similar. Two-component spectra of GX 304−1, A 0535+262, and X Per are shown in Figure 3.6. In many cases, spectra were modeled by a combination of two `comptt` models. Polar cap emission with (Mushtukov et al. 2021) and without (Sokolova-Lapa et al. 2021) significant contribution of the cyclotron emission and the emission of extended collisionless shock (Becker & Wolff 2022) were suggested as possible physical interpretations.

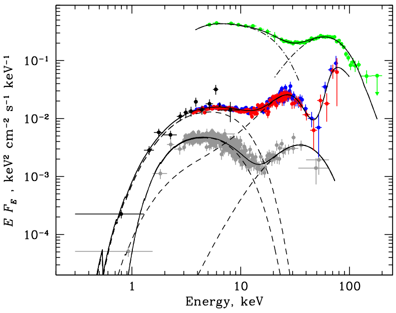

Figure 3.6: Spectra of X Per, A 0535+262, and GX 304−1 (from top to bottom). Figure 2 of Tsygankov et al. (2019b).

3.1.2 *Cyclotron Lines*

Cyclotron lines, or Cyclotron Resonance Scattering Features, were already discussed in the previous chapter (see Section 2.4). They are typically observed as broad absorption lines on top of the Comptonized X-ray continuum. They are provide the most direct measurement of the neutron star magnetic field in the line-forming region, which is expected to locate close to the surface at the magnetic pole. The magnetic field can be estimated from the line centroid energy using the "12-B-12 rule" (see Equation 2.22). All phenomenological and physical spectral models discussed in Section 3.1.1 require the ad-hoc inclusion of an additional feature to account for the cyclotron line. Two main multiplicative models are typically used to describe the cyclotron lines: a Gaussian given by the `gabs` model and a pseudo-Lorentzian profile given by `cyclabs` (Makishima et al. 1990, and references therein). Both models are characterized by the centroid energy E_{CRSF}, the width of the line σ_{CRSF}, and its depth d_{CRSF} (or the optical depth τ_{CRSF} used instead in `cyclabs`). Unlike `gabs`, the minimum of the `cyclabs` profile is located not at E_{CRSF} but slightly higher. This results in ∼2-20% lower cyclotron line energies (Falkner 2018). A few physically-motivated convolutional models based on Monte Carlo simulations were made available by the Remeis group for `XSPEC`-like analysis packages as well: `cyclomc` by Schönherr et al. (2007b) and `cyclofs` by Schwarm et al. (2017b).

About 50 accretion-powered X-ray pulsars in High-Mass X-ray Binaries are known in our Galaxy to date (see Figure 2.26 and references therein). Together with ∼40 pulsars in Be X-ray Binaries in the LMC and SMC, we are looking at a sample of about a 100 sources. From the Galactic sources, more than 30 show confirmed cyclotron lines in their X-ray spectra, with additional 12 candidates (see Staubert et al. 2019; Mushtukov & Tsygankov 2022). This together amounts to ∼80% of the X-ray pulsars in the Milky Way exhibiting confirmed or candidate cyclotron lines. This could suggest that the presence of cyclotron lines is more likely the rule than the exception. In this way, one can note that the presence of the cyclotron line is rather common. For the Magellanic Clouds, only three of such sources are confirmed: SMC X-2 and SXP 15.3 in SMC, and RX 0520.5−6932 in LMC, with one additional candidate, LMC X-2. This fact is likely related to the much lower signal-to-noise ratio due to the large distance (compared to the galactic X-ray binaries) to the Magellanic Clouds, which impedes the study of subtle spectral features located at intermediate and high energies.

The reported lowest cyclotron line energy is at ∼ 5 keV for SXP 15.3 (Maitra et al. 2018) and Swift J1626.6−5156 (Molkov et al. 2021). However,

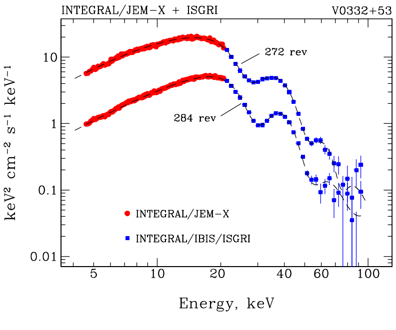

Figure 3.7: Spectra of V 0332+53 at two luminosity states, with pronounced cyclotron harmonics. Figure 3 of Tsygankov et al. (2006).

features that were confirmed by other observations are slightly higher, ~9–12 keV, found in the spectra of 4U 0115+63 (Nagase et al. 1991; Ferrigno et al. 2009) and Swift J1626.6−5156 (DeCesar et al. 2013; Molkov et al. 2021). These two sources also have the highest number of reported cyclotron harmonics: five for 4U 0115+63 (Heindl et al. 2000) and four for Swift J1626.6−5156 (Molkov et al. 2021). For the majority of sources, the fundamental line is located above ~ 20 keV, and higher harmonics can be difficult to observe. Examples of non-harmonically spaced lines are also exist. Although relativistic effects introduce some non-harmonicity to the line spacing (Araya & Harding 1999), not all observed centroid line energy ratios can be easily explained in this way. Fürst et al. (2018) reported two cyclotron lines in the spectrum of GX 301−2 at ~35 keV and ~50 keV. An additional line at ~15 keV, possibly a second fundamental, was found between the ~11 keV and ~20 keV cyclotron lines of 4U 0115+63 (Iyer et al. 2015; Liu et al. 2020). The suggested explanations are two separated emission regions at different heights in the accretion column (Fürst et al. 2018) and the possible contribution of the magnetic poles with the difference field strength to the total spectrum (Liu et al. 2020).

As noted by Staubert et al. (2019), there are multiple underlying effects that could cause deviation of the cyclotron harmonics from multiples of the fundamental. The general recommendation is to leave the centroid energy of the lines uncoupled while fitting the data.

In many cases, a dependency of cyclotron line parameters on X-ray luminosity was observed. The anticorrelation of the line energy with luminosity was reported for a few sources at their brightest states ($L_X \gtrsim 10^{38}\,\mathrm{erg\,s^{-1}}$): V 0332+53 (Tsygankov et al. 2006), SMC X-2 (Jaisawal & Naik 2016), and A 0535+262 (Kong et al. 2021). Similar behavior was discussed, but not consistently confirmed for, 4U 0115+63 (see Doroshenko 2017, for more details). In less bright states, A 0535+262 and V 0332+53 exhibit a positive correlation with luminosity (Klochkov et al. 2011; Doroshenko et al. 2017). This behavior is common for subcritical sources, including GX 304−1 (Rothschild et al. 2017), Cep X-4 (Vybornov et al. 2017), and Vela X-1 (Fürst et al. 2014b). A negative correlation, similar to the flattening of the continuum hardness, is typically associated with the launch of the accretion column under the radiation-dominated shock. Sources with the positive correlation are assumed to remain below the critical luminosity value, when the radiation pressure is not effectively braking the accretion flow. A more detailed discussion on the related physical scenarios for both types of behavior is given in Section 3.2. The reader is also referred to the excellent review by Staubert et al. (2019) for

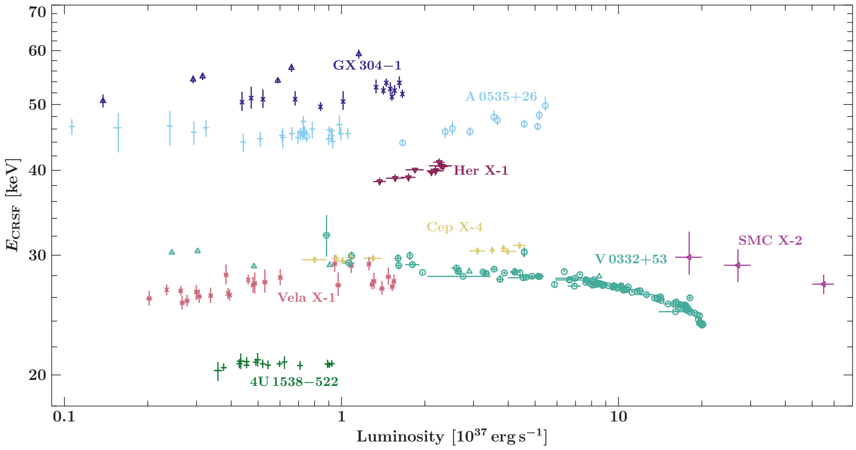

Figure 3.8: Examples of observed dependency of the cyclotron line energy from X-ray luminosity. Figure 9 of Staubert et al. (2019), reproduced with permission © ESO.

more details on cyclotron lines, including their rotational phase variation and long-term decay.

3.1.3 *Pulse Profiles*

As previously mentioned, confinement of the emission regions to a small fraction of the surface area, imposed by the strong magnetic field, results in coherent pulsations during the rotation of a neutron star. So far, mainly phase-averaged characteristics of the cyclotron lines and the continuum in the spectra of accreting X-ray pulsars in High-Mass X-ray Binaries were discussed in this thesis. Both, continuum and cyclotron lines, typically show variation over the rotational period. In the general case, the direction to the observer is misaligned with the dipolar axis, which denotes the location of the poles (moreover, in the case of a distorted dipole or a multipolar field, this alignment is not physically possible). It means that at different rotational phases, the observer sees the pole from different angles. In some rotational phases, one of the poles can be completely invisible, being obscured by the neutron star. Here, relativistic effects due to the strong gravitational field of the neutron star become important. They can significantly alter the observed picture compared to the flat space-time case, especially for high accretion columns.In addition, due to the strong magnetic field, the radiation emergent from the poles is highly anisotropic, both in the continuum and in the cyclotron lines. Together, the change in the observed emitting area with light-bending effects and anisotropic emission results in a variation of the observed spectra. Integrated within a selected energy range and averaged over the observation time, it gives an important characteristic of a pulsar, the *pulse profile*.

Often, due to their complexity, pulse profiles are a unique signature of the source. However, depending on the source, the profile can vary significantly with luminosity and the energy band. For some sources, such as, for example, XTE J1859+083, the general shape of the pulse profile is stable over different energy bands. However, even then structural changes, such as the strength of individual major peaks and additional components, can evolve (Stierhof et al., in prep.).Conversely, some sources, such as A 0535+262 and GX 304−1, show a significant variation of the pulse profile shape with energy (Kong et al. 2021; Jaisawal et al. 2016). Figure 3.9 illustrates the change in the pulse profile of A 0535+262 with energy. This difference in pulse profile behavior could potentially be related to the energy of the fundamental cyclotron line, that is, the local magnetic field value. Thus, for XTE J1859+083 no indication of cyclotron lines in the spectrum has been observed within the *NuSTAR* energy range (see, e.g., Salganik et al. 2022).

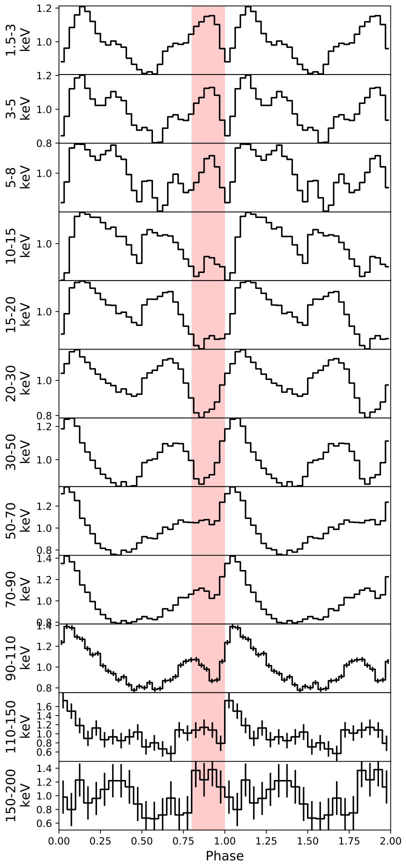

Figure 3.9: Pulse profile of A 0535+262 in different energy bands, from the Insight HXMT data obtained during the 2020 giant outburst. Figure 1 (left panel) from Kong et al. (2022a). CC BY-4.0 – AAS.

The change of the pulse profiles with energy is sometimes presented via a *phase-energy map*. These maps can be a powerful tool that potentially (depending on the chosen normalization) display a variation of the spectrum with phase and the pulse profile with energy. Their usage in the High-Mass X-ray Binary community is, unfortunately, uncommon. Phase-energy maps often display lags of the pulse profile components. Sometimes, such lags steadily propagate throughout a wide energy range, as in the case of GS 0834−430 (see Miyasaka et al. 2013, for more details). In some cases, noticeable lags and structural changes were associated with cyclotron lines. Ferrigno et al. (2011) reported phase lags at the fundamental line and higher harmonics for 4U 0115+63. Sometimes, near the fundamental cyclotron line, a principle change in the pulse profile structure was observed. The pulse profile of V 0332+53 showed a splitting from one- to two-component structure above the cyclotron line energy (Tsygankov et al. 2006). An inverse behavior was observed in the pulse profile of XTE J1946+274 by Gorban et al. (2021). There, the two-peaked pulse profile at low energies merge to a single-peaked structure near the cyclotron line energy ~38 keV. It remains single-peaked up to the highest energies accessed with the observation (see Figure 3.10). In general, this behavior is attributed to energy-dependent beaming from the emitting region (Tsygankov et al. 2006). The angular dependency of emission near the cyclotron line can significantly differ from the continuum one. However, none of the currently available spectral models for intermediate and high mass-accretion rates include a full treatment of angular and energy redistribution in the continuum and cyclotron line. This question is one of the direct objectives of the present work and will be discussed in more detail in Chapter 5 and Chapter 6. Energy dependency of emission profiles in combination with geometrical effects due to the poles and the observer's location, as well as light bending, can result in this complex changing behavior of a pulse profile with energy.

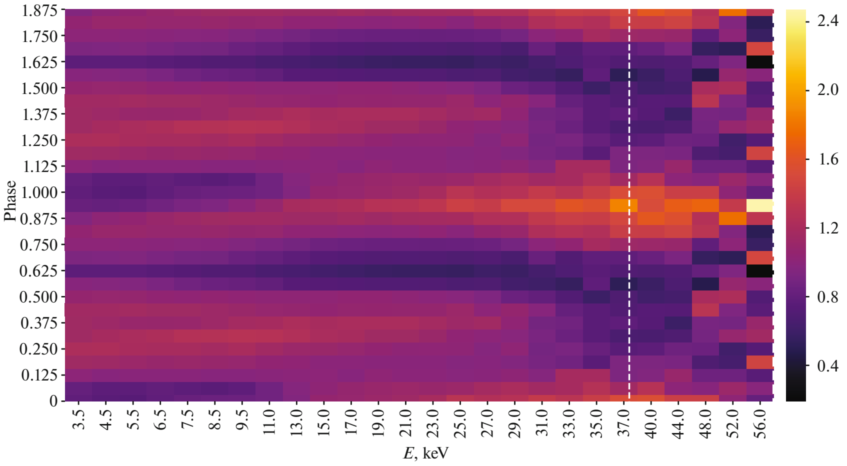

Figure 3.10: Phase-energy map for the XTE J1946+274 observation with *NuSTAR*. Figure 3 of Gorban et al. (2021). Reproduced with permission from Springer Nature.

Interestingly, the changes of pulse profiles near the cyclotron scattering features are not only source-specific. They also depend on the source luminosity and can evidently serve as indicators of transitions between different accretion regimes (Sasaki et al. 2012). Tsygankov et al. (2006) noted that during the brightest state of V 0332+53, corresponding to $L \sim 5 \times 10^{38}\,\mathrm{erg\,s^{-1}}$, no phase lags between the main peaks of the profile at different energies evolve. Only the relative intensities of the peaks change with increasing energies. The more complex behavior discussed above occurs only after the luminosity drops below $L \sim 7 \times 10^{37}\,\mathrm{erg\,s^{-1}}$. Curious luminosity-dependent pulse-profile behavior was also observed by Wang et al. (2022) for A 0535+262 during its 2020 giant outburst. The complex (up to five peaks) structure known for this source at lower luminosity (up to $\sim 10^{37}\,\mathrm{erg\,s^{-1}}$) below 10 keV becomes smoother above the luminosity associated with the critical value (based on the cyclotron line behavior, see Kong et al. 2021, and a short summary in Section 3.1.2). Figure 3.11 shows the phase-energy maps, corresponding to the highest observed luminosity ($\sim 10^{38}\,\mathrm{erg\,s^{-1}}$, left panel), critical luminosity ($\sim 4 \times$

10^{37} erg s^{-1}, middle panel), and lower luminosity of $\sim 10^{37}$ erg s^{-1} (right panel).

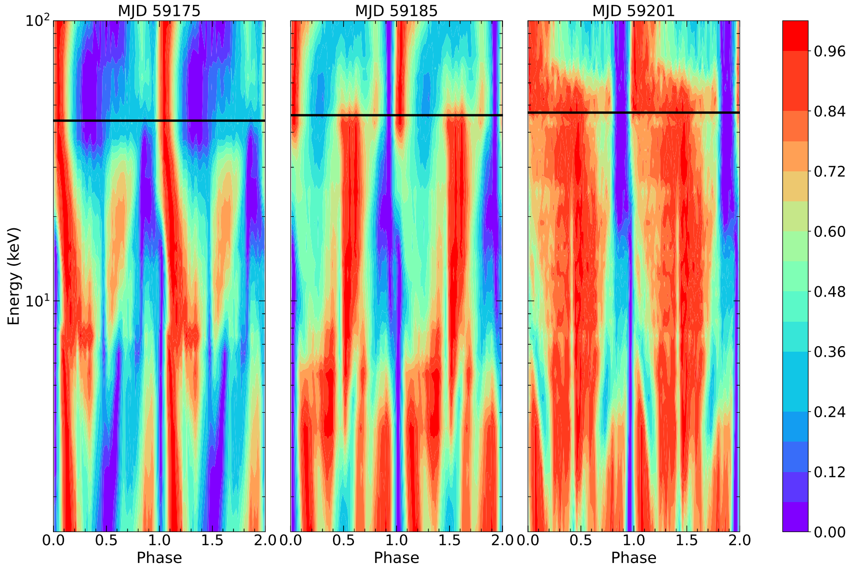

Figure 3.11: Phase-energy maps for three different luminosity states of A 0535+262, from the data taken during the decline of the 2020 giant outburst. The maps are shown from left to right: for the peak of the outburst ($\sim 10^{38}$ erg s^{-1}), the state associated with the critical luminosity ($\sim 4 \times 10^{37}$ erg s^{-1}), and the lower state ($\sim 10^{37}$ erg s^{-1}). Figure 4 of Wang et al. (2022). CC BY-4.0 – AAS.

Noticeably, at soft energies the structure of the pulse profile is simplified down to a two-peaked structure. At the intermediate energies below the cyclotron resonance ($\sim$10–40 keV), a wide plateau-like structure evolves to a more pronounced, narrower, dominant peak with less intense components on the side with the higher luminosity. The dominant peak changes above the critical luminosity. Near the cyclotron line energy ($\sim$ 45 keV, indicated by the black line in Figure 3.11), a wide single-peaked structure transforms to a clearly double-peaked structure at the critical luminosity. An indication of some kind of transition in the pulse profile was also observed, for example, during the giant outburst of 4U 0115+63 in 1999. There, the second pronounced hump appeared in the pulse profiles for energies above 5 keV at luminosity above $\sim 10^{37}$ erg s^{-1} (Sasaki et al. 2012).

When the luminosity is significantly reduced and the source enters the quiescent state, the shape of the pulse profile tends to simplify. Apart from the lower count rate that affects our ability to determine a fine structure of low-luminosity pulse profiles, their general complexity seems to be noticeably reduced. Tsygankov et al. (2019b) reported a single-peaked profile without significant lags between soft and hard energies for the quiescent state of A 0535+262 ($L \sim 7 \times 10^{34}$ erg s^{-1}). The transition to this state was characterized by a dramatic change of the spectral shape from the power law to the two-hump structure discussed in Section 3.1.1. It was also accompanied by a significant reduction of the pulsed fraction from $\sim$50% to $\sim$20% (Tsygankov et al. 2019b). A similar decrease of the pulsed fraction was observed for GRO J1008−57 during its transition to a quiescent state (Lutovinov et al. 2021). At the same time, the total shape of the pulse profile remained similar to the higher states. For IGR J19294+1816, the low-luminosity pulse profile shows energy dependency, developing an additional component above $\sim$ 15 keV

In the context of the systems discussed in the present and following chapters, the quiescent state is assumed to exist for Be X-ray Binaries. Wind-fed systems are typically persistent sources.

(Tsygankov et al. 2019a). In general, the presence of pulsations at such low luminosity levels indicates the dominance of emission from the neutron star poles. For slowly rotating sources, such as A0535+262 ($P \sim 100\,\mathrm{s}$), GRO J1008−57 ($P \sim 90\,\mathrm{s}$), and GX 304−1 ($P \sim 270\,\mathrm{s}$), the presence of pulsations at luminosities as low as $\sim 10^{34}\,\mathrm{erg\,s^{-1}}$ *together with hard high-energy emission* and aperiodic variability (see, e.g., Doroshenko et al. 2014, for A 0535+262), solidly hints at the presence of accretion in quiescence. For fast-spinning sources, such as 4U 0115+63 with $P \sim 3.6\,\mathrm{s}$, pulsations recently reported by Rouco Escorial et al. (2020) at the very low luminosity $L \sim 10^{33}\,\mathrm{erg\,s^{-1}}$, hints at our poor understanding of the propeller regime, which is expected and was previously claimed for this source (Tsygankov et al. 2016). One would expect that a transition to the propeller regime is accompanied by a cessation of pulsation. However, it is possible that in this case one detects emission from the cooling poles, if their luminosity is still higher than the luminosity of the matter at the Alfvén surface.

Together with changes in continua shape and cyclotron lines, pulse profiles can be a useful tool to identify changes in emission geometry. Especially valuable are observations for one source over a wide luminosity range. This allows one to probe the energy- and luminosity-dependent beaming, avoiding the interference of geometrical effects such as the location of the poles and the observer's inclination.

3.1.4 *Polarization*

The final property that we address is polarization. X-ray polarimetry is a powerful tool that can potentially allow us to access information about the geometry of the emission region, the type of beaming, and the influence of vacuum polarization on spectral formation. Unfortunately, few observations of accreting X-ray pulsars in High-Mass X-ray Binaries with X-ray polarimeters exist to date. The first X-ray polarimetry data was taken in the 1970s with the Orbiting Solar Observatory (OSO-8). They obtained three-sigma upper levels for the X-ray polarization at 2.6 keV of Cen X-3 and Her X-1 of 13.5% and 60%, respectively (Silver et al. 1979). For a few decades after that, the polarimetry of X-ray sources faced a quiet period. The reader is referred to the historical sections of reviews by Weisskopf et al. (2006) and Weisskopf (2018) for a discussion of the underlying causes leading to the absence of X-ray polarization measurements by the early 2000s. The spectrometer SPI on board *INTEGRAL* (launched in 2002) allows for the reconstruction of polarization using coincidence events (see Kalemci et al. 2007; Laurent et al. 2011, and references therein). However, the energy range is too high to study accreting X-ray pulsars. The later balloon-borne polarization mission *X-Calibur* constrained the polarization signal from GX 301−2 in 15–35 keV energy band (Abarr et al. 2020). Since longer exposure times are difficult to achieve with balloon-borne experiments due to their short flight time of hours to a few days, it was not possible to distinguish between fan- and pencil-like emission in the observed energy band (Abarr et al. 2020). The follow-up mission *XL-Calibur* offers significantly increased sensitivity and lower background rates (Abarr et al. 2021). The first flight of *XL-Calibur* was conducted in July 2022 and the second launch is planned for 2023. The latest result on polarization signal from accreting highly magnetized neutron stars came from the Imaging X-ray Polarimetry Explorer (*IXPE*), which is sensitive to linear polarization at soft X-rays (2–8 keV). Its observations of Her X-1 revealed an unexpected degree of linear polarization of only ~10% (Doroshenko et al. 2022). This value differs drastically from the predictions of theoretical models (see, e.g., Caiazzo & Heyl 2021a,b). For Cen X-3, observations were performed in the high- and low-luminosity states. While in the low-luminosity state no significant polarization was observed, the polarization degree of ∼5.8% was found (Tsygankov et al. 2022). The very low polarization degree observed for these sources at soft X-rays will be partly addressed in Chapter 5.

3.2 STATE OF THE THEORY AND MODELING

The modeling of accretion and emission processes in the vicinity of highly magnetized neutron star is somewhat less developed than the rich observational background. The full picture, especially for the intermediate luminosity states and transitions between different regimes, remains piecewise and rather uncertain. It is clear, however, that observed luminosity dependencies and their switch should be associated with the change of the mass-accretion rate and physical processes dominating matter deceleration in the accretion channel. In this section, I present the most advanced theoretical and modeling efforts in the field. Section 3.2.1 presents the reader with a concept of the critical luminosity, which was mentioned in Section 3.1. Section 3.2.2 and Section 3.2.3 describe modeling efforts for supercritical and subcritical accretion regimes, respectively.

3.2.1 *Critical Luminosity*

One of the most accepted concepts in the field is the existence of the *critical luminosity* $L_{\rm crit}$ (also often denoted as L^*), which corresponds to the onset of the dynamic influence of photons emitted near the surface of the neutron star on the accretion flow. This effect is associated with the beginning of the rise of the radiation-dominated shock in the accretion channel. The concept of critical luminosity for accretion onto a magnetized neutron star was proposed by Basko & Sunyaev (1976). The meaning of $L_{\rm crit}$ introduced by these authors has direct similarity with the Eddington luminosity for the hydrogen plasma (see Section 2.3), but somehow differs from the classical Eddington definition. It corresponds to the luminosity at which *the distance where the light stops the flow is equal to the wall thickness d_0 (or a_0 for the filled cylinder)* and the optical depth for scattering becomes ∼1 across the channel (Basko & Sunyaev 1976).

The introduced expression in some sense represents the Eddington luminosity modified by the geometry of the accretion channel and corrected to the magnetic scattering cross section[1],

$$\begin{aligned} L_{\rm crit}^{\rm BS} &= 2\pi \frac{a_0}{R_{\rm NS}} \frac{G M_{\rm NS} c m_{\rm p}}{\sigma_{\rm s}} \\ &\approx 6.3\times10^{36} \left(\frac{\sigma_{\rm Th}}{\sigma_{\rm s}}\right) \left(\frac{a_0}{10^5\,{\rm cm}}\right) \left(\frac{10^6\,{\rm cm}}{R_{\rm NS}}\right) \left(\frac{M_{\rm NS}}{M_\odot}\right) {\rm erg\,s^{-1}}, \end{aligned} \quad (3.4)$$

where a_0 is the inner radius of the axisymmetric accretion channel as imprinted on the surface of the neutron star, and $\sigma_{\rm s}$ is the characteristic scattering cross section. For a filled channel, a_0 is the cylinder radius, and the factor of 2 in Equation 3.4 should be replace by $\sqrt{2}$ (see Equation 40

---

[1] I would like to note that Equation 1 of Basko & Sunyaev (1976) erroneously contains an additional factor with the neutron star radius in the denominator. In addition, the factor in their Equation 38 used here should be 6.3, not 6.2. This small divergence is probably related to the approximate values for some constants used by Basko & Sunyaev (1976) for the estimate.

of Basko & Sunyaev 1976). Basko & Sunyaev considered scattering cross sections which resemble the behavior of the extraordinary mode in the continuum, significantly below the fundamental cyclotron resonance energy, where $\sigma_\mathrm{s} \propto (E/E_\mathrm{cyc})^2$. According to Equation 3.4, any effect reducing the cross section increases the critical luminosity.

When the total luminosity exceeds L_crit, the accretion column grows above the surface of the neutron star. The accretion flow loses a significant part of its kinetic energy by passing through the extended radiative shock. Within the shock region, the bulk motion of particles drags the photons down toward the neutron star surface. In this way, radiation in the shock is locked by advection, with only a small fraction radiated away from the region. After the shock, the kinetic energy of the flow is significantly reduced ($v \sim v_\mathrm{ff}/7$), and the so-called *sinking zone* is formed with a low plasma velocity and high energy density (Basko & Sunyaev 1976). In this way, the sinking zone becomes the primary emitting region, radiating the flux away through the channel walls. Usually, the part of the accretion channel with the extended regions of the radiative shock and the sinking zone is referred to as the accretion column.

The limiting accretion luminosity is also sometimes denoted as L^{**} or L^max, while L_lim is also used for the lowest possible luminosity of an accretor, before accretion is ceased by the propeller effect (see, e.g., Mushtukov & Tsygankov 2022)

In this way, the critical luminosity does not reflect the limit of the mass-accretion rate, but the transition of the flow to the accretion column regime. To determine the principal restriction for the mass accretion onto a highly magnetized neutron star, Basko & Sunyaev introduced the *limiting luminosity* L_lim. Being translated to the mass-accretion rate (see Equation 2.15), it serves as an analog of the Eddington luminosity in the sense of $\dot{M}$ limitation. Here, the difference from the spherically-symmetric, non-magnetic accretion becomes crucial. Accretion column walls at $L > L_\mathrm{crit}$ radiate away part of the flux, preventing its participation in the braking of the infalling plasma (Burnard et al. 1991). Because of this effect and the modification of the photon–electron interactions in the strong magnetic field ($\sigma_\mathrm{s} \neq \sigma_\mathrm{Th}$), the luminosity of accretion columns can significantly exceed the classical Eddington limit. This regime is referred to as *super-Eddington* accretion. The rise of the shock and the saturation of the luminosity growth are expected to stop when the shock reaches the Alfvén surface or when the ram pressure excess the magnetic pressure near the surface of the neutron star.

Alternative ways of estimating the critical and limiting luminosities for accreting X-ray pulsars have also been suggested by various authors. Burnard et al. (1991) noted that L_crit should also depend on the opening angle of the field lines θ_c and related the effective cross sections to the Rosseland averaged along the field lines $\langle\sigma_\parallel\rangle$,

$$\begin{aligned} L^\mathrm{B91}_\mathrm{crit} &= \frac{\theta_\mathrm{c}^2}{4}\frac{\sigma_\mathrm{Th}}{\langle\sigma_\parallel\rangle}L_\mathrm{Edd} \\ &\approx 10^{35.5}\left(\frac{\theta_\mathrm{c}}{0.1\,\mathrm{rad}}\right)^2\left(\frac{\sigma_\mathrm{Th}}{\langle\sigma_\parallel\rangle}\right)\left(\frac{M_\mathrm{NS}}{M_\odot}\right)\mathrm{erg\,s^{-1}}, \end{aligned} \tag{3.5}$$

for a filled accretion channel. Based on simplified considerations about the kinematics of gas deceleration, Becker et al. (2012) suggested an expression for the critical luminosity for a cylinder-like accretion channel,

$$L^\mathrm{B12}_\mathrm{crit} = \frac{\pi r_0^2}{4\pi R_\mathrm{NS}^2}\frac{\sigma_\mathrm{Th}}{\sigma_\parallel}L_\mathrm{Edd}\left(\frac{R_\mathrm{NS}}{49H}+1\right), \tag{3.6}$$

where H is the height of the radiation-dominated shock above the stellar surface and r_0 is the polar cap radius. Their estimate for the shock height, $R_{\rm NS}/(49H) \ll 1$, results in

$$L_{\rm crit}^{\rm B12} = \frac{\pi r_0^2}{4\pi R_{\rm NS}^2} \frac{\sigma_{\rm Th}}{\sigma_{\|}} L_{\rm Edd}. \tag{3.7}$$

This is similar to Burnard et al. (1991), if one assumes that the opening angle can be expressed as $r_0/R_{\rm NS}$ and $\sigma_{\|}$ represents the Rosseland mean (which is not specifically stated by Becker et al. 2012, and actually contradicts their further derivations discussed below). After considering the rotation of the inclined dipole and the dependency of r_0 on the Alfvén radius, $R_{\rm A}$, Becker et al. introduced a parameter Λ, which reflects the Alfvén radius variation. It is suggested to be set to 1 for spherical accretion and expected to be < 1 for disk accretion. In addition, the same dominance of cross sections parallel to the magnetic field line by the extraordinary mode, as suggested by Basko & Sunyaev (1976), and some mean photon energy for photons propagating in this direction were assumed. It resulted in the parameter w, which reflects the characteristic spectral shape and is expected to be ~1–3. The final expression for the critical luminosity is then

$$L_{\rm crit}^{\rm B12*} = 1.28 \times 10^{37} \left(\frac{\Lambda}{0.1}\right)^{-7/5} w^{-28/15} \left(\frac{M_{\rm NS}}{1.4\,M_{\odot}}\right)^{29/30} \times \left(\frac{R}{10\,\rm km}\right)^{1/10} \left(\frac{E_{\rm cyc}}{10\,\rm keV}\right)^{16/15} \rm erg\,s^{-1}, \tag{3.8}$$

where $E_{\rm cyc} = 11.58\,{\rm keV}(B/10^{12}\,{\rm G})$. Equation 3.8 is more commonly used in the literature. The light blue line in Figure 3.12 shows the dependence of the critical luminosity on the magnetic field.

The latest attempt to improve on the physical picture of $L_{\rm crit}$ determination was made by Mushtukov et al. (2015b). They took proper cross sections for a magnetized plasma, including cyclotron resonances affected by thermal broadening into account. The latter can significantly modify the total picture. In addition, radiative acceleration was found within the cone of the opening angle of the field lines by calculating the Rosseland mean value with the energy- and angle-dependent opacity and intensity, given by black-body radiation. The effective mean cross section, $\sigma_{\rm eff}$, was used to allow for the mixture of the two polarization modes. The effective temperature of the black body, $T_{\rm eff}$, entering the expression for $\sigma_{\rm eff}$, is dependent on the polar cap radius and the mass-accretion rate (directly related to the accretion luminosity). In this way, the problem was solved by iterating through the mass-accretion rate values for the given magnetic field. A correction parameter ξ for $T_{\rm eff}$ was introduced to account for the photon energy shift in the electron rest frame and the deviation of the input spectrum from the black body. The resulting critical luminosity appeared to be a non-monotonic function of the magnetic field. It anticorrelates with the magnetic field for small field values, reaching a minimum at $E_{\rm cyc} \sim 10\,\rm keV$. It steadily increases with the field for larger field values (see Figure 3.13).

Mushtukov et al. (2015b) note that the derivation of the critical luminosity in Becker et al. (2012) is erroneously related to the Eddington limit. Contrary to this statement, however, the derivation in Becker et al. (2012), although starting from the direct modification of the Eddington luminosity (similar to the initial discussion in Basko & Sunyaev 1976), contains some kinematic considerations of the flow braking (see their Equation 4–9). In my opinion, the association of both, the critical and limiting luminosity to the Eddington limit can be valid. For the critical luminosity, it is justified by its definition via the principle balance of the radiative and gravitational forces. For the limiting luminosity, as stated above, the similarity comes from the limiting mass-accretion rate $\dot{M}$ onto a central object.

With present observational data, however, it is seems that the model noticeably underestimates the critical luminosity for higher magnetic field values ($E_{\rm cyc} \gtrsim 40\,\rm keV$). Thus, the highest observed luminosity for Her X-1, which is known as a persistent sub-critical source with a positive correlation of the cyclotron line with luminosity, is found ~3 times above the predicted limit within the expected parameter variation. Choosing

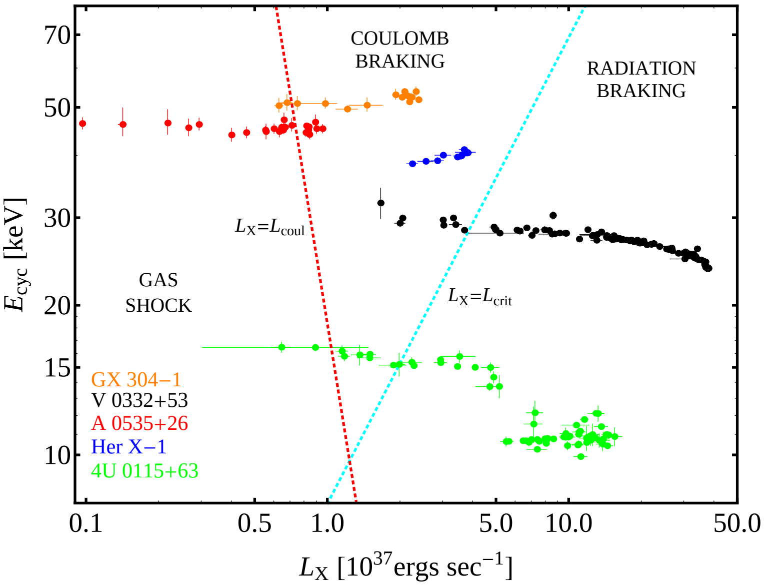

Figure 3.12: Dependency of the cyclotron line on luminosity for a few known sources. The light blue dashed line corresponds to the critical luminosity given by Becker et al. (2012). The red dashed line denotes the so-called Coulomb luminosity. This concept and low-luminosity regimes, including gas-mediated shock and Coulomb braking, are discussed in Section 3.2.3. It is important to note that Müller et al. (2013) showed that the presented negative correlation for 4U 0115+634 is an artifact of the assumptions adopted by the continuum model. Figure 2 (right panel) of Becker et al. (2012), reproduced with permission © ESO.

a low value $\Lambda = 0.1$ would improve the situation, but Mushtukov et al. note that this would be inconsistent with the known theory of disc accretion. A similar discrepancy is now known for A 0535+262, for which the transition to the supercritical regime has been recently observed at $L_X \approx 7 \times 10^{37}$ erg s^{-1} (Kong et al. 2021). In Becker et al. (2012), the predicted critical luminosity matches observations of high-field sources better, because of the assumption $\Lambda = 0.1$.

3.2.2 *Supercritical Accretion*

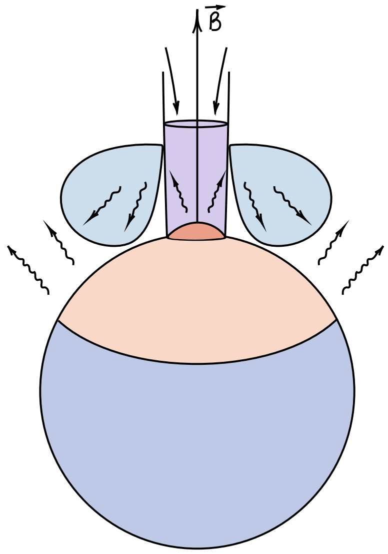

Figure 3.14: Schematic depiction of reflection.

The assumption of the existence of an accretion column above some critical level of mass supply (translated to the critical accretion luminosity L_{crit}) is the foundation for the theory of supercritical accretion onto a highly magnetized neutron star. The transition from the subcritical to the supercritical regime is associated with observational phenomena such as changes in the pulse profile structure, a saturation of the hardness ratio and a decrease of the cyclotron line energy with further increasing luminosity (see Section 3.1 for details). The spectral dependencies were addressed by a number of works. Interestingly, a consensus about the exact formation of the continuum and, in particular, of the cyclotron line is not yet reached in the community.

The height of the radiation-dominated shock, and so the accretion column, is expected to increase with increasing mass-accretion rate (see, e.g., Basko & Sunyaev 1976; Becker et al. 2012). According to Becker et al. (2012), the shock position increases linearly with luminosity, $H \propto L_X$ (similar to Basko & Sunyaev 1976), as well the characteristic height of the line-forming region, h_s, independently of the source magnetic

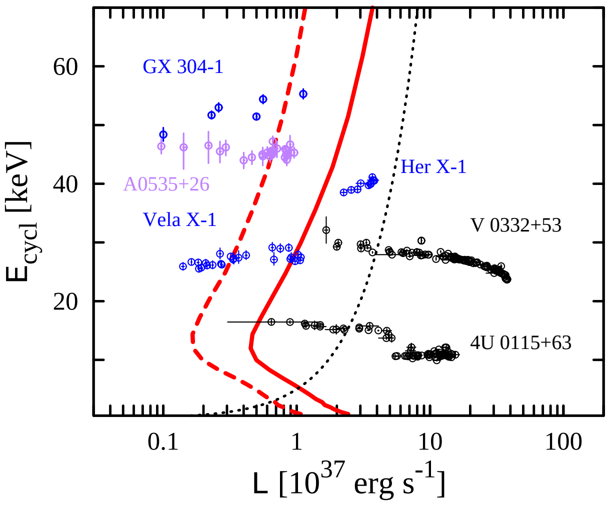

Figure 3.13: Cyclotron line energy dependency on luminosity for a few selected sources. The red dashed and solid lines show the prediction of the critical luminosity for disk accretion by Mushtukov et al. (2015b), employing different assumptions on the accretion channel geometry and contribution of the polarization modes. The black dotted line shows prediction by Becker et al. (2012). See the comment regarding the negative correlation for 4U 0115+634 in the caption of Figure 3.12. Figure 7 from Mushtukov et al. (2015b).

field. The shock height was estimated as ∼1 km above the surface for $L_X = 10^{37}\,\mathrm{erg\,s^{-1}}$. At the same time, the line-forming region is located significantly below the shock, at $h_s \sim 10\,\mathrm{m}$. This variation of the accretion column height scales was suggested by Becker et al. as an explanation for the observed negative correlation of the cyclotron line with luminosity. In this case, the characteristic height of the line-forming region shifts up to lower magnetic field regions with increasing L_X.

Poutanen et al. (2013) argue that the linear dependency of the cyclotron line position with luminosity is inconsistent with the observed variation, predicting a too large shift of the line energy. They proposed an alternative scenario, based on the fact that photons emitted from the accretion column can experience strong downward beaming by the falling relativistic flow. If the whole column structure up to the shock height emits, then a significant amount of the flux can be intercepted by the neutron star surface. The effect is expected to be enhanced by the strong light bending in the gravitational field of the neutron star. The intercepted radiation is the reprocessed by the atmosphere and re-emitted. This concept is known as the *reflection model* for accreting highly magnetized neutron stars (see Figure 3.14). In this model, the resulting variation of the cyclotron line indicates the change of the highest latitude, illuminated by the column emission. Assuming a dipolar magnetic field, the difference between the magnetic field at the pole and the equator is only a factor of 2. It is much lower than the variation with the height, $B \propto r^{-3}$, when the height is directly proportional to the luminosity. However, the reflection model also has challenges. Simulations by Kylafis et al. (2021) showed that the flux intercepting the neutron star surface samples the continuously changing magnetic field. The resulting absorption features overlap, leaving a contribution from the line with energy close to the pole magnetic field. In addition to this, it is unclear whether strong illumination of a significant amount of the stellar surface is consistent with the observed

Reflection in this case should be seen rather differently from the specular or diffuse light reflection off a solid body. Photon flux can penetrate to higher optical depths of the atmospheric plasma. It can be re-emitted after a few scatterings or experience a true absorption, deposing the energy to the thermal reservoir. In any case, the radiation field is significantly reprocessed by the atmosphere and no simple law for the reemission angle can be written. Such reflected spectra have to be modeled by the radiative transfer, as done, for example for the reflection model `XILLVER` *for accretion disks around black holes (García & Kallman 2010; García et al. 2013).*

pulsations. One would expect a significantly lower pulsed fraction for the high energy radiation and simpler pulse profiles if the emission is not confined to the small polar region, than what is observed for accreting X-ray pulsars (see, e.g., Wang et al. 2022).

In addition, the accretion columns do not necessarily emit constant luminosity per unit height, as assumed by the reflection model. Several authors attempted to calculate the stationary hydrodynamic structure of the column (see, e.g., Davidson & Ostriker 1973; Wang & Frank 1981; Postnov et al. 2015; Gornostaev 2021). The most common approach was to solve the two-dimensional momentum equation for gas flow and radiation, using the radiation-diffusion approximation with gray diffusion coefficients perpendicular and parallel to the magnetic field (see, however, Gornostaev 2021, for spatially three-dimensional models and two-dimensional computations together with a kinetic equation for photon number density). These models agree on the extended structure of the radiative shock and the formation of the mound-like zone below it. In the shock region, the accretion flow loses $\sim 90\%$ of its kinetic energy (see, e.g., the contours of constant $v/v_{\rm ff}$ in Figure 5.20). In this way, the mound represents the sinking zone introduced by Basko & Sunyaev (1976). It is expected that the most significant amount of flux originates in this structure. Postnov et al. (2015) showed that, depending on whether the accretion channel is hollow or filled, the mound can either be located closer to the surface or higher above. Even in the case of the filled accretion channel with high mounds ($\sim$7 km for $\dot{M} = 5 \times 10^{17}\,\mathrm{g\,s^{-1}}$), the greatest fraction of the emission comes from near the surface. At these altitudes, photons can still experience some downward beaming near the walls of the column due to the decreasing energy density in this direction. For the filled cylinder case, Postnov et al. showed that some part of the radiation can be intercepted by the neutron star surface (at $\dot{M} \gtrsim 3 \times 10^{17}\,\mathrm{g\,s^{-1}}$). They showed that for a filled column, the changing fraction of the reflection component results in a saturation of the hardness ratio with increasing luminosity, as was observed for some sources (e.g., 4U 0115+63 and V 0332+63). This result, however, is based on simply taking the X-ray albedo of the neutron star into account, and should be confirmed with full radiative transfer treatment.

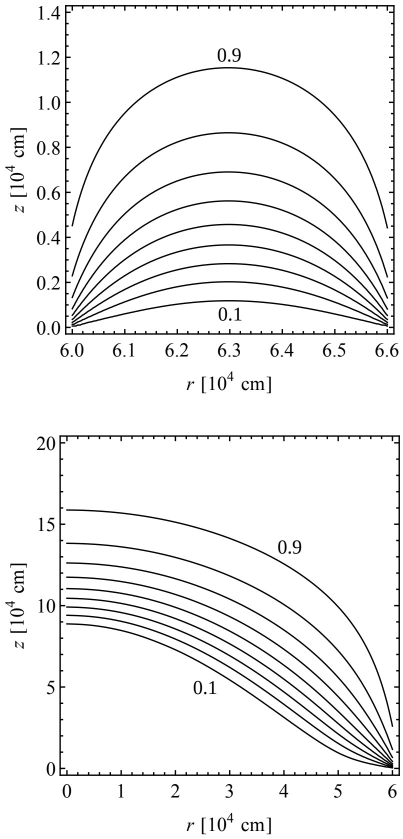

Figure 3.15: Lines of the equal squared velocity of the flow normalized to $v_{\rm ff}$. The profiles are calculated by Postnov et al. (2015) for the mass-accretion rate $\dot{M} = 10^{17}\,\mathrm{g\,s^{-1}}$. *Top:* hollow accretion column, *bottom:* filled accretion column. Figure 2 (top and bottom left panels) of Postnov et al. (2015).

An alternative radiative-hydrodynamic model was proposed by West et al. (2017a,b), exploiting the iterative solution of the hydrodynamic code with the generalized Kompaneets-like equation (similar to Becker & Wolff 2007; Farinelli et al. 2016). The spatially one-dimensional model includes the dynamical effect of gas and radiative pressure. However, it finds significantly larger heights of the sinking zone, $\sim$2–3 km, and predicts the strongest emission of flux from the top of this zone. In this case, however, the reasonable concern by Poutanen et al. (2013) about surface illumination should be taken into account. For such intense emission from above the surface, reflection can play a significant role in the formation of the spectrum and back-illumination of the column itself. The disagreement with other simulations of the column structure described above could be caused by the one-dimensional nature of the model.

Time-dependent radiation-hydrodynamic simulations of the column structure were performed by Klein & Arons (1989), based on the approach introduced by Arons et al. (1987). They found that outflows were formed in the non-stationary structure, which leads to the formation of regions with lower density. They showed that photons leak in regions with low optical depth, forming so-called *photon bubbles*. The presence of these large outflowing bubbles makes the accretion column structure highly inhomogeneous. This effect, if present, can seriously affect the spectral formation inside the column. Klein & Arons noted that outward streaming photon bubbles can potentially result in the formation of pencil-beam emission from the top of the accretion column, radiating away ∼80% of the accretion energy. Simulations by Klein et al. (1996) showed a significantly larger contribution of the wall emission (addressed as a "fan beam"). They found that the growth of photon bubbles leads to the appearance of quasi-periodic oscillations with luminosity.

All of the simulations of accretion column structures mentioned above, however, do not take into account the magnetic properties of the plasma and the effect it can have on the magnetic field of the neutron star. Recently, time-dependent magnetohydrodynamic simulations were performed by Abolmasov & Lipunova (2022). They also showed that at large mass-accretion rates, when the thermal pressure exceeds radiation pressure, plasma starts leaking from the column. The region where leakage starts (*vent*), is located above the surface. Its location depends on the mass-accretion rate and the geometry of the flow. This mass loss leads to the deformation of the accretion column and to an increase of its transverse size. In addition, Abolmasov & Lipunova (2022) showed that the shock front position can oscillate in the hecto- to kiloherz range. Recent magnetohydrodynamic simulations with angle-dependent and energy-averaged radiative transfer by Zhang et al. (2022) confirmed the existence of this effect. They showed that oscillations of the shock front is not a dynamic effect, but a thermal effect related to heat transport and cooling. According to Zhang et al., the origin of these oscillations is not related to the photon bubble instability. However, the presence of photon bubbles in the form of radiatively amplified acoustic waves propagating through the plasma of the column can increase the amplitude of the oscillations by enhancing the vertical radiation transport. The radiation transport was solved in the grey approximation and a black-body spectrum was assumed. Throughout their work, non-magnetic isotropic opacities were used. The latter was justified by assuming a low magnetic field value of 8×10^{10} G due to expected numerical problems in the scheme. Zhang et al. (2022) also noted that the field is sufficient to confine the flow in the accretion column, but magnetic opacities, which should be used for higher fields ($B \gtrsim 10^{12}$ G), can affect the non-linear dynamic of the flow. An example of the time-averaged structure of the accretion column is shown in Figure 3.16. This non-linear dynamic and the lower (time-averaged) height of the accretion columns were mentioned by Zhang et al. as the main differences between their model and one-dimensional models by Basko & Sunyaev (1976) and West et al. (2017a).

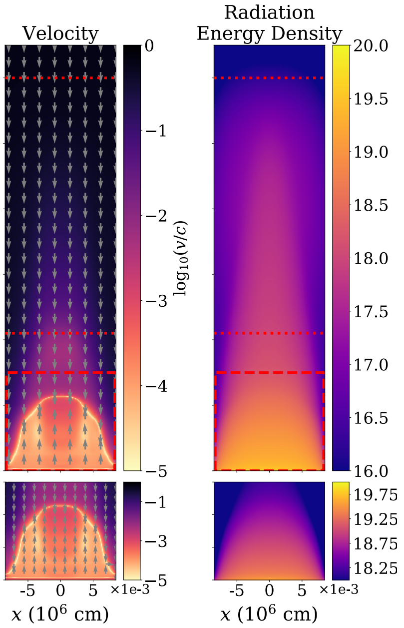

Figure 3.16: Time-averaged profiles of the accretion column, simulated by Zhang et al. (2022). The dotted red lines indicate the regions affected by the shock oscillation. The lower panel shows the bottom regions in the red dashed boxes in more detail. Figure 14 (two middle panels) of Zhang et al. (2022).

3.2.3 *Subcritical Accretion*

When the mass-accretion rate decreases (along with the corresponding accretion luminosity $L_{\rm acc}$), the pressure of the flux emitted from the pole of the neutron star also goes down. Eventually, it becomes insufficient to produce dynamic effects on the falling plasma. This accretion regime is called *subcritical*. It is associated with mass-accretion rates below the ones corresponding to the critical accretion luminosity. With the absence of a radiation-supported accretion column, our understanding of the physical processes in the accretion channel is even poorer than in the supercritical case. Partly, it is created by striking disagreement in the application of models having overall similar basic assumptions on physical processes.

These disagreements will be illustrated by examples of models based on the flow deceleration in collisionless shocks and by Coulomb collisions in neutron star atmospheres.

Basko & Sunyaev (1976) suggested that at $L < L_{\rm crit}$, the free-fall non-radiating zone extends almost down to the very surface of the neutron star. At a short distance above the surface, however, the radiative shock is still present, where the flow loses some fraction of its kinetic energy in the shock. The deceleration power of this region rapidly decreases with the luminosity. According to Basko & Sunyaev, at $L \sim 0.5 L_{\rm crit}$, the postshock velocity is about $0.8 v_{\rm ff}$. In this way, a decrease of luminosity in the sub-critical regime fairly quickly leads to the case where radiation influence on the falling plasma can be ignored. Final deceleration below the weak radiative shock is expected to proceed via Coulomb or nuclear collisions and collective effects of magnetized plasma.

Becker et al. (2012) suggested a sequence of accretion regimes accompanying the change of luminosity. At the supercritical regime, the formation of a radiation-dominated shock with the properties discussed in Section 3.2.2 is expected. The emission is expected to be emitted from the accretion column walls. Below the critical luminosity, $L < L_{\rm crit}$, following Basko & Sunyaev (1976), the radiative shock was assumed to account for some deceleration of the falling plasma. After the shock, the matter is stopped by Coulomb interactions. Becker et al. suggested that the depth at which Coulomb collisions begin to decelerate the plasma is then associated with the line-forming region. They showed that this depth can grow with the increasing mass-accretion rate, resulting in the observed positive correlation of the cyclotron line energy and luminosity. However, the estimated emission height $h_{\rm c}$ is $\sim 10^4$–10^5 cm (see their Equation 51), with the radiative shock above it. This picture differs significantly from the assumptions made by Basko & Sunyaev (1976) for this regime. It was proposed by Becker et al. (2012), that the combined emission from the top (pencil) and the sidewalls (fan) of the column is observed in this case. According to Becker et al., once $h_{\rm c}$ exceeds the height of the radiative shock H, the Coulomb deceleration becomes inefficient due to the reduced vertical optical depth of the channel. They suggest that this happens at the luminosity $L_{\rm coul} \sim 10^{36}$–$10^{37}$ erg s^{-1}. Below this value, the authors suggest that the emission region settles onto the stellar surface. At very low luminosities $L < 10^{34}$–10^{35} erg s^{-1} they consider dissipation of the radiative shock and the Coulomb atmosphere, arguing that the flow strikes the stellar surface after passing through the extended gas-mediated shock ("collisionless shock" as proposed by Shapiro & Salpeter 1975; Langer & Rappaport 1982). It is unclear, however, which type of deceleration is assumed at the surface in this case, as some sort of atmosphere would still be expected to be present above the ocean and the crust of the neutron star. Essentially, according to the suggested picture, some sort of accretion column is always present above the stellar surface, except for the relatively small range of luminosities, $L \sim 10^{35}$–10^{36} erg s^{-1}, when the Coulomb deceleration is allowed to act right near the surface of the neutron star. In the community, however, a few alternative scenarios for luminosities lower than the critical value are discussed (see below).

Based on the arguments from Becker et al. (2012) it is unclear, however, why $h_{\rm c}$ is not directly associated with the base of the radiative shock. In addition, in highly magnetized plasma, Coulomb interactions are expected to act gradually, veering out the falling particles, away from the magnetic field lines in multiple collisions (Miller et al. 1987). The claim that $h_{\rm c}$ can be associated with some narrow region within the column thus does not seem substantiated. On the other hand, if the line formation is associated with a somehow extended region, then it is unclear how the sampled vertical range of the magnetic field values would affect the resulting cyclotron line in the spectrum.

In my opinion, it is unclear why Coulomb interactions can be insufficient to decelerate the flow at the very base of the accretion channel, where the density of the ambient plasma grows rapidly due to the high gravitational field of the neutron star. And if they are insufficient, why nuclear collisions are not considered as an alternative.

Regimes of plasma deceleration via collisionless shock and Coulomb collisions were proposed by early models of accretion onto neutron stars. Zel'dovich & Shakura (1969) first considered stopping of the accretion flow by Coulomb encounters in the atmosphere of a non-magnetized neutron star. They obtained the structure of the atmosphere and the radiation field in a diffusion approximation. They showed that when the flow strikes the atmosphere at the free-fall velocity, the atmosphere acquires a hot, optically thick top layer and a much colder isothermal interior (see Figure 3.17). Similar results were obtained later by Alme & Wilson (1973), Turolla et al. (1994), Deufel et al. (2001), and Suleimanov et al. (2018) in the context of accreting neutron stars with low magnetic fields, as expected from Low-Mass X-ray Binaries. The main attribute of this regime is that most of the kinetic energy of the flow is lost in proton–electron (in a hydrogen plasma) or ion–electron collisions. Protons decelerate via interactions with ambient atmospheric electrons in the nearly-static extended atmosphere where the ion temperature is close to the electron temperature, $T_\mathrm{i} \sim T_\mathrm{e}$ (Shapiro & Salpeter 1975). In a strong magnetic field, the process of Coulomb deceleration, however, differs from the non-magnetic case. Miller et al. (1987) showed that collisions result in the gradual veering of protons away from the magnetic field lines, decreasing their efficiency. This results in a higher characteristic stopping depth for protons. Another effect introduced by the strong field is collisional excitations of atmospheric electrons to higher Landau levels. As such excitations are most likely to result in radiative decay (see Section 4.4), this process removes accretion energy from the thermal plasma reservoir, converting it into radiation. Nelson et al. (1993, 1995) showed that for moderate magnetic fields, where excitation to very high levels is possible, this process can create a noticeable excess close to the cyclotron fundamental energy in the radiation spectrum. For strong magnetic fields, $B \gtrsim 5 \times 10^{12}$ G, only excitations to the first few Landau levels are possible. Miller et al. (1987, 1989) calculated that only a small fraction of the accretion energy, $\sim$10%, goes into *nonthermal* collisional excitations. The thermal structure of the atmosphere depends, however, on the temperature of the falling plasma, its velocity, and the surface magnetic field. Meszaros et al. (1983) and Harding et al. (1984) showed that the temperature profiles of this nearly-static collision-dominated atmosphere can differ significantly for $B = 5 \times 10^{12}$ G and $B = 10^{13}$ G. Staubert et al. (2007) proposed Coulomb collisions as the deceleration channel at high yet subcritical luminosities, characteristic for Her X-1 ($L \sim 10^{37}\,\mathrm{erg\,s^{-1}}$). They associated a positive correlation of E_cyc with L_X with the change of the proton stopping depth, which is one of the most crucial parameters for atmospheric models. However, recent models by Mushtukov et al. (2021) and Sokolova-Lapa et al. (2021) linked this regime with much lower luminosities, $\leq 10^{35}\,\mathrm{erg\,s^{-1}}$ (see Chapter 6 for more details). They proposed that deceleration of the accretion flow via Coulomb encounters from the free-fall velocity in the neutron star atmosphere can explain the two-component continuum observed in the low-luminous states of Be X-ray Binaries with highly-magnetized slowly-rotating neutron stars, such as GX 304−1, A0535+262, and X Per (see Section 3.1.1). These models, although similar, disagree about the contribution of nonthermal collisional excitation to the formation of the emergent radiation field. The model by Sokolova-Lapa et al. (2021), its extension, and its application to observational data is discussed in detail in Chapter 6.

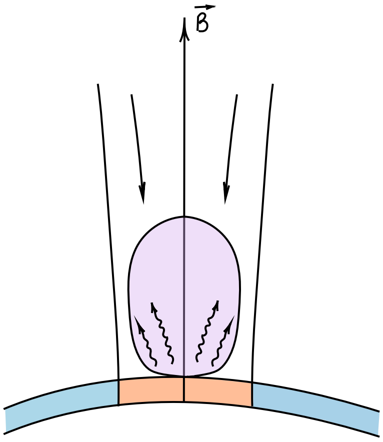

Figure 3.17: Schematic depiction of Coulomb deceleration in the atmosphere of a neutron star.

Here, the word nonthermal *means that collisions are produced not by thermal, but by bulk motion of charged particles. As discussed in Section 4.4.2, collisional excitations due to the thermal motion should be treated as a resonant part of free-free absorption and emission under the typical conditions in the accretion channel.*

The possibility of a standing gas-mediated adiabatic (i.e., non-radiative; Caditz & Tsuruta 1998) shock wave above the surface of a magnetized neutron star was proposed by Shapiro & Salpeter (1975) for the spherically-symmetric accretion flow. The model was suggested as an alternative to the collision-dominated scenario proposed by Zel'dovich & Shakura (1969) and requires a mechanism of randomization of two inter-penetrating ion beams on short time scales (rapid growth of plasma instabilities was considered by Shapiro & Salpeter 1975). In this case, the emission originates in the region between the collisionless shock and the neutron star surface. The height of the shock was shown to decrease with increasing mass-accretion rate, $\propto A_{\rm cap}/\dot{M}$, where $A_{\rm cap}$ is the polar cap area. Langer & Rappaport (1982), postulating the existence of the collisionless shock, calculated the velocity and temperature profiles in the post-shock region. The obtained ion temperature is ~2 orders of magnitude higher than the electron temperature. Bykov & Krasil'Shchikov (2004) simulated the formation of the quasi-stationary collisionless shock in a magnetized accretion channel, assuming the appropriate growth rate of randomizing multistream instabilities. They found a one-dimensional structure of the shock with a characteristic height of a few hundred meters above the surface. As expected, the shock height was increasing with decreasing mass-accretion rate. Based on the inverse variation of the shock front with $\dot{M}$, and therefore luminosity, the collisionless shock was proposed as a possible explanation for the positive correlation of $E_{\rm cyc}$ with $L_{\rm X}$ for GX 304−1 (Rothschild et al. 2017) and Cep X-4 (Vybornov et al. 2017) observations at intermediate flux levels (corresponding to $L_{\rm X} \sim 10^{36}\,{\rm erg\,s^{-1}}$). In these applications of the collisionless shock models, it was assumed that the resulting spectrum follows a power law with a high-energy exponential cutoff, as typically observed for intermediate luminosities (aside the additional spectral components discussed in Section 3.1.1). Alternatively, Becker & Wolff (2022) suggested that the collisionless shock model should describe the two-humped spectra at the lowest luminosities, such as X Per. Their assumed velocity profile places the shock front at a large distance, $\sim 10\,{\rm km}$ above the neutron surface. The high-energy excess (the second hump in the spectra) is then produced by cyclotron emission in addition to the Comptonized continuum. Figure 3.18 shows sketches of the two alternative models for the collisionless shock regime.

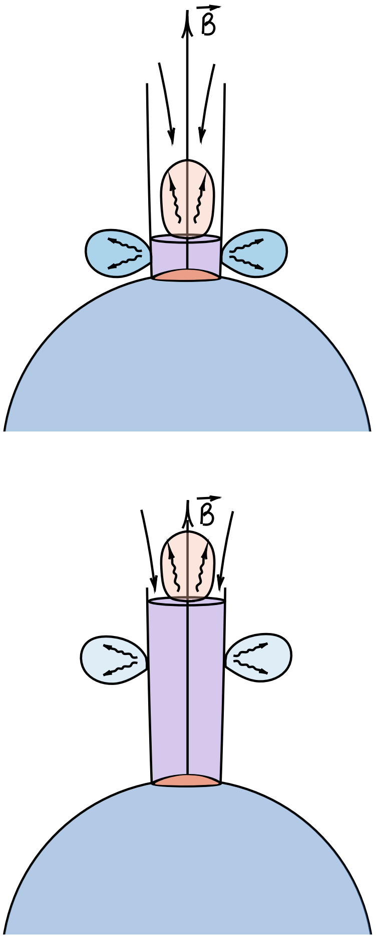

Figure 3.18: Schematic depiction of two collisioless shock models. Top: shock of a low height considered, e.g., by Rothschild et al. (2017), Vybornov et al. (2017); bottom: extended shock proposed by Becker & Wolff (2022).

It is still unclear whether conditions for the strong plasma collective effects causing the formation of the collisionless shock are met in the accretion channel of highly magnetized neutron stars. The collective plasma response to a moving proton was included in the kinetic calculations by Miller et al. (1987) and Miller et al. (1989), together with Coulomb collisions and collisional excitations. Miller et al. (1989) concluded that for hot plasma the effect of the collective effects on the plasma stopping is negligible. All simulations related to the collisionless shock models had to postulate the conditions for its origination. It is important to mention that both main models for subcritical accretion, a collisionless shock and Coulomb collisions, were proposed by different groups to explain different phenomena. These models are mainly mutually exclusive. Thus, the collisionless shock regime was proposed to explain intermediate luminosities with the positive cyclotron line correlation and more typical spectra for the X-ray pulsars in High-Mass X-ray Binaries (Rothschild et al. 2017; Vybornov et al. 2017) and low-luminous states exhibiting two-humped spectra (Becker & Wolff 2022). The same is true for the Coulomb collisions: the model was proposed for the subcritical Her X-1 with positive $E_{\rm cyc}(L_{\rm X})$ correlation (Staubert et al. 2007) and low-luminosity two-component spectra (Sokolova-Lapa et al. 2021; Mushtukov et al. 2021). Whether either of these regimes or their sequence plays a role in the accretion flow deceleration needs to be answered in the future. So far, *models of such kind often lack clear falsifiable predictions*, which, in my opinion, is one of the main problems in the field. Some tests, however, can be devised for subcritical models. For the low-luminosity regime, Sokolova-Lapa et al. (2021) suggested that predicted pulse profiles and behavior of the cyclotron lines should differ significantly from the case of the atmospheric hot-spot emission (such as described for example, in their work and in Mushtukov et al. 2021), and radiation by the extended, ~ 10 km high accretion column Becker & Wolff (as assumed by 2022).

Another explanation, not related to the collisionless shock or Coulomb collisions, was proposed by Nishimura (2014) and Mushtukov et al. (2015c), who considered the Doppler effect on the observed cyclotron resonance energy. Mushtukov et al. (2015c) argued that variation of the accretion flow velocity profile is caused by the growing dynamic effect of the radiation from the surface of the neutron star, below the critical luminosity value. This variation moderates the Doppler effect on the photons with near-resonance energies, for whom the accretion channel can remain optically thick at intermediate $\dot{M}$. The higher the remaining velocity near the surface (the lower the luminosity), the more shifted the cyclotron line to lower energies.

3.3 FINAL REMARKS

The observed spectra and pulse profiles of accreting neutron stars in High-Mass X-ray Binaries present a great variety of phenomena, many of which are yet to be explained. The complexity of the continuum shapes, which rarely resembles purely power-law-like behavior at intermediate energies, as well as the correlation of the spectral components with the source luminosity, remain the questions of current interest. The suggested classification of the accretion regimes is constantly challenged by new observational evidence and is often contradictory between different theoretical works. Solid agreement in the field is reached regarding the critical luminosity, which separates the supercritical and subcritical accretion. It is important to note that evidence of the supercritical accretion was observed only for a handful of sources. Some of them (e.g., A 0535+262) apparently exhibit this behavior only at the brightest outbursts. In this sense, the subcritical regime, which is more often associated with the near-surface emission and the relative unimportance of bulk Comptonization, could be the one of current interest. It is, however, less frequently addressed by theoretical and numerical modeling than the supercritical accretion columns.

The location of the emission regions on the surface of the neutron star and the viewing angle of the observer are another crucial component for understanding the emission formation. Disentangling them from the beam shape and the geometrical extension of the emission region allows us to answer such important questions about the accretion onto a magnetized neutron star, such as the existence of accretion columns at different luminosity states and the influence of reflection from the surface. Although hints about these parameters can be obtained by studying pulse profiles (Sasaki et al. 2012; Iwakiri et al. 2019), contribution of the beam shape and the geometry of the poles are indistinguishable. Self-consistent simulations of the angle-dependent spectra and pulse profiles are then required to break this degeneracy, providing the prior information.

In the nest chapters, I address some of the questions and problems that have been raised. First of all, in Chapter 5 the main properties of the polarized emission from highly magnetized plasma are studied in detail. There, I show the complexity of the spectral shapes, which result from simulations when both continuum and cyclotron line contributions are included in the polarized radiative transfer simulations. The angular distribution of the radiation in the neutron star rest frame is also studied there. Chapter 6 takes a step forward and presents a physical model with consistently simulated spectra, beams, and pulse profiles from a neutron star accreting at low mass-accretion rates. I apply this model to observations of Be X-ray binary GX 304−1 in quiescence and I show that even in the case of the very simple observed pulse profile, one can significantly constrain the geometry of the emitting poles and the observer's viewing angle. Polarization signal is another powerful tool that can be used to access geometrical information (see, e.g., Tsygankov et al. 2022). Here, however, I do not address the observed polarization signal, limiting the study of the polarization contribution in the frame of the neutron star and considering the total spectra seen by a remote observer.

Part II

RADIATIVE PROCESSES AND RADIATIVE TRANSFER

4

RADIATIVE TRANSFER IN HIGHLY MAGNETIZED MEDIA

"The exact equation for any given law of scattering is easy to formulate but difficult to solve..."
E. A. Milne, Thermodynamics of the Stars

As shown in Chapter 3, spectroscopic observations are one of the main tools of X-ray astronomy. However, understanding the formation of the observed spectra has proven to be a highly non-trivial task. Partially ionized, magnetized plasmas in the vicinity of stellar and compact objects, as well as the interstellar medium, can introduce significant modification to the radiation field and serve as its source. The shaping of the radiation spectrum is done via interactions with real or virtual particles by *absorption*, *emission*, and *scattering*. The net effect of the media on the radiation field, translated to the observed spectrum, is given by the solution of the *equation of the radiation transport*. In astrophysics, this term is reserved for the time-dependent task, whereas the stationary problem is represented by the *radiative transfer equation* (see, e.g., Hubeny & Mihalas 2014). Mathematically, both equations can be seen as a statement of photon number conservation (Pomraning 1973). In this work, I only follow a stationary approach, discussing solutions of the radiative transfer equation for different media.

The problem of radiation propagation in a cosmic plasma has a long history of investigation. The work of Schuster (1905), who considered the transfer of radiation through a "foggy" - scattering - atmosphere, marks the beginning of this history. Schuster emphasized the difference between scattering and absorption and discussed the conditions under which absorption ("dark") lines or emission ("bright") lines originate. Schwarzschild (1906) introduced the radiative transfer equation in its classical form and noted the importance of *radiative equilibrium*, as opposed to the *adiabatic equilibrium* for the solar atmosphere. Later, Schwarzschild (1914) presented a formal solution for the mean intensity and analyzed the formation of the Fraunhofer lines in case of pure scattering and pure absorption with re-emission. These works provided the foundation for the famous *Schwarzschild-Schuster model* for line formation in the outer, *reversing* layer of the atmosphere.[1] The work of Eddington (1916) brought the focus to the importance of the radiation pressure and the transfer of energy by radiation for the equilibrium of the stars. Finally, a comprehensive study by Milne (1930b) formulated and reviewed fundamentals of the theory of radiation, introducing, among other things, the solution for the radiative transfer in a "grey" atmosphere (when the opacity coefficient is independent of the photon's energy)[2] These papers are published together in the collection by Menzel & Milne (1966), including translated works of Schwarzschild (1906), and Schwarzschild (1914).

The term Schwarzschild-Schuster model *or* Schwarzschild-Schuster approximation *is also used to describe the two-stream nature of the approach.*

Historically, the discussion of radiation propagation through plasma began with attempts to explain the results of stellar observations, such as the Fraunhofer lines in the solar spectrum and the limb darkening effect. However, soon its importance for other processes in cosmic plasmas was recognized. These processes include, for example, propagation of

---

[1] This model is actively used to this day when the complexity of the line formation does not allow to treat it together with a continuum in a computationally reasonable way (see, e.g., the proposed model for accretion column emission in Chapter 3 of Falkner 2018).

[2] This formulation of the radiative transfer is known as *Milne's problem*, and its formal solution is given by *Milne's equation* (see Chapter 3 of Mihalas 1978, for more detail)

radiation through the partially ionized tenuous gas of the interstellar medium and emission of accretion flows around compact objects. For these tasks, Compton scattering becomes crucially important for the continuum formation. In high-temperature atmospheres, such as expanding atmospheres of Wolf-Rayet stars, Compton scattering affects not only the continuum but the shapes of spectral lines, inducing broadening, asymmetry, and formation of emission wings (see, e.g., Peraiah & Srinivasa Rao 2013). As was mentioned before, in the highly magnetized media around neutron stars, Compton scattering is also responsible for the formation of such spectral features as cyclotron lines.

Compton scattering plays a crucial role in the models of accretion channels near highly magnetized neutron stars by shaping and energizing the radiation field. In turn, even when a simulation does not focus on the radiation, it can be an important component for modeling, for example, the structure of the accretion column (see, e.g., Zhang et al. 2022; West et al. 2017a). In an optically thick medium the *diffusion approximation* is often a valid simplification of the radiative transfer problem. This approach naturally involves angle averaging of physical quantities and provides a solution for radiation energy density within the medium. This approximation was evoked, for example, by Nagel (1980), Nagel (1981b), Davidson (1973), Arons et al. (1987), Postnov et al. (2015), and Gornostaev (2021, for their spatially three-dimensional models). If the spatial dependency of the radiation field is of direct interest, it sometimes in addition results in the energy-averaged form (see, e.g., Davidson 1973; Gornostaev 2021). Some conclusions on the photon spectrum can then be made by, for example, using the assumption of the black-body spectrum of the radiation and an obtained local flux value (Davidson 1973). Sometimes, the diffusion approximation is used to describe the line transfer, as was done for cyclotron emission by Bykov & Krasil'Shchikov (2004).

There are, though, suggested approximations, which allow to obtain the angular dependency of the radiation field after the photon density is known from the solution of the diffusion equation (see Nagel 1981b, and references therein).

Another approach to the radiation field description is based on the Kompaneets-like form of the transfer equation. Kompaneets (1957) derived an equation for time-dependent thermal Comptonization. The space diffusion terms were added to this equation by Katz (1976). Payne (1980) derived a similar expression for the coupled spatial photon transport and Comptonization. For the moving medium, the equation was obtained by Blandford & Payne (1981). This approach allows the inclusion of thermal and bulk Comptonization. It is often used in various modifications for modeling the accretion channels near the magnetized neutron stars Becker & Wolff (2005), Becker & Wolff (2007), Wolff et al. (2016), Farinelli et al. (2012), Farinelli et al. (2016), West et al. (2017a,b), and Gornostaev (2021). Different analytical and numerical solutions are discussed in these works. The major limitation of this form of the transfer equation is the inability to include angular redistribution of photons and polarization effects.

The discussed approximations are obtained from a full form of the classical radiation transport equation, which is discussed in this chapter. It includes the energy and angular redistribution of photons during the scattering event and allows treating polarized radiation field. The complexity of the task, when coherent scattering or grey approximation are not evoked, usually makes it treatable only by numerical methods, especially in the strongly anisotropic and polarizing medium present near highly magnetized neutron stars. Examples of the solution of the (steady-state) transfer equation in this form include Yahel (1979), Yahel (1980a,b), Nagel (1981a), Meszaros & Nagel (1985a,b), Alexander et al.

(1989), Burnard et al. (1991), Mushtukov et al. (2021), and Sokolova-Lapa et al. (2021). Most of these works focused on the joint simulations of the continuum and the cyclotron resonances (except for Burnard et al. 1991, where the cyclotron line region was excluded). Examples of the radiative transfer simulation only within the cyclotron harmonics, with the assumed phenomenological continuum, are given by Araya & Harding (1999), Schönherr et al. (2007b), Nishimura (2008) Schwarm et al. (2017a), Schwarm et al. (2017b), Kumar et al. (2022).

The interest in a joint simulation of the continuum and the cyclotron lines of accreting X-ray pulsars, which was sparked by the discovery of the cyclotron line in the spectrum of Her X-1 in 1976 (Trümper et al. 1977), resulted in the series of works in the 1980s and seemingly faded away after a decade. It gave way to the purely continuum models, which aimed at the supercritical accretion regime and considered spectral formation in the extended accretion columns (such as Becker & Wolff 2005; Postnov et al. 2015; Farinelli et al. 2016; West et al. 2017a,b), and the separate cyclotron line simulations on top of the given continuum (see, e.g., Araya & Harding 1999; Schwarm et al. 2017a,b). An attempt to combine two physical models for the continuum and the cyclotron lines was made, for example, by Falkner (2018). The continuum models are mainly based on the Kompaneets-like transfer equation and diffusion approximation, naturally leading to the angle- and polarization-averaged calculations. These models typically result in a smooth shape of the Comptonized spectrum, mainly reproducing the power law with high-energy cutoff. Only recently the attempts to solve the polarized radiative transfer with angular and energy redistribution were revived (Mushtukov et al. 2021; Sokolova-Lapa et al. 2021) for quiescent accretion.

This chapter is dedicated to the discussion of the solution of the radiative transfer equation in highly magnetized media. This discussion, however, is not possible without setting up the scene for the radiative processes and radiation polarization in the strong magnetic field. In Section 4.1, I outline the basic properties used to describe the radiation field, mainly from the microscopic and quantum mechanical point of view. The general form of the equation of radiation transport and its components are presented in Section 4.2. Section 4.3 describes the polarization properties of a high-energy radiation field in magnetized plasma and QED vacuum, introducing the necessity to solve the *polarized radiative transfer*. In Section 4.4, I discuss opacities, relevant for the case of accreting neutron stars environment, with major focus on resonant Compton scattering. The details of the Feautrier method for the polarized radiative transfer and its implementation are described in Section 4.5. This chapter ends with some remarks on the applicability and natural limitations of the approach in Section 4.6.

4.1 RADIATION FIELD

To describe the evolution of the radiation field, one first needs to determine its basic properties. Typically, the formalism to describe the radiation field combines macroscopic, electromagnetic, and quantum treatment (Hubeny & Mihalas 2014). One of the most commonly used microscopic quantities is the *specific intensity* of the radiation, which is defined as an amount of energy $\delta\mathcal{E}$ transported at a position $\mathbf{r}$, at time t by radiation of frequencies in the range $(\nu, \nu + \mathrm{d}\nu)$, traveling in the direction **k** into a solid angle $\mathrm{d}\Omega$ through the unit area $\mathrm{d}s$ per unit time $\mathrm{d}t$,

$$I_\nu = I(\nu, \mathbf{k}, \mathbf{r}, t) = \frac{\delta\mathcal{E}}{\mathrm{d}s\,\mathrm{d}\Omega\,\mathrm{d}\nu\,\mathrm{d}t}. \tag{4.1}$$

Figure 4.1 illustrates a pencil of radiation, which defines the specific intensity.

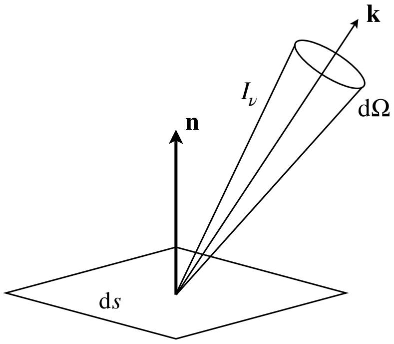

Figure 4.1: Definition of the specific intensity I_ν. The surface normal is **n**, **k** is the direction of the radiation field propagation, $\mathrm{d}\Omega$ is the solid angle element, and $\mathrm{d}s$ is the unit area.

Various angular averages of the specific intensity, also known as the *moments* of the specific intensity, are used for the description of the radiation field. The *zeroth moment* is the *mean intensity*

$$J_\nu = J(\nu, \mathbf{r}, t) = \frac{1}{4\pi}\oint I(\nu, \mathbf{k}, \mathbf{r}, t)\mathrm{d}\Omega. \tag{4.2}$$

For a homogeneous and isotropic radiation field, $I_\nu = J_\nu$. The mean intensity, as integrated over the solid angle quantity, allows to define the *monochromatic energy density* in an elementary volume,

$$\varepsilon_\nu = \frac{4\pi}{c}J_\nu. \tag{4.3}$$

The *total energy density* is obtained by integrating Equation 4.3 over all frequencies.

The *first moment* of the specific intensity is given by the *Eddington flux*,

$$\mathbf{H}_\nu = H(\nu, \mathbf{r}, t) = \frac{1}{4\pi}\oint I(\nu, \mathbf{k}, \mathbf{r}, t)\mathbf{k}\mathrm{d}\Omega. \tag{4.4}$$

It is more common, however, to use the *radiation flux*, defined as

$$\mathbf{F}_\nu = 4\pi H_\nu = \oint I(\nu, \mathbf{k}, \mathbf{r}, t)\mathbf{k}\mathrm{d}\Omega. \tag{4.5}$$

In addition to the Eddington flux and (monochromatic) radiation flux, sometimes so-called astrophysical flux, $\mathcal{F} = \pi^{-1}F_\nu$, *is used.*

This is a vector quantity, which gives the net rate of radiant energy flow across a given area. Later, for the case of the plane-parallel atmosphere, I will use only one component of this vector, referring to it as "flux", unless specified otherwise. The radiation flux is the only quantity one can measure for unresolved objects. In this way, the modeling of emitting astronomical objects must result in the prediction of the emitted and observed flux, as well as its variation.

From the point of view of statistical quantum mechanics, the radiation field is an ensemble of photons and can also be characterized in terms of the *photon occupation number*, $n = n(q, \mathbf{r}, t)$, which is the number of photons in quantum state q at the position $\mathbf{r}$ and time t. The state q is characterized by the photon's energy, $h\nu$, the wave vector **k** and the polarization. The connection of the photon occupation number to the specific intensity is given by

$$I = \frac{h\nu^3}{c^2}n. \tag{4.6}$$

As photons are bosons with zero rest mass, they posses only two principle polarization states, and for mixed unpolarized radiation field, the numerator in Equation 4.6 includes an additional factor of 2. The quantum nature of the radiation field can significantly affect its evolution, leading to such effects as induced processes. They originate from the properties of bosons: the probability of a particle entering the state, already occupied by n particles, is enhanced by the factor $[1 + n]$. The consequences of this property for radiative transfer are discussed in Section 4.2.

The characteristics of the photon field described above provide a sufficient foundation for the discussion of the radiative transfer problem. For more information, such as higher moments of intensity, discussion of the photon distribution function, and electromagnetic description of the radiation field in connection with the energy density and energy flux, see the classical works, such as Mihalas (1978), Hubeny & Mihalas (2014), Pomraning (1973), Peraiah (2001), and the detailed lecture notes by Prof. C. P. Dullemond[3].

4.2 RADIATIVE TRANSFER EQUATION

There are several ways to obtain the radiative transfer equation, such as classical Eulerian and Lagrangian derivations based on balancing the radiative processes in the elementary volume (see details in, e.g., Pomraning 1973). Here I would like to refer to an approach which takes into account the quantum statistics of photons and describes the evolution of the photon occupation number n by the collisional Boltzmann equation[4] (see, e.g., Mészáros 1992). This approach leads to the full, time-dependent radiation transport equation in its general form. For unpolarized radiation, taking into account Equation 4.6 for the relation of the photon occupation number and the specific intensity, it can be written as

$$\begin{aligned}\frac{1}{c}\frac{\partial I(\nu,\mathbf{k})}{\partial t} &+ \mathbf{k}\cdot\boldsymbol{\nabla} I(\nu,\mathbf{k}) = j(\nu,\mathbf{k})\left[1+\frac{c^2}{2h\nu^3}I(\nu,\mathbf{k})\right] \\ &+ \int \mathrm{d}\nu' \int \mathrm{d}\Omega' \frac{\nu}{\nu'}\frac{\mathrm{d}^2\sigma}{\mathrm{d}\nu\mathrm{d}\Omega}(\nu',\mathbf{k}'\to\nu,\mathbf{k})I(\nu',\mathbf{k}')\left[1+\frac{c^2}{2h\nu^3}I(\nu,\mathbf{k})\right] \\ &- \int \mathrm{d}\nu' \int \mathrm{d}\Omega' \frac{\mathrm{d}\sigma}{\mathrm{d}\nu'\mathrm{d}\Omega'}(\nu,\mathbf{k}\to\nu',\mathbf{k}')I(\nu,\mathbf{k})\left[1+\frac{c^2}{2h\nu'^3}I(\nu',\mathbf{k}')\right] \\ &- \chi(\nu,\mathbf{k})I(\nu,\mathbf{k}), \end{aligned} \tag{4.7}$$

where each quantity dependent on the frequency of the photon ν and the direction of its propagation $\mathbf{k}$ is to be understood as also a function of the spatial coordinate $\mathbf{r}$ and time t, such as $I(\nu,\mathbf{k}) = I(\nu,\mathbf{k},\mathbf{r},t)$. The coefficients entering this equation describe the interaction of the radiation field with the medium. The *absorption coefficient*, $\chi = \chi(\nu,\mathbf{k},\mathbf{r},t)$, is defined such that $\chi \mathrm{d}l$ gives the probability of a photon to be absorbed while traveling the distance $\mathrm{d}l$. Here, I refer to the *true absorption*, that results in the photon being destroyed, or *thermalized*, when its energy is converted to the thermal energy of the medium. The *emission coefficient*, $j = j(\nu,\mathbf{k},\mathbf{r},t)$, gives the rate of photon emission by particles, which were excited by inelastic collision. It is often mentioned in the classical literature (see, e.g., Mihalas 1978), that scattering and absorption coefficients are independent of the angle of photon propagation. Generally speaking, this is not true if a source of anisotropy is introduced in the medium, such as a strong magnetic field. For this reason, the dependency is kept in Equation 4.7. The differential scattering cross section, $\mathrm{d}\sigma/\mathrm{d}\nu\mathrm{d}\Omega(\nu,\mathbf{k},\nu',\mathbf{k}';\mathbf{r},t)$, depends in addition on the final photon frequency ν' and propagation direction $\mathbf{k}'$, that is, $\mathrm{d}\sigma/\mathrm{d}\nu\mathrm{d}\Omega$ represents the probability for the photon to acquire them after the scattering event. In this way, inelastic scattering provides a channel for energy and angular redistribution of photons, which might

---

[3] The lecture notes and exercises for the course "Radiative transfer in astrophysics" can be found at `https://www.ita.uni-heidelberg.de/~dullemond/lectures/radtrans_2012/index.shtml`

[4] The Boltzmann kinetic equation, also represents the conservation of photons, in a phase-space.

have a very pronounced effect onto the formation of the observed spectra. Coefficients which contribute to the total opacity depend on the nature of processes that couple the radiation field and the medium and the number of particles that can support this interaction. For a highly magnetized medium in the vicinity of accreting neutron stars, the main processes determining the opacities are photon–electron interactions. They will be discussed in detail in Section 4.4.

The factors in square brackets in Equation 4.7 result from induced effects: stimulated emission and scattering due to the boson nature of photons. The unity term represents regular scattering and emission, while the second term, being the photon number density of unpolarized radiation, $n = c^2 I/2h\nu^3$, describes the induced processes. Unlike stimulated emission, stimulated scattering is proportional to n^2 and introduces a non-linearity to the radiation transport problem, which makes its treatment numerically challenging. In many cases, however, there are ways to linearize the problem. For example, when the scattering process is *coherent*, or *elastic* (meaning no energy redistribution occurs), the two terms of Equation 4.7 for the direct and inverse scattering cancel each other out. Another opportunity to ignore stimulated scattering occurs when the photon occupation number is small, $n \ll 1$. The latter, however, can rarely be satisfied throughout the whole atmosphere[5] in a consistent treatment, which includes greater depths with typically large photon occupation numbers, as well as the tenuous surface layer. Stimulated scattering has important consequences for the equilibrium spectrum. In the absence of this effect, the equilibrium distribution for the specific intensity approaches the Wien spectrum, whereas the Planck spectrum is reached otherwise (see, e.g., Pomraning 1973; Meszaros et al. 1989). To account for stimulated emission, one can use the corrected absorption coefficient in case of Local Thermodynamic Equilibrium (LTE) (see, e.g., derivation based on the Einstein coefficients in Mihalas 1978)

Local Thermodynamic Equilibrium describes a state of a medium when its opacity, emissivity, and other thermodynamic properties are determined by their thermodynamic equilibrium values at the local temperature and density. At the same time, the radiation field is allowed to deviate from the case of thermodynamic equilibrium (Mihalas 1978).

$$\alpha = \chi \left[1 - \exp\left(-\frac{h\nu}{k_{\mathrm{B}} T} \right) \right], \tag{4.8}$$

where k_{B} is the Boltzmann constant. A similar trick was introduced by Meszaros et al. (1989) to treat stimulated scattering while keeping the linear equation. This approximation, used throughout the present work, will be described in Section 4.5. For now, it is assumed that linearization is possible.

Equation 4.7 has a general form with respect to the emission coefficient j. However, often *Kirchhoff's law of thermal radiation* is a valid approximation for cosmic plasmas, connecting the emission and absorption coefficients. This law is applied even beyond the validity of the required assumption of the LTE

$$j_\nu = \alpha_\nu B(\nu, T(\mathbf{r}, t)), \tag{4.9}$$

where $B(\nu, T)$ is the Planckian spectrum of a temperature T in the case of the LTE or under some other conditions, enforcing the LTE-like level populations for the emitting particles (see, for example, Section 4.4).

---

[5] Following the tradition of the field, the term "atmosphere" is often used for all kinds of considered regions where radiation is reprocessed.

Taking into account Equation 4.8 and Equation 4.9, the transport equation can be rewritten as

$$\begin{aligned}\frac{1}{c}\frac{\partial I(\nu,\mathbf{k})}{\partial t} &+ \mathbf{k}\cdot\boldsymbol{\nabla} I(\nu,\mathbf{k}) = \alpha(\nu,\mathbf{k})B(\nu,T) - \alpha(\nu,\mathbf{k})I(\nu,\mathbf{k})\\ &+ \int \mathrm{d}\nu' \int \mathrm{d}\Omega' \frac{\nu}{\nu'}\frac{\mathrm{d}^2\sigma}{\mathrm{d}\nu\mathrm{d}\Omega}(\nu',\mathbf{k}'\to\nu,\mathbf{k})I(\nu',\mathbf{k}')\\ &- \int \mathrm{d}\nu' \int \mathrm{d}\Omega' \frac{\mathrm{d}\sigma}{\mathrm{d}\nu'\mathrm{d}\Omega'}(\nu,\mathbf{k}\to\nu',\mathbf{k}')I(\nu,\mathbf{k}). \qquad (4.10)\end{aligned}$$

Here one can notice that the $I(\nu,\mathbf{k})$ factor can be pulled out of the second integral, leaving the integral over the differential cross section. This, in its turn, gives just a total scattering coefficient σ, resulting in

$$\begin{aligned}\frac{1}{c}\frac{\partial I(\nu,\mathbf{k})}{\partial t} &+ \mathbf{k}\cdot\boldsymbol{\nabla} I(\nu,\mathbf{k}) = \alpha(\nu,\mathbf{k})B(\nu,T) - \kappa(\nu,\mathbf{k})I(\nu,\mathbf{k})\\ &+ \int \mathrm{d}\nu' \int \mathrm{d}\Omega' \frac{\nu}{\nu'}\frac{\mathrm{d}^2\sigma}{\mathrm{d}\nu\mathrm{d}\Omega}(\nu',\mathbf{k}'\to\nu,\mathbf{k})I(\nu',\mathbf{k}'), \qquad (4.11)\end{aligned}$$

where the total opacity, or *extinction coefficient*, $\kappa = \alpha + \sigma$, now includes both, absorption and scattering. An important concept related to the extinction coefficient is the optical depth

$$\tau = \int_0^{l^*} \kappa \mathrm{d}l, \qquad (4.12)$$

along the line of sight l, calculated up to the point l^*. Often, the *Thomson optical depth* τ_T, which is the optical depth due to purely Thomson scattering, is used as a common measure for the atmosphere (as, for example, in Chapter 6).

It is often convenient to divide Equation 4.11 by κ and gather all source- and redistribution-related parts into one term

$$\begin{aligned}S_\nu = S(\nu,\mathbf{k},\mathbf{r},t) = \frac{\alpha_\nu B_\nu}{\kappa_\nu} &+\\ \frac{1}{\kappa_\nu}\int \mathrm{d}\nu' \int \mathrm{d}\Omega' &\frac{\nu}{\nu'}\frac{\mathrm{d}^2\sigma}{\mathrm{d}\nu\mathrm{d}\Omega}(\nu',\mathbf{k}'\to\nu,\mathbf{k})I_{\nu'} \qquad (4.13)\end{aligned}$$

called the *source function*. This function characterizes the radiative processes in the medium and, in some cases, provides a qualitative description of the resulting spectrum, even when the exact opacity coefficients are not known. For example, when the LTE condition is satisfied, the source function equals the Planck function, $S_\nu = B_\nu$. The case of the coherent and isotropic scattering, when the differential cross section in Equation 4.13 is not dependent on ν', and $\mathbf{k}'$, gives another convenient form of the source function,

$$S_\nu = \frac{\alpha_\nu B_\nu + \sigma_\nu J_\nu}{\kappa_\nu}. \qquad (4.14)$$

In this case, no redistribution of photons in energy and angles occurs. In the situation when scattering proceeds under multiple elastic collisions with the surrounding particles, the incoming photon is randomly reshuffled between the sublevels of the scattering particle. As a result, the outgoing photon after scattering "has no memory" about the characteristics of the incoming one. This situation is referred to as *complete redistribution* and is often adopted to describe the formation of the atomic absorption lines. It allows for the separation of energy and angular contribution to the differential cross section, with the energy part being the profile of the absorption line. Under the conditions studied in the present work, these approximations are not valid due to the specifics of scattering in a highly magnetized plasma (see Section 4.4 for more details). The general form of the source function given by Equation 4.13, which describes so-called *partial redistribution* has to be used. Chapter 7 illustrates the importance of the partial redistribution effect in the heated inhomogeneous atmosphere of an accreting neutron star.

With the introduced source function, and now considering a steady-state problem, the radiative transfer equation becomes

$$\frac{\mathbf{k}\cdot\boldsymbol{\nabla} I_\nu}{\kappa_\nu} = -I_\nu + S_\nu. \tag{4.15}$$

This is one of the most commonly used forms of the radiative transfer equation, with possible further simplifications related to the gradient operator under consideration for the geometry of the problem. The case of the plane-parallel one-dimensional atmospheres, relevant to this works, is presented in Section 4.5.

The radiation transport equation in its classical form involves some necessary assumptions. It inherently treats photons as point particles and does not incorporate any strong wave-like behavior based on the interference among the waves. In this way, diffraction and reflection of the electromagnetic wave cannot be described by Equation 4.7. In the same way, it is assumed that the emitted photons are incoherent, that is, they do not interfere with each other, and that the radiative processes and collisions occur instantaneously. The latter imposes a limit on the time resolution for the transport equation (Pomraning 1973). Another important limitation is the *geometric optics approximation*. It is based on the assumption that the refractive index is close to unity, $|N-1| \ll 1$, throughout the considered medium. In this way, photons propagate along rays and only able to change the direction by interaction with particles - by scattering or absorption. This approximation can be violated in some extreme environments. For example, when the external magnetic field exceeds the Schwinger's limit ($B_{\rm crit} \simeq 4.413 \times 10^{13}\,$G), the non-linearity of the electromagnetic field due to non-elastic photon-photon scattering can break this approximation. The present work investitages atmospheres with magnetic fields below the Schwinger's limit and use an assumption of geometric optics. Some notes on the validity of this assumption are presented in Section 4.4. Finally, in this section, I described the general problem of radiation transfer, not focusing on photons polarization. The treatment of a polarized radiative transfer equation will be discussed in Section 4.5.

In the case of a nonlinear electromagnetic field, the nonlinear Maxwell's equations have to be used. These equations are based on nonlinear dynamics of the electromagnetic field, for example, on Euler–Heisenberg Lagrangian.

The solution of Equation 4.15 could be a relatively easy task, if not for the complexity of the source function. The calculation of the source function and corresponding opacities can be a non-trivial problem, depending on the type of absorption, emission, and scattering processes in the medium. Here, I consider the problem of the X-ray radiation transfer in a magnetoactive ionized non-homogeneous plasma and a strongly magnetized vacuum in the vicinity of accreting neutron stars. Under these conditions, free-free absorption, bremsstrahlung, and Compton scattering are the main processes that affect the photon field. These processes are substantially modified by the presence of a strong magnetic field. They also act differently on the photons in different polarization states. The following sections are focused on these problems.

4.3 RADIATION IN STRONG MAGNETIC FIELDS

The study of wave propagation in plasmas started in laboratory experiments (see, e.g., Langmuir 1928; Tonks & Langmuir 1929), with the word "plasma" for an ionized gas being used by Langmuir for the first time. Soon, its importance for cosmic plasmas, from the propagation of radio waves in the ionosphere to the emission of the accreting neutron star and pulsars magnetospheres were understood.

A plasma is a complex medium which can support various wave modes - the types of waves. A fundamental distinction can be made between *longitudinal electrostatic* and *transverse electromagnetic* waves. The first ones represent a broad class of phenomena, such as Langmuir waves, sound waves, and Alfvén (magnetohydrodynamic, or MHD) waves. The transverse waves represent well-known electromagnetic waves with the electric vector **E** orthogonal to the direction of propagation **k**, and with the magnetic vector $\mathbf{B} \perp (\mathbf{k}, \mathbf{E})$. Propagation of this type of wave in a plasma is only possible at frequencies $\omega > \omega_{\mathrm{pe}}$, where ω_{pe} is the electron plasma frequency

$$\omega_{\mathrm{pe}} = \sqrt{\frac{4\pi n_{\mathrm{e}} e^2}{m_{\mathrm{e}}}}, \tag{4.16}$$

which represents one of the fundamental scales in plasmas. Here n_{e} is the electron number density, m_{e} is the electron mass, and e is the elementary charge. In the following, I focus only on transverse waves, discussing the modes in magnetized media. The two kinds of transverse waves propagating through dispersive media represent two polarization normal modes. In general, their "normality" (orthogonality) can be a subject of a question, as will be shown in Section 4.3.4. When the treatment of the polarized radiation in terms of the two normal polarization modes is feasible, the modes provide a foundation for the polarized radiative transfer calculation (see Section 4.5).

In strong external magnetic fields, $B \gtrsim 10^{12}$–10^{13} G, expected for the vicinity of accreting neutron stars, a few major effects influence the propagation of the radiation in the plasma. The first one is the quantization of charged particles in the plasma onto Landau levels, when the Larmor radius of particles becomes comparable with the de Broglie wavelength. In this case, particles and their localization can no longer be treated classically. In their motion around the magnetic field lines, charged particles are allowed to occupy only specific orbits, characterized by the quantized transverse energy values (in the nonrelativistic limit)

$$E_n = n\hbar\omega_{\mathrm{cyc}}, \tag{4.17}$$

where ω_{cyc} is the cyclotron frequency. In the present work I study the propagation of the high-energy (X-ray) radiation in plasma, assuming that the frequency of the photons is much higher than the ion cyclotron frequency, $\omega \gg \omega_{\mathrm{cyc}}^{\mathrm{i}}$. It means that only plasma electrons need to be considered in the plasma response. Under these conditions, only the quantization of electrons plays an important role, while protons can be treated classically. In this way, the electron cyclotron frequency

$$\omega_{\mathrm{cyc}}^{\mathrm{e}} = \omega_{\mathrm{cyc}} = \frac{eB}{m_{\mathrm{e}}c} \tag{4.18}$$

represents another important scale for the plasma. I also assume that $\omega \gg \omega_{\mathrm{pe}}$, which allows for neglecting collective plasma effects. As electron motion perpendicular to the field lines is constrained, the electron momentum distribution is one-dimensional along the field lines. In the following, the electron temperature kT_e should be understood as the longitudinal temperature $kT_\mathrm{e}^{\|}$.

Another effect that becomes important for the magnetic fields considered here is vacuum polarization due to the production of virtual electron–positron pairs (the *virtual plasma*). This QED effect can have a significant influence on radiation propagation, especially at energies, close to the cyclotron resonances Equation 4.17. It is sometimes claimed that for magnetic fields as high as a few $10^{12}\,\mathrm{G}$ vacuum polarization does not affect the total spectrum, but only the polarization signal (Lai & Ho 2003a). However, these statements are made for much lower plasma temperatures, appropriate for the atmospheres of isolated neutron stars, but not always for the conditions near the surface of an accreting neutron star. In practice, the effect of vacuum polarization on the radiative transfer in hot atmospheres and accretion columns of accretion-powered X-ray pulsars still lacks detailed study. This subject will be discussed in the following Chapter 6, based on the description of the polarization modes introduced in the following sections.

This section is organized as follows: in Section 4.3.1, the plasma normal modes are obtained, accompanied by the discussion of their refractive indices and polarization. Section 4.3.2 introduces QED vacuum corrections to the normal modes. The joint magnetized plasma and polarized vacuum effect on the polarization modes is discussed in the Section 4.3.3. Finally, Section 4.3.4 addresses the ambiguity arising in the definition of the polarization modes cased by vacuum resonance effects and the validity of the description of the radiation field in terms of two polarization modes.

4.3.1 *Magnetoactive plasma*

The passage of waves through plasma is described by the *wave equation* (see, e.g., a derivation based on Fourier transformations of the field quantities in Maxwell's equations by Bekefi 1966; Melrose 1980). Typically, it is sufficient to treat only the *linear response* of the plasma to the disturbance by the electromagnetic wave propagation, which is described by the *dielectric tensor*

$$\hat{\boldsymbol{\epsilon}}(\mathbf{k},\omega) := \hat{\mathbf{1}} + i\frac{4\pi}{\omega}\hat{\boldsymbol{\sigma}}(\mathbf{k},\omega), \tag{4.19}$$

where $\hat{\mathbf{1}} = \delta_{ij}$ is the Kronecker delta (unit tensor), and where $\hat{\boldsymbol{\sigma}}(\mathbf{k},\omega)$ is the conductivity tensor. It is often convenient not to use $\hat{\boldsymbol{\sigma}}(\mathbf{k},\omega)$ but to use the *susceptibility tensor*, which reflects a linear dependence of the polarization of a dielectric medium on the present electric field, $\hat{\boldsymbol{\alpha}}(\mathbf{k},\omega) = i\omega^{-1}\hat{\boldsymbol{\sigma}}(\mathbf{k},\omega)$. If the dielectric tensor in the medium depends on the frequency of the wave ω, the medium is called *dispersive*. When it depends on both, $\mathbf{k}$ and ω, the term *spatially dispersive* medium is used (Melrose 1980).

The wave equation with a linear response can be written as

$$\left[\frac{c^2}{\omega^2}(\mathbf{k}\mathbf{k} - \hat{\mathbf{1}}) + \hat{\boldsymbol{\epsilon}}\right]\cdot\mathbf{E} = 0, \tag{4.20}$$

which is often written as

$$\left[\hat{\boldsymbol{\Lambda}} + 4\pi\hat{\boldsymbol{\alpha}}\right]\cdot\mathbf{E} = 0, \tag{4.21}$$

where the Maxwell tensor $\widehat{\mathbf{\Lambda}}$,

$$\widehat{\mathbf{\Lambda}} = \widehat{\mathbf{1}} - N^2(\widehat{\mathbf{1}} - \mathbf{kk}), \tag{4.22}$$

describes wave propagation in the non-dispersive (classical) vacuum, while the influence of the plasma is included via the susceptibility tensor $\widehat{\boldsymbol{\alpha}}$. Here N is the refractive index, which in general is a complex number

$$N = \mathrm{Re}\{N\} + i\,\mathrm{Im}\{N\} = \frac{kc}{\omega}. \tag{4.23}$$

The complex nature of the refractive index means that the wave can also be damped. A result is then that the wave frequency becomes complex, $\omega = \omega - i\gamma/2$, in which case the wave's energy damps as $\exp(-\gamma t)$ (Melrose 1980). This approach allows to include higher-order processes (as, for example, Compton scattering) in the linear approximation of the plasma response. In this case, $\mathrm{Re}\{N\}$ is called the real refractive index, and $\mathrm{Im}\{N\}$ is named the extinction coefficient.

The *dispersion relation*, which determines the relation between the wave's frequency and the wave number (or, in other words, the refractive index), is given by

$$\mathrm{Det}\left(N^2(\widehat{\mathbf{1}} - \mathbf{kk}) + \widehat{\varepsilon}\right) = 0. \tag{4.24}$$

This expression is an eigenvalue problem, where the eigenvalues are the possible refractive indexes. The polarization normal modes are the corresponding eigenvectors. The solution of Equation 4.21, based on the obtained refractive indices, is the set of modes which can exist in the medium. For the response in a magnetoactive plasma consisting of electrons, two solutions are given by the transverse[6] electromagnetic waves, which propagate in the medium with different speeds, $v_{1,2} = c/N_{1,2}$ (see Mészáros 1992, for the detailed derivation). In the general case, the modes are elliptically polarized with the opposite direction of rotation. Under certain conditions, only circular or linear polarization is expected, which is discussed below.

Normal modes for a *cold plasma* in a strong magnetic field were obtained and discussed by, for example, Shafranov (1967), Ventura (1979), and Wang et al. (1988). This approximation, in which the thermal motion of the plasma electrons is ignored, is well-studied and has simple expressions for the normal modes. For many problems, the cold plasma limit provides a good description of the radiation field and its evolution. However, the present work targets a consistent joint simulation of the continuum and the cyclotron resonance. Near the resonance, the cold plasma approximation gives a significantly incorrect result already at temperatures of a few keV, due to the angle-dependent thermal broadening of the line (see Section 4.4.1). Moreover, in the case of low-rate accretion onto a magnetized neutron star, studied in Chapter 7, the overheated part of the atmosphere is expected to reach much higher temperatures of $kT_\mathrm{e}{\sim}30\,\mathrm{keV}$. Under these conditions, the redistribution of photons in the hot plasma can also significantly affect the high-energy continuum. In this way, the inclusion of thermal effects is crucial for the present work.

The normal polarization modes in the hot nonrelativistic ($kT_\mathrm{e} \ll m_\mathrm{e}c^2$) plasma were derived, for example, by Kirk (1980) and Nagel (1981a)

---

[6] Generally, the two waves are not purely transverse, with the polarization plane not strictly parallel to the wave vector (see, e.g., Dong & Yeh 2002). However, for high-energy radiation the magnetized plasma is a tenuous and weakly-dispersive medium, such that electromagnetic waves are essentially transverse (Garasev et al. 2016).

including first-order thermal and quantum corrections. The modes appropriate for a mildly relativistic or relativistic plasma were discussed, for example, by Pavlov et al. (1980), Bussard et al. (1986), and Garasev et al. (2016). Mészáros (1992) provides a comprehensive overview of some of these approaches for both relativistic and nonrelativistic cases. In this thesis, the normal modes for the hot nonrelativistic plasma are used (later, with the inclusion of the polarized vacuum effect; see Section 4.3.2). They provide a sufficient description of the cyclotron resonance. However, their limitations and possible deviations between the results presented below and those found when using a fully relativistic treatment will be mentioned in Section 6.4.

The exact form of the polarization modes is crucially dependent on the dielectric tensor of the medium. In turn, the components of the dielectric tensor are governed by the photon–electron interactions in the plasma. This connection is represented by the relation between the susceptibility tensor $\widehat{\boldsymbol{\alpha}}$ and the forward-scattering amplitude tensor (see, e.g., Mészáros 1992)

$$\widehat{\boldsymbol{\alpha}} = \frac{1}{4\pi}\left(\frac{\omega_{\rm pe}}{\omega}\right)^2 \widehat{\boldsymbol{\Pi}}, \tag{4.25}$$

where $\widehat{\boldsymbol{\Pi}}$ is a dimensionless tensor given by the forward-scattering amplitude divided by $-r_{\rm e}$, where $r_{\rm e}$ is the classical electron radius. The exact form of the scattering amplitude will be given in Section 4.4.1, together with a discussion of the derivation of the Compton scattering cross sections.

It is important to set the basis, in which the polarization vectors and the scattering amplitude tensor are written. As the right choice of the coordinate system can significantly simplify the form of the solution and its search for the certain task, a few coordinate systems are used throughout this chapter. The main coordinate system used here and, consequently, for the radiative transfer, is chosen to be a right-handed one, with the z-axis pointing along the external magnetic field direction, $\mathbf{B}$ (see Figure 4.2). The photon (wave) propagation vector, $\mathbf{k}$, is defined by the polar angle to the magnetic field, θ, and the azimuthal angle, ϕ. This coordinate system is appropriate for the radiative transfer calculation. However, it is more convenient to obtain the expressions for normal modes and scattering amplitude in a corresponding *rotating* coordinate system. This system has the same z-axis, but two other coordinates defined as

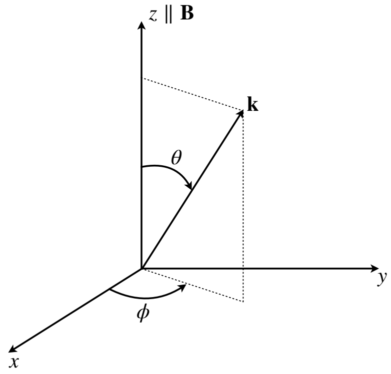

Figure 4.2: The main coordinate system for photon propagation used throughout the present work.

$$e_{\pm} = e_x \pm i e_y. \tag{4.26}$$

Then the vectors for polarization modes $j = 1, 2$ are given by

$$\mathbf{e_p} = (e_+, e_-, e_z), \tag{4.27}$$

where $p = 1, 2$ for *extraordinary* and *ordinary* modes, respectively. When using the rotating coordinate systems and applying the dipole approximation, the only non-zero elements of the scattering amplitude tensor are its diagonal components, Π_+, Π_-, and Π_z (Nagel 1981a). The normal mode vectors can then be defined in rotating coordinates as (Mészáros 1992)

$$e^p_{\pm} = 2^{-1/2} C_p \left[K_p \cos\theta \pm 1\right] \exp(\mp\phi), \tag{4.28}$$

and

$$e^p_z = C_p K_p \sin\theta, \tag{4.29}$$

with

$$C_p = (1 + K_p^2)^{-1/2}, \tag{4.30}$$

The parameter related to the ellipticity of the normal modes is given by

$$K_p = b\left[1 + (-1)^p (1 + b^{-2})^{1/2}\right]. \tag{4.31}$$

The expressions for the electric vector of the normal modes depend only on the parameter b, which is defined by the scattering amplitude and the angle of propagation to the magnetic field

$$b = \frac{2\cos\theta}{\sin\theta^2} \frac{\Pi_+^f - \Pi_-^f}{2\Pi_z^f - \Pi_+^f - \Pi_-^f}, \tag{4.32}$$

where "f" denotes an averaged quantity over the electron distribution. The elements of the forward-scattering matrix here are averaged over the one-dimensional Maxwellian distribution of electrons along the B-field lines (see Section 4.4.1). The ellipticity parameter K_p can be better understood by introducing a coordinate system (x', y', z') with the z'-axis aligned with the photon's wave vector $\mathbf{k}$ (see Figure 4.3). In this case, K_p is given by the aspect ration, $E_{x'}/E_{y'}$, of an ellipse that the polarization vector (the electric vector $\mathbf{E}$ of the wave) draws during its oscillation. In this case, the extraordinary mode is usually defined as the right-hand elliptically polarized wave with $|K_1| \ll 1$, while the ordinary mode is the left-hand one with $|K_2| \gg 1$ (Pavlov & Shibanov 1979). In this way, the polarization vectors of the ordinary and extraordinary modes oscillate mainly in the $(\mathbf{B}, \mathbf{k})$-plane and perpendicularly to it, respectively. This definition is illustrated by Figure 4.3 and assumed for now, although it will be questioned in Section 4.3.4.

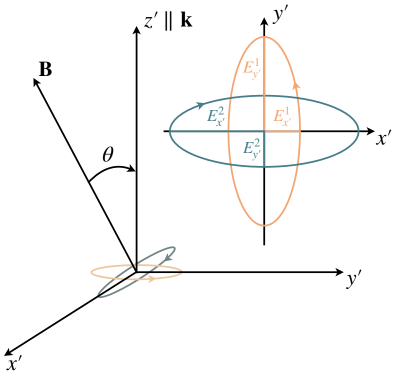

Figure 4.3: The coordinate system used for the definition of the normal modes ellipticity. Figure 1 (left panel) from Sokolova-Lapa et al. (2023). CC BY-4.0 – ESO.

The rotational direction of the polarization vector plays a crucial role in the ability of the wave to interact with the plasma electrons.The polarization vector of the extraordinary mode co-rotates with electrons in their motion around the magnetic field lines, allowing the wave to resonate at the cyclotron frequency. In a cold plasma and the absence of damping, the ellipses of two polarization modes are of equal shape, but perpendicular to each other. However, thermal effects, the influence of the virtual plasma due to the vacuum polarization, and dissipation will significantly alter this picture.

4.3.2 *Vacuum Polarization*

The propagation of photons in very strong magnetic fields is influenced by the so-called vacuum polarization. This is due to the production of virtual electron–positron pairs (see, e.g., Adler 1971; Gnedin et al. 1978; Meszaros & Ventura 1979). This virtual plasma, similar to a real one, leads to a deviation of the "classical vacuum" dielectric tensor from unity and influences the refractive index of the medium. Photon interactions with virtual pairs result in the birefringence of the vacuum. The normal modes in the polarized vacuum, without the influence of the plasma, are linear and strictly orthogonal to each other, with polarization vectors lying in the $(\mathbf{B}, \mathbf{k})$-plane (*parallel* mode) and perpendicular to it (*perpendicular* mode), except for the direction of photon propagation parallel to the magnetic field. The linearity of the modes results from the equality of the virtual charges, which are involved in the opposite rotation in the strong magnetic field.

The presence of the real thermal electrons induces an ellipticity of the modes and, under certain conditions, their departure from the orthogonality. The contribution of the polarized vacuum to the dielectric tensor competes with the contribution of the magnetoactive plasma. If $B < B_{\text{crit}}$, the plasma $\hat{\boldsymbol{\alpha}}^{(p)}$ and vacuum $\hat{\boldsymbol{\alpha}}^{(v)}$ susceptibilities can be added linearly, resulting in the total dielectric tensor (Meszaros & Ventura 1979; Mészáros 1992)

$$\hat{\boldsymbol{\epsilon}} := \hat{\mathbf{1}} + 4\pi\, [\hat{\boldsymbol{\alpha}}^{(p)} + \hat{\boldsymbol{\alpha}}^{(v)}]. \tag{4.33}$$

The importance of the plasma and vacuum effects on the polarization vectors of the normal modes and the photon–electron interactions in the medium depends mainly on the particle density of the real electrons, the strength of the magnetic field, and the energy of the considered photons. As suggested by Wang et al. (1988), the relative contribution of these effects can be estimated by introducing the ratio of the parameters $w = (\omega_{\text{pe}}/\omega)^2$ and $\delta_{\text{V}} = (1/45\pi)\alpha(B/B_{\text{crit}})^2$,

$$\frac{w}{\delta_{\text{V}}} = \frac{45\pi}{\alpha_{\text{F}}} \left(\frac{\omega_{\text{pe}}}{\omega}\right)^2 \left(\frac{m_{\text{e}}c^2}{E_{\text{cyc}}}\right)^2, \tag{4.34}$$

where α_{F} is the fine structure constant. If $w/\delta_{\text{V}} < 1$, the vacuum polarization governs the photon polarization. The opposite case, $w/\delta_{\text{V}} > 1$, corresponds to the dominance of the magnetized plasma response. However, if $w/\delta_{\text{V}} \approx 1$, it is important to consider both effects. The occurrence of these latter circumstances is discussed in more detail in the following sections. In general, the increase of the electron density will lead to a greater role of the magnetized plasma effect. On the other hand, the higher the magnetic field and photon energy, the more vacuum effects come into play.

Practically, the effect of the vacuum polarization can be taken into account in the expressions for the normal modes by introducing a correction to the Π_z element in the denominator of the b-parameter (Meszaros & Nagel 1985a; Kirk 1980),

$$b = \frac{2\cos\theta}{\sin\theta^2} \frac{\Pi_+^f - \Pi_-^f}{2(\Pi_z^f - 3\sigma_V w^{-1}) - \Pi_+^f - \Pi_-^f}, \tag{4.35}$$

which in the limit of $w/\delta_{\text{V}} \ll 1$ converges toward the pure plasma case (Equation 4.32).

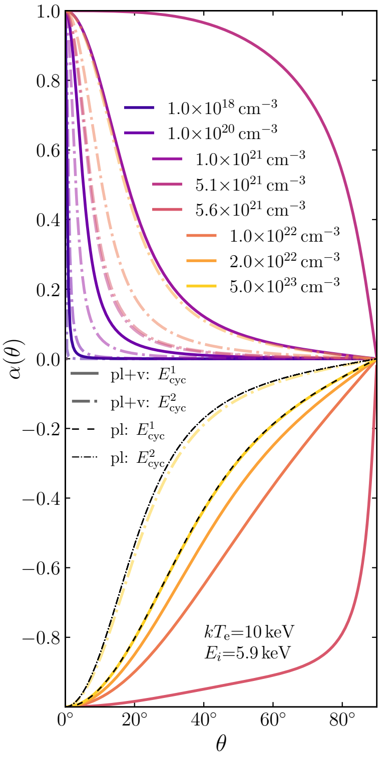

Figure 4.4: Ellipticity of the polarization ellipses, $\alpha(\theta)$, depending on the angle of propagation with respect to the magnetic field θ, shown for various electron number densities n_{e} for a normal wave of $E_i = 5.9\,\text{keV}$. The medium is a warm magnetized plasma, $kT_{\text{e}} = 10\,\text{keV}$, with an external magnetic field corresponding to the $E_{\text{cyc}} = 20\,\text{keV}$ ($B \approx 1.7 \times 10^{12}\,\text{G}$, thick solid colored lines) and $E_{\text{cyc}} = 60\,\text{keV}$ ($B \approx 5.2 \times 10^{12}\,\text{G}$, thick dash-dotted colored lines). All colored (thick) lines include the effect of vacuum polarization, while black (thin) lines are obtained for the pure real plasma case.

4.3.3 *Ellipticity of the Normal Modes*

The type of polarization which is acquired by the normal modes during the propagation in the medium, that is, generally elliptical, circular, or linear, is conveniently described in terms of the ellipticity

$$\alpha = -b^{-1}\left[1 + (1 + b^{-2})^{1/2}\right]^{-1}. \tag{4.36}$$

The ellipticity is obviously closely connected to the parameter K_p. However, as for the extraordinary mode $E_{x'}$ is the semi-minor and $E_{y'}$ is the semi-major axis and vice versa for the ordinary mode, $\alpha = K_1 = -K_2^{-1}$. Here, only the real part of the ellipticity parameter is considered, which is a fair approximation for most of the cases, except for the special situation that occurs at some critical values of the plasma parameters for a very narrow range of frequencies and photon angles, at which the real part of the refractive index turns zero, $\mathrm{Re}\{N_1 - N_2\} = 0$, accompanied by $K_p = \pm i$ (Soffel et al. 1983; Ho & Lai 2003, see also Section 4.3.4).

Figure 4.4 shows the ellipticity of the polarization ellipses of the normal modes for a warm and highly magnetized plasma for various values of the electron number density and two different values of the magnetic field strength, $B \approx 1.7 \times 10^{12}\,\mathrm{G}$ ($E_{\mathrm{cyc}} = 20\,\mathrm{keV}$) and $B \approx 4.3 \times 10^{12}\,\mathrm{G}$ ($E_{\mathrm{cyc}} = 50\,\mathrm{keV}$). The electron number density and the magnetic field clearly have a crucial impact on the polarization of the normal waves, as they are competing for the dominance of the real and virtual plasma. For the moderate magnetic field, corresponding to $E_{\mathrm{cyc}} = 20\,\mathrm{keV}$ and a low electron number density of $n_{\mathrm{e}} = 10^{18}\,\mathrm{cm}^{-3}$ (dark solid blue line in Figure 4.4), which translates into density $\rho \approx 1.7 \times 10^{-2}\,\mathrm{g\,cm}^{-2}$, the propagation of the normal waves is dominated by the polarized vacuum. Since the density of negative and positive charges induced is equal, the waves are linearly polarized and $\alpha \to 0$ for almost all θ, except for the direction close to the magnetic field, $\theta \approx 0^\circ$, where the waves become circularly polarized. As the density is increased, the wave propagation is disturbed by the presence of the real electrons and the polarization becomes elliptical. In the narrow region of the electron number density values (colored solid curves corresponding to $E_{\mathrm{cyc}} = 20$ keV and $n_{\mathrm{e}} = 0.5 \times 10^{22}\,\mathrm{cm}^{-3}$, $n_{\mathrm{e}} = 0.6 \times 10^{22}\,\mathrm{cm}^{-3}$ on Figure 4.4), specific for the chosen magnetic field, the polarization of the modes is close to circular for a large range of propagation angles. This behavior corresponds to the proximity of the so-called *vacuum resonance*, where the effects of the magnetized plasma and polarized vacuum cancel each other out. The normal modes are circularly polarized near the vacuum and cyclotron resonances, as at these points the vacuum and the plasma enforce linear polarization in a mutually orthogonal direction (Lai & Ho 2003a). Further increasing the density suppresses the influence of the polarized vacuum and brings it to the pure (real) plasma case, as determined by the b-parameter given by Equation 4.32 (black thin dashed line). For the higher magnetic field, corresponding to $E_{\mathrm{cyc}} = 50$ keV, the modes deviate more slowly from the linear case due to the enhanced effect of the vacuum polarization. The small region of the electron number densities at which the waves are close to the circular polarization is not resolved here. It is seen that in this case, even at $n_{\mathrm{e}} = 1 \times 10^{24}\,\mathrm{cm}^{-3}$ the polarization modes are still affected by the virtual plasma.

The ellipticity parameter $\alpha(\theta)$ is shown for a set of different photon energies E_i in Figure 4.5. For energies far away from the cyclotron resonance at $E_{\mathrm{cyc}} = 20\,\mathrm{keV}$, the modes are linearly polarized at almost all angles, except for the direction longitudinal to the magnetic field, where the polarization is again circular. Closer to the cyclotron resonance, $E_i = 0.1$–$10\,\mathrm{keV}$, the modes become elliptically polarized, approaching a significant fraction of the circular polarization at energies close to the vacuum resonance (the solid light-green curve corresponds to the dark-pink solid curve in Figure 4.4). The ellipticity is shown for two different electron temperatures. The lower temperature, $kT_{\mathrm{e}} = 0.1\,\mathrm{keV}$, reproduces the case of the cold plasma approximation (see, e.g., Meszaros & Ventura 1979). The deviation of the cold plasma from the hot plasma case is not very pronounced here. This is because thermal effects influence the region near the cyclotron resonance the most, that was consciously omitted in the current discussion. However, a deviation of the normal modes ellipticity in the warm plasma from the cold plasma case is also noticeable close to the vacuum resonance ($E_i = 5.5$, $5.9\,\mathrm{keV}$). Both resonances must be considered with more care and are best discussed in the context of the

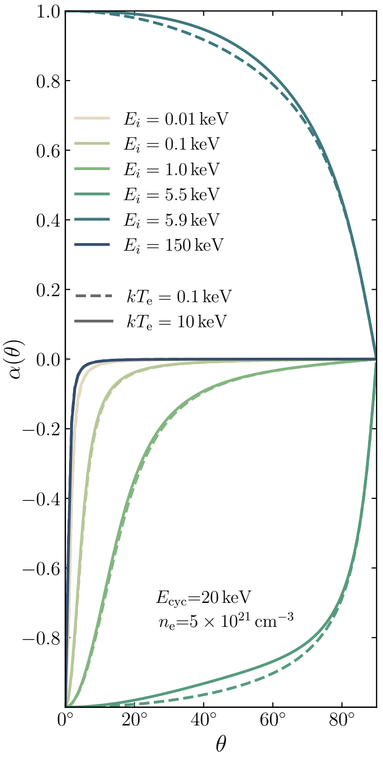

Figure 4.5: Same as in Figure 4.4, but here the ellipticity $\alpha(\theta)$ is shown for waves propagating at different frequencies. The magnetic field is fixed to the value, corresponding to the $E_{\mathrm{cyc}} = 20$ keV ($B \approx 1.7 \times 10^{12}\,\mathrm{G}$), and the electron number density is $n_{\mathrm{e}} = 5 \times 10^{21}\,\mathrm{cm}^{-3}$. The ellipticity parameter is calculated for two different electron temperatures in the plasma: $kT_{\mathrm{e}} = 0.1\,\mathrm{keV}$ ("cold plasma" limit, dashed lines) and $kT_{\mathrm{e}} = 10\,\mathrm{keV}$ (solid lines).

cross sections for the photon–electron interactions. I therefore defer this discussion to Section 4.4.1.

4.3.4 *Mode Ambiguities*

In this section, I will finalize the discussion of the polarization modes that need to be considered for the radiative processes and radiative transfer calculation in a highly magnetized dispersive medium. Here, I will address the question of how polarization can be included in the radiative transfer equation discussed in Section 4.2.

The rotation of the polarization vector during the wave propagation in highly magnetized plasma in general means that even in a homogeneous plasma the cross sections, which are highly polarization-dependent, vary along a light ray. However, as long as a wave experiences many rotations of the polarization vector between subsequent scattering events, the radiation field can be described in terms of two normal modes (Gnedin & Pavlov 1974). This condition is known as *Faraday depolarization* and requires

$$|\,\mathrm{Re}(N_1 - N_2)| \gg \mathrm{Im}(N_1 + N_2), \tag{4.37}$$

where $N_{1,2}$ are the refractive indices of two normal modes. Under this condition, the interaction of the modes with plasma electrons can be described by the cross sections presented in Section 4.4. Then radiative transfer can be calculated for two polarization modes coupled via scattering. Otherwise, it has to be treated in terms of four coupled Stokes parameters.

Mode Collapse

In general, the condition of Faraday depolarization is satisfied for the X-ray radiation in the vicinity of accreting highly magnetized neutron stars. Normal modes exhibit some minor non-orthogonality due to damping and Doppler effect, but the imaginary part of their refractive indices remains small, and their ellipticity is well described only by the real part (see Section 4.3.3). However, this is not the case for two critical points, which appear near the vacuum and the cyclotron resonance under certain critical values of the plasma parameters and angles of photon propagation (Soffel et al. 1983). As mentioned previously, these points are characterized by

$$K_1(b) = K_2(b) = b = \pm i, \tag{4.38}$$

which results in $\mathrm{Re}\{N_1 - N_2\} = 0$.

The local values of B, n_e, and kT_e define the critical values of photon energy and propagation angle, $(E_\mathrm{c}, \theta_\mathrm{c})$, also known as the *mode collapse point*, at which the condition Equation 4.38 is met (see, e.g., Kirk 1980; Soffel et al. 1983). This situation occurs because of the dissipation effects, acting on top of the cancellation of the vacuum and the plasma effects. The damping rate near the energy, corresponding to the vacuum and cyclotron resonances $E_\mathrm{c} \approx E_\mathrm{V}, E_\mathrm{cyc}$, denotes the critical angle θ_c at which $b = \pm i$ (Ho & Lai 2003). At the mode collapse points, the polarization modes are strongly non-orthogonal and their designation in terms of the ordinary and extraordinary waves becomes obsolete as both modes coincide (see, e.g., Pavlov & Shibanov 1979). This phenomenon is not specific to the high-energy emission from the neutron stars and is also

For protons in a fully ionized plasma, the mode collapse point also occurs near the proton cyclotron resonance, which should be taken into account if the respective energy band is considered (Zane et al. 2000; Bulik & Pavlov 1996).

known for atomic resonances under the influence of collisional damping (Soffel et al. 1983).

Soffel et al. (1983) studied this problem on the Riemannian surfaces formed by the real and imaginary parts of the refractive indices in the (E, θ)-plane. They noted that the unique designation of polarization modes over the full range of photon energies and angles (as, for example, given in Section 4.3.1) is impossible if the mode collapse point is met. In turn, the breakdown of the normal mode formalism (and Faraday depolarization due to $\mathrm{Re}\{N_1 - N_2\} = 0$) calls for a description of the problem in Stokes parameters (see, e.g., Garasev et al. 2016, for a formulation of the problem). The problem of these discontinuities in the normal modes definition was, among others, also discussed by Pavlov et al. (1980), Kirk (1980), and Wang et al. (1988). However, the range of energies and angles directly affected by the mode collapse is very small compared to the full range typically considered in the simulations. For this reason, the normal mode description is still widely used in the works mentioned above (as weel as, e.g., by Soffel et al. 1985; Meszaros & Nagel 1985a). In this thesis, I follow the same line and use the normal mode formalism.

Mode Conversion

A different problem with the mode definition occurs due to the change of the vacuum and plasma domination across the resonances. As was mentioned before, the resonances at E_V and E_cyc are in general characterized by circular polarization, which follows from $b = 0$ and $K_p = \pm 1$. The plasma and the vacuum induce different properties of the normal waves below and above E_V, which does not allow to enforce the same mode definition of the ordinary and extraordinary modes as used, for example, in Section 4.3.1. For a chosen n_e, B, and kT_e, it can be seen as a problem of the continuity of the refraction indices of the polarization modes as a function of photon energy (Kirk 1980). While the refractive indices of the normal modes do not coincide, unless the condition for the mode collapse point is met (see Equation 4.38), their cross sections have the same values at the resonances. The discontinuous refractive indices result in sharp resonance-like features in the cross sections at E_V (see, e.g., Ventura et al. 1979). In case the refractive indices are continuous functions of photon energy, the modes significantly change their opacity across the resonance (e.g., Meszaros & Nagel 1985a). This problem will be addressed again in the discussion of the cross sections in Section 4.4.1.

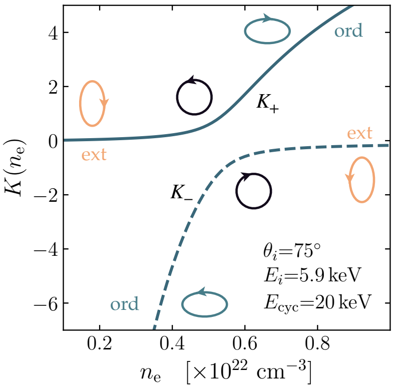

Figure 4.6: Mode conversion due to vacuum resonance through the dependency of the ellipticity of the normal modes K from the electron number density n_e for a photon of energy $E_i = 5.9\,\mathrm{keV}$, propagating under the angle $\theta_i = 75°$ to the magnetic field, $B \approx 1.7 \times 10^{12}\,\mathrm{G}$. The rotation of the ellipses at higher densities correspond to the mode definition in Figure 4.3. This case represents the adiabatic mode propagation, while the non-adiabatic case would show a jump between the curves at the resonance density (at about the center of the figure). After Figure 1 of Lai & Ho (2003a). Figure 1 (right panel) from Sokolova-Lapa et al. (2023). CC BY-4.0 – ESO.

The problem of the mode definition becomes more striking if one considers the propagation of a photon of a certain energy in the atmosphere of a neutron star or inside an accretion column, where some density gradient is expected along the path of the photon. For example, the photon can pass from a high-density region, where the medium response is dominated by the real plasma and the photon energy is below the resonance value, $E < E_\mathrm{V}$, to a low-density vacuum-dominated region, where $E > E_\mathrm{V}$. At the"resonant" density, where $E = E_\mathrm{V}$, the classically defined plasma extraordinary ($|K_1| \ll 1$) and ordinary ($|K_2| \gg 1$) waves will acquire left-hand and right-hand polarization, respectively. This makes the definition given in Section 4.3.1 internally inconsistent. Lai & Ho (2002) noted that if the density gradient is smooth, polarization states will evolve adiabatically above a certain photon energy (see, also, the related discussion in Özel 2003), providing the channel for mode conversion, similar to the Mikheyev-Smirnov-Wolfenstein mechanism for neutrino oscillations (see, e.g., Haxton 1995). They suggested defining two modes based on the fixed helicity as the plus-mode, which always has $K_+ > 0$, and the minus-mode, with $K_- < 0$. In this case, the orientation of the polarization ellipse of the plus-mode behaves as the extraordinary mode's one before the vacuum resonance and as the ordinary mode's one after that. The opposite is true for the minus-mode (see Figure 4.6). Both modes keep their original direction of the polarization vector rotation in this case, which also corresponds to the continuous behavior of the refractive indices. In general, however, the adiabatic condition might not be fulfilled, and photons can undergo partial mode conversion with some probability of the non-adiabatic jump (van Adelsberg & Lai 2006). This regime is also know as "linear mode coupling" (Zhelezniakov et al. 1983; Lai & Ho 2003b).

I address the cases of continuous and discontinuous refractive indices discussing the corresponding Compton scattering cross sections (see Section 4.4.1) and results of the radiative transfer simulations in Chapter 5. Chapter 5 also includes some examples of the radiative transfer simulations in an inhomogeneous medium for fully adiabatic and fully non-adiabatic mode conversion. Implementing the jump condition for the partial mode conversion is challenging for the Feautrier method used here for the radiative transfer solution (see Section 4.5), and thus will be studied elsewhere.

In the following, I use the notations "mode 1" and "mode 2" for the two polarization modes, to avoid the confusions in the case when the vacuum resonance and mode conversion are present. In the absence of vacuum polarization, mode 1 and mode 2 correspond to the classically defined extraordinary and ordinary modes, respectively.

Although, the literature is not coherent in this choice. For example, terms "extraordinary" and "ordinary" modes were used for the mixed case of the vacuum and plasma effects by Meszaros & Nagel (1985a,b) and Soffel et al. (1985).

4.4 RADIATIVE PROCESSES

The response of the real plasma on the propagation of the electromagnetic wave is governed by the elementary radiative processes. Here, I proceed with the regime $\omega \gg \omega_{\rm cyc}$, such than only the radiative processes related to the interaction of photons with plasma electrons are considered. However, ions also enter the picture indirectly, via interactions with electrons. The radiative processes in the anisotropic magnetoactive medium are modified compared to the regular, non-magnetic case. One of the discussed alterations is the behavior of polarization vectors of the photon normal modes due to plasma and vacuum birefringence. In this respect, cross sections for all relevant processes need to be considered for each polarization mode separately. In addition, scattering involves a non-zero probability of mode conversion. The other crucial modification is the presence of the cyclotron resonance due to the quantization of electrons onto the Landau levels. For a typical plasma in an accretion column, the electrons are expected to remain primarily in the ground state (Wasserman & Salpeter 1980). Excitation of electrons to the higher Landau levels can happen via collisional and radiative processes. The collisional excitations are mainly efficient via ion–electron interactions (more precisely, proton–electron interactions, for the case of a purely hydrogen plasma, which is considered throughout this work). Collisions can happen due to the bulk or thermal motion of the particles. At field strengths of a few 10^{12} G as expected from highly magnetized accreting neutron stars, $B \gtrsim$ a few$\times 10^{12}$ G, the radiative decay time is shorter than the time between particle collisions even at high densities (Yahel 1979; Nagel & Ventura 1983; Harding & Daugherty 1991). This fact has a number of important consequences. First of all, in this case the resonant absorption and emission of a photon by the plasma electrons are correlated processes and have to be treated as scattering with partial redistribution (Hubeny & Mihalas 2014), which greatly complicates the numerical treatment. Secondly, under these conditions, collisional excitations mainly result in radiative decay and serve as a source of photons in the medium via *cyclotron emission*. The fact that an electron that was excited by thermal motion collisions undergoes radiative decay means that it cannot restore the local thermodynamic equilibrium. As the result, the level population, which is controlled by the radiative processes, is in general non-LTE, and Kirchhoff's law cannot be directly used to calculate the cyclotron emissivity (Nagel & Ventura 1983). Instead, it has to be related to the free-free absorption coefficient, which acquires a resonant part (see details in Section 4.4.2 below).

In this way, Compton scattering and free-free processes, both modified by the cyclotron resonance, determine the opacity and are mainly responsible for the formation of the radiation spectrum considered here. Due to the effect of the strong magnetic field, these processes are strongly anisotropic and depend on the energy and polarization of the photons, as well as on the density and temperature of the medium. In this section, I consider these processes in the nonrelativistic quantum-mechanical treatment, taking into account the polarization state, thermal electron motion, and vacuum polarization. However, the electron spin is neglected and only transitions between the ground and the first Landau levels are taken into account. Unfortunately, the full QED-based treatment of the radiative processes in a highly magnetized plasma (as done, for example, by Alexander et al. 1989), is beyond the scope of the present work as the result of the compromise between a realistic approximation and the tractability of the full task of the radiative transfer with the complex redistribution in the non-homogeneous media. Some possible consequences of these adopted simplifications are mentioned in Chapter 6. Section 4.4.1 describes the details of the Compton scattering in a highly magnetized plasma, studying the behavior of the cross sections for various plasma parameters. The free-free processes and the analog of Kirchhoff's law for the considered conditions are discussed in Section 4.4.2.

4.4.1 *Compton Scattering*

Compton Scattering is the most important mechanism for generating the spectral shape in the accretion channel near a highly magnetized neutron star. The reason is the significant energy and momentum transfer in photon–electron interactions and the very short radiative life time of the excited Landau levels. The drastic effect of the strong magnetic field onto scattering was demonstrated in the work of Canuto (1970), who obtained the expressions for the transverse and longitudinal propagation of photons with respect to the magnetic field. Canuto et al. (1971) presented the Thomson scattering opacities in a highly magnetized plasma for two polarization modes, using the quantum mechanical treatment for the angles parallel and perpendicular to the magnetic fields, and classical - for arbitrary angles of photon propagation. Later, Mészáros & Ventura (1978) included the effect of vacuum polarization for Thomson scattering cross sections. In the cold plasma approximation, the cross sections were also obtained and studied by Kaminker et al. (1982). The dramatic modification of the scattering of high-energy radiation, introduced by strong magnetic fields, $B \gtrsim 10^{12}\,\mathrm{G}$, became evident with the discovery of the first cyclotron line in the spectrum of Her X-1 by Truemper et al. (1978).

In the attempt to treat *inelastic* Compton scattering, the historical community efforts can be roughly divided into two directions. The first direction concentrated on the inclusion of the cyclotron resonance into the broadband cross sections for normal modes, focusing on the different types of damping in the medium. These works often aimed for consistent modeling of the continuum and the fundamental cyclotron line in the emergent spectra. The quantum mechanical treatment for the hot nonrelativistic plasma, with first-order relativistic corrections, was presented by Nagel (1981a), Nagel (1982), and Kirk & Meszaros (1980). Meszaros & Nagel (1985a) included the polarized vacuum effect to the cross sections derived by Nagel (1981a). These cross sections were used for spectral modeling by Meszaros & Nagel (1985a), Meszaros & Nagel (1985b), Meszaros & Riffert (1988), and Bulik et al. (1995). Relativistic corrections and spin-flip transitions were considered by Pavlov et al. (1980). Using a similar formalism as Nagel (1981a), Garasev et al. (2016) derived expressions for the scattering matrix elements for the case of a mildly-relativistic plasma, including the effect of vacuum polarization. The full QED treatment for the hot plasma was done by Bussard et al. (1986) and adopted by Alexander et al. (1989) to model only the fundamental cyclotron line and continuum. The effect of *two-photon Compton scattering* was already included by Bussard et al. (1986) and later investigated by Alexander & Meszaros (1991) in more detail. In this process, an electron is excited to a Landau level $n > 1$ and then reaches the ground state by two subsequent de-excitations. Similar to regular (one-photon) Compton scattering, this is a second order process, $\propto \alpha_{\mathrm{F}}^2$, unlike *double Compton scattering*, where the two final photons are emitted simultaneously. Similarly, *two-photon cyclotron emission* can be considered (see, e.g., Alexander & Meszaros 1991). These multi-photons processes provide an additional mechanism for *photon splitting*, which converts a single hard photon to several soft photons.

Radiative transfer modeling of the broadband spectrum becomes more numerically challenging when higher cyclotron harmonics and higher-order processes need to be considered. The second line of effort in cyclotron processes modeling aimed exactly at this description of the detailed complex physics of cyclotron resonance within the QED framework, but mostly assumed simple normal modes for the pure vacuum case. This approach was widely used to obtain more precisely the structure and shape of the cyclotron harmonics by modifying the input continuum in a thin layer of the medium. The relativistic Compton and Thomson scattering cross sections, including higher harmonics, were derived by Herold (1979) for the final Landau level $n = 0$. Daugherty & Harding (1986) obtained expressions that also include the higher final states, resulting in multi-photon emission. With a similar, QED-based treatment, but with a corrected electron wave function (see detailed discussion by Gonthier et al. 2014), the cross sections were derived by Sina (1996). The numerical implementation of these expressions was later adopted by Araya & Harding (1999), Schönherr et al. (2007a), Schwarm et al. (2017a,b), and Kumar et al. (2022) for Monte Carlo simulations of cyclotron lines. Similar cross sections were also obtained by Mushtukov et al. (2016).

Here, I follow the approach of Nagel (1981a) and Meszaros & Nagel (1985b), considering the quantum mechanical derivation of the differential and total Compton scattering cross sections, which takes into account thermal motion of electrons in a hot plasma (at $kT_{\mathrm{e}} \ll m_{\mathrm{e}}c^2$). This approach includes the first-order recoil and relativistic corrections, but neglects the electron spin and makes use of the assumption that the initial and final state of an electron (before and after scattering) is the ground one.

Scattering Matrix Amplitudes

Resonant Compton scattering of a thermal electron off a photon is represented by the five Feynman diagrams shown in Figure 4.7. A nonrelativistic electron is described by the wave function $|0, s, p\rangle$, where p is the electron momentum along the magnetic field lines, $p \equiv p_z$ (see Figure 4.2) and where s is the quantum number of the guiding center. As was mentioned before, the initial and final Landau level is a ground state, $n = n' = 0$. Here and after, primed quantities represent the final state. In natural units ($\hbar = c = m_{\rm e} = 1$), the scattering amplitude for a photon with initial frequency ω and polarization vector $\mathbf{e}$ can be obtained in the form (Mészáros 1992)

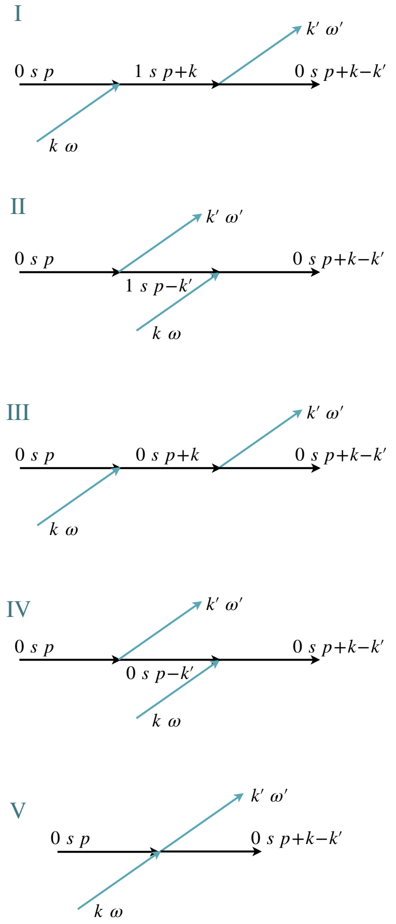

Figure 4.7: Feynman diagrams for one-photon scattering in a hot nonrelativistic plasma. Before and after scattering electron is in the ground state. After Figure 4.3.1 of Mészáros (1992).

$$\begin{aligned}\langle f|\,T\,|i\rangle &= \frac{2\pi\alpha_{\rm F}}{\sqrt{\omega\omega' L^3}}\,\langle \mathbf{e}'|\,\mathbf{\Pi}\,|\mathbf{e}\rangle \\ &= \frac{2\pi\alpha_{\rm F}}{\sqrt{\omega\omega' L^3}}\left(\Pi_+ e'^*_+ e_+ + \Pi_- e'^*_- e_- + \Pi_z e'^*_z e_z\right),\end{aligned} \tag{4.39}$$

where the components of the scattering matrix are written, same as in Section 4.3, in rotating coordinates, and where L^3 is the normalization volume. The components are

$$\begin{aligned}\Pi_+ &= 1 - \frac{\omega_{\rm cyc}}{\omega' + \omega_{\rm cyc} - pk' + k'^2/2},\\ \Pi_- &= 1 + \frac{\omega_{\rm cyc}}{\omega' - \omega_{\rm cyc} - pk' - k'^2/2},\\ \Pi_z &= 1 + \frac{(p+k/2)(p+k-k'/2)}{\omega - pk - k^2/2} \\ &\quad - \frac{(p-k'/2)(p-k'+k/2)}{\omega' - pk' + k'^2/2},\end{aligned} \tag{4.40}$$

where k is the photon wave vector. The contribution of the diagrams presented in Figure 4.7 can be clearly seen in this form of the scattering matrix components (Kirk & Meszaros 1980). The unity in each component arises from the so-called seagull diagram V. The second terms of Π_+ and Π_- result from diagrams I and II, respectively, where the electron in the intermediate state is excited to the level $n = 1$. Diagrams III and IV contribute the second and third terms of Π_z component.

Differential Cross Sections

With the help of Fermi's Golden Rule, the scattering rate now can be written as

$$w_{i,f} = \frac{2\pi}{\hbar}|\,\langle f|\,T\,|i\rangle\,|^2 \rho_f \delta(E_i - E_f), \tag{4.41}$$

where $\rho_f = L^3\omega'^2/(2\pi c)^3\hbar$ is the density of the final photon state. The delta function ensures energy conservation in the scattering event. The differential scattering cross section now can be obtained by dividing

Equation 4.41 by the incoming photon flux c/L^3 and then averaging over the nonrelativistic Maxwellian distribution $f(p)$ (Nagel 1982),

$$\frac{\mathrm{d}^2\sigma}{\mathrm{d}\omega'\mathrm{d}\Omega'}(\omega,\mathbf{k},\mathbf{e}\rightarrow\omega',\mathbf{k}',\mathbf{e}') \\ = r_\mathrm{e}^2\frac{\omega'}{\omega}\int \mathrm{d}p f(p)|\langle\mathbf{e}'|\mathbf{\Pi}|\mathbf{e}\rangle|^2\delta\left(\hbar\omega-\hbar\omega'+\hbar\Delta\omega\right), \quad (4.42)$$

where $\mathrm{d}\Omega = \sin\theta\mathrm{d}\theta\mathrm{d}\phi$ is the solid angle element, and the photon energy change is given by $\hbar\Delta\omega = (p^2-p'^2)/2m_\mathrm{e}$. For the chosen initial (ω,θ) and final (ω',θ') photons, there is only one initial electron momentum,

$$p_\mathrm{c} = m\frac{\Delta\omega}{\Delta k}+\frac{\hbar\Delta k}{2}, \quad (4.43)$$

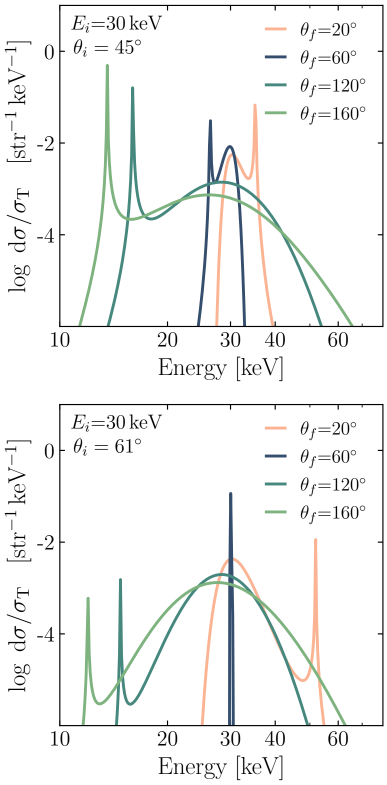

Figure 4.8: Differential scattering cross section normalized to the Thomson value for the photon of mode 1 with initial energy $E_i = 30$ keV and initial propagation angle $\theta_i = 45°$ (*top*) and $\theta_i = 61°$ (*bottom*), shown for a set of final angles. The final state is mode 2. The magnetic field strength corresponds to $E_\mathrm{cyc} = 20$ keV ($B \approx 1.7\times10^{12}$ G), the electron temperature $kT_\mathrm{e} = 10$ keV, and the electron number density $n_\mathrm{e} = 10^{23}\,\mathrm{cm}^{-3}$.

which satisfies energy and momentum conservation, with $\Delta k = (\omega'\cos\theta' - \omega\cos\theta)/c$. Then averaging over the electron momentum distribution and azimuthal angle results in (Nagel 1981a)

$$\frac{\mathrm{d}^2\sigma}{\mathrm{d}\omega'\mathrm{d}\Omega'}(\omega,\mathbf{k},\mathbf{e}\rightarrow\omega',\mathbf{k}',\mathbf{e}') = r_\mathrm{e}^2\frac{\omega'}{\omega}\frac{m}{|\Delta k|}f(p_\mathrm{c})|\langle\mathbf{e}'|\mathbf{\Pi}|\mathbf{e}\rangle|^2 \\ = r_\mathrm{e}^2\frac{\omega'}{\omega}\frac{m}{|\Delta k|}f(p_\mathrm{c})\left(|\Pi_+e'_+e_+|^2+|\Pi_-e'_-e_-|^2+|\Pi_ze'_ze_z|^2\right). \quad (4.44)$$

It is important to note that the forward-scattering matrix elements, Π^f_+, Π^f_-, Π^f_z, that enter the b-parameter for polarization modes (see Equation 4.32 and Equation 4.35), have to be obtained from Equation 4.40 by assuming $\omega' = \omega$, $\theta' = \theta$ and integrating the elements over the Maxwellian distribution with included radiative damping, $\gamma_r = 2e^2\omega^2/3m_\mathrm{e}c^3$, to the denominators. The resulting integrals can be expressed via the plasma dispersion (also known as Faddeeva, or Kramp) function (Fried & Conte 1961), which has efficient numerical implementations (see, e.g., Gautschi 1970). The exact expressions are given by Equation 4.3.23 of Mészáros (1992).

The differential scattering cross section represents the probability that a photon with initial energy $\hbar\omega$ and polarization vector $\mathbf{e}$, which propagates in the direction $\mathbf{k}$, will acquire $\hbar\omega'$, $\mathbf{k}'$, and $\mathbf{e}'$ after the scattering event. In terms of the radiative transfer calculation, it gives the redistribution function for the case of partial redistribution, which requires a careful treatment for the radiative transfer calculation. Some examples of the differential scattering cross section for the parameters relevant for this work are shown in Figure 4.8.

Total Compton scattering cross sections

The total Compton scattering cross section now can be found via the optical theorem, which relates it to the forward scattering amplitude

$$\sigma_p = -4\pi r_\mathrm{e}\frac{c}{\omega}\left(\mathrm{Im}\left\{\Pi^f_+\right\}|e^p_+|^2 \right. \\ \left. +\mathrm{Im}\left\{\Pi^f_-\right\}|e^p_-|^2+\mathrm{Im}\left\{\Pi^f_z\right\}|e^p_z|^2\right). \quad (4.45)$$

This expression allows one to obtain the total scattering cross section for mode 2, $\sigma_2 = \sigma_{22}+\sigma_{21}$, and mode 1, $\sigma_1 = \sigma_{11}+\sigma_{12}$. The individual cross sections for scattering from one mode to another, σ_{11}, σ_{12}, σ_{21}, σ_{22} have to be found by the numerical integration of Equation 4.44.

The behavior of the total Compton scattering cross section in a highly magnetized plasma, with the influence of the polarized vacuum, dramatically depends on the magnetic field strength, the electron number density, and the temperature of the plasma. The top panel of Figure 4.9 illustrates the strong energy and angular dependency of the total scattering cross section for both polarization modes for low electron temperature, $kT_\mathrm{e} = 0.01\,\mathrm{keV}$, and high electron number density, $n_\mathrm{e} = 10^{25}\,\mathrm{cm}^{-3}$. Here, only mode 1 experiences resonant scattering, while mode 2 acquires the classical Thomson value of the cross section for transverse propagation to the magnetic field. This case exactly reproduces the cross sections for the cold plasma limit, as obtained, for example, by Ventura (1979).

With increased plasma temperature, $kT_\mathrm{e} = 6\,\mathrm{keV}$, (Figure 4.9, bottom panel), one can see a pronounced effect of the electron thermal motion on the shape of the cyclotron resonance. It depends dramatically on the angle of photon propagation with respect to the magnetic field. This is the result of the one-dimensional Maxwellian distribution due to the Landau quantization. By looking along the magnetic field direction, one observes the strongest Doppler broadening, which becomes less pronounced with the increasing angle to the field. Another pronounced effect is the appearance of cyclotron resonance in the cross sections of mode 2. Only at angles $\theta \approx 0^\circ$ and $\theta \approx 90^\circ$, the modes stay orthogonal. One can say that in the absence of vacuum polarization, the damping of mode 1 occurs due to the interaction with the real electrons, quantized in the strong magnetic field, that is, transverse to the global B-field component of the electric field. In this limit, mode 2 can resonate with electrons only if their thermal motion along the magnetic field lines is taken into account. In these cases of high density presented in Figure 4.9, the two modes directly correspond to ordinary and extraordinary plasma modes.

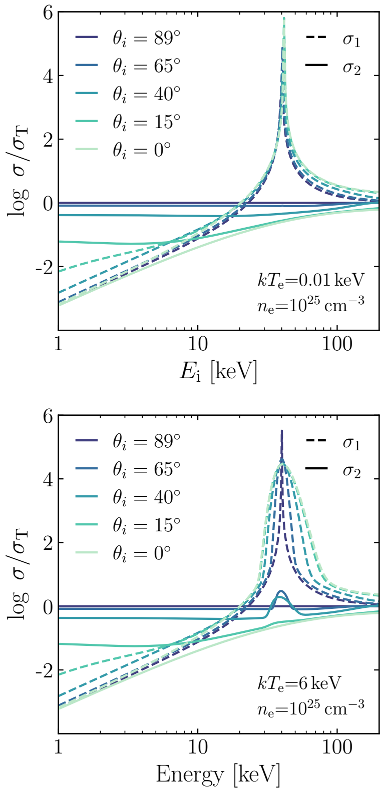

Figure 4.9: Total Compton scattering cross section magnetic field in a highly magnetized medium with high electron number, density $n_\mathrm{e} = 10^{25}\,\mathrm{cm}^{-3}$, for a set of initial photon propagation angles. The cyclotron energy is $E_\mathrm{cyc} = 40\,\mathrm{keV}$ ($B \approx 3.5 \times 10^{12}\,\mathrm{G}$), the electron temperature is $kT_\mathrm{e} = 0.01\,\mathrm{keV}$ (*top*) and $kT_\mathrm{e} = 6\,\mathrm{keV}$ (*bottom*). The dashed and dotted lines represent mode 1, and mode 2, respectively.

To illustrate the influence of the choice of polarization modes, Figure 4.10 presents the cross section for the same physical parameters as in Figure 4.9, but calculated with the pure vacuum polarization modes, that is, omitting the effects of a magnetized plasma. Here, as discussed before, both modes become resonant at the cyclotron energy. In addition, the angular dependency of mode 1 is greatly simplified, being fully isotropic in the low-energy continuum.

Figure 4.11 illustrates the situation for intermediate values of the electron number density for the mixed polarization modes, when both virtual and real plasma affect the scattering cross section. The vacuum resonance is seen here as a step in the cross section profile (at ∼4 keV for the parameters used in the top panel). This step denotes a switch of the domination of the magnetized plasma effects at low energies by the polarized vacuum at the energies above the vacuum resonance. The figure also shows how the position of the vacuum resonance changes with n_e. This choice of the polarization modes corresponds to the continuous behavior of the refractive indices with photon energy (see Section 4.3.4).

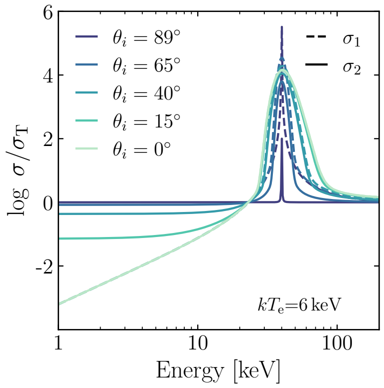

Figure 4.10: Same as in Figure 4.9 (bottom), but for the case of vacuum polarization modes. Curves for all angles for mode 1 are merged in continuum into one light green line.

The opposite case of the discontinuous behavior of the refractive indices of the modes is displayed in Figure 4.12 for the same parameters as in Figure 4.11 (top). The main difference between the cross sections is the appearance of the vacuum resonance as a sharp line-like feature and the asymmetric cyclotron resonance for both polarization modes in the discontinuous case. As suggested by Ventura et al. (1979) and Pavlov & Shibanov (1979), this form of cross sections can lead to the soft-energy absorption line-like features in the spectra of accreting neutron stars. Ho & Lai (2003) showed, however, that due to the expected inhomogeneity of the medium, it will more likely result in a broad depression region at soft energies. This problem will be addressed in Chapter 5.

Figure 4.13 displays angular dependency of the cross sections in polar coordinates for different photon energies for the four principal choices of polarization modes: pure plasma, pure vacuum, and two types of mixed polarization modes (for the continuous and discontinuous refractive indices), which will be used for modeling in Chapter 5.

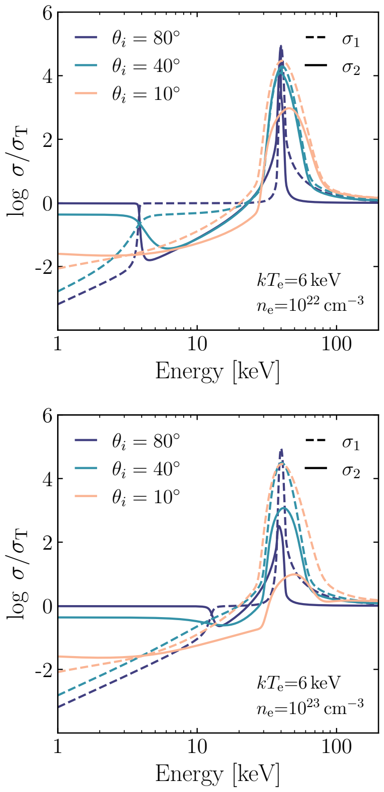

Figure 4.11: Same as in Figure 4.9, but for smaller number of angles and different values of electron number density. *Top:* $n_e = 10^{22}\,\mathrm{cm}^{-3}$, *bottom:* $n_e = 10^{23}\,\mathrm{cm}^{-3}$.

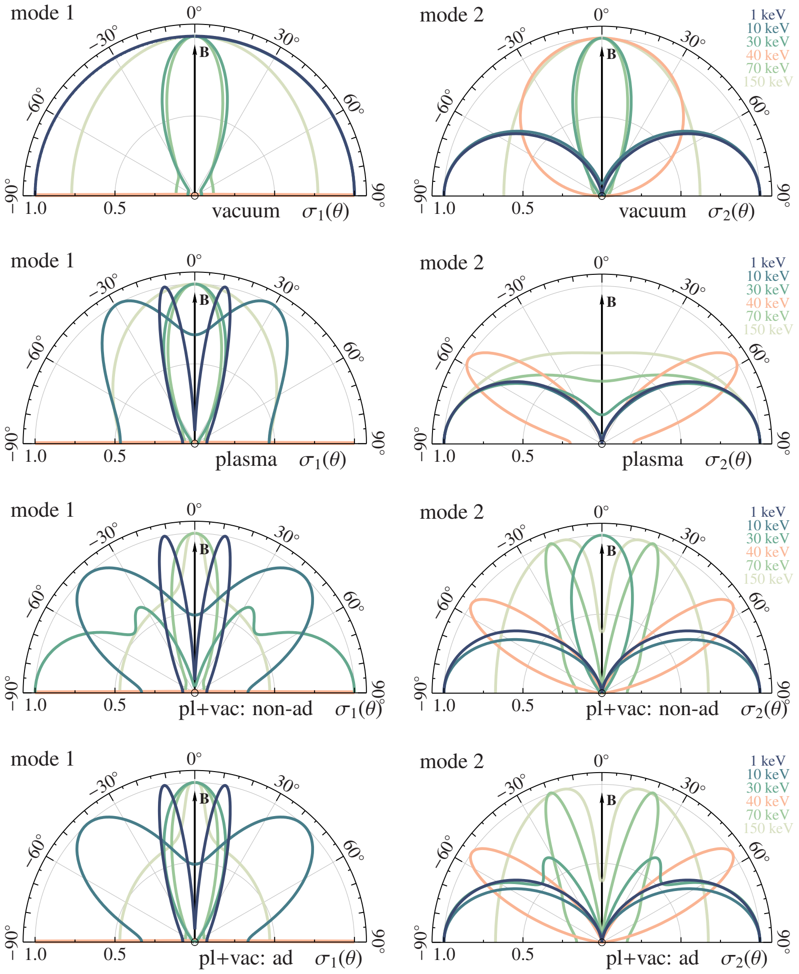

Figure 4.13: Dependency of the total Compton scattering cross sections for the two polarization modes on the angle (two columns) shown as polar diagrams for different photon energies. The cross sections are presented for $E_{\mathrm{cyc}} = 40\,\mathrm{keV}$ ($B \approx 3.5 \times 10^{12}$ G), $kT_e = 6\,\mathrm{keV}$, $n_e = 10^{23}\,\mathrm{cm}^{-3}$, for different types of the photon polarization modes, from top to bottom: for the vacuum, plasma, and mixed plasma and vacuum polarization modes, for the continuous and discontinuous refractive indices of the modes. The cross sections are normalized to the maximum value in each energy band and for each polarization independently.

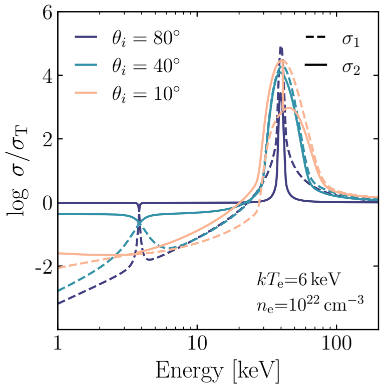

Figure 4.12: Same cross sections as in Figure 4.11 (top), but for discontinuous refractive index.

4.4.2 *Absorption and Emission*

Absorption, unlike scattering, results in the thermalization of a photon. This involves a mechanism of photon destruction before it can be reemitted, which is usually provided by inelastic collisions. However, as was mentioned before, in a highly magnetized plasma, the collisional rate is much lower than the radiative one. This translates into a very low probability of thermalization of a photon after electron excitation.

Resonant Compton scattering (see Section 4.4.1) in this case describes cyclotron processes that involve radiative decay. On the other hand, true absorption and emission at energies close to the cyclotron resonance have to be treated as a resonant part of the *thermal* free-free absorption and emission (Nagel 1980; Nagel & Ventura 1983). Under these conditions, the absorption coefficient can be expressed as (Meszaros & Nagel 1985a)

$$\alpha^{\mathrm{ff}} = \alpha_0 \frac{3}{2}\frac{c}{\omega r_{\mathrm{e}}} \Big(\mathrm{Im}\Big\{\Pi^f_+\Big\}|e^p_+|^2 g_\perp \\ + \mathrm{Im}\Big\{\Pi^f_-\Big\}|e^p_-|^2 g_\perp + \mathrm{Im}\Big\{\Pi^f_z\Big\}|e^p_z|^2 g_\parallel \Big), \quad (4.46)$$

where α_0 is the classical non-magnetic free-free absorption coefficient (see, e.g., Rybicki & Lightman 1986) without the quantum mechanical correction given by the Gaunt factor (Gaunt 1930). The analogs of the Gaunt factor corrections enter the formula via the terms $g_\perp$ and $g_\parallel$. These coefficients are the dimensionless momentum-averaged *magnetic Gaunt factors* (Mészáros 1992),

$$g_\perp = \frac{1}{2}\int_{-\infty}^{\infty} \exp\left(-\frac{p^2}{2m_{\mathrm{e}}kT_{\mathrm{e}}}\right) \frac{C_1(a_+) + C_1(a_-)}{(p^2 + 2m_{\mathrm{e}}\hbar\omega)^{1/2}} \quad (4.47)$$

and

$$g_\parallel = \int_{-\infty}^{\infty} \exp\left(-\frac{p^2}{2m_{\mathrm{e}}kT_{\mathrm{e}}}\right) \frac{a_+ C_0(a_+) + a_- C_0(a_-)}{(p^2 + 2m_{\mathrm{e}}\hbar\omega)^{1/2}}, \quad (4.48)$$

where $a_\pm = (p \pm \sqrt{p^2 + 2m_{\mathrm{e}}\hbar\omega})^2 (2m_{\mathrm{e}}\hbar\omega)^{-1}$, and where C_0, C_1 are Coulomb matrix elements as given by Virtamo & Jauho (1975). These functions are expressed in terms of exponential integrals and thus are computationally expensive. The factors $g_\perp$ and $g_\parallel$ can be understood as describing resonant and continuum parts, respectively.

Figure 4.14 shows the free-free absorption cross section in a highly magnetized plasma for two different electron number density values. The absorption coefficient resembles similar polarization, energy, and angular dependency as the total scattering cross section. For parameters, relevant to the present work, absorption cross sections at the cyclotron resonance are orders of magnitude lower than the scattering ones.

Due to the radiation-controlled population of Landau levels, Kirchoff's law also cannot be used directly for cyclotron emissivity. As shown by Nagel & Ventura (1983), an equivalent expression can be obtained by linking cyclotron emissivity to the thermal production rate of photons

$$j^{\mathrm{ff}}_p = \alpha^{\mathrm{ff}}_p B(\omega, T_{\mathrm{e}}). \quad (4.49)$$

This expression will be used used in Section 4.5 for the radiative transfer simulation.

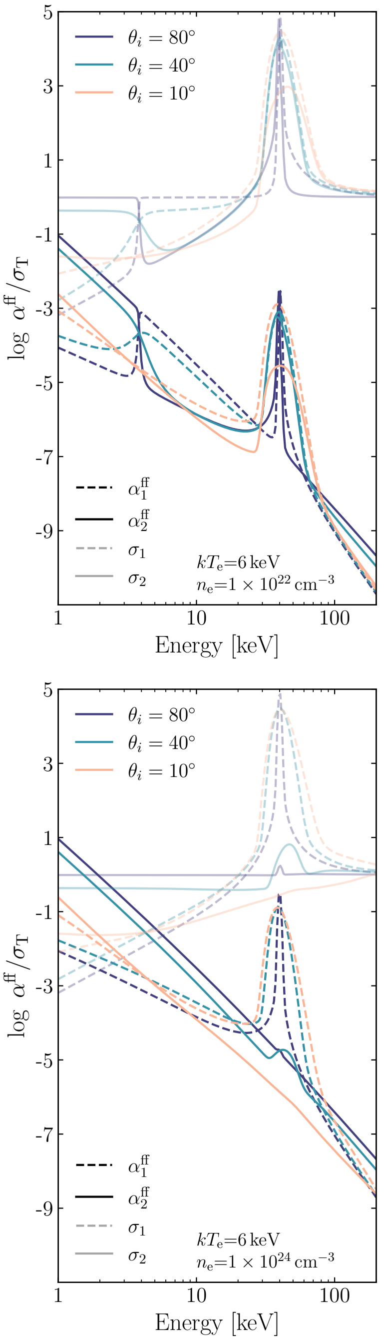

Figure 4.14: Total free-free absorption cross sections and total Compton scattering cross section (fade, transparent lines) for both polarization modes. The cyclotron energy is $E_{\mathrm{cyc}} = 40\,\mathrm{keV}$, the electron temperature is $kT_{\mathrm{e}} = 6\,\mathrm{keV}$, the electron number density is $n_{\mathrm{e}} = 10^{22}\,\mathrm{cm}^{-3}$ (*top*) and $n_{\mathrm{e}} = 10^{24}\,\mathrm{cm}^{-3}$ (*bottom*).

4.5 POLARIZED RADIATIVE TRANSFER

After the preparatory discussion in the previous sections, where I described fundamentals of radiative transfer, photon polarization modes, and opacities governed by the radiative processes in a highly magnetized medium, I will now address the solution of the radiative transfer equation. To summarize, the problem of radiative transfer in the vicinity of accretion-powered X-ray pulsars is complicated by the strong anisotropy introduced by the magnetic field, the resonant nature of the photon-electron interactions due to the Landau quantization, and the polarization properties of the magnetized plasma and vacuum. In this case, it is impossible to avoid a full integro-differential form of the transfer equation discussed in Section 4.2, which presents even more challenges for consistent simulations of the continuum and lines formation. An accurate treatment of the redistribution process during the scattering is a non-trivial task for differential schemes, which are often used for the radiative transfer solution. The common alternative is the Monte Carlo approach, which, however, is significantly challenged by the high continuum optical depth in combination with resonance processes due to increasing computational time (Schwarm 2017).

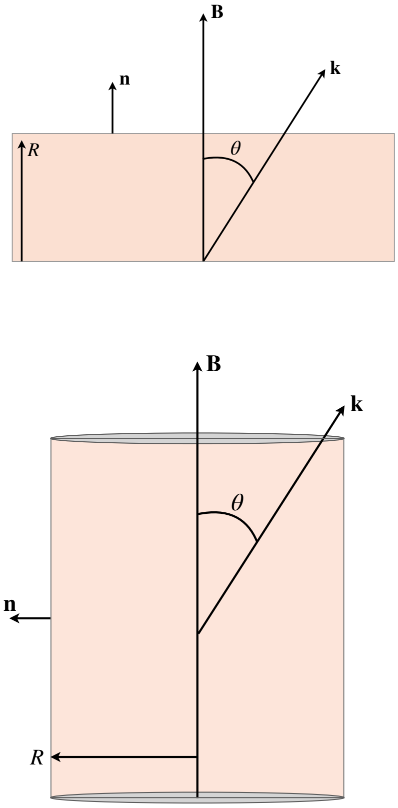

Figure 4.15: Two different geometries of the emitting region: a slab (*top*) and a cylinder (*bottom*).

An efficient approach to model polarized radiative transfer taking into account complex angular and energy redistribution was suggested in the works of Nagel (1981a), Nagel (1982), and further extended by Meszaros & Nagel (1985a), Meszaros & Nagel (1985b), Mészáros (1992), and Alexander et al. (1989). It is based on the *Feautrier method* proposed by Feautrier (1964). Feautrier introduced a representation of the radiative transfer equation as a second-order differential equation and its treatment in a matrix form. The method is efficient for high and low optical depths and allows for treating together continuum and lines formation in a consistent way. The approach developed by Nagel (1981a), Nagel (1982), and Meszaros & Nagel (1985a) combines the classical Feautrier method for the solution of the radiative transfer equation and the description of the field in terms of two polarization modes.

Here, I consider two main geometries: a plane-parallel semi-infinite slab, perpendicular to the magnetic field, and a semi-infinite cylinder with the magnetic field along its axis (see Figure 4.15). For both geometries, azimuthal symmetry is assumed. Here, I again sometimes refer to both, slab and cylinder, as an "atmosphere". The basic concept of the Feautrier method in two polarization modes and the specifics of the radiative transfer treatment are discussed in Section 4.5.1. Section 4.5.2 outlines the major details of the numerical implementation of the Feautrier method in the `FINRAD` code. Some information on the Feautrier approach and the `FINRAD` code was already presented in Sokolova-Lapa et al. (2021). Here, however, I significantly extend this description, providing more detailed formulation of the problem and addressing the treatment of the cylinder geometry, symmetry of the source function, and redistribution calculation.

4.5.1 *Feautrier Method*

For a static semi-infinite, plane-parallel atmosphere, the radiative transfer equation (see Equation 4.11) can be simplified by considering only the derivative along the vertical coordinate, r. Feautrier (1964) suggested that the radiation field can be separated into the components propagating strictly upwards, $I_+ = I(E,\mu,r)$, and downwards, $I_- = I(E,-\mu,r)$. Here $\mu = \cos\theta$ is now restricted to the half-space $0 \leq \mu \leq 1$ and θ, as before, is the angle with respect to the magnetic field (see also Figure 4.15). Then two equation describe the radiative transfer of the unpolarized radiation,

$$\pm\mu\frac{\partial I_\pm}{\partial r} = \kappa(S - I_\pm), \tag{4.50}$$

where $\kappa = \sigma + \alpha^{\mathrm{ff}}$ is the total opacity, and S is the source function.

The symmetric and anti-symmetric averages of the specific intensity can be written as

$$u = \frac{1}{2}(I_+ + I_-), \tag{4.51a}$$

$$v = \frac{1}{2}(I_+ - I_-), \tag{4.51b}$$

where u and v are the analogs of the mean intensity and the specific flux, respectively (see Equation 4.2 and Equation 4.5). Adding and subtracting equations for $\pm\mu$ given by Equation 4.50 and dividing them by 2, one can write two transfer equations,

$$\mu \frac{\partial v}{\partial r} = \kappa \frac{(S_+ - S_-)}{2} - \kappa u, \tag{4.52a}$$

$$\mu \frac{\partial u}{\partial r} = \kappa \frac{(S_+ - S_-)}{2} - \kappa v. \tag{4.52b}$$

In case symmetry of the source function can be assumed, $S_+ = S_-$, the problem can be simplified further. The forward-backward symmetry of the source function is one of the basic assumptions of the classical Feautrier method. In general, when this approximation breaks, a different method for the solution should be chosen (see, e.g., Milkey et al. 1975). In the case considered here, the probabilities of the forward and backward scattering ($\pm\mu$) are also not equal. I account for this, however, using the approach suggested by Meszaros & Nagel (1985a), where the average of the forward and backward ($\pm\mu$) scattering probabilities are used for the differential scattering cross section. This approach allows to preserve the classical Feautrier scheme. The legitimacy of this approximation will have to be checked in future works.

Equation 4.52b allows to express v in terms of u. By substituting it to Equation 4.52a, one obtains the second-order equation,

$$\frac{\mu^2}{\kappa} \frac{\partial^2 u}{\partial r^2} = \kappa (u - S). \tag{4.53}$$

This equation can be written for each polarization mode as

$$\begin{aligned} &\frac{\mu^2}{\kappa_p} \frac{\partial^2 u_p}{\partial r^2} - \kappa_p u_p \\ &\qquad + 4\pi \sum_{p'=1,2} \iint \frac{\mathrm{d}^2 \sigma_{pp'}}{\mathrm{d}E \mathrm{d}\mu} \frac{E}{E'} u_{p'} \,\mathrm{d}E' \mathrm{d}\mu' + \alpha_p^{\mathrm{ff}} \frac{\tilde{u}_{\mathrm{B}}}{2} = 0, \end{aligned} \tag{4.54}$$

where $\tilde{u}_{\mathrm{B}}$ is the equilibrium spectrum and $p = 1,2$ for mode 1 and mode 2, respectively, and the differential scattering cross section is to be understood in the forward-backward averaged sense, as mentioned above.

A similar derivation, but ignoring the derivatives for the azimuthal coordinate, and taking the mean value for $\sin(\theta) = 1/\sqrt{2}$, can be performed for the cylinder case (see details in, e.g., Mészáros 1992). By introducing a factor $\gamma = 0,1$ for a slab and a cylinder, respectively, the general radiative transfer is then given by

$$\begin{aligned} &D_p \left(\frac{\partial^2 u_p}{\partial r^2} + \frac{\gamma}{2} \frac{\partial u_p}{\partial r} \right) - \kappa_p u_p \\ &\qquad + 4\pi \sum_{p'=1,2} \iint \frac{\mathrm{d}^2 \sigma_{pp'}}{\mathrm{d}E \mathrm{d}\mu} \frac{E}{E'} u_{p'} \,\mathrm{d}E' \mathrm{d}\mu' + \alpha_p^{\mathrm{ff}} \frac{\tilde{u}_{\mathrm{B}}}{2} = 0, \end{aligned} \tag{4.55}$$

where the diffusion coefficient is (Meszaros & Nagel 1985a)

$$D_p = \left[(1-\gamma)\mu^2 + \gamma(1-\mu^2)/2\right] \kappa_p^{-1}. \tag{4.56}$$

The Feautrier method for the polarized radiative transfer is based on discretizing Equation 4.55 for each combination of energy and angle (and for the two polarizations) on a chosen numerical grid in E and μ. Put together as a system, these equations, whose terms are coupled via the differential scattering cross section inside the integral, can be considered as a matrix equation for the N-dimensional vector $\mathbf{u}$ for each step of a spatial grid $\{r\}$. The dimension is given by $N = N_E \times N_\mu \times 2$, where N_E and N_μ are a number of points in energy $\{E\}$ and angular $\{\mu\}$ grids, respectively, while the factor of 2 stands for two polarization modes. Matrix equations, written for each spatial step, together form a *block tridiagonal system*, which can be solved by the well-known *tridiagonal matrix algorithm* (also known as *Thomas algorithm*, named after Llewellyn Thomas, Thomas 1949), based on a forward elimination and backward substitution scheme. The classical detailed formulation of the method can be found, for example, in Mihalas (1978) and Hubeny & Mihalas (2014), while its version for the polarized transfer is comprehensively described in Nagel (1982) and Mészáros (1992).

Boundary Conditions

Equation 4.55 should be supplemented by appropriate boundary conditions. I refer to the top of the slab and the outer wall of the cylinder as the “upper boundary”. The assumption which is used throughout this work and which dictates the upper boundary condition is that there is no external illumination of the atmosphere, $I_-(R) = 0$. In this case, from Equation 4.51 it follows that $u(R) = v(R)$ and Equation 4.52b gives

$$\frac{\beta}{\kappa_p}\frac{\partial u_p}{\partial r} = -u_p, \tag{4.57}$$

where $\beta = (1-\gamma)\cos(\theta) + \gamma\sin(\theta)/\sqrt{2}$.

The center of the cylinder and the bottom of the slab represent the “lower boundary”. The general lower boundary condition is

$$\frac{\beta}{\kappa_p}\frac{\partial u_p}{\partial r} = u_p - I_+, \tag{4.58}$$

where $I_+ = I_+(0)$ is the illumination of the atmosphere from below. In case $I_+(0) = 0$ and $I_-(R) = 0$, the atmosphere is self-emitting and due to the symmetry only the half of the slab has to be considered. For the cylinder this is always the case (see Figure 4.15). Then the lower boundary condition

$$\frac{\beta}{\kappa_p}\frac{\partial u_p}{\partial r} = 0. \tag{4.59}$$

can be put at the half-depth of the slab, or in the center of the cylinder (Meszaros & Nagel 1985a). In the following, I assume that there is no illumination from below, that is, $I_+(0) = 0$, for all cases considered in Chapter 5 and Chapter 6. In practice, I used the approach suggested by Auer (1967) by making a Taylor expansion away from the boundary to improve the accuracy of the solution at the boundary. The terms up to the second order were included.

Stimulated Scattering and Emission

A final note has to be made on this modeling approach, related to the discussion of stimulated processes and equilibrium spectra in Section 4.2. As seen from its form, Equation 4.55 does not include stimulated processes. The equilibrium spectrum $\tilde{u}_\mathrm{B}$ is a Wien one, and in principle, the factor $[1-\exp(-E/k_\mathrm{B}T_\mathrm{e})]$ should be omitted in the non-magnetic free-free absorption coefficient α_0 (see Equation 4.46) to ignore stimulated emission as well. Stimulated scattering, however, can be an important effect for an optically thick plasma. Alexander et al. (1989) showed that ignoring this effect can lead to a large high-energy excess (more than a factor of 2), compared to the case which includes stimulated scattering. While the full problem requires an extended Feautrier method with an iterative approach (see the scheme described in Alexander et al. 1989), Meszaros et al. (1989) introduced a simple solution that allows taking stimulated scattering into account indirectly, but still keeping the problem linear. In general, the differential cross sections given by Equation 4.44 are connected to the ones used in Equation 4.55 via the detailed balance condition

$$\frac{\mathrm{d}^2\sigma}{\mathrm{d}E'\mathrm{d}\mu'}(E,\mu,e_p \rightarrow E',\mu',e'_p) = \left(\frac{E'}{E}\right)^2 \exp\left(\frac{E-E'}{k_\mathrm{B}T_\mathrm{e}}\right)\frac{\mathrm{d}^2\sigma}{\mathrm{d}E\mathrm{d}\mu}(E',\mu',e'_p \rightarrow E,\mu,e_p). \tag{4.60}$$

Meszaros et al. (1989) suggested to replace this relation with the artificial detailed balance condition,

$$\frac{\mathrm{d}^2\sigma}{\mathrm{d}E'\mathrm{d}\mu'}(E,\mu,e_p \rightarrow E',\mu',e'_p) = \left(\frac{E'}{E}\right)^2 \left(\frac{\exp\left(E/k_\mathrm{B}T_\mathrm{e}\right)-1}{\exp\left(E'/k_\mathrm{B}T_\mathrm{e}\right)-1}\right)\frac{\mathrm{d}^2\sigma}{\mathrm{d}E\mathrm{d}\mu}(E',\mu',e'_p \rightarrow E,\mu,e_p). \tag{4.61}$$

Alexander et al. (1989) showed that this approach reproduces the spectral shape at soft energies and results in a small underestimation of the flux at high energies (see their Figure 2 and Figure 3, however, no quantitative comparison was provided). This approach is used throughout the modeling chapters.

4.5.2 *Implementation: The* `FINRAD` *Code*

Following the approach described above, I implemented the radiative transfer calculation in the code `FINRAD` (Python 3). This code provides the polarized and non-polarized radiative transfer calculation and is independent of the cross sections, which have to be provided as input. Special care has to be taken for the rapidly growing dimension of the matrices in the Feautrier method with increasing density of angular and energy grids. Part of the matrices always stays diagonal, whereas the density of the ones describing scattering redistribution depends crucially on the electron temperature. For this reason, `FINRAD` operates with sparse matrices, using `scipy.sparse.linalg` (based on C-library `SuperLU`[7]) for LU-decomposition required by the tridiagonal matrix algorithm. The code was successfully tested with the known analytical and numerical solutions

---

[7] https://portal.nersc.gov/project/sparse/superlu/

for atmospheres with complete and partial redistribution, and also in the absence of redistribution. The well-known transfer code `XILLVER` for reflection from accretion disks was also used for a series of tests (J. A. Garcia priv. comm.). Some examples of this code verification were presented in the appendix of Sokolova-Lapa et al. (2021).

The `FINRAD` code is not specific to the problem of transfer in the neutron star atmospheres and accretion columns and can be used with arbitrary cross sections, which have to be provided together with the scattering matrix as an input. I implemented the cross sections for the magnetic Compton scattering and free-free absorption as a separate Python 3 package, which makes use of the `Numba`[8] just-in-time compiler and memoization. The cross sections are typically tabulated for the radiative transfer simulations, especially in the case of non-homogenous atmospheres.

For the purposes of this work, the angular discretization is performed according to the N_μ-point double-Gauss formula, where N_μ values of μ are given by the roots of the Legendre polynomial scaled from $[-1, 1]$ to the range $[0, 1]$ (see Sykes 1951; Mihalas 1978, Chapter 3). The number of angular points, N_μ, stays within the range 8–10 for different simulations. The energy grid also requires a careful approach. It is important to provide a fine grid near the cyclotron resonance. In the continuum, however, the coarser grid can be used, which also prevents the unwanted growth of the matrix dimensions. In addition, no abrupt changes should be present in the energy grid, as it can severely affect energy redistribution. For this reason, I implemented a nonuniform mesh generator by Tavella & Randall (2000), which allows the creation of a grid, whose points become gradually denser towards a so-called target. In this case, the target is the cyclotron energy. The generator gives the grid points

In the current version of the code, grid refinement is implemented only near the cyclotron resonance. It is less straightforward to use this approach for the vacuum resonance, as in an inhomogeneous medium it changes the position across the calculated region. A similar problem will arise in case of a non-constant magnetic field. In these cases, a fine uniform energy grid is probably a better choice.

$$E_i = E_{\rm cyc} + \zeta \sinh\left(c_2 \frac{i}{N} + c_1\left(1 - \frac{i}{N}\right)\right), \tag{4.62}$$

with coefficients

$$c_{1,2} = \sinh^{-1}\left(\frac{E_{\rm min,max} - E_{\rm cyc}}{\zeta}\right), \tag{4.63}$$

and where the parameter ζ describes the uniformity of the grid. In the following simulations, $\zeta = 0.1$–0.3. Typically, 100–300 energy points are used in the simulations.

Special care has to be taken for the discretization of the scattering integral in the source function, as the differential scattering cross section varies on much shorter scales than the intensity of the radiative field. These variations cannot be covered by any reasonable energy grid used for the radiative transfer solutions. These types of problems are well-known for redistribution functions (see, e.g., Adams et al. 1971). Here, I follow the prescriptions of Nagel (1981b), where each matrix element is obtained by integrating the differential cross section on a much finer energy grid defined between the points of the transfer grid, with a weight given by a piecewise linear function. The detailed description can be found in Nagel (1981a), Nagel (1982), and Mészáros (1992). In the calculations presented here, the 20-point auxiliary grid is used. I would like to stress that for the cases presented here, it is impossible to obtain a satisfactory result for energy and angular redistribution without this procedure, which is naturally computationally expensive.

---

[8] https://numba.pydata.org

4.6 CONCLUSION

In this chapter, I provided physical and methodological foundations for modeling of the spectra of accreting highly magnetized neutron stars. Using the tools presented here, I will study the general properties of the spectra formation in the accretion channel in Chapter 6 and then perform more complex modeling for the case of an accreting neutron star atmosphere in Chapter 7.

To summarize the main points addressed in this chapter, I would like to stress that Compton scattering, free-free absorption, and bremsstrahlung are generally the most important processes for spectral formation in the vicinity of accreting neutron stars. As I showed above, the cross sections for these processes are strongly angle-, energy-, and polarization-dependent. Their behavior also differs for the different types of polarization modes. For the conditions typical for the accretion channel, both real and virtual (due to vacuum polarization) charges, can affect the wave propagation. It is common, though, to limit the treatment to only one of these effects. For the pure plasma case, the polarization vectors of the two modes mainly oscillate in the $(\mathbf{B}, \mathbf{k})$-plane (ordinary mode) and perpendicularly to it (extraordinary mode). For the pure vacuum case, the modes are strictly orthogonal, except for the case of propagation along the magnetic field, and their vectors are confined to these planes. Taking into account both plasma and vacuum influences results in parameter regions, dominated by one or the other effect. At certain parameter combinations, the effects can cancel each other out and the phenomenon of vacuum resonance occurs. The behavior of the modes across the vacuum resonance has, generally, a probabilistic nature and can lead to mode conversion. The modes are mainly linearly polarized far from the vacuum and cyclotron resonances and become more circularly polarized approaching the resonances. I showed how cross sections for Compton scattering change when the behavior of the modes is determined by both plasma and vacuum effects, versus pure plasma and pure vacuum cases. In Chapter 6, I will study how the choice of polarization modes and the occurrence of the vacuum resonance affect the resulting spectra.

A few words need to be said about the modeling approach, as it involves several approximations. The most obvious approximations are the treatment of polarization modes near the vacuum and the cyclotron resonances, the neglect of higher-order relativistic corrections in the Compton scattering cross sections, and an approximate treatment of stimulated scattering. A less obvious approximation is, for example, the basic assumption of the Feautrier method that the source function is symmetric with respect to $\pm\mu$. For an anisotropic medium this approximation is to some degree compensated by using differential cross sections that averaged over $\pm\mu$ in the numerical scheme. Most of these limitations were individually eliminated in modeling setups of other authors, providing us with means to test the influence of the approximations. Thus, fully relativistic cross sections and non-linear treatment of the Feautrier method were used by Alexander et al. (1989), while a Monte-Carlo approach for modeling the emission from the atmosphere of an accreting neutron star by Mushtukov et al. (2021) did not invoke the symmetry of the source function. These different modeling approaches do not provide qualitatively different results compared to the one used here. In cases where a quantitative comparison was possible, only well-understood non-dramatic differences were found (such as, for example, the overall narrower shape of the fundamental cyclotron line in the fully relativistic treatment of Alexander et al. 1989). In this way, one can say that there is an understanding of the degree of adequacy of the approach, used in this work, and its limits.

Part III

MODELING

5

EMISSION FROM HIGHLY MAGNETIZED MEDIA

> *"The X-rays produced in accretion columns on neutron stars are thought to be generated by a combination of thermal and non-thermal processes."*
> ChatGPT

This chapter focuses on the results of radiative transfer calculations, as described in Chapter 4, for various conditions expected in the vicinity of highly magnetized accreting neutron stars. The main goal is to demonstrate the influence of the choice of polarization modes, of the redistribution near the cyclotron resonance, and of basic plasma parameters onto the broad-band continuum and the cyclotron line formation. Apart from that, I will address tests of the validity of some common assumptions made about the emission from accretion columns and hot spots.

In Chapter 4, I showed how cross sections for magnetic Compton scattering and free-free absorption for the two polarization modes can be dramatically affected by the parameters of the medium in a strong magnetic field. Depending on the conditions, different approximations for polarization modes can be used. Various choices of polarization modes were made in different works attempting to describe a continuum of High-Mass X-ray Binaries. For the modeling of the cyclotron lines, a common choice is the polarization modes for the pure vacuum case (see, e.g., Schönherr et al. 2007a; Mushtukov et al. 2015c; Schwarm et al. 2017a,b). Under these conditions, the strong cyclotron resonance always arises for both polarization modes. Sometimes this choice is also made for the joint continuum and line transfer modeling, as was done for the atmospheric emission under the low-rate accretion onto a neutron star by Sokolova-Lapa et al. (2021). For the same task, however, Mushtukov et al. (2021) used the polarization modes for the pure magnetized plasma. Becker & Wolff (2022) considered polarization modes for the cold plasma given by Ventura (1979) in their model for bulk and thermal Comptonization in accretion columns. They included the effect of vacuum polarization for the models where lower plasma density is expected (as they argued, for example, for X Per). It is, however, not possible to see the direct influence of this choice on the obtained continua, as in their approach only energy- and polarization-averaged cross sections enter the transfer equation. In this chapter, I consider four principle types of polarization modes: for *the pure vacuum*, for *pure magnetized plasma*, for the case of combined *plasma and QED-vacuum case* (that is, including the effect of vacuum polarization) with *continuous* refractive indices, and for the case of combined *plasma and QED-vacuum case* with *discontinuous* refractive indices. With this, I attempt to demonstrate the influence of the choice of polarization modes onto the continuum and the cyclotron line formation and bring the effect of vacuum resonance into focus.

Involvement of various kinds of approximations is inevitable to solve the problem of radiative transfer in a highly magnetized medium. For this reason, it is important to understand which part of the solution is a direct consequence of the assumption made. As an example, the energy- and polarization-averaged approximations for cross sections and the flux (see, e.g., Becker & Wolff 2007, 2022) result in a smooth continuum without a noticeable contribution of additional components at medium energy ($\sim$10–30 keV), unless an additional source of photons is directly inserted. As was discussed in Chapter 3, however, the spectra of accretion-powered

X-ray pulsars often exhibit peculiarities at intermediate energies, which are sometimes modelled using the "10-keV" feature or two-component Comptonization models. In this chapter, I show that a complex continuum is often expected due to polarization effects and redistribution during Compton scattering and discuss the possible formation of additional spectral components at intermediate energies.

Another common assumption made when modeling the radiation spectra from accretion columns and hot spots is that the angular dependency of the cross sections allows treating the problem for a selected geometry (column/spot) only in one polarization mode, with a predictable simple emission pattern. For the accretion columns, often only the transfer of radiation perpendicular to the magnetic field is considered, assuming that the emission is only in the classically defined extraordinary mode with a fan-beam pattern due to its nearly-isotropic behavior below the cyclotron resonance (Postnov et al. 2015; Falkner 2018). For the slab-like hot spots on the surface of the neutron star, the predominant direction of the radiation propagation is outwards, along the magnetic field, and sometimes the assumption of the transfer only in the ordinary mode is made, resulting in a narrower, pencil-like beam (see, e.g., Basko & Sunyaev 1975). Often, these geometry-based arguments are used without specification of the polarization modes, and the pencil beam description is invoked for upward-emitting regions (for example, the top of the accretion column), while the fan beam is thought to represent the emission from the column walls (Leahy 2004; Farinelli et al. 2016). The dominance of pencil and fan beams is also often attributed to the accretion regime, with pencil-beam emission at lower and fan-beam emission at higher luminosities (Becker et al. 2012; Schönherr et al. 2007b), due to expectation of the transition to the column-like geometry at higher mass-accretion rates (see Figure 3.1). However, the complexity of observed pulse profiles in different energy bands and the dependency of the spectral components on the rotational phase suggests a more sophisticated picture of emission. Some parts of this problem, such as an emission pattern from the top of the accretion column compared to its walls, can be properly addressed only by two-dimensional modeling. Here some foundation for this discussion is presented.

The work presented here is also intended to illustrate how the fundamental parameters – the electron temperature, density, optical depth, and the magnitude of the magnetic field – affect the spectrum. In studying two different geometries - a slab and a cylinder - this research closely resembles the works of Meszaros & Nagel (1985a,b) and Alexander et al. (1989). It focuses, however, on a more detailed investigation of the parameter space and, in particular, on the choice of the polarization modes. This approach allows to relate to the finer details of the continuum formation, which can be important for the interpretation of observed spectra. The cylinder geometry is used to make an analogy with emission of the walls near the base of the accretion column, while the slab geometry represents the case of an atmospheric (polar cap) or the accretion mound emission.

The following questions are the direct objectives for this chapter:

- Does vacuum polarization affect the spectral formation under the conditions typical for accreting X-ray pulsars in High-Mass X-ray Binaries? In which way can the cyclotron line, the broad-band continuum, and the polarization signal be affected by the vacuum resonance?

- Is a power-law-like continuum expected at the intermediate X-ray energies from $\sim$5 keV and up to the cyclotron resonance? Which effects are responsible for its deviation from the simple shape?

- Is the common assumption of the extraordinary mode dominating the emission of the accretion column wall (forming a *fan-beam*) and the ordinary mode photons prevailing in the flux from the polar cap (forming a *pencil-beam*) correct and unambiguous?

Section 5.1 illustrates the influence of the polarization modes choice and the vacuum resonance onto the emergent spectra. The basic dependencies of the outgoing radiation on the parameters of the plasma and the emission region are presented in Section 5.2, under the assumption of a homogeneous medium. In Section 5.3, the angular dependency of the outgoing radiation is addressed with examples of the beam shapes in different energy bands. Section 5.4 introduces a simplified model for inhomogeneous accretion mound and discussed the vacuum polarization effect for this more realistic medium. Finally, Section 5.5 provides the summary and conclusions for the present study.

A few notes should be made. The term "vacuum resonance" is still used with respect to the energy where the vacuum and plasma effect cancel each other out, and which does not correspond to the cyclotron resonance (see Section 4.3.4), which is in the literature sometimes referred to as the "first vacuum resonance" (see, e.g., Meszaros & Nagel 1985a). I always use the notations "mode 1" and "mode 2" for the two polarization modes, to avoid the confusions in the case when the vacuum resonance and mode conversion are present. In the absence of vacuum polarization, mode 1 and mode 2 correspond to the classically defined extraordinary and ordinary modes, respectively. Some of the results from this chapter are submitted for publication to A&A Letters[1].

5.1 VACUUM POLARIZATION AND RADIATION SPECTRA

The peculiar behavior of the photon polarization modes discussed in Chapter 4 raises an obvious question of how the vacuum polarization affects the spectral formation in a magnetized medium in the vicinity of accreting neutron stars. The current section provides some insights on this topic.

5.1.1 *Previous Studies of the Vacuum Resonance in Accreting X-ray pulsars*

For magnetic fields characteristic of accretion-powered X-ray pulsars in High-Mass X-ray Binaries, the effect of vacuum polarization on the opacities was extensively studied (see discussion in Section 4.3.4), but the respective spectral simulations remain few to this day. Pavlov & Shibanov (1979) modeled spectra of the optically thick magnetized plasma dominated by free-free absorption, with the source function varying linearly with optical depth. They argued that the effect of vacuum polarization can manifest itself in the form of absorption and emission features, mimicking weak cyclotron lines. The same result was obtained by Ventura et al. (1979), while including Thomson scattering to their analytical solution. Ventura et al. (1979) emphasized the influence of the change of the polarization state by photons during scattering (not related to the mode conversion discussed in Section 4.3.4) on the observability of the

---

[1] Published in June 2023: Sokolova-Lapa et al. (2023)

vacuum signature. Kaminker et al. (1982) considered a purely scattering atmosphere without energy redistribution (no Comptonization) for the weak and strong influence of vacuum polarization with a similar choice of cross sections characterized by a sharp line-like appearance of the vacuum resonance (corresponding to discontinuous behavior of the refractive indices). Similar to previous works, they found the vacuum modification of the spectra by the resonant feature. In addition, they studied emission beaming in different energy bands and noted that the resonances in the spectra are due to angular redistribution. A different choice of the smooth transport coefficients (continuous refractive indices) as a function of energy was made by Soffel et al. (1985), who treated radiative transport in the zero-scattering approximation for the optically thin plasma and in the diffusion approximation, neglecting Compton scattering, in the optically thick case. These authors also obtained a weak line-like modification at low energies, omitting detailed discussions of this effect. Meszaros & Nagel (1985a,b) included the effect of vacuum polarization in the more sophisticated modeling, taking into account Comptonization with partial energy and angular redistribution. Similar to Soffel et al. (1985), they assumed continuous behavior of the refractive indices. These works, however, only studied high- and low-density models, resulting in the vacuum resonance not being visible in the spectra. These authors noted the vacuum polarization significantly modifies polarization signal and is important for the cyclotron line modeling, but the direct influence of the vacuum resonance and detailed spectra modifications due to this effect were not addressed. I would like to note, that all models discussed assumed a homogeneous medium, where the vacuum resonance, which is density-dependent, occurs only at a certain photon energy. For the magnetic fields of $B \sim 10^{12}$–10^{13} G, a radiative transfer without Comptonization was calculated by Zane et al. (2000) in an inhomogeneous medium. The focus of this work, however, was on the proton cyclotron lines in the spectra of isolated neutron stars and thus only soft energies, $E \lesssim 5$ keV were studied.

5.1.2 *Vacuum Resonance in the Magnetar-Like Fields*

More recently, the influence of vacuum resonance on the emission spectra from cold atmospheres of highly magnetized neutron stars, such as X-ray Dim Isolated Neutron Stars and magnetars was extensively studied (Bulik & Miller 1997; Lai & Ho 2002; Ho & Lai 2003; Lai & Ho 2003a,b; Özel 2003; Ho & Lai 2004; van Adelsberg & Lai 2006; Wang & Lai 2009). Bulik & Miller (1997) performed Monte Carlo simulations in cold plasma with magnetar-like magnetic fields, choosing non-adiabatic mode conversion at the vacuum resonance. They found that vacuum polarization results in a pronounced broad absorption feature. The authors noted that Comptonization has the strongest effect, making the feature noticeable even in the presence of a density gradient. Later, Lai & Ho (2002), Özel (2003), and Ho & Lai (2003), showed that in cold atmospheres of isolated neutron stars ($B{\sim}10^{14}$ G) the mode conversion across the vacuum resonances is expected to proceed in the adiabatic regime (see Chapter 4). This leads to the depletion of the high-energy tail and the suppression of a proton cyclotron line. It was argued that this effect onto the formation of proton cyclotron line can explain the fact that they are rarely observed (Özel 2003; Ho & Lai 2003). Such a depletion results from a reduction of the decoupling depth of photons from the medium and hence in a decrease of the effective optical depth for photons with energies above the resonance value. Ho & Lai (2004) compared the spectra in the case of the present vacuum polarization (including the case of the partial mode conversion), with the spectra from a magnetized plasma in the absence of this effect. They found a similar depletion effect as the previous studies and noted that the spectral shapes are only affected in the case of very high magnetic fields, $B \gtrsim 7 \times 10^{13}\,\mathrm{G}$. For lower magnetic fields, the effect manifests itself only in polarization signal, but not in the total flux. A more careful treatment of partial mode conversion was presented by van Adelsberg & Lai (2006), confirming these results. It would seem that the question of the effect of vacuum polarization onto the spectra of accretion-powered X-ray pulsars in High-Mass X-ray Binaries ($B \sim 10^{12}$–$10^{13}\,\mathrm{G}$), has been put to rest.

5.1.3 *Vacuum Resonance in the Comptonized Spectra at* $B{\sim}10^{12}\,\mathrm{G}$

There is, however, a contradiction between the obvious presence of the vacuum resonance in the cross sections within the X-ray energy band for a wide range of expected density values at magnetic fields of $B{\sim}10^{12}$–$10^{13}\,\mathrm{G}$ and the statement made by Ho & Lai (2004) and van Adelsberg & Lai (2006) that only the polarization signal is affected in this case. This contradiction has to be addressed. The solution to this apparent paradox is that the limiting value of the magnetic field B_l, below which the vacuum resonance (Ho & Lai 2003),

$$E_\mathrm{V}(B \ll B_\mathrm{crit}) \approx 1.02 \left(\frac{\rho}{1\,\mathrm{g\,cm^{-3}}}\right)^{1/2} \left(\frac{B}{10^{14}\,\mathrm{G}}\right)^{-1} \mathrm{keV} \tag{5.1}$$

lies outside the photospheres of both polarization modes, is derived for the case when decoupling densities of the modes are governed by absorption in the medium. This assumption is clearly violated in the accretion channel of High-Mass X-ray Binaries, where magnetic Compton scattering becomes a dominant process. The derivation of decoupling densities for this case is much less trivial and lies outside the scope of the present work. However, the series of numerical simulations performed here allows the demonstration of the vacuum polarization effect.

Figure 5.1 and Figure 5.2 illustrate the effect of vacuum polarization on the radiation spectrum from self-emitting homogeneous atmospheres at various densities and electron temperatures, compared to pure plasma and vacuum polarization modes. The specific flux is given by

$$F = 4\pi \int_0^1 I(E,\theta) \cos\theta \mathrm{d}\theta \tag{5.2}$$

for the slab case and

$$F = 4\pi \int_0^1 I(E,\theta) \sin\theta \mathrm{d}\theta \tag{5.3}$$

for the cylinder case. Here θ, as before, is the angle between the direction of photon propagation and the magnetic field. At low temperatures, $kT_\mathrm{e} = 0.5\,\mathrm{keV}$ (spectra with lower flux shown by families of blue lines in Figure 5.1 and Figure 5.2), the influence of vacuum polarization on the spectrum is very minor for the slab case. It is more pronounced for the cylinder, leading to more noticeable suppression of the flux at the intermediate energies. With increasing electron temperature, $kT_\mathrm{e} = 6\,\mathrm{keV}$, the effect becomes more dramatic for both geometries. Along with Comptonization of the spectra in a hot medium and appearance of the broadened cyclotron resonance, the difference in the choice of polarization

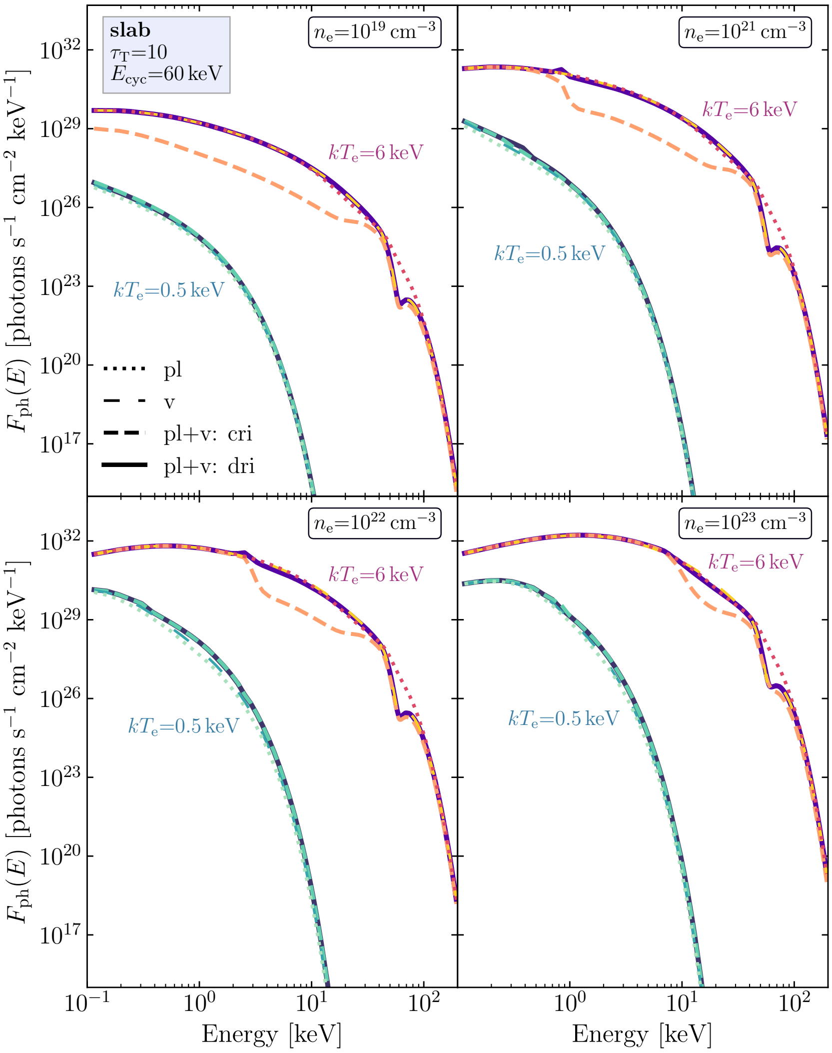

Figure 5.1: Total photon flux summed over two polarization modes from a highly magnetized medium in *slab* geometry with different electron number density values for low, $kT_e = 0.5$ keV (lower, cold-colored curves on each panel, without visible cyclotron resonance), and medium, $kT_e = 6$ keV (higher, warm-colored curves on each panel, with cyclotron resonance) electron temperature. For each panel (fixed electron number density) and each electron temperature, spectra are shown for the different polarization modes: pure magnetized plasma (*dotted*), pure vacuum (*loosely dashes*), magnetized plasma with the vacuum polarization effect and continuous refractive indices (*dashed*), and magnetized plasma with the vacuum polarization effects and discontinuous refractive indices (*solid*) modes. The magnetic field strength corresponds to $E_{cyc} = 60$ keV ($B \approx 5.2 \times 10^{12}$ G) and the total Thomson optical depth $\tau_T = 10$.

modes becomes overall more pronounced. In the case of a pure magnetized plasma, the cyclotron line region is dominated by the ordinary mode (see Figure 5.4, where contribution of polarization modes is shown), and so the resonance is barely noticeable on the angle-integrated spectra. For the pure vacuum polarization modes, the continuum shape follows the plasma case, but the cyclotron resonance, as expected, is strongly exhibited by both modes. In the case when plasma and vacuum polarization are included and the discontinuous refractive indices are assumed (see cross sections with the resonant low-energy feature in Figure 4.11), the spectrum does not deviate significantly from the pure vacuum case

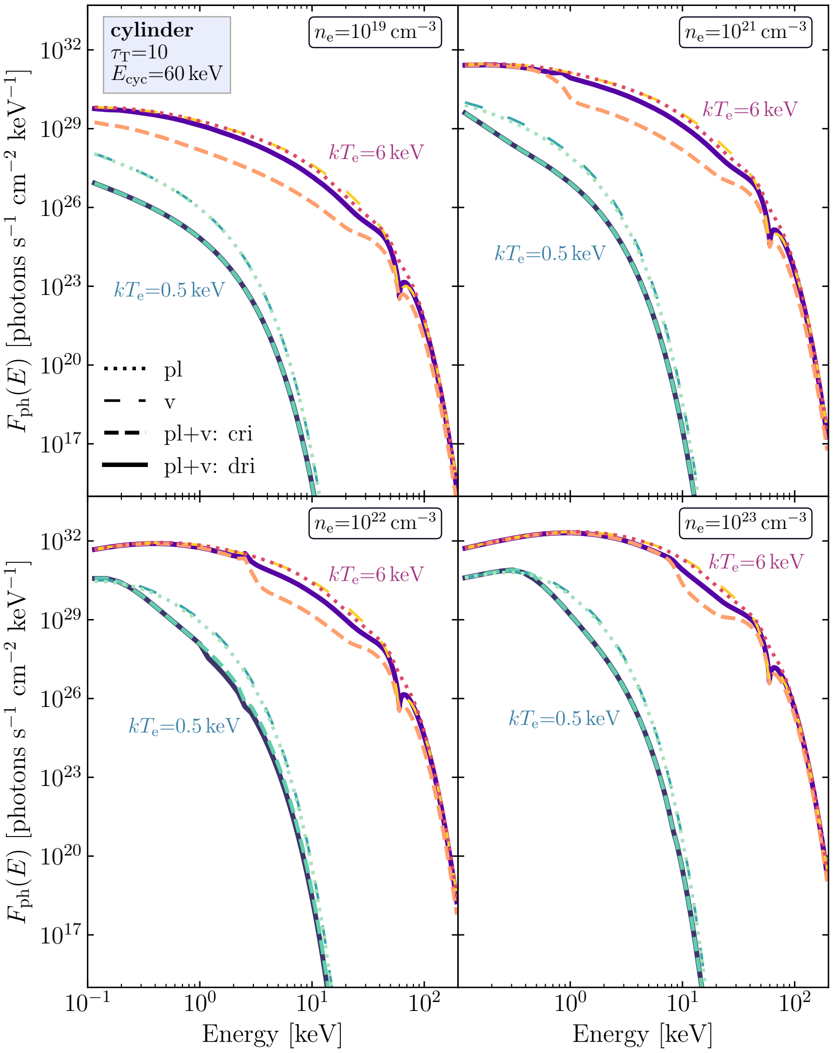

Figure 5.2: Same as in Figure 5.1 but for cylinder geometry.

for the slab, and shows small suppression for the cylinder geometry. For some models (e.g., $n_{\rm e} = 10^{21}\,{\rm cm}^{-3}$ in Figure 5.1), a small emission-line-like feature is seen at the energy corresponding to the vacuum resonance. The spectral shape is significantly modified in the case of continuous refractive indices (corresponding to, for example, Figure 4.12), showing a strong depression for the energies above the vacuum resonance. In some cases, the cyclotron line is also significantly suppressed. In the examples given here, this is especially noticeable for the cylinder geometry. However, such behavior of the cyclotron resonance is not geometry-specific and can occur for the slab as well for cases when the vacuum resonance lies closer to the cyclotron energy. An example of such clear cyclotron line suppression for the slab geometry is presented in Figure 5.3. This example also shows a more complex continuum shape, where the smoothed step of the depression after the vacuum resonance mimics a weak cyclotron line at energies below the real fundamental feature.

As shown in the examples above, the cases of the continuous and discontinuous refractive indices are so vastly different from each other that the question naturally arises which case is closer to reality. In general, the behavior of the refractive indices is by no means a free choice and depends on the parameters of the radiation and the medium (see, e.g., Pavlov & Shibanov 1979). In many cases, a certain behavior is expected to dominate over a large range of parameters and thus a generalization can be made (by choosing, for example, continous refractive indices, as was done in Zane et al. 2000). In general, for an inhomogeneous atmosphere, whether or not the polarization state of a photon with a certain energy evolves adiabatically, that is, keeping the original helicity and a continuous refractive index (see Section 4.3.4), depends on the density scale height along the ray, the angle of photon propagation, and the magnetic field value. From the adiabatic condition as given, for example, by Equation 3 of Ho & Lai (2004), it follows that for magnetic fields typical of neutron stars in High-Mass X-ray Binaries, the adiabatic condition is satisfied for photon energies $E \gg E_{\mathrm{ad}} \approx 0.01\text{–}2.5\,\mathrm{keV}$, depending on the angle of the photon propagation (and much more mildly on the plasma temperature). These estimates are valid for the emission regions near the neutron star surface, where the scale height is set by the gravitational field. In this way, for the broad band of intermediate and high-energy X-rays, the mode propagation is expected to proceed in the adiabatic ("complete mode conversion") regime, that is, with full adiabatic conversion. For energies $E \sim E_{\mathrm{ad}}$, there is a non-zero probability for the non-adiabatic jump (see, e.g., van Adelsberg & Lai 2006). This is the case of partial mode conversion. For the broadband continuum, adiabatic and non-adiabatic mode evolution across the vacuum resonant represent two limiting cases, with the true solution being between them (Ho & Lai 2003; van Adelsberg & Lai 2006). For the Feautrier method used in the present study, the partial mode conversion case is challenging, it is easier to study this using, for example, Monte Carlo methods.

As for a large energy band above a few keV studied under the conditions stated above, the refractive indices are expected to stay a continuous function of energy and density, a comment on peculiarities of the corresponding obtained solutions is required. First of all, the steepness of the step at the vacuum resonance with subsequent depression is expected to be significantly smoothed at soft energies due to partial mode conversion compared to the cases presented in this section. For energies far above the step, the effect of vacuum polarization acts effectively as a reduction of the optical depth of the emitting region. This phenomenon was noted for higher magnetic fields in the atmospheres of isolated neutron stars by Lai & Ho (2002) and Ho & Lai (2003). Figure 5.5 and Figure 5.6 illustrate the reduction of the effective optical depth for the cylinder geometry at two different electron number density values. This effect, however, acts more gently on the wings of the cyclotron line, which are more pronounced in the case of the true law optical Thomson depth. Finally, the models presented above are for self-emitting atmospheres with a homogeneous density profile. Any realistic environment near the surface of a neutron star, along the extended radiation shock or a sinking region, will possess a significant density gradient. The exact spectral shaping in this case requires detailed modeling. However, the net effect is expected to smooth the spectral depression. One of the inhomogeneous cases, corresponding to the thermal mound at the base of the accretion column, is discussed in Section 5.4.

The results show that for the case when an approximate solution is sufficient for a given task, it can still be feasible to use pure plasma or pure vacuum polarization modes to describe the spectral shape of accreting X-ray pulsars. In this case, the "more correct" choice are the vacuum modes when the vacuum resonance lies below the cyclotron one, and the pure plasma modes when the vacuum resonance energy is higher than the

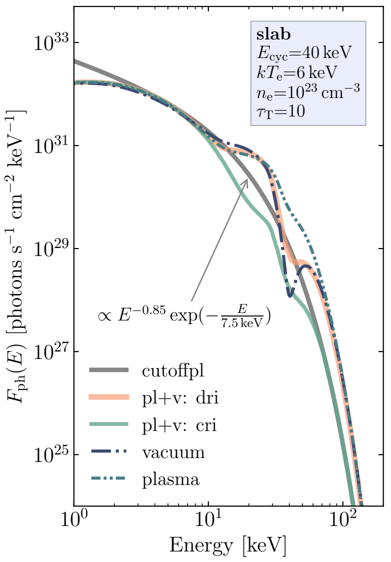

Figure 5.3: Example of cyclotron line suppression due to the effect of vacuum polarization compared to the pure plasma and vacuum photon normal modes. The total photon flux summed over polarization modes is shown for the case of slab geometry. A curve corresponding to the `cutoffpl` model is shown to illustrate a general behavior of the continuum. The parameters of the medium are as stated in the figure.

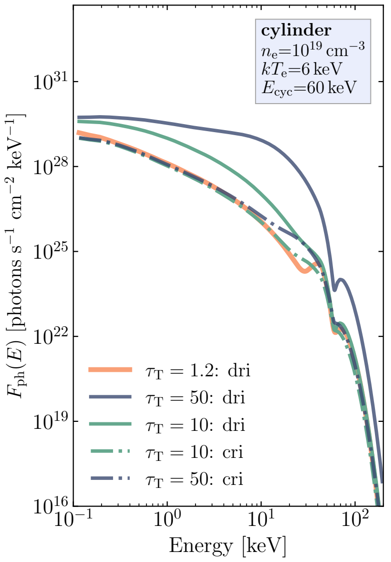

Figure 5.5: Example of optical depth reduction due to adiabatic mode conversion. Photon flux summed over two polarization modes shown for the case of *cylinder* geometry for various optical depths. Parameters are as stated in the figure.

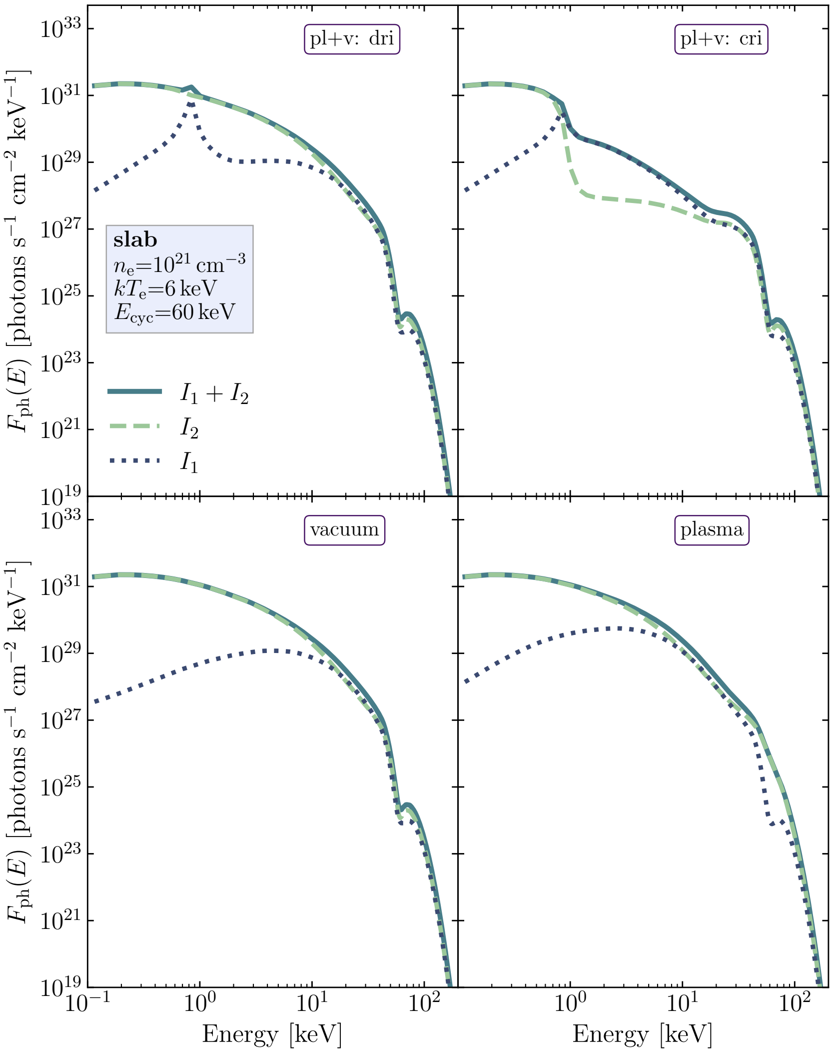

Figure 5.4: Spectra from highly magnetized slab shown with polarization components for different types of polarization modes (different panels). Parameters are as stated in the figure.

cyclotron one. It is important to note that for consistent, continuum and cyclotron line modeling, thermal effects for all types of modes will become crucial. I would like to emphasize that for magnetic fields $B \gtrsim 4 \times 10^{12}$ G, the location of the vacuum resonance is still below the cyclotron one even at electron number densities as high as $n_e = 10^{24}\,\mathrm{cm}^{-3}$. For example, for such densities and for a magnetic field appropriate for Her X-1, $E_{cyc} \approx 40(1+z)$ keV ≈ 50 keV, assuming a gravitational redshift near the surface of the neutron star $z = 0.24$, the vacuum resonance lies at ~31 keV. However, polarization of the radiation in the approximate treatment discussed above will produce a knowingly wrong result. As will be shown in the following, the approximation by pure vacuum and plasma cases also results in a different beaming of the radiation field.

5.2 BASIC PROPERTIES OF THE EMISSION

The properties of the radiation emergent from the homogeneous self-emitting region will significantly depend on the basic parameters of the medium. In this section, I will discuss how the spectra depend on the

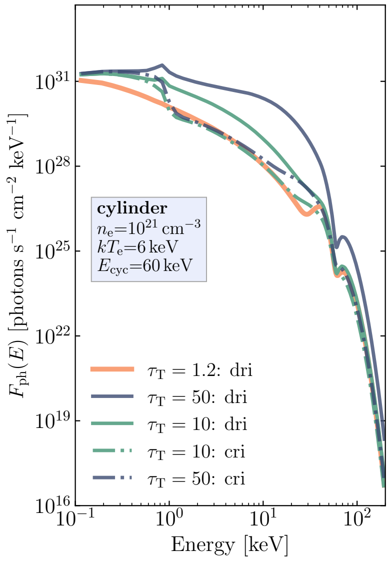

Figure 5.6: Same as in Figure 5.5 but for a higher electron density, $n_e = 10^{21}$ cm^{-3}.

basic parameters of the medium, such as the electron number density, the electron temperature, the strength of the magnetic field, and the optical depth is presented. The evolution of the spectra is shown for one changing parameter at a time for both geometries: a slab and a cylinder. The photon flux is shown in two polarization modes and angle-integrated in the same manner as described in Section 5.1. The angular dependency for both geometries is discussed in Section 5.3. Here, I consider the case where the effects of vacuum polarization and magnetized plasma are always included to describe the polarization modes of photons. For all case I performed calculations for both, continuous and discontinuous refractive indices, which can be understood as the two limiting cases as discussed in Section 5.1.

Figure 5.7 and Figure 5.8 illustrate the influence of the electron number density on the emission spectra for the slab and the cylinder case, respectively. The spectra saturate and become harder with increasing electron number density. The flux noticeably increases in both polarization modes (no additional scaling was applied) due to the increasing role of the free-free emission $\propto n_e^2$, which remains the only source of photons (Alexander et al. 1989). The low-energy part of the spectra converges to the Planckian shape at higher densities for the same reason (the equilibrium spectrum is Planckian because the artificial balance condition given by Equation 4.61 allows accounting for the stimulated effects). Simultaneously, the vacuum resonance manifests itself as an absorption- or emission-like feature, depending on the characteristic optical depth for both polarization modes at these energies (which can significantly differ from the total Thomson optical depth, which was fixed to $\tau_T = 50$ for the models). The manifestation of the vacuum resonance as a stand-alone feature is more characteristic for the discontinuous behavior of the refractive indices, when the cross sections also exhibit the resonance. With increasing density and for a fixed magnetic field value, the vacuum resonance shifts to the higher energies $\propto n_e^{0.5}$ (see Equation 5.1). For the case of the continuous refractive indices, a broad depression appears between the vacuum and the cyclotron resonances, resulting in unphysically-looking spectra. This effect, however, is expected to be smoothed by any real density gradient in the emitting region. In addition, the strong depression region already disappears for $n_e = 10^{23}$ cm^{-3}, where the main difference from the discontinuous case comes from the softer high-energy spectra and the change of the modes contribution after the vacuum resonance. These densities (and even higher) are realistically expected from the bottom of any emission region on the surface of the neutron star due to the strong gravitational field, and govern the emissivity of the region.

Spectra for varying optical depth are shown in Figure 5.9 and Figure 5.10. At low energies, the continuum is again flattened with increasing optical depth, emphasizing the net role of free-free processes. At higher energies, spectra become significantly more Comptonized due to the increased number of interactions with electrons, reaching a saturated state. The polarization modes saturate to different spectral shapes, bringing up noticeable additional spectral components. Such components can be seen as excess above the average power-law-like behavior, and are potential candidates to explain the observed complex continuum shape (such as the "10-keV" feature). I would like to note that they are often accompanied by a change of polarization, especially for the case of the continuous refractive indices.

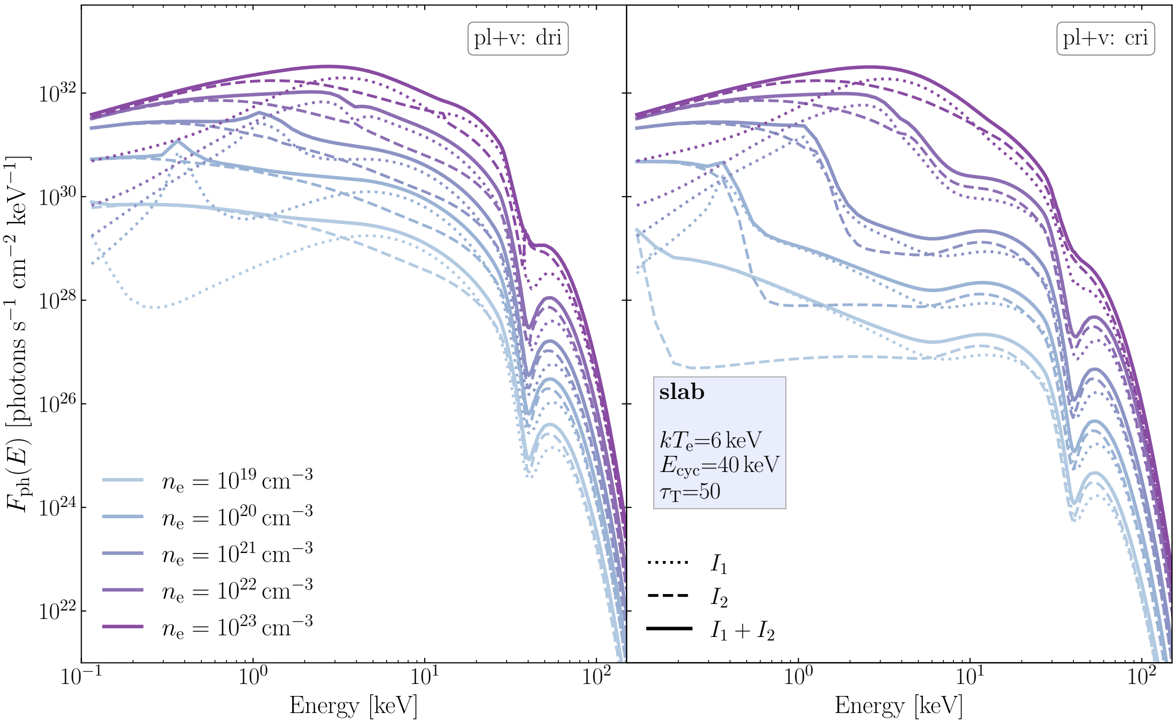

Figure 5.7: Emission from a highly magnetized slab for different values of electron number density of the medium shown for the case of the discontinuous (left) and continuous (right) refractive indices as functions of energy.

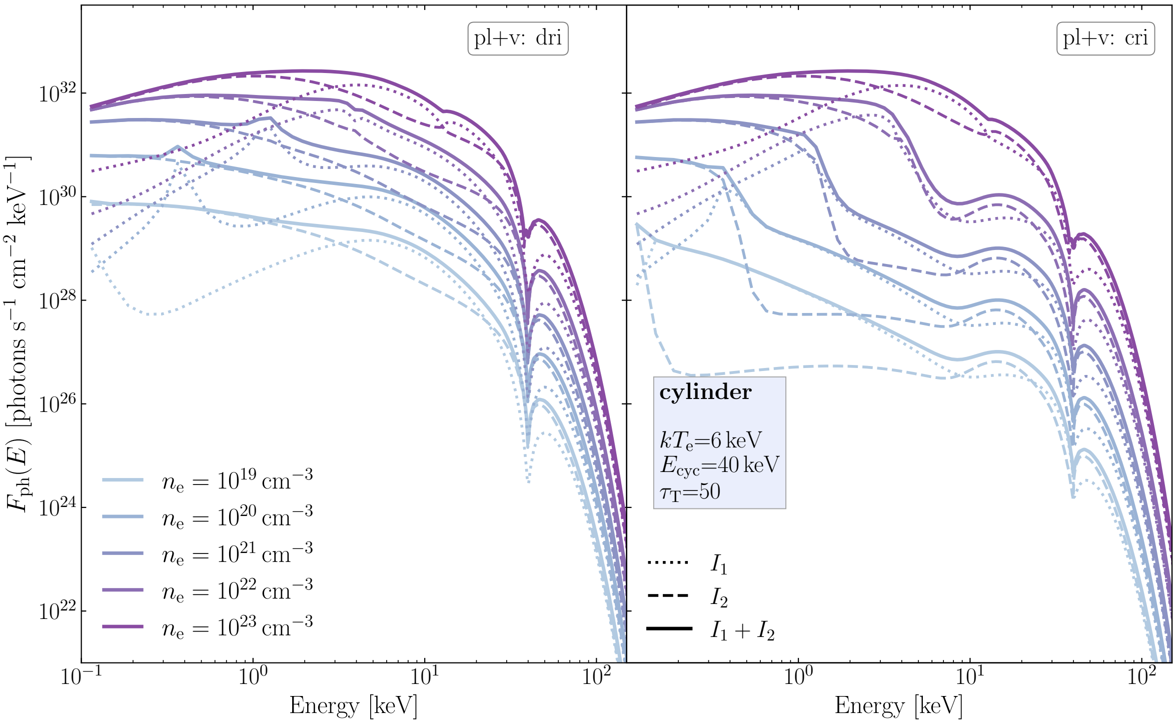

Figure 5.8: Same as in Figure 5.7, but for the cylinder geometry.

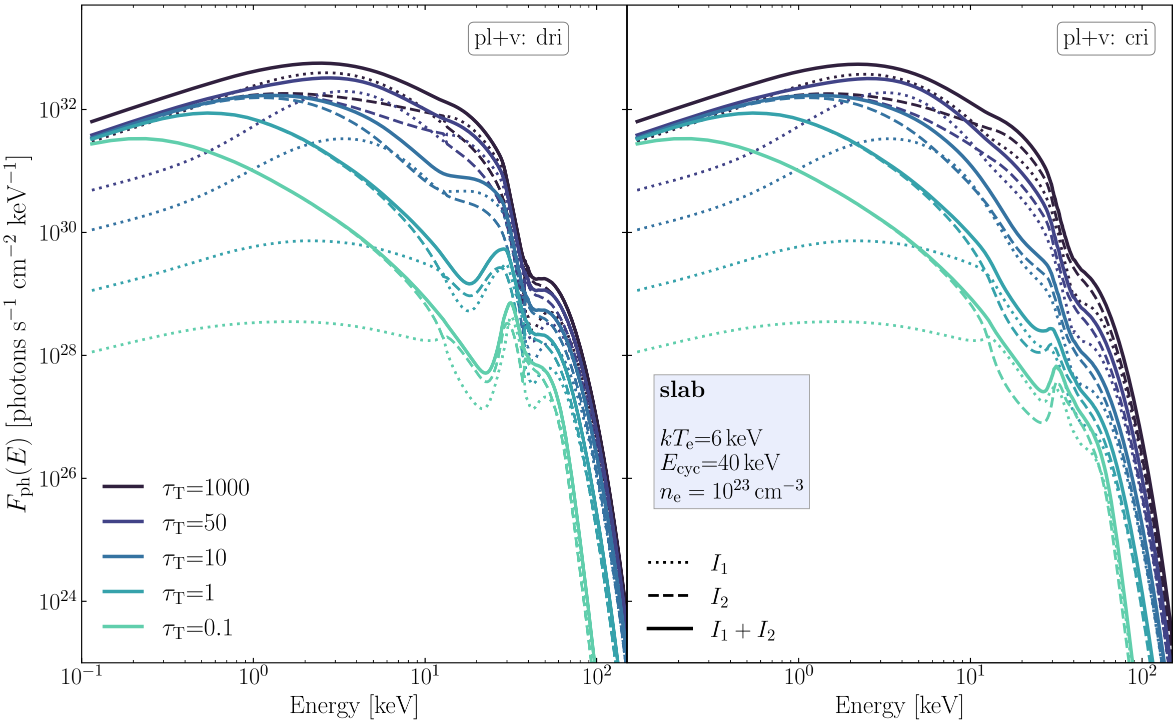

Figure 5.9: Emission from a highly magnetized slab of various optical depths shown for the case of the discontinuous (left) and continuous (right) refractive indices as functions of energy.

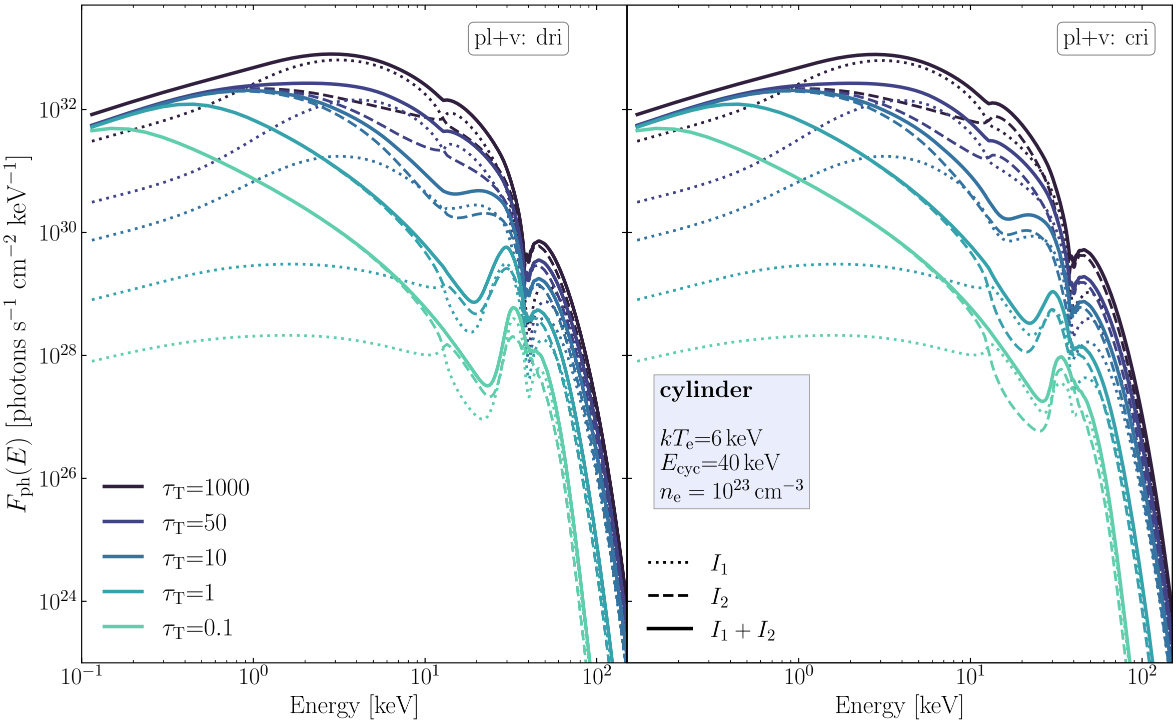

Figure 5.10: Same as in Figure 5.9, but for the cylinder geometry

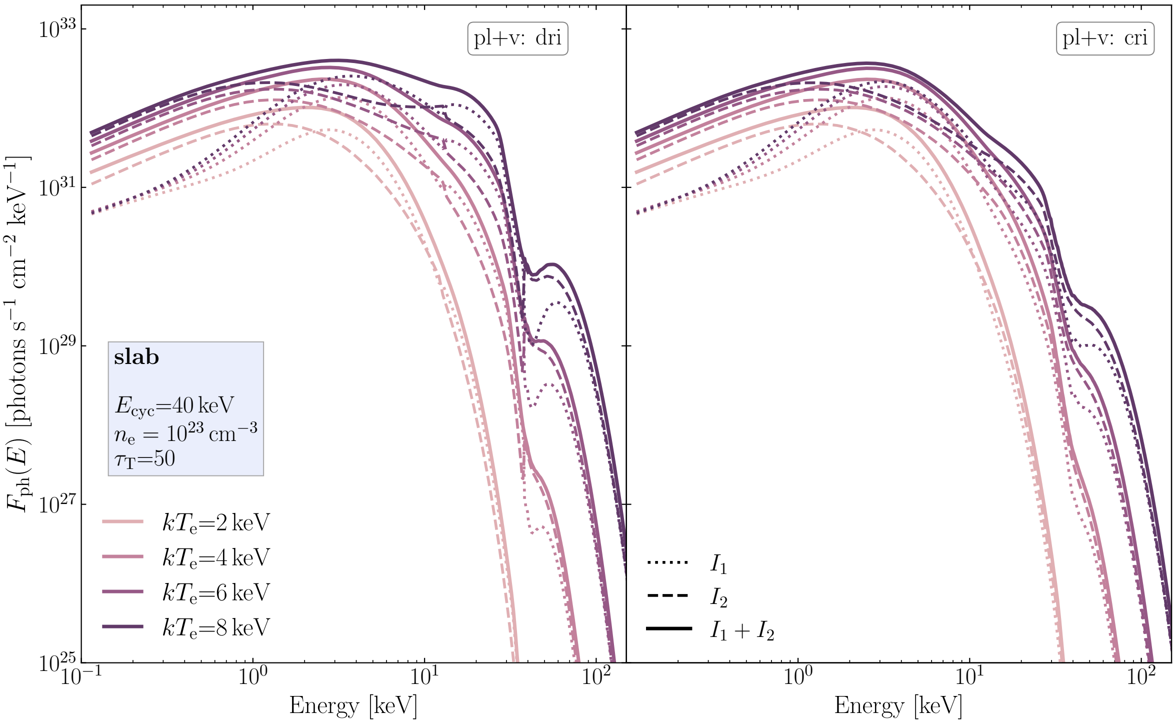

Figure 5.11: Emission from a highly magnetized optically thick slab for different electron temperature, shown for the case of the discontinuous (left) and continuous (right) refractive indices as functions of energy.

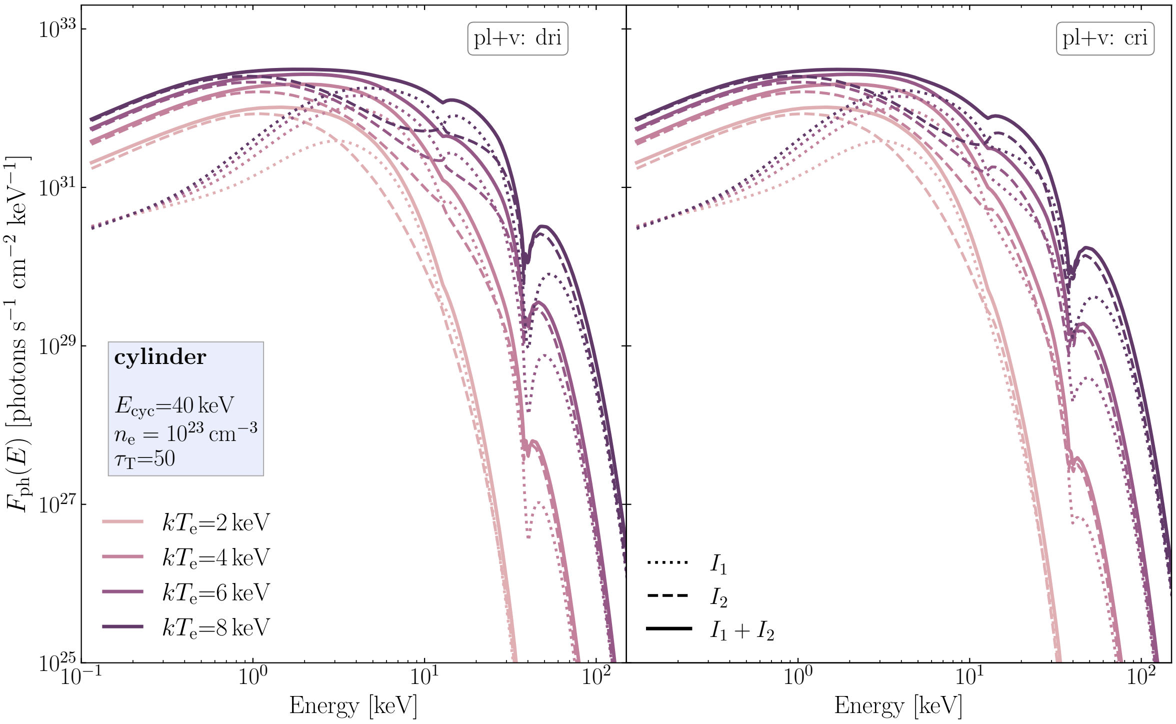

Figure 5.12: Same as in Figure 5.11, but for the cylinder geometry

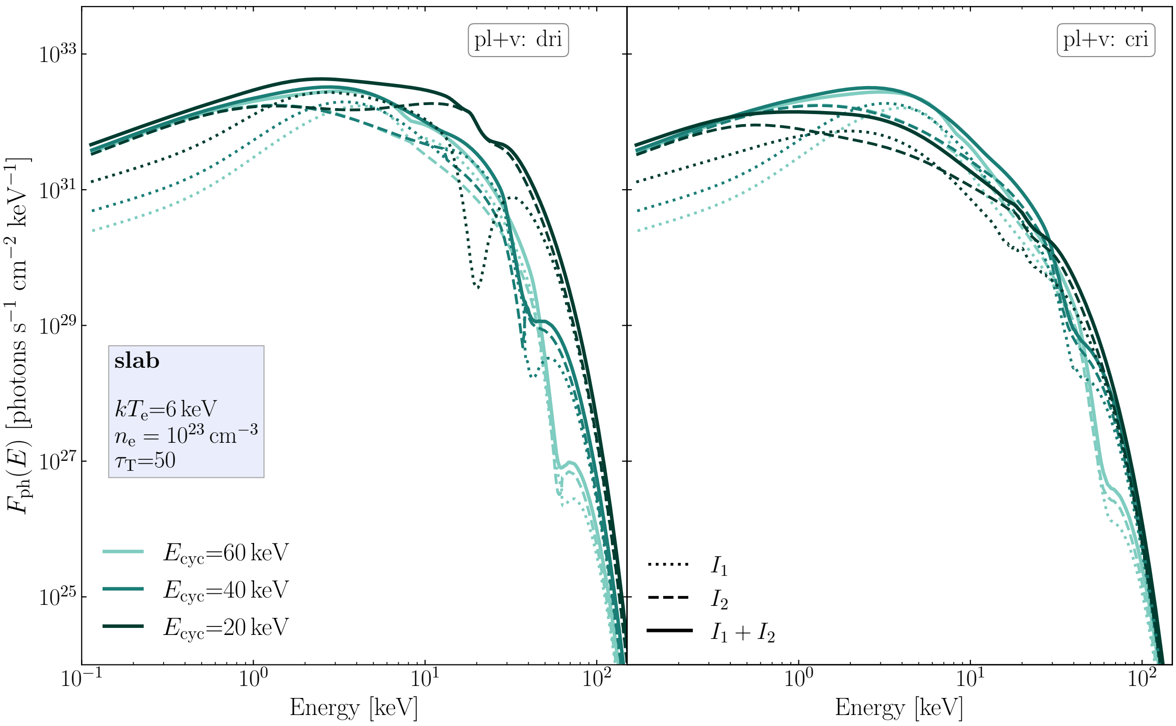

Figure 5.13: Emission from a highly magnetized optically thick slab for different magnetic field values, shown for the case of the discontinuous (left) and continuous (right) refractive indices as functions of energy.

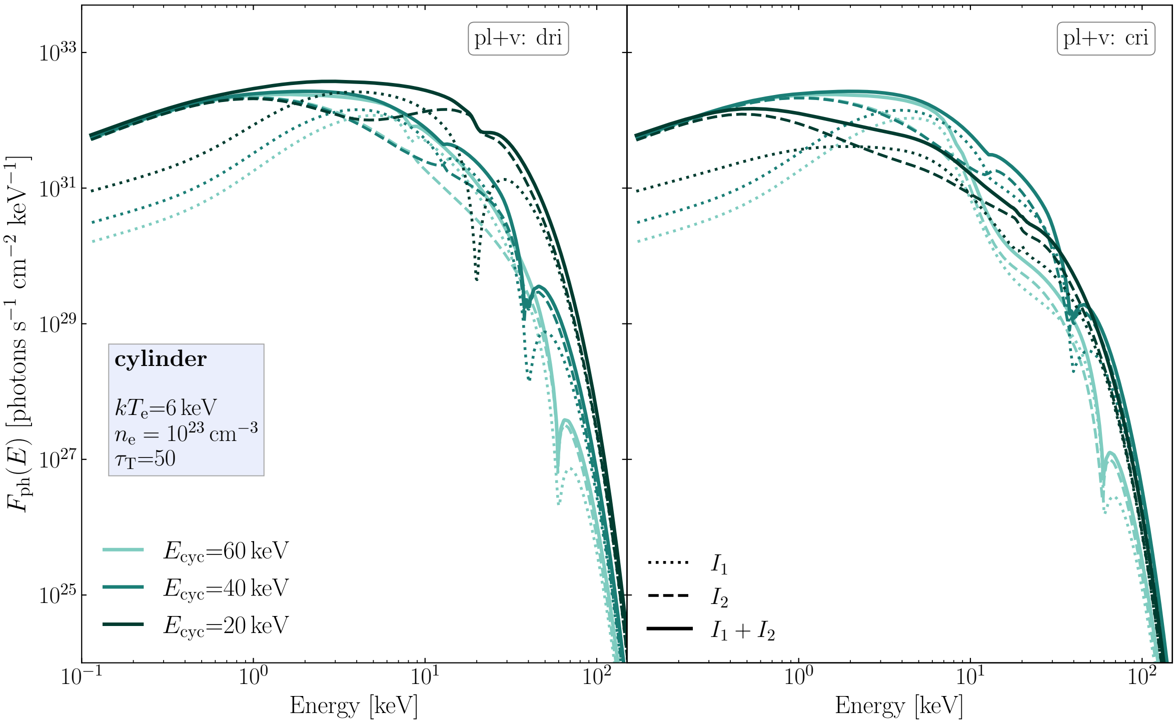

Figure 5.14: Same as in Figure 5.13, but for the cylinder geometry

Figure 5.11 and Figure 5.12 illustrate a role of the electron temperature on the spectral shape for the optically thick case. The low-energy part clearly reflects the equilibrium spectrum of the corresponding temperature. With increasing temperature, the role of the up-scatterings noticeably increases, resulting in harder spectra with an increased cutoff energy. Simultaneously, more intense redistribution of photons around the cyclotron resonance, accompanied by the broadening of the resonance, results in a more complex continuum shape below the resonance. The excess in the red wing of the cyclotron line can be significantly separated from the resonance energy, manifesting itself as a continuum feature.

Finally, the effect of the variation of the magnetic field is shown in Figure 5.13 and Figure 5.14. Here, adiabatic and non-adiabatic cases differ more dramatically. For the models considered here, the vacuum resonance, $\propto B^{-1}$, is located at approximately 24, 12, and 8 keV. For the lowest field with $E_{\rm cyc} = 20\,\text{keV}$ ($E_{\rm V} \approx 24\,\text{keV}$), the cyclotron line is barely visible for the case of the continuous refractive indices for both geometries.

For the parameters considered here, spectra for both studied geometries exhibit similar tendencies. The spectra for the cylinder geometry being harder, with a more pronounced cyclotron line and a vacuum resonance. The reasons behind this behavior are discussed in the following section.

5.3 DIFFERENTIAL FLUX AND BEAMING

A more pronounced difference between the two geometries occurs when one considers the angular dependency of the specific intensity. So far, only angular-integrated spectra (the specific flux) were shown. In this section, I present a view on angular dependency from a few different perspectives.

5.3.1 *Differential Flux*

Figure 5.15 illustrates the contribution of the differential fluxes at different angles to the total angle-averaged spectra, scaled down by a factor of ten from the angle with the highest flux level in order to improve the readability of the figures. It can be seen that for the slab (left) and the cylinder (right), the highest flux level originates from different directions, which reflects the difference in the angle-dependent diffusion coefficient for the radiative transfer equation for these two geometries (see Equation 4.56) and is enhanced by the geometrical factor $\sin\theta/\cos\theta$ which enters the differential flux. For the cylinder, the major contribution to the total flux comes at ∼90° to the magnetic field. For the slab, vise-versa, the flux is higher closer to the magnetic field direction. This difference in angular contributions explains why for the cylinder geometry the cyclotron line is more pronounced than for the slab one. The reason is that in the case of the slab the strongest contribution to the flux coincides with the strongest Doppler broadening of the cyclotron resonance close to the magnetic field direction. In the case of the cylinder, however, the highest flux level is accompanied by a narrow and sharp line profile at ∼90°, which makes the line more pronounced after averaging over angles. Qualitatively, this picture does not depend on the choice of the plasma parameters and reflects a *fundamental difference in two geometries*. For the same models, the differential flux is shown as a function of angle θ for selected energies in Figure 5.16. The major trend of the curves is defined by the factor of $\cos\theta$ for a slab and $\sin\theta$ for a cylinder. For the

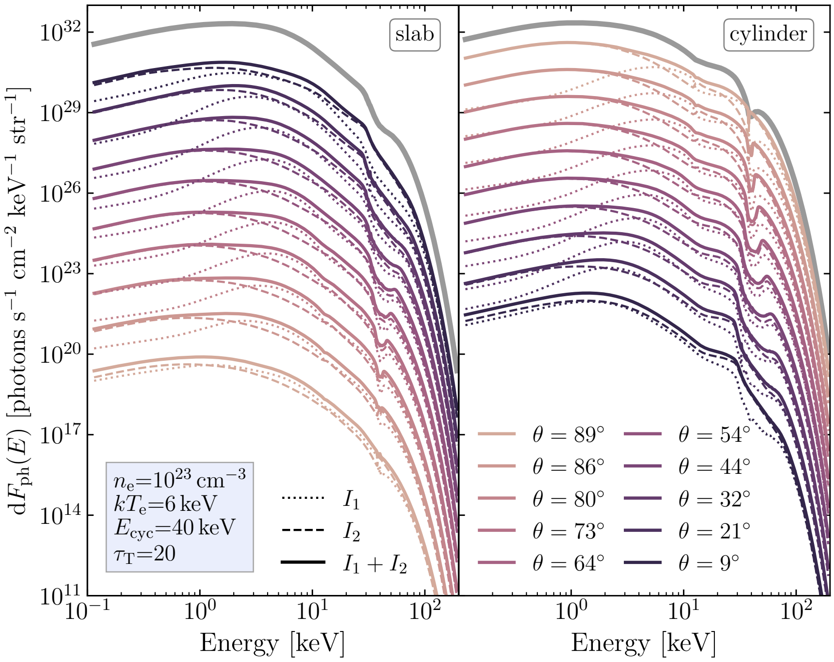

Figure 5.15: Differential flux emitted from the magnetized slab, $\mathrm{d}F = I(E, \theta) \cos \theta$ (*left*), and the magnetized cylinder, $\mathrm{d}F = I(E, \theta) \sin \theta$ (*right*). The grey thick curve shows the total angle-integrated spectrum. Fluxes from each angle are additionally scaled down by a factor of ten to improve visibility, starting after the top thin (colored) curve (*purple*, $\theta = 9°$, for the slab and *yellow*, $\theta = 89°$, for the cylinder), which remains at the original position and provides one of the major contributions to the total flux. Spectra of individual polarization modes are also shown, as before, in dashed (mode 2) and in dotted (mode 1) colored lines for each angle. The spectra are shown for the continuous behavior of the refractive indices.

slab case, the flux is the smallest for large angles to the magnetic field at all energies. A reduction at small angles in the cylinder case is less noticeable, especially for the energies close to the cyclotron resonance. For both geometries, the differential flux shows a significant excess at large angles for energies below and above the cyclotron resonance. This effect was noted already by Meszaros & Nagel (1985b) and reflects the strong dependency of the cyclotron resonance profile on θ. For θ close to perpendicular to the magnetic field direction, the resonance becomes very narrow and sharp, compared to much broader profile at smaller angles. The optical depth at energies right below and above the cyclotron energy is thus lower for the large angles. As a result, for resonant photons it is easier to escape the line core at large angles to the magnetic field. This effect is also responsible for the formation of the line wings and illustrates the importance of the redistribution in a highly magnetized medium (see also Schwarm et al. 2017b; Schönherr et al. 2007b).

5.3.2 *Emission Profiles*

For the discussion of the expected beam shapes, it is important to have a look at the angular distribution of the specific intensity, apart from the differential flux. The corresponding emission patterns are shown in Figure 5.17 (slab) and Figure 5.18 (cylinder), for all four choices of the polarization modes discussed in Section 5.1. The normalization is

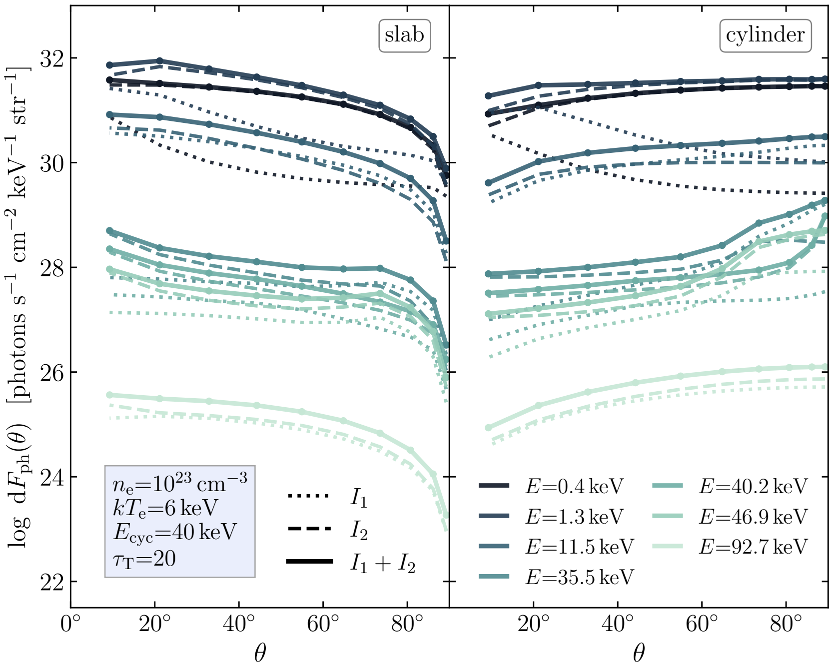

Figure 5.16: Differential flux emitted from the slab (*left*) and the cylinder (*right*) dependent on the angle for a few selected photon energies for the same model as in Figure 5.15.

performed independently for each mode and each energy beam to improve the readability of the figure, the last column with the sum over two polarization modes is important to get an impression of the total emission profile. The emission profiles for the slab case reveal overall more complex shapes than for the cylinder.

The first interesting result is a striking difference of the profiles at two soft energy bands: 0.1–2 keV and 2–12 keV. At the softest bands, the profiles of mode 1 are largely stretched along the direction perpendicular to the magnetic field. In all cases, when plasma influence is included (first three rows of Figure 5.17), the profiles obtain a local maximum along the magnetic field direction. Only for the pure vacuum polarization modes the profile remains stretched in a thin line perpendicular to the field value. The profiles for mode 2 remain to a high degree isotropic (except for some flattening closer to 0° and ±90°) and similar for all types of polarization modes. For the band 2–12 keV, the profiles are more stretched along the magnetic field direction and significantly split to the sides, with the maxima at ∼20° forming a "cat diagram" (Peter Kretschmar, priv. comm.). This pattern is seen for *for both modes of all types*, except for mode 1 in the pure vacuum case. This peculiar behavior of the profiles and a significant difference between the two *continuum* energy bands, where cross section behave in the similar way, can be understood by exploring the angle- and energy-dependent optical depth of photons of different polarization modes.

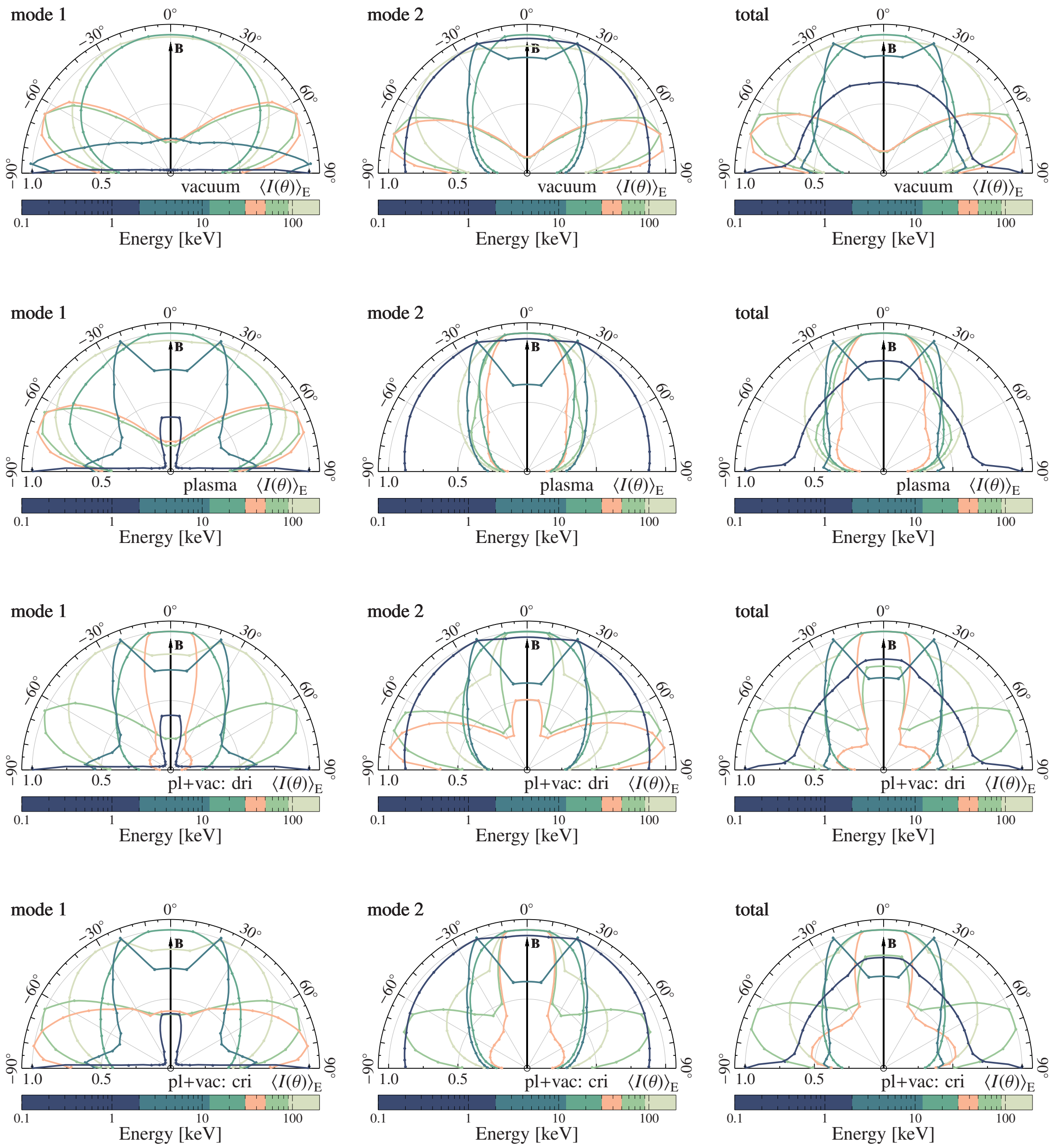

Figure 5.17: Emission profiles of the radiation field in the case of the optically thick slab geometry for different types of polarization modes, from top to bottom: pure vacuum, pure plasma, including vacuum polarization and discontinuous refractive indices, including vacuum polarization and continuous refractive indices. The parameters of the model are the same as in Figure 5.15.

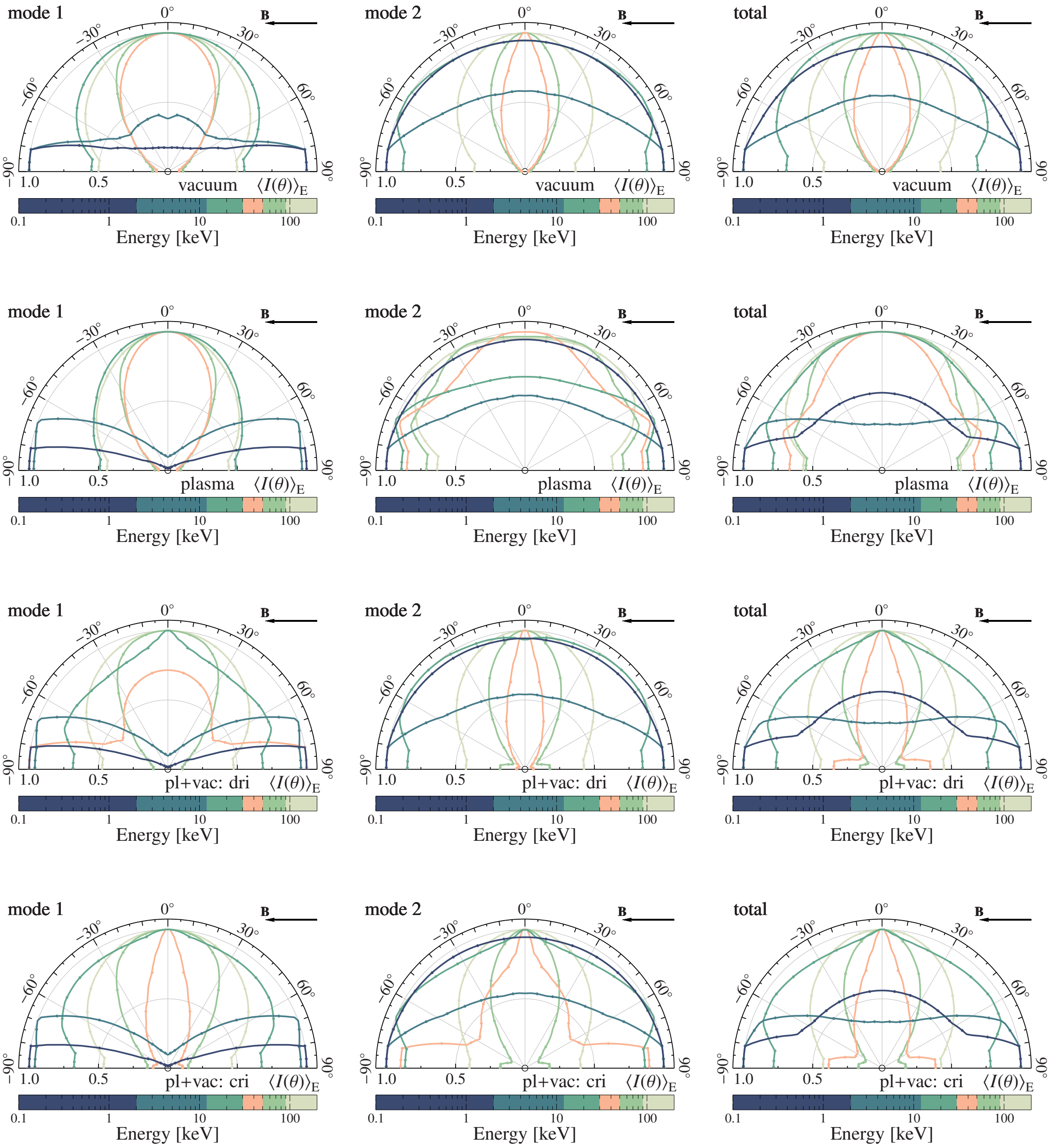

Figure 5.18: Emission profiles of the radiation field in the case of the optically thick cylinder geometry for different types of polarization modes, from top to bottom: pure vacuum, pure plasma, including vacuum polarization and discontinuous refractive indices, including vacuum polarization and continuous refractive indices. The parameters of the model are the same as in Figure 5.15.

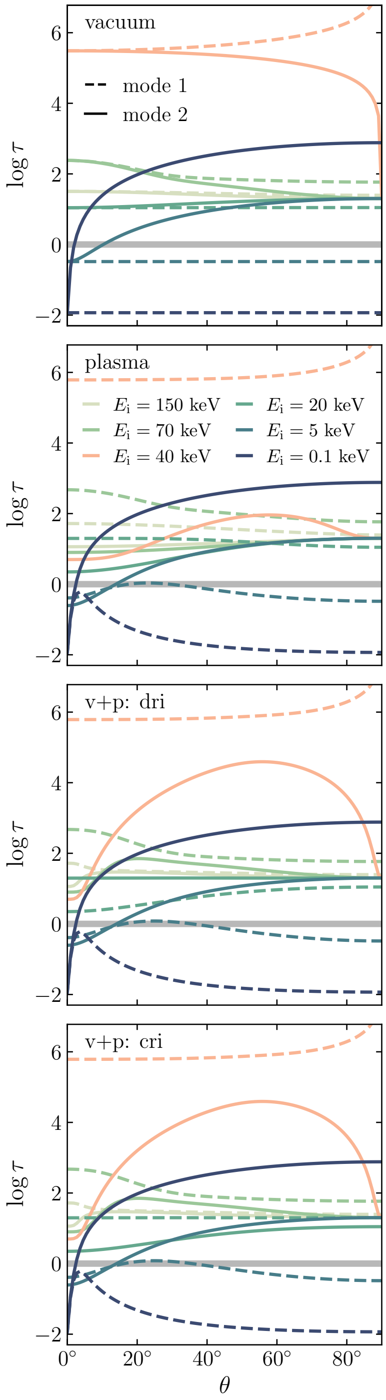

Figure 5.19: The total optical depth of the emitting region as a function of angle for photons of different energies, for the same plasma parameters as in Figure 5.15, shown for mode 1 (dashed) and mode 2 (solid) for the four types of polarization modes (different panels).

Figure 5.19 shows how the total optical depth depends on the direction of photon's propagation and its energy for mode 1 and mode 2 for each type of polarization mode. Naturally, the lines simply reflect the behavior of the corresponding cross sections, scaled by the total geometrical depth of the slab, the electron number density, and contributions of both, absorption and scattering (which show the same angular dependency; see Section 4.4.2). The thick gray line marks $\tau = 1$ and separates the optically thick and optically thin cases. These cases result in a fundamentally different dependency of the specific intensity on the underlying cross sections. As was noted by Nagel (1981b) and Mészáros (1992), in the case of the optically thin slab, all photons produced by free-free emission ($\propto \alpha_\mathrm{ff} B$) escape and the intensity shows the dependency $I(\theta) \propto \alpha_\mathrm{ff}(\theta)/\cos\theta \propto \sigma(\theta)/\cos\theta$, where $\cos\theta$ accounts for the total path length along the given direction. It is clear from Figure 5.19, that for the lowest energy band, the slab is transparent for mode 1 for all angles and types of polarization modes. For the pure vacuum case, its cross sections are isotropic (as seen from $\tau(\theta) \propto \sigma$ in Figure 5.19) and thus the angular dependency of intensity is determined by the $1/\cos\theta$ factor, which is responsible for the spikes at 90° in the emission profiles. For the cases including the real plasma contribution (three lower panels of Figure 5.19), the cross sections for mode 1 have a maximum at a few degrees above 0°, which results in the additional petal along the magnetic field direction. This petal is also expected to be slightly split near ∼0°, following the minimum in the cross sections, weighted by $1/\cos\theta$. This part, however, cannot be resolved with the coarse angular grid used for these simulations. For mode 2, on the other hand, the slab is transparent only close to ∼0° and is optically thick in all other directions. In this case, photon escape is governed by the characteristic mean free path along the ray and $I(\theta) \propto \cos\theta/\sigma(\theta)$ (the suggested analogue of the Eddington-Barbier relation; Mészáros 1992). This behavior explains why spikes at 90° do not appear in low-energy profiles of mode 2.

For the energy band 2–12 keV, all cases for both polarization modes show the cat diagrams, except for mode 1 in the pure vacuum case. For the latter one, the slab is again transparent at all angles with the optical depth slightly below unity and the emission profile is characterized by two petals close to 90°. The peculiar cat diagrams in the remainder of the cases for mode 1 originate from the behavior of the corresponding optical depth curves, with the regions near the "ears" (∼20°) being optically thick, unlike the rest of the profile. The "whiskers" close to 90° have the same mechanism of formation as in the previously discussed optically thin cases. A similar total shape of the profile for mode 2 also results from the mixed optical depths cases. The optical depth is again $\tau < 1$ near the magnetic field direction, where the minimum in the cross sections is enhanced by the $1/\cos\theta$ factor. At ∼20°, there is a transition to the optically thick regime, at the rest of the profile behaves as $\cos\theta/\sigma(\theta)$, which explains the minimum at 90°.

The profiles for the energy band below the cyclotron resonance, 12–30 keV, are significantly simplified due to the high optical depth at all angles and yet rather simple behavior of the respective cross sections (the lightest blue line in Figure 5.19). Even crossing the vacuum resonance at ∼12 keV does not bring a dramatic difference in the cases where plasma and vacuum effects are both included together. In the cyclotron resonance (red lines, 30–50 keV), the redistribution effects create more peculiar profiles. In the pure vacuum case, the angular dependency of the cyclotron line profiles on θ is the same for both polarization modes, and thus the profiles have a very similar shape. The two-petal structure with the maxima at ∼70° has its origin in the energy and angle redistribution within the resonance. This effect has already been described above and results from the photon escape at the line wings at larger angles, where the cross section is smaller that at the lower angles to the magnetic field (Meszaros & Nagel 1985b). For the pure plasma case, mode 2 does not exhibit resonance at angles close to 0° and the profile takes shape of a pencil beam. Due to the mix of the mode properties and redistribution effects, the profiles in the combined plasma and vacuum case acquire a more complex shape near the cyclotron resonance. For the summed mode contributions (last column in Figure 5.17), the total profile has three distinct petals peaking at 0° and around ±80°. Similar profiles appear for the blue wing of the cyclotron line, with even enhanced side petals. At even higher energies, however, the side petals are noticeably reduced as the high-energy photons can resonate with ambient electrons, when propagating at larger angles.

In the case of the cylinder (Figure 5.18), the same reasoning as before is applied, except for the factor $\cos\theta$ for the characteristics along the ray, which should be changed to $\sin\theta$. At soft energies, the profiles are now stretched along the magnetic field direction. In the optically thick case at intermediate energies, most of the profiles acquire minor side peaks at ∼ 70° and a slight suppression near ∼ 90° to the normal (here, 90° corresponds to the magnetic field direction). In the cyclotron resonance, the beams exhibit again most complex shape for the mixed case of plasma and vacuum contribution, with the total profiles having three petals: the strongest one along the normal, and two along the magnetic field lines. At higher energies, however, this shape is almost completely suppressed by the geometrical factor $1/\sin\theta$, which focuses the emission along the normal of the cylinder wall.

5.4 ACCRETION MOUND MODEL

In the previous sections, I described some properties of emission from homogeneous highly-magnetized atmospheres. Many of the peculiarities in the spectral shape were created by polarization and redistribution effects. In this section, I present a simplified model for the accretion mound to study the influence of the *inhomogeneous* medium on the formation of the spectrum, especially in the presence of the vacuum resonance.

As was described in Chapter 3, at higher mass-accretion rates onto a highly magnetized neutron star, matter deceleration occurs in the extended radiative shock. The deceleration of the flow occurs gradually and throughout most of the accretion column, such that the plasma flow is likely too tenuous to provide significant emission by itself. It, however, affects the total spectrum by thermal and bulk Comptonization and angular redistribution of photons in the moving flow. The major contribution to the emission is expected to come from near the surface, where a dense thermal mound is formed (see, e.g., Wang & Frank 1981; Postnov et al. 2015; Gornostaev 2021). Some fraction of the emission of the mound can escape preferentially from the sides, and the rest serves as "seed" photons, which are reprocessed in a more tenuous part of the column (a similar model was proposed by Yahel 1980a). Often, seed photons for the accretion column are assumed to have a black-body spectral energy distribution (see, e.g., Becker & Wolff 2007). However, the emission from a dense, optically thick, and highly magnetized plasma can differ significantly from the Planckian one (see, e.g., the homogeneous models for high density discussed in Section 5.2).

With the simplified model presented in this section, I attempt to address two main questions:

- What are the spectral properties of emission from a dense inhomogeneous thermal mound?
- How does vacuum polarization in the inhomogeneous medium affect these properties?

Here, as earlier in Section 5.2, only angle-averaged properties of emission in the rest frame of the emitting plasma will be discussed.

I model the mound as a slab of a total thickness $h = 500\,\mathrm{m}$ and a radius of $r_0 = 300\,\mathrm{m}$. It is assumed that at the top of the mound, the velocity of the flow remains at 5% of its free-fall value v_{ff}. At the bottom, the velocity is almost zero, $v/v_{\mathrm{ff}} = 10^{-3}$. Between the top and the bottom of the mound, I assume a linear velocity profile. Then the density profile in the mound can be found from the continuity equation,

$$\rho v = \frac{\dot{M}}{\pi r_0^2}, \tag{5.4}$$

where the mass accretion rate $\dot{M} = 10^{17}\,\mathrm{g\,s^{-1}}$. The sketch of the model is shown in Figure 5.20. Under these conditions, the electron number density varies from $\sim$a few $\times 10^{22}\,\mathrm{cm^{-3}}$ at the top of the mound, up to $\sim 10^{24}\,\mathrm{cm^{-3}}$ at the bottom. The electron temperature and the magnetic field are assumed to stay constant within the mound, $kT_{\mathrm{e}} = 5\,\mathrm{keV}$ and $E_{\mathrm{cyc}} = 40\,\mathrm{keV}$.

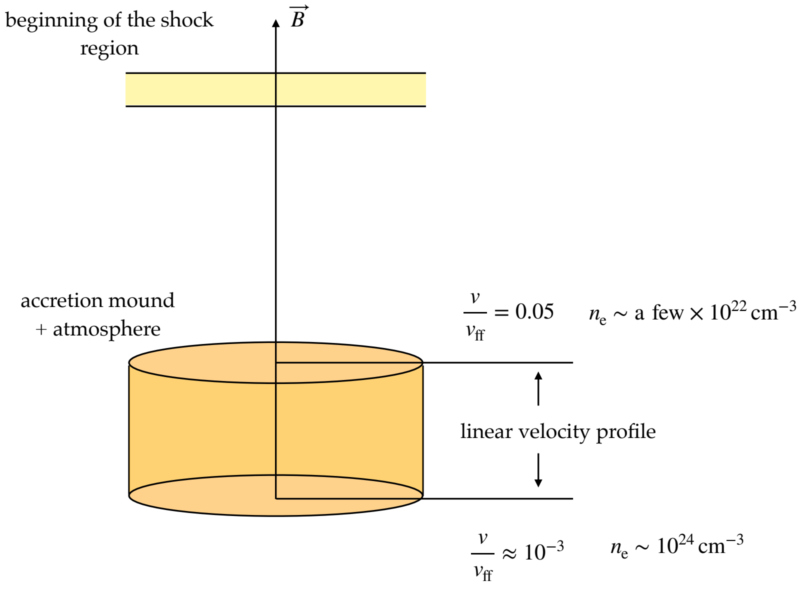

Figure 5.20: Schematic depiction of the thermal mound model. Only the bottom (orange) region is considered in the calculations.

Figure 5.21 shows the flux from the thermal mound in two polarization modes for the case of adiabatic and non-adiabatic mode propagation across the vacuum resonance. It illustrates that in an inhomogeneous medium, with the density profile changing by a few orders of magnitude, there is no dramatic difference between the adiabatic and non-adiabatic case. For the chosen density profile, the vacuum resonance changes from $\sim$38 keV at the bottom of the mound to $\sim$7 keV at its top layer. The line is then imprinted in the emerging spectrum as a weak absorption feature *for both cases*. In case of adiabatic mode conversion the spectrum has a higher suppression near the vacuum and cyclotron resonances. The high-energy continuum is only slightly affected by the adiabatic propagation of polarization modes. As expected, the continuum at soft energies converges to the shape of the corresponding black-body spectrum (for $kT = 5$ keV).

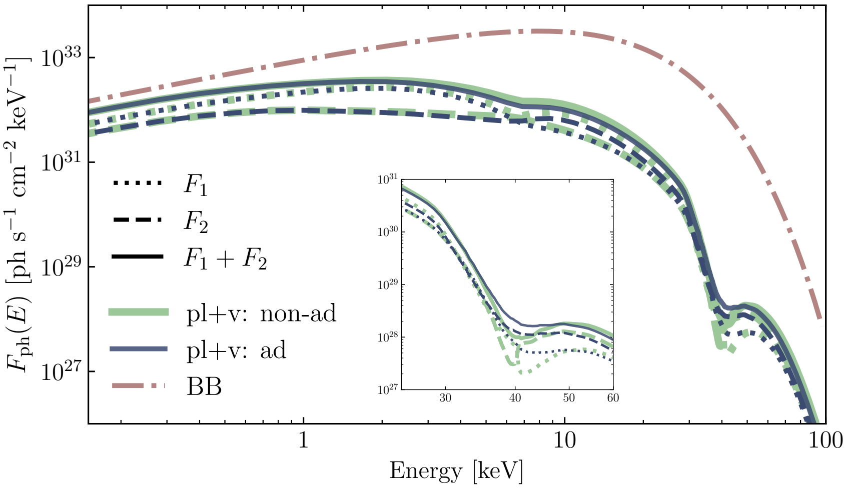

Figure 5.21: Spectrum from the inhomogeneous accretion mound with its polarization components. The cases of adiabatic (thin, coral) and non-adiabatic (thick, blue) mode propagation are presented. The dash-dotted line shows the Planckian spectrum of the same temperature, $kT = 5$ keV.

A comparison of spectra calculated including vacuum polarization to the pure plasma and vacuum cases is shown in Figure 5.22 (top). As before, the spectra of the radiation emergent from the dense optically thick slab in the pure plasma case exhibit a very weak cyclotron line as mode 2 (ordinary) dominates at these energies. For the pure vacuum modes, the cyclotron resonance is significantly deeper than for both cases including both vacuum and plasma effects.

The polarization degree for each type of polarization modes is shown in Figure 5.22 (bottom). The spectrum calculated with the pure vacuum modes provides the highest degree of polarization at energies below $\sim$10 keV. At higher energies, above $\sim$20 keV, the pure plasma modes predict the largest polarization degree, reaching almost 100% in the cyclotron resonance. Both cases including plasma and vacuum contribution show strong depolarization at energies near the vacuum resonance and in the red wing of the cyclotron line. The case of adiabatic mode propagation results in the overall lowest degree of polarization.

Caiazzo & Heyl (2021b) suggested that the net effect of the vacuum polarization in the accretion column is a small depolarization at the energy above the minimum resonance determined by the lowest density. The simulations presented here are in agreement with the fact that the net effect of the vacuum polarization is introduced to the energies above the vacuum resonance, corresponding to the region of lowest density. The case of the mixed plasma and vacuum contribution introduces, however, significant depolarization at mid and high energies compared to the pure plasma case chosen by Caiazzo & Heyl (2021b) (there, however, the thermal effects for the cyclotron resonance were omitted). The only

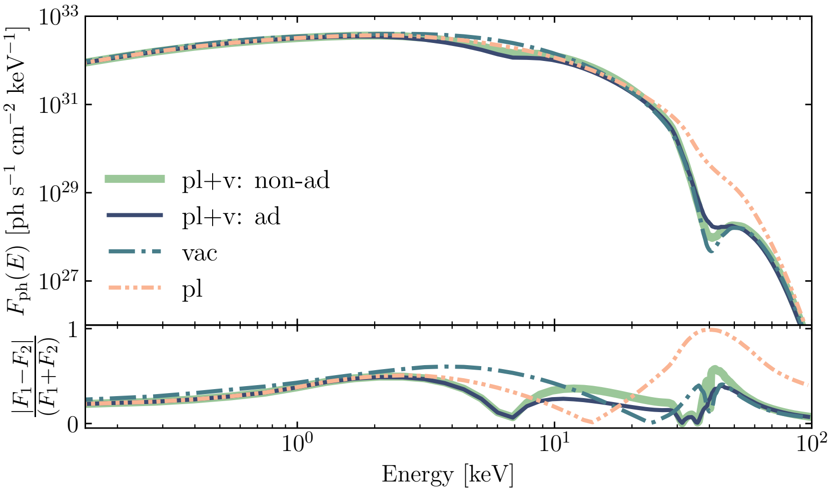

Figure 5.22: *Top:* Total flux emitted from the inhomogeneous accretion mound for different types of polarization modes: pure magnetized plasma (*dotted*), pure vacuum (*loosely dashes*), magnetized plasma with the vacuum polarization effects and adiabatic conversion (*dashed*), and magnetized plasma with the vacuum polarization effects and non-adiabatic conversion (*solid*) modes. *Bottom:* Corresponding polarization degree.

exception is a narrow range of energies around 10–11 keV, where the intersection of the spectra for the two modes cancel out their contributions in the plasma case. In fact, depolarization starts slightly below the lowest vacuum resonance, at ∼3 keV. It results from the angle averaging and the fact that the vacuum resonance has different width at different angles.

The polarization signal for the case of included contributions of vacuum polarization and magnetized plasma, obtained with the polarized radiative transfer, is overall lower than that predicted by the accretion model of Caiazzo & Heyl (2021b) in the neutron star rest frame. I attribute this difference to the radiative transfer effects, including photon redistribution in the warm medium and mode conversion, which were not included in that model.

In reality, a number of additional effects are expected to further decrease the polarization degree. First of all, some part of the emission is processed in the inhomogeneous, but much more tenuous, accretion column above the mound. In addition, the velocity of the flow near the side-walls is expected to drop down much closer to the surface than at the center of the column due to the rapidly decreasing energy density (see, e.g., Wang & Frank 1981). This means that radiation from the thermal mound, which is already depolarized to some degree by vacuum polarization, will pass through the tenuous inhomogeneous medium. This is likely to move the "last vacuum resonance" to even lower energies, furthermore depolarizing the continuum above. Together with some depolarization in the magnetosphere of the neutron star, the vacuum polarization affecting propagation of photons throughout the whole emission region could be the reason for the low polarization degree of Her X-1 (Doroshenko et al. 2022, ∼ 10%) and Cen X-3 (Tsygankov et al. 2022, ∼ 5.8%) observed by *IXPE*, which is far below theoretical predictions for accretion columns (Caiazzo & Heyl 2021b,a).

5.5 CONCLUSIONS

The main message of this chapter is that when modeling the broad-band X-ray spectra from highly magnetized accreting neutron stars, effects of anisotropy, redistribution and polarization, as well as the correct choice of polarization modes are crucial for obtaining realistic results. Modeling the continuum while omitting effects of the resonant scattering, as well as simulating cyclotron lines only in the optically thin region with a predefined phenomenological continuum input, will naturally prevent the reproduction of more sophisticated spectral shapes observed for many High-Mass X-ray Binaries (see Chapter 3). On the other hand, even the simplified models for the emission considered here, which include these basic effects in a combined treatment of the continuum and the cyclotron line, result in a variety of complex broadband spectra. The main results can be summarized as follows:

- Polarization-dependent modeling is crucial for reproducing the complex continuum shape, which is created by the interplay of the two polarization modes. The natural alternation in the dominance of the modes in the total flux across the spectrum can result in excesses and dips on top of the power-law-like continuum. This effect can explain the need to use the "10-keV" feature and two-component Comptonization models to describe the observed spectra. Vacuum polarization can enhance this effect by introducing additional interplay between classically defined polarization modes.

- I showed that for warm Comptonizing inhomogeneous atmospheres the vacuum resonance can introduce a weak dip in the spectra, mimicking a cyclotron line, which in fact is located at much higher energies (a similar effect was shown, e.g., by Ventura et al. 1979; Kaminker et al. 1982; Soffel et al. 1985, in the absence of energy redistribution).

- In the case of continuous refractive indices and adiabatic mode propagation, a depression of the continuum between the vacuum and cyclotron resonances can form, and the cyclotron line can be slightly suppressed (this effect was described for magnetar-like fields by Ho & Lai 2003).

- Angular redistribution and thermal effects are also key elements of complex continuum formation. These, combined with polarization effects, can produce a broad excess below the cyclotron line energy (sometimes as low as at $E \sim 0.5E_{\mathrm{cyc}}$) without any additional sources of photons. This excess is the red wing of the cyclotron line, which is enhanced by photons escaping the line core during Compton scattering. This feature is more connected to the cyclotron line (the emission feature at $\sim$20 keV in the spectra of A 0535+262 is a possible example; Ballhausen et al. 2017) and potentially will show variability with the observed rotational phase.

- The vacuum polarization can significantly affect the polarization signal across a wide energy range due to the additional interplay of the modes. Within the frame of this model, the complexity of the continuum can be naturally accompanied by a reduction of the polarization signal.

- The spectra derived for the polarization modes for a slab and a cylinder show that due to the complexity of mode interchange, treatment of the task in terms of one polarization mode predominantly leaving the walls of the cylinder or the top of the slab is rarely justified. An exemption could be the softest X-ray energies, $\lesssim 1\,\mathrm{keV}$. There, however, emission spectra are defined by mode 2 for both geometries.

- The beam shapes of the outgoing radiation are more complex in the case of the slab geometry, exhibiting a splitting of the profiles along the magnetic field direction at soft energies. The emission profiles in different continuum bands can differ dramatically due to the angle- and energy-dependency of the optical depth. Vacuum polarization produces more complex three-petal structure of the beam near the cyclotron resonance. For the cases studied here, the slab profiles can only rarely be described as a "traditional" pencil beam. For the cylinder case, the patterns are in general broader, with lower modulation, except for the cyclotron resonance, where the beam is stretched to the sharp pencil beam along the surface normal (except for the case of mode 2 for the pure plasma normal modes). For energies away from the cyclotron resonance, a fan beam could provide a feasible description for the profiles.

To answer the question about the beam shapes in the case of the extended accretion column, emitting from the walls and the top, two-dimensional radiative transfer is required. One would expect that for a high column, the emission component propagating outwards in a pencil-like shape can also leave the column walls (especially considering its side petals), as it is locked in the vertical direction by the falling flow. In this case, the profile from the walls will have a more complex shape. For the same reason, it is likely that attributes of the slab and cylinder models are mixed in the properties of the emission from accretion columns. At the subcritical regime, however, the emission region is expected to resemble the slab geometry. The extreme case of this regime is quiescent accretion onto a magnetized neutron star, where the slab geometry gives a feasible approximation, and is presented in the following Chapter 6.

6

X-RAY EMISSION FROM POLAR CAPS AT LOW MASS-ACCRETION RATES

"Why in the world would anyone *want to study stellar atmospheres?"*
E. Salpeter to D. Mihalas (Hubeny & Mihalas 2014)

The combined calculations for the angle-, energy-, and polarization-dependent radiative transfer and the hydrodynamic structure of the accretion channel near the surface of a neutron star is a complex task, which has not yet been tackled in its fullness. The various models presented in Chapter 5 investigate basic aspects of the polarized emission formation, but yet are too elementary for a more sophisticated comparison against the rich variety of observational data. In this chapter, I restrict the problem to very low mass-accretion rates, $\dot{M} \lesssim 10^{15}\,\mathrm{g\,s^{-1}}$, where a simplified physical picture of accretion allows one to push the modeling further compared to the previously discussed cases.

In Section 3.1.1, I described that according to recent observations, Be X-ray Binaries with slowly rotating neutron stars can enter the regime of stable accretion in quiescence. The spectra of X-ray pulsars observed in this state exhibit a two-hump shape, peaking at $\sim$5 keV and $\sim$30–60 keV (see, e.g., Tsygankov et al. 2019b; Lutovinov et al. 2021). In this regime, penetration of the matter inside the magnetosphere is limited to very low mass-accretion rates. Here, I adopt the common assumption that, in this case, the tenuous flow falls onto the surface of the neutron star and is stopped in the atmosphere by collisions with ambient particles (Zel'dovich & Shakura 1969; Nelson et al. 1993). The detailed discussion of this collision-dominated braking regime in the neutron star atmosphere is given in Section 3.2.3. The structure of the nearly-static atmosphere with negligible pressure of the radiation field is easier to model than in the dynamic case at higher mass-accretion rates. Moreover, this problem is significantly restricted to the vertical direction, along the normal to the atmosphere. Thus, the one-dimensional radiative transfer provides a fair approximation to obtain the radiation field. This simplified physical picture presents an opportunity for more extended and consistent modeling, which involves the atmospheric structure, the polarized spectra with cyclotron lines, energy-dependent radiation beaming, and pulse profiles seen by a remote observer. This level of consistency is not easily accessible for the higher mass-accretion rates when the contribution of dynamic effects on the spectral formation cannot be ignored.

This chapter describes a model for the X-ray emission from the atmosphere of a highly magnetized neutron star, accreting at low mass-accretion rates. The foundation of this model was published in Sokolova-Lapa et al. (2021). Here, however, the basic emission model is reformulated in a slightly more general way, which is less specific to the exact deceleration process, as long as collisional excitations provide a negligible contribution to braking. For this reason, the model is restricted only to strong magnetic fields, $B \gtrsim 4 \times 10^{12}\,\mathrm{G}$, when this contribution is expected to be small, as even protons at the free-fall velocity are not likely to excite the ambient electrons from the ground Landau level (see, e.g., Miller et al. 1989). This results in a reduction of the principal parameters. More detailed information is provided in the general description of the model in the following section. In addition, it is important to note that the radiative transfer simulations for the model are still based on the pure vacuum polarization modes, as given in Sokolova-Lapa et al. (2021).

The possible consequences of this choice are discussed in Section 6.4, in the context of the results obtained in Chapter 5.

The chapter is organized as follows. Section 6.1 describes the general physical picture adopted for modeling in the neutron star rest frame and the dependency of the emergent flux on the atmospheric structure and basic parameters. It also presents a simplified model compatible with X-ray packages for data analysis, which can be applied to phase-averaged spectra. The research presented in this first section was published in Sokolova-Lapa et al. (2021, hereafter, Paper I), in tight collaboration with co-authors of this paper. The text of Section 6.1 therefore follows closely Paper I, but also addresses the modification to the model mentioned above and includes some necessary corrections to the published version. The second principal part of the problem is presented in Section 6.2 and includes the analysis of the angular dependency of the radiation field and the coupling of the obtained emission with a ray-tracing code for slowly rotating neutron stars by S. Falkner (Falkner 2018) to obtain pulse profiles and phase-dependent spectra for the remote observer. It studies the influence of neutron star rotation and geometry on the phase-averaged and phase-resolved spectra and pulse profiles. Based on these most recent calculations, a new model, which includes the effects of the gravitational field and rotation of the neutron star, is presented in Section 6.3. This model can be used for the phase-resolved and phase-averaged data analysis. It permits us to constrain the geometrical parameters of the system: the location of the poles and the inclination of the observer's line of sight with respect to the rotation axis of the neutron star. The results obtained in Section 6.2 and Section 6.3 are prepared for publication in a separate paper (Sokolova-Lapa et al., in prep.). Section 6.4 summarizes the results, adds remarks on the model limitations, and outlines prospects for future work.

6.1 ATMOSPHERIC EMISSION

This section presents the basis of the model for the emission from accretion-heated polar caps of a neutron star. It is referred to as `polcap` and serves as a foundation for several models applicable to spectral fitting. The model considers the accretion of the tenuous ionized plasma at low mass-accretion rates, $\dot{M} \lesssim 10^{15}\,\mathrm{g\,s^{-1}}$ onto the polar caps of a highly magnetized neutron star with $B \gtrsim 4 \times 10^{12}\,\mathrm{G}$. It is assumed that the flow merges into the neutron star atmosphere and decelerates predominantly by Coulomb collisions. The reprocessed energy of the accretion flow is emitted in X-rays by magnetic bremsstrahlung and shaped by resonant Comptonization inside the nearly-static atmosphere. The tenuous flow does not affect the emergent radiation field.

The model is characterized by the following parameters: the mass-accretion rate $\dot{M}$, the polar cap radius r_0, and the surface magnetic field B of the neutron star, expressed in the cyclotron energy E_{cyc}. The standard parameters for the neutron star mass and radius are considered: $M_{\mathrm{NS}} = 1.4\,M_{\odot}$ and $R_{\mathrm{NS}} = 12\,\mathrm{km}$. The previous version of `polcap` published in Paper I included one additional parameter, the amount of accretion energy which is deposited to the collisional excitations in the atmosphere, f_{cyc}. The influence of these excitations was included in a simplified way and the resulting effect on the spectra, such as reduced strength of the low-energy component, has other potential channels of origination. The new version of the model is restricted to the high values of the magnetic field, when the collisional excitations are not expected to modify significantly the braking process and the emergent radiation field, and is constructed without the f_{cyc} parameter. The possible consequences and some additional reasonings on this topic are provided in Section 6.4.

Section 6.1.1 describes the approach to model the temperature and density structure of the atmosphere by solving the energy balance equation. Section 6.1.2 explains how the atmospheric structure is coupled to the polarized radiative transfer calculation. These two sections present the foundation of the model. The methodology of this solution was obtained in collaboration with M. Gornostaev (MSU), who provided a major contribution to the idea of the atmospheric structure calculation and the way it could be coupled to the radiative transfer. All necessary scripts for simulations were written by me. I also had valuable discussions with K. Postnov, J. Wilms, and N. Shakura on this topic. Section 6.1.3 demonstrates the resulting atmospheric structure and the formation of the spectra of the emergent radiation field. A simple model for spectral fitting based on the assumption of isotropic emission is presented in Section 6.1.4.

6.1.1 *Atmosphere Model*

The atmosphere is modeled by a one-dimensional plane-parallel slab, as introduced in Section 4.5, similar to the other slab models presented in Chapter 4. When ionized flow collides with the atmosphere of the neutron star, it gradually loses its energy in collisions with ambient particles. It is expected that proton–electron Coulomb collisions are the most efficient in decelerating the flow (Kirk & Galloway 1982; Miller et al. 1987), although proton–proton scattering could also play an important role for the magnetic fields of interest (Miller et al. 1989). As the current version of the `polcap` model does not include modeling of the kinetics of the braking process and also assumes negligible influence of excitations due to proton–electron collisions, it is irrelevant which of these two processes prevails in the atmosphere. The deceleration process enters the model only via the assumption of a fixed energy deposition profile, which provides atmospheric heating. The geometry is shown in Figure 6.1.

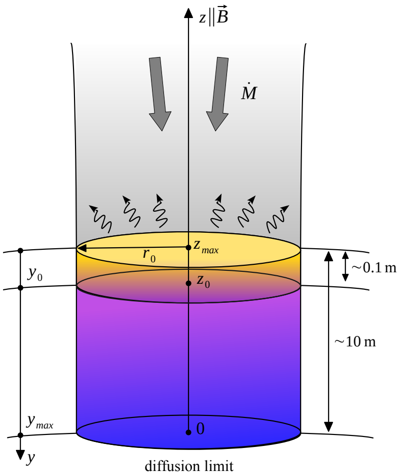

Figure 6.1: Sketch of the accretion-heated polar cap. The cap represents an emitting layer of the neutron star atmosphere with the total column density $y_{\max}$. The corresponding geometrical depth is $z_{\max}{\sim}10$ m and the polar cap radius is $r_0{\sim}100$ m. The characteristic stopping depth in column density (and geometrical) scale is indicated as y_0 (z_0). Figure 1 from Sokolova-Lapa et al. (2021), reproduced with permission © ESO.

The spatial variation of the atmosphere is convenient to describe in terms of the column density

$$y(z) = \int_z^{z_{\max}} \rho(z')\mathrm{d}z', \tag{6.1}$$

where $\rho(z)$ is the vertical density profile and $z_{\max}$ is the total geometrical depth of the considered layer. The atmosphere is calculated down to high column density values, $y = 10^3\,\mathrm{g\,cm^{-2}}$, which ensures thermalization of the radiation field and validity of the diffusion boundary condition at the bottom. At the same time, the corresponding geometrical depth is only $z_{\max} \sim 10$ m. Another important length of this task is y_0, the characteristic depth above which the majority of the kinetic energy of the accretion flow is deposited. It can be understood as a measure of the proton stopping depth in the atmosphere. Without the kinetic calculations, however, this analogy should be taken with care. For now, y_0 is assumed to be known. It is not a free parameter of the model, and its value will be found from the energy conservation considerations described in Section 6.1.2.

The accretion process thus provides the heating of the atmosphere, characterized by some profile $\mathrm{d}E/\mathrm{d}y$, in addition to the free-free absorption and Compton scattering. The plasma cools down by bremsstrahlung and inverse Compton scattering. To obtain the temperature and density profiles, the model closely follows derivation by Zel'dovich & Shakura

(1969) for a collisionally heated non-magnetized atmosphere of a neutron star. They assumed that all energy is released above y_0, which was associated with the proton stopping depth, with constant energy deposition per unit mass. The discontinuity at y_0 has to be addressed if one attempts to simulate the atmosphere below this value. In the `polcap` model, this energy deposition profile is modified by an exponential cutoff. The main effect of this modification is smoothing of the transition region near y_0. Thus, the energy balance in the atmosphere is given by

$$\Lambda_\mathrm{B} + \Lambda_\mathrm{C} = \frac{\rho F_\mathrm{eff}}{y_0} \exp\left(-\frac{y^2}{y_0^2}\right), \tag{6.2}$$

where Λ_B and Λ_C represent the contribution of free-free and Compton processes, respectively, and are taken for non-magnetic processes, as given by Equation 1.3 of Zel'dovich & Shakura (1969, see also Equation 2-3 in Sokolova-Lapa et al. 2021). The effective flux, F_eff, is the bolometric flux in the assumption that all kinetic energy transferred at the rate $\dot{M}$ is re-emitted from the polar cap of a surface area πr_0^2

$$F_\mathrm{eff} = \frac{G M_\mathrm{NS} \dot{M}}{R_\mathrm{NS}} \frac{1}{\pi r_0^2}. \tag{6.3}$$

The efficiency of Compton processes depends on the radiation field. Here, the diffusion approximation is adopted to obtain the dependency of the radiant energy density, $\epsilon(y)$, on the depth in the atmosphere

$$\frac{d\epsilon}{dy} = -\frac{3\varkappa_\mathrm{T}}{c} F(y), \tag{6.4}$$

where the flux is changing as

$$F(y) = F_\mathrm{eff} \frac{(y - y_0)}{y_0} \exp\left(-\frac{y^2}{y_0^2}\right) \tag{6.5}$$

and $\varkappa_\mathrm{T} = \sigma_\mathrm{T}/m_\mathrm{p}$ is the opacity for Thomson scattering. This, together with the Marshak boundary condition, which imposes flux continuity, $\epsilon(0) = F_\mathrm{eff}\sqrt{3}/c$, yields the solution for the radiation energy density

$$\epsilon(y) = \frac{3\varkappa_\mathrm{T}}{c} \frac{y_0}{2} F_\mathrm{eff} \left(\exp\left(-\frac{y^2}{y_0^2}\right) - \sqrt{\pi}\,\mathrm{erf}\left(\frac{y}{y_0}\right) \right) + C, \tag{6.6}$$

where the constant is $C = \sqrt{3}F_\mathrm{eff}/c(1 - \sqrt{3}\varkappa_\mathrm{T} y_0/2)$.

The density distribution can then be obtained from the hydrostatic equilibrium equation, taking into account the pressure created by the flow with a density $\rho_0 = \dot{M}/(\pi r_0^2 v_\mathrm{ff})$ at the upper boundary of the atmosphere

$$P = \frac{2\rho k T_\mathrm{e}}{m_\mathrm{p}} = \begin{cases} \left(\frac{GM}{R^2} + \frac{\rho_0 v_\mathrm{ff}^2}{y_0}\right) y, & \text{for } y \le y_0 \\ \left(\frac{GM}{R^2} + \frac{\rho_0 v_\mathrm{ff}^2}{y}\right) y. & \text{for } y > y_0, \end{cases} \tag{6.7}$$

The structure of the atmosphere, that is, temperature and density profiles, is then obtained by solving together Equation 6.2 and Equation 6.7 using a root-finding algorithm (in this case, Newton's method). This is undoubtedly a very simplified approach, which does not provide a proper coupling to the radiative field. As the model does not simulate the kinetics of the braking process, the energy deposition profile and the characteristic depth of energy release have to be assumed. The following section describes an approach to determine y_0, based on the energy conservation arguments. The discussion of the simplifications stated above is provided in Section 6.4.

6.1.2 *Connection to the Radiative Transfer*

To couple the atmospheric structure with the radiative transfer, energy conservation is imposed in the form that all kinetic energy of the flow is converted to the radiation. In this way, the bolometric flux from the atmosphere is restricted to

$$L_{\mathrm{num}} = \pi r_0^2 \int (F_1(E) + F_2(E))\mathrm{d}E \overset{!}{=} L_{\mathrm{acc}}, \tag{6.8}$$

where the accretion luminosity L_{acc} is given by Equation 2.15, and F_1 and F_2 are the specific bolometric fluxes of two polarization modes.

To obtain the energy-conserving solution for the atmosphere, for each set of parameters $\{\dot{M}, r_0, E_{\mathrm{cyc}}\}$, an initial value for y_0 is chosen (typically, $y_0 = 6$–$9\,\mathrm{g\,cm^{-2}}$). After that, the atmospheric structure and radiative transfer are calculated. The total luminosity of the polar cap is then compared to L_{acc} with 10% tolerance, that is $|L_{\mathrm{num}} - L_{\mathrm{acc}}|/L_{\mathrm{acc}} < 0.1$. If the condition is not fulfilled, y_0 is adjust iteratively, until convergence is achieved.

6.1.3 *Spectral Formation and Atmospheric Structure*

Following the procedure discussed in the previous sections, the atmospheric structure and the emitted flux are calculated for the atmosphere on the spatial scale within the range $y = 10^{-3}$–$10^{3}\,\mathrm{g\,cm^{-2}}$. The atmosphere is extended down to these high column densities, compared to y_0, in order to ensure that both polarization modes reach their thermalization depth. A further increase of the depth does not affect the obtained solution. Here, spectra within the following parameter ranges are discussed: $\dot{M} = [4$–$16] \times 10^{13}\,\mathrm{g\,s^{-1}}$, $r_0 = [80$–$140]\,\mathrm{m}$, $E_{\mathrm{cyc}} = [50$–$80]\,\mathrm{keV}$.

Figure 6.2 shows typical temperature and density distributions in the atmosphere, obtained in the simulations for our "baseline" model with $\dot{M} = 1.6 \times 10^{14}\,\mathrm{g\,s^{-1}}$, $E_{\mathrm{cyc}} = 70\,\mathrm{keV}$, and $r_0 = 140\,\mathrm{m}$. As expected, the atmosphere consists of two principal regions: a hotter upper part, heated up by the decelerating accretion flow to $kT_{\mathrm{e}} \approx 30\,\mathrm{keV}$, and a cooler and isothermal interior with $kT_{\mathrm{e}} \approx 2\,\mathrm{keV}$. The separation "depth" is approximately given by y_0. The atmosphere above y_0 can be further divided into an optically thin top layer with the approximately constant highest temperature, and an intermediate layer with high temperature gradient, extending down to an optical depth of a few.

Due to the strong gravitational field of the neutron star, the density rapidly increases in the atmosphere. The result is that although the total column density is high, the geometrical thickness of the atmospheric layer is only $z_{\mathrm{max}} \sim 10\,\mathrm{m}$ (see additional scales in Figure 6.2). This fact validates the choice of the constant magnetic field within the emitting region. It also to a high degree justifies the one-dimensional treatment of the problem. In this case, even in the assumption of the free flux escape, the luminosity of the top area of the polar cap, L_{top}, is much higher than the side-wall luminosity L_{sw}. It can be estimated from the ratio of the respective surface areas, $A_{\mathrm{top}} = \pi r_0^2$ and $A_{\mathrm{sw}} = 2\pi z_{\mathrm{max}} r_0$, $L_{\mathrm{sw}}/L_{\mathrm{top}} < 2z_{\mathrm{max}}/r_0 \ll 1$. The escape of the photon flux from the side-wall depends, however, on the radiant thermal conductivity of the magnetized medium and will be investigated elsewhere.

The corresponding energy flux emitted by this atmosphere is shown in Figure 6.3. In this section, following Paper I, I only discuss the total energy flux, which is given, as before, by $F_p(E) = 4\pi \int_0^1 I_p(E,\theta)\cos(\theta)\mathrm{d}\theta$

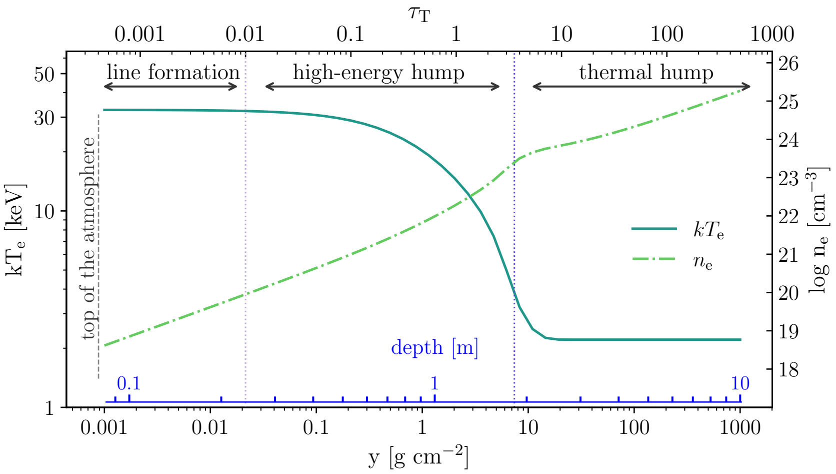

Figure 6.2: Atmospheric structure given by the electron temperature (darker solid line) and the electron number density (lighter dashed line). Spectral components and the associated formation regions are indicated on the panels. The calculations were made for $\dot{M} = 1.6 \times 10^{14}\,\mathrm{g\,s^{-1}}$, $E_{\mathrm{cyc}} = 70\,\mathrm{keV}$, and $r_0 = 140\,\mathrm{m}$. Figure 4 (left panel) from Sokolova-Lapa et al. (2021), reproduced with permission © ESO.

for the polarization modes, $p = 1, 2$. The detailed investigation of how it depends on the angle will be given in Section 6.2. The spectra of the emergent radiation have a double-hump shape, with a thermal hump brought up by mode 1 at soft energies, and a high-energy Comptonized component modified by the pronounced cyclotron line with the overall mixed contribution of the normal modes.

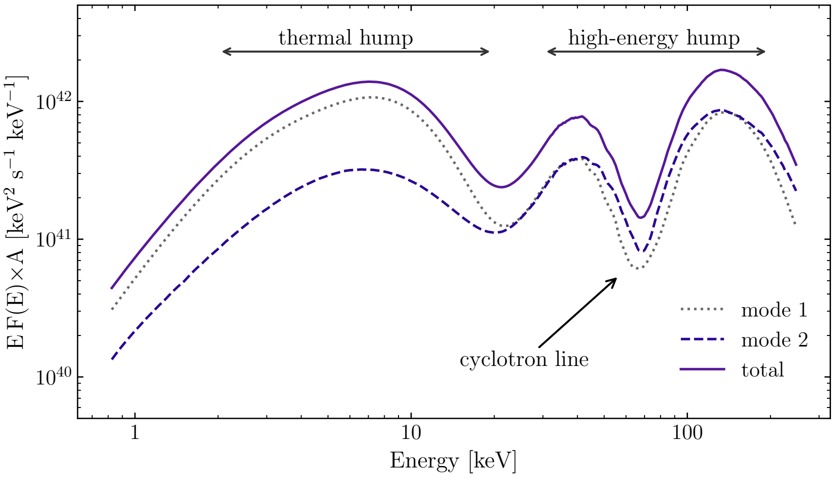

Figure 6.3: Flux from the atmosphere in two polarization modes. Figure 4 (left panel) from Sokolova-Lapa et al. (2021), reproduced with permission © ESO.

To understand the origin of the two spectral components, one can study the evolution of the photon density

$$f_p(E, y) = \frac{4\pi}{c} \frac{J_p(E, y)}{E}, \tag{6.9}$$

where J_p is the mean intensity as given in Section 4.1. Figure 6.4 (top) shows the photon density at different depths inside the atmosphere. At the bottom of the calculated atmosphere, $\tau_T = 4 \times 10^2$ (yellow line), the spectrum is Planckian with the local $kT_e \approx 2\,\mathrm{keV}$. At these depths, the opacity is dominated by free-free absorption and the radiation field is thermalized. The effect of magnetic Comptonization becomes pronounced in the higher layers of the atmosphere. Between $\tau_\mathrm{T} = 10$ and $\tau_\mathrm{T} = 1$, the soft photons experience up-scatterings in the inhomogeneous medium, which becomes hotter closer to the surface. Thus, the hard-energy component starts to form. At the cyclotron resonance, $E_\mathrm{cyc} = 70\,\mathrm{keV}$, the scattering coefficient rises dramatically, forcing the photons to scatter out of the cyclotron line core and forming pronounced wings to the line. A high temperature gradient, starting from $\tau_\mathrm{T} \approx 3$ (see Figure 6.2, right) and further growing line wings result in a near line-less smooth continuum at $\tau_\mathrm{T} = 5 \times 10^{-2}$. Above this depth, the continuum is not further affected and only the broad cyclotron line is gradually imprinted at the uppermost layers. The width of the final cyclotron line is ~30 keV, in agreement with an estimate for the Doppler broadening for a highly magnetized medium (see, for example Equation 13 from Meszaros & Nagel 1985a).

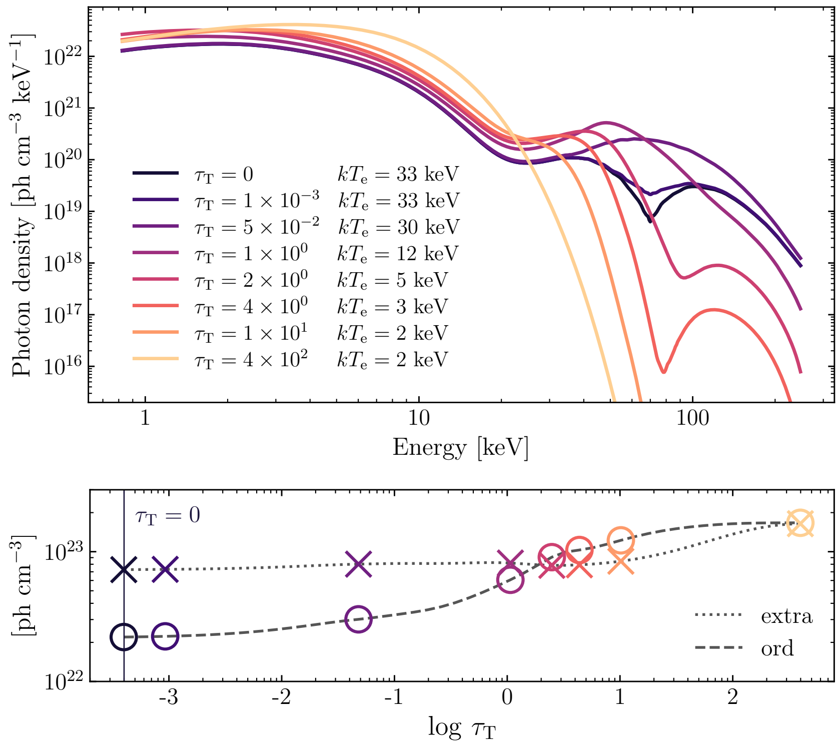

Figure 6.4: *Top:* Evolution of the photon density spectra with the optical depth inside the atmosphere. *Bottom:* Energy-integrated photon density in each polarization mode. Figure 5 from Sokolova-Lapa et al. (2021), reproduced with permission ©ESO.

Figure 6.4 (bottom) illustrates the evolution of the bolometric photon flux for each polarization mode. Here it is important to remember that the simulations were performed for the pure vacuum normal modes, and thus no mode conversion across the vacuum resonance was taken into account. In the deep layers of the atmosphere, both modes are thermalized and mixed, resulting in unpolarized radiation. Mode 1, which in the absence of the vacuum resonance keeps low opacity at energies up to the vicinity of the cyclotron resonance, has a much longer mean free path and escapes the atmosphere from greater depths. The density of the photons of mode 1 thus drops down deeper in the atmosphere. The density of mode 2 gradually decreases on the way to the surface, also due

It is probably more correct to call mode 1 a "perpendicular" mode, in tradition for pure vacuum linear normal modes, than "extraordinary", as was done in Paper I. Similarly, it is more correct to avoid the naming "extraordinary" and "ordinary" modes for the mixed case of the magnetized plasma and vacuum. However, I already mentioned in Section 4.3.4, both examples are present in the literature (see, e.g., Meszaros & Nagel 1985a).

to the scattering to the mode 1. The density of both modes reaches its minimal value approximately at their corresponding photospheres. These results are in agreement with the simulations of the deep optically thick slab by Meszaros & Nagel (1985b), although the effect of the vacuum resonance is omitted in this modeling. This similarity results from the constant high density chosen by Meszaros & Nagel, which shifted the vacuum resonance to higher energies, closer to the cyclotron line. Below the resonance, polarization modes behave in a classical way, with no interchanges (see **??** for the behavior of the cross sections in similar conditions). I expect that this picture will be affected by the proper inclusion of the vacuum resonance, which will be one of the immediate goals of the future development of the model.

To summarize, the two-hump shape of the emission spectra at low mass-accretion rate onto the polar caps of a magnetized neutron star can be explained within the frame of the model as mainly due to photon redistribution and polarization effects. The soft "thermal" hump is strongly increased by the low-opacity mode 1 from deeper atmospheric layers, while the high-energy hump is due to near-resonance Comptonization in an inhomogeneous atmosphere with a high temperature gradient. The cyclotron line is then formed on top of the high-energy hump in the uppermost layers and is expected to reflect the surface magnetic field value.

Figure 6.5 shows the energy-dependent luminosity (left) and the corresponding atmospheric structure (right) for various combinations of parameters. The baseline model is always shown in dark purple. At a lower mass-accretion rate (Figure 6.5 a), the solution presented in Section 6.1.2 gives overall lower temperature throughout the atmosphere, which results in a softer thermal hump and overall less intense Comptonization in the upper layers. The reduction of the polar cap radius (Figure 6.5 b) leads to the overall decreased volume in which the accretion energy is released. It heats up the atmosphere to higher temperatures and makes the thermal hump much harder. The overall luminosity is still lower though than for the higher r_0, simply because of the larger emission area in the latter case. In the case of a lower surface magnetic field (Figure 6.5 c), the atmospheric profile stays almost the same. The wings, forming the high-energy excess, shift to lower energies together with the cyclotron resonance. The line width stays approximately the same at around 30 keV.

6.1.4 *Isotropic Phase-Averaged Model*

The general spectral shape of the modeled polar cap emission qualitatively agrees with the observed two-hump spectra from Be X-ray Binaries in quiescence. The second hump observed at $\sim$30 keV and higher, is given by the red wing of the cyclotron line, formed in the heated atmosphere with high temperature gradient. To get a clear understanding of the model's applicability, it is necessary, however, to obtain a quantitative description of the observational data. That is, the model should be used for spectral fitting taking into account proper instrumental responses.

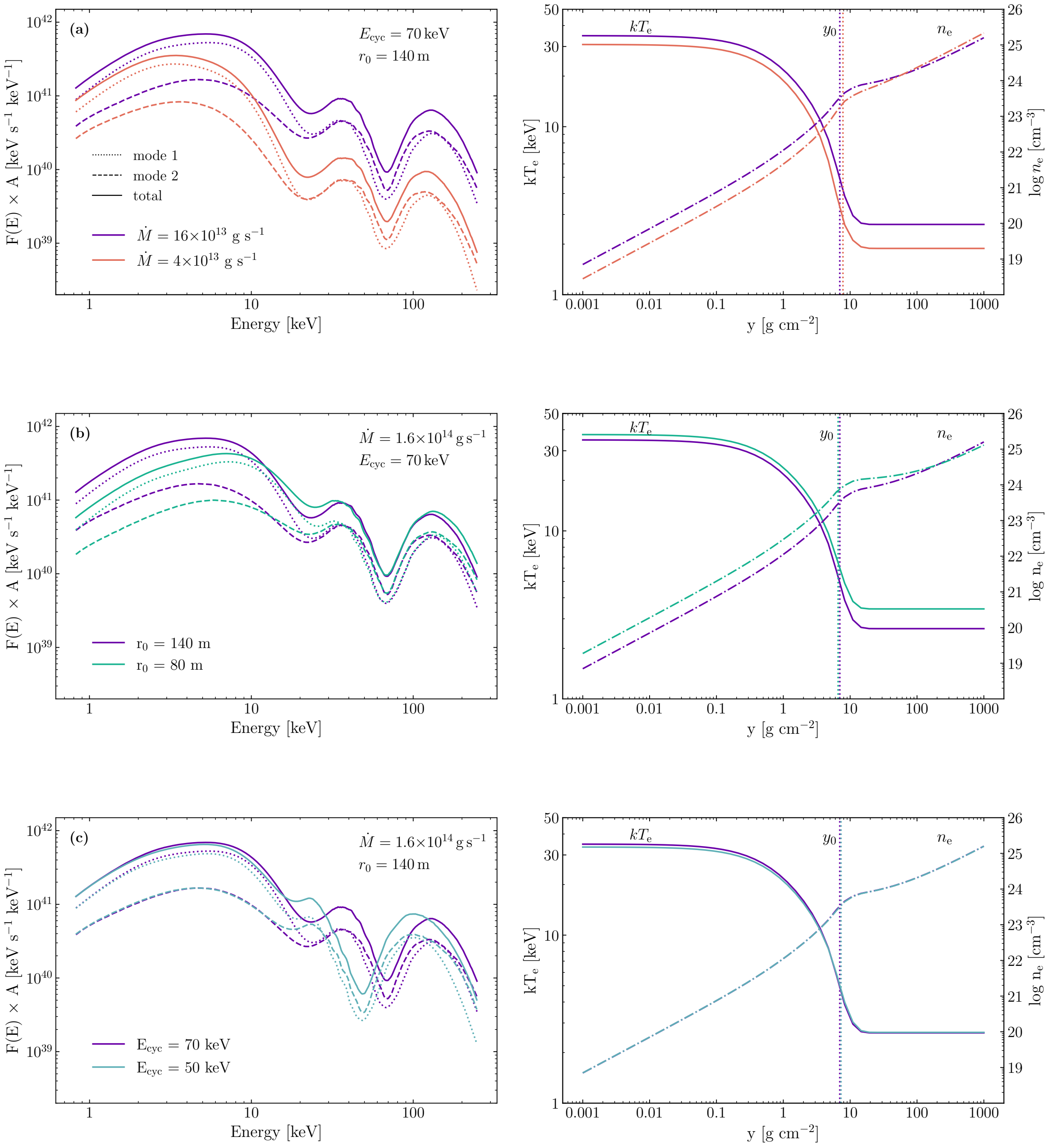

Figure 6.5: Variation of the energy-dependent luminosity (*left column*) and the atmospheric structure (*right column*) from the principle parameters of the model: a) the mass-accretion rate, b) the polar cap radius, c) the surface magnetic field. Based on Figure 6 from Sokolova-Lapa et al. (2021).

In Paper I, a simplified approach based on the assumption of isotropic emission was suggested to generate an additive table model compatible with modern X-ray data-analysis packages. Here, I repeat the necessary derivations with 36 spectra, calculated within the ranges of the three principal parameters stated above. The flux in the observer's rest frame is obtained by assuming the symmetric accretion onto two poles and dividing the flux in the neutron star rest frame by the factor $4\pi D^2$. The gravitational redshift is set to $z = 0.24$, according to the chosen M_{NS} and R_{NS}. Compared to the model presented in Paper I, here I apply an additional factor of $(1+z)^{-2}$ to the photon flux written in the table model to account for the intensity correction due to gravitational redshift, which was erroneously omitted in Paper I.

*The redshift can be taken into account, according to the FITS file standard for the **`XSPEC`** table model, with setting the **`REDSHIFT`** keyword to true. In this case, however, only the shift of the energy grid and the correction to the time dilation are applied (see OGIP memo 92-009 on the **`XSPEC`** table model file format). The correction to flux due to the phase space element invariance is, however, not taken into account. In this way, the flux inserted into the table model has been corrected (through the intensity from each it is obtained) in advance according to*

$$\frac{I_{\mathrm{o}}}{\nu_{\mathrm{o}}} = \frac{I_{\mathrm{e}}}{\nu_{\mathrm{e}}} \tag{6.10}$$

and

$$\nu_{\mathrm{o}} = \nu_{\mathrm{e}}(1+z)^{-1}, \tag{6.11}$$

*where subscripts "o" and "e" correspond to the observed and emitted quantities, respectively. As a table model contains spectra in units of photons/cm^2/s, that is, bin-integrated photon flux, only the factor $(1+z)^{-2}$ is required in addition to the internal **`XSPEC`** correction. The necessity of this factor is verified by performing ray tracing in the Schwarzschild metric (see Section 6.2.2).*

The model is applied to *NuSTAR* and *Swift*/XRT data of the low-luminosity observation of GX 304−1– a Be X-ray binary with a highly magnetized slowly rotating neutron star. The period of X-ray pulsations is about 272 s (McClintock et al. 1977). During the outbursts, a cyclotron line at ∼54 keV is observed on top of the power-law-like continuum (Yamamoto et al. 2011). The line was detected at all rotational phases, with the maximum measured centroid energy at ∼62 keV (Malacaria et al. 2015). The source is known for its low-duty cycle, with the previous quiescent state lasting 28 yr. The last activity was observed from 2008 until mid-2013, since then the source stayed in quiescence. This state is characterized for GX 304−1 by a low stable flux level with detected X-ray pulsations (Rouco Escorial et al. 2018) and a transition to a two-hump continuum (Tsygankov et al. 2019c). Considering its close distance of ∼2 kpc (Parkes et al. 1980; Rouco Escorial et al. 2018) and stable quiescent state, the source is a good candidate to test the `polcap` model.

The source was observed in quiescence by *NuSTAR* and *Swift*/XRT on 2018 June 3 (ObsID 90401326002). The data were re-extracted for Paper I using `NUSTARDAS` pipeline version 2.0.0 with CalDB version 20201101 under `HEASoft` V6.28 and `xrtpipeline` version 0.13.5. The extraction parameters are as stated in Paper I. For this thesis, I redid the data analysis, applying the modified `polcap` model as discussed above. The spectral analysis is performed with ISIS v. 1.6.2−51 (Houck & Denicola 2000), using Cash statistics (Cash 1979). The data are binned following the optimal binning procedure (Kaastra & Bleeker 2016). The low flux level of the observation in deep quiescence resulted in the strong background domination about ∼40 keV. For the analysis, I set the energy range to 4–35 keV for *NuSTAR* and to 1–6 keV for *Swift*/XRT.

The total model used for the spectral fits includes the correction of the `polcap` flux for photoelectric absorption in the interstellar medium given by the `tbnew` model (cross sections by Verner et al. 1996, and abundances by Wilms et al. 2000),

$$S(E) = \mathtt{detconst} \times \mathtt{tbnew} \times \mathtt{polcap}, \tag{6.14}$$

where `detconst` accounts for the cross-calibration of two *NuSTAR* instruments (focal plane modules FPMA and FPMB) and *Swift*/XRT. Figure 6.6 shows the unfolded phase-averaged spectra from all three instruments and the best-fit model (*top*) and corresponding ratio (*bottom*). The best-fit parameters are given in Table 6.1. To investigate the parameter space, the confidence contours on two-dimensional maps are calculated by stepping through the grids for two chosen parameters simultaneously, fitting the model to the data at each point, and comparing the obtained statistics to the best fit. Figure 6.7 show the result of this procedure. Contours for r_0 are cut by the range in which models are calculated for this parameter.

Table 6.1: Best-fit parameters for the model plotted in Figure 6.6. Detector cross-calibration constants are given with respect to *NuSTAR*/FPMA. The indicated uncertainties are at 1.6σ (90%) confidence level.

PARAMETER	BEST-FIT
N_{H} [10^{22} cm^{-2}]	1.1 *(fixed)*
$\log_{10}(\dot{M}/[\mathrm{g\,s^{-1}}])$	13.928 ± 0.009
r_0 *[m]*	$\left(1.386^{+0.014}_{-0.044}\right) \times 10^2$
E_{cyc} *[keV]*	56.6 ± 1.3
z	0.24 *(fixed)*
C_{FPMA}	1 *(fixed)*
C_{FPMB}	1.00 ± 0.04
C_{XRT}	$1.00^{+0.13}_{-0.11}$
Cash/d.o.f.	$397.92/213 = 1.87$

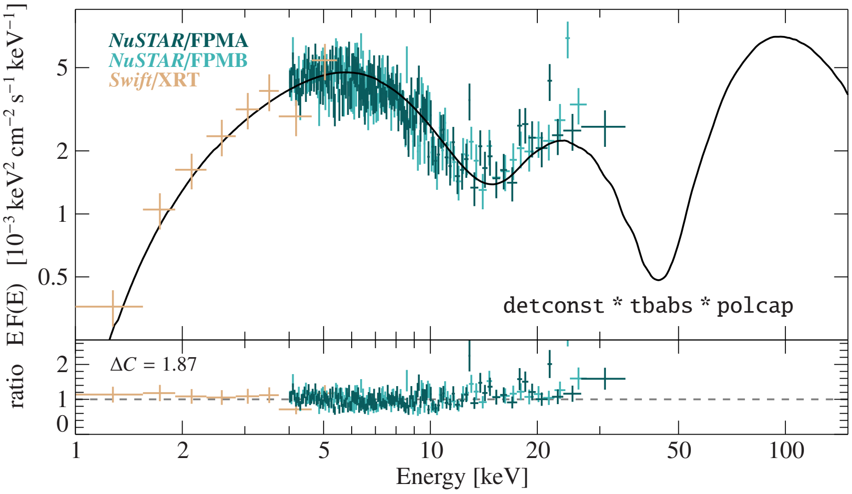

Figure 6.6: *Top:* Unfolded phase-averaged spectrum of GX 304−1 in quiescence by *NuSTAR* FPMA (dark green), FPMB (aquamarine), and *Swift*/XRT (gold), with the best-fit model assuming isotropic emission (solid black line). The spectrum is rebinned for better visualization. *Bottom:* Ratio of the data to best-fit model.

This situation did not occur in Paper I and is a consequence of the flux correction by the $(1+z)^2$ factor discussed above. It brought the flux level down and required higher values of r_0 and $\dot{M}$ compared to the ones obtained in Paper I. The parameter ranges for the model have not yet been extended due to the focus on the angle-dependent analysis presented in the following sections. In future work, the model is planned to cover significantly broader parameter ranges.

Increasing the ranges for r_0 and $\dot{M}$ requires, however, the solution of additional problems. Due to the condition of energy conservation in the model, a valid solution does not exist for each combination of r_0 and $\dot{M}$. Some combinations of higher r_0 and lower $\dot{M}$ create a higher emitted flux than required by L_{acc} (see Section 6.1.2). The way out is to set r_0 constant, based on $\dot{M}$ and E_{cyc}. For example, an estimate from the Alfvén radius can be used (Lamb et al. 1973), or the independent magnetohydrodynamic simulations can provide this value (P. Das, A. L. Watts, priv. comm.).

The polar cap radius from the best-fit model is thus close to the upper border of the parameter range, $r_0 \approx 140\,\text{cm}$. The cyclotron line energy is $\sim$57 keV, which corresponds to a surface magnetic field $\sim 5 \times 10^{12}$ G and brings the cyclotron line at the energy around $57(1+z)^{-1}\,\text{keV} \approx 46\,\text{keV}$ in the observer's frame. This is about 20% lower than one would expect from previously measured cyclotron lines (see, e.g., Malacaria et al. 2015; Jaisawal et al. 2016). This is not unexpected, as in the presented observation, the cyclotron line region is not accessible, nor the second hump described by the red wing of the cyclotron line with the frame of the `polcap` model is constrained. The small uncertainties of the best-fit parameter are likely the artifact of the angular integration and the non-relativistic cross sections for the resonant Compton scattering, both of which result in the wide profile of the cyclotron line. The latter is expected to push the red wing to the lower energies, thus providing a lower field estimate. The mass accretion rate is $\sim 8.5 \times 10^{13}\,\text{g}\,\text{s}^{-1}$ and the total observed luminosity is $\sim 1.1 \times 10^{34}\,\text{erg}\,\text{s}^{-1}$.

6.2 PHASE-DEPENDENT OBSERVED EMISSION

So far, only angular-averaged properties of the obtained solutions were discussed, following the methodology published in Paper I. The angular dependency is, however, crucial for the emission from the highly anisotropic plasma. The reader only had a glimpse on this problem in Chapter 5. In the following sections, I will focus on the anisotropic properties of the radiation field. In particular, the angle and energy dependency of the outgoing radiation in combination with ray tracing from the rotating neutron star is very important for the consistent description of the

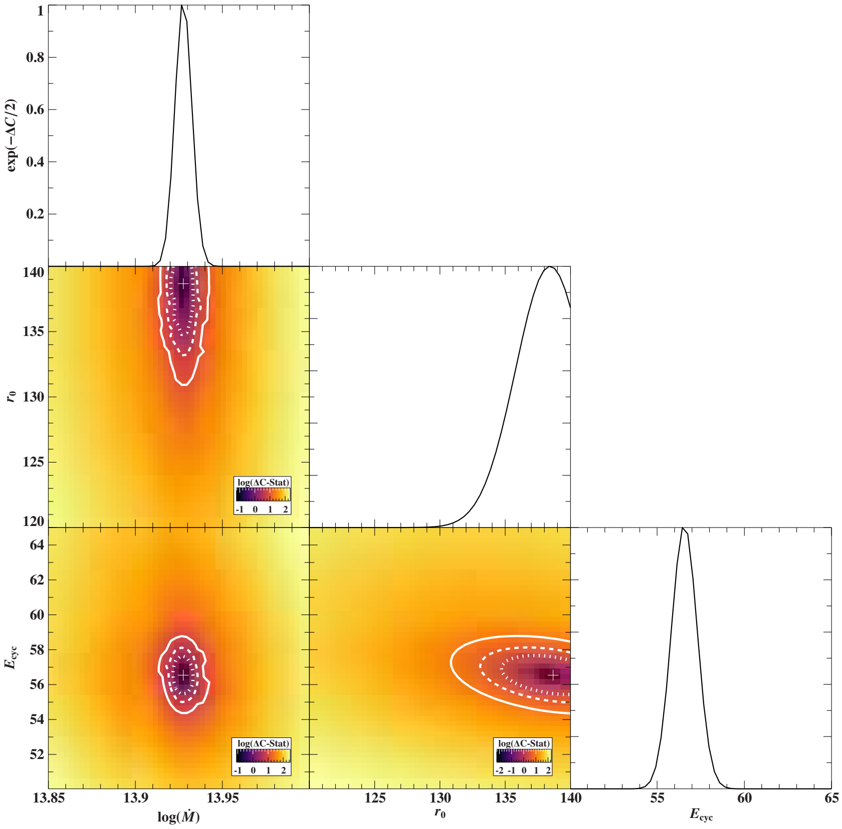

Figure 6.7: Two-dimensional parameter probabilities for the model fit to the observation of GX 304−1 in quiescence (colored maps) and the one-dimensional probabilities (side plots). Dotted, dashed, and solid contours correspond to the 99%, 90%, and 68% confidence regions, respectively. The change in statistics is shown with respect to the best-fit model.

spectra and pulse profiles of accreting neutron stars. Here I demonstrate how the model, which allows for the description of the phase-resolved spectra, leads to significant constraints of the principal geometrical parameters: the location of the magnetic poles and the observer's inclination with respect to the rotational axis of the neutron star.

Although significant advances were achieved in this field over the past decades, there are principal limitations of models which are aimed at determining geometrical parameters of a neutron star without underlying physical simulations of the emission properties. For example, a powerful method introduced by Kraus et al. (1995) for the pulse profile decomposition to obtain the intrinsic beam pattern of the emitting pole and geometrical parameter requires prior knowledge of the observer's inclination to obtain polar angles of the poles with respect to the rotational axis. Even with the assumed observer's inclination and a fairly complex pulse profile shape, the method results in multiple solutions which have to be discriminated based on the plausibility arguments (see, e.g., Sasaki et al. 2010, for the example of EXO 2030+375). The methods used to model pulse profiles based on the general assumptions about the emission angular behavior are also known to produce wide areas of degenerate solutions when the parameter space is studied in detail (Fürst et al. 2018). The geometry can be inferred from pulse profile fitting of multiple datasets using the empirical emission profiles (typically, Gaussian-like or a periodic function) as an input, as was done, for example, by Iwakiri et al. (2019) and Cappallo et al. (2019). From these studies it is unclear, however, how the chosen emission profiles bias the obtained solutions. The approach proposed in the following sections undoubtedly has pitfalls as well, which I attempt to address in detail. The main message is, however, that the combination of spectral and angular information obtained consistently within the frame of the same physical model can significantly constrain the solutions.

Section 6.2.1 presents emission profiles and angle-dependent spectra in the neutron star rest frame. Section 6.2.2 provides the basic information about a ray tracing code for slowly rotating neutron stars by S. Falkner (Falkner 2018), which is used in combination with the `polcap` model to obtain spectra and pulse profile seen by the remote observer. The resulting pulse profiles and the phase-dependent and phase-averaged spectra are discussed in Section 6.2.3, Section 6.2.4, and Section 6.2.5, respectively.

6.2.1 *Emission Profiles and Differential Flux*

In this section, the angular dependency of the emission in the rest frame of the neutron star is investigated in the same way, as was done in Section 5.3.

Figure 6.8 shows the differential flux, $\mathrm{d}F = I(E,\mu)\mu$, at various angles to the magnetic field. Here, as before, $\mu = \cos(\theta)$, where θ is the angle between the direction of the photon propagation with respect to the magnetic field. The total flux used as an input for the previously discussed `polcap` table model for spectral fitting is shown on top, with a gray thick line. Here, the origin of small kinks in the line profile from the angle averaging becomes more obvious. I would like to note that here the specific intensity is scaled with μ to illustrate the contributions to the total flux.

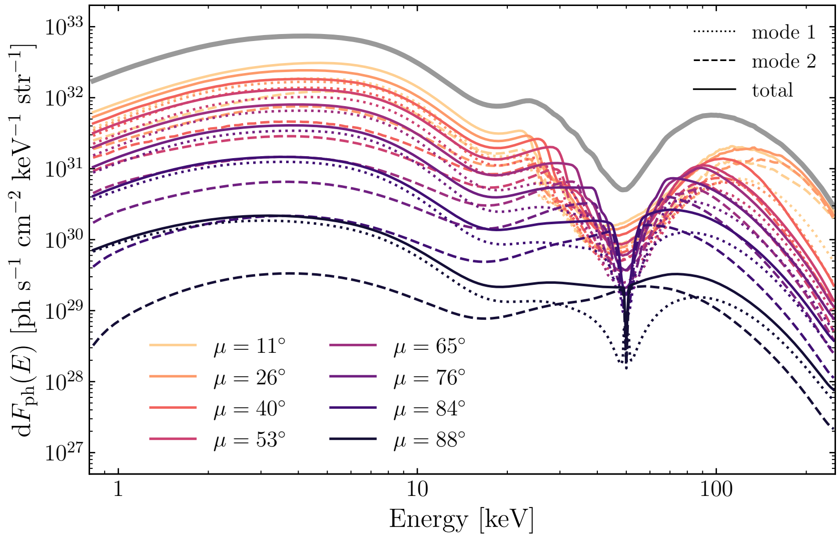

Figure 6.8: Differential flux from the accretion-heated polar cap, $\mathrm{d}F = I(\mu, E)\mu$ (colored thin lines). The total flux, discussed in the angle-averaged case, is shown by a thick grey line. The spectra are shown for the model with $E_{\mathrm{cyc}} = 50\,\mathrm{keV}$, $\dot{M} = 8 \times 10^{13}\,\mathrm{g\,s^{-1}}$, and $r_0 = 140\,\mathrm{m}$.

As before, the line profiles follow the shape of the resonance in the Compton scattering cross sections. This behavior results in a wider width when a photon travels closer to the magnetic field direction, experiencing the strongest Doppler broadening. After the dip, which follows the thermal hump, the maxima in the differential fluxes at each angle are reached in one of the wings of the line (red wing for lower angles and blue wing for higher ones). The shape of the thermal hump is also affected; the hump becomes harder at smaller angles. A likely explanation for this phenomenon is the mode conversion through Compton scattering and the angle dependency of mode 2. The harder the shape of the thermal hump, the less processing by Compton scattering is present (see Figure 6.4). This is also the reason why the thermal hump is softer in mode 2 than in mode 1 (see Figure 6.3). At smaller angles, mode 2 is also much less affected by the medium due to lower cross sections, and the thermal hump is brought up from deeper layers of the atmosphere less modified (harder). The higher the angle to the magnetic field, the larger the cross sections of mode 2 in the continuum. The thermal hump is softened by Compton up-scatterings, which redistribute photons to the high-energy component. This behavior is translated to mode 1 via the resonant (scattering-based) mode conversion. After a photon of mode 2 was converted to mode 1, it is more likely to leave the medium in this mode.

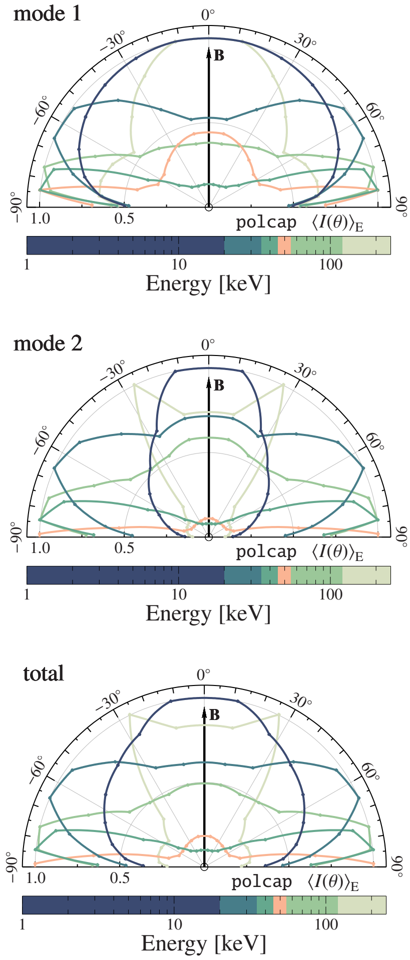

Figure 6.9: Emission profiles from the highly magnetized atmosphere of an accreting neutron star shown for different energy bins. The bin corresponding to the core of the cyclotron line is marked in red.

Emission profiles in different energy bands are presented in Figure 6.9. The low-energy profile of mode 1 takes a form of a broad fan beam. At the same band, mode 2 reveals a classical pencil beam stretched along the magnetic field. Above 20 keV, in the second energy band from the left, the spectra are already affected by the redistribution near the cyclotron line at small angles (see Figure 6.8). Already here, the emission profiles in the (soft) continuum are noticeably modified for both polarization modes. The pencil-beam-like profile of mode 2 acquires broad side petals. Similar petals are formed in the profile of mode 1, following the suppression of the fan beam at small angles. Near the cyclotron resonance and at its vicinity, the profiles are characterized by the large contribution of the side petals, illustrating the fact that photons can escape the line core mainly at the large angles to the magnetic fields, which was already mentioned in Section 5.3. At higher energies, $\gtrsim 120\,\mathrm{keV}$, the profiles attempt to restore their original form, but are still affected by the cyclotron processes. Taken together, this creates a minimum at $\sim 60°$, which results in the resonant energy of a high-energy photon in the rest frame of an electron. It results in a three-petal structure of the more fan-beam-like profile of mode 1 and a four-petal structure (the previously mentioned "cat diagram") of the pencil-beam-like profile of mode 2.

The results discussed here are not specific for the model chosen for illustration ($E_{\mathrm{cyc}} = 50\,\mathrm{keV}$, $\dot{M} = 8 \times 10^{13}\,\mathrm{g\,s^{-1}}$, and $r_0 = 140\,\mathrm{m}$), but reflects general trends for all calculated spectra. The variation of r_0 and $\dot{M}$ does not affect the conclusions. The same applied to E_{cyc}, providing the shift of the cyclotron line and corresponding choice of the energy bands for the line core and wings. The combination of the parameters above was chosen as closest among all calculated spectra, to the best-fit parameters obtained in Section 6.1.4, for which many following simulations are performed.

6.2.2 *Ray Tracing from Rotating Neutron Star*

The knowledge of the angle properties of radiation allows one to make final steps to determine the emission seen by the remote observer. As was discussed in Section 3.1.3, rotation of a neutron star and general misalignment of the observer's line of sight and the rotational axis give rise to the periodic variation of the observed flux. Together with anisotropy of the emission and strong light bending near the surface of the neutron star, these effects can result in complex shapes of the pulse profiles. To take into account geometrical effects of changing emission regions as seen by the remote observer during the rotation of the neutron star in curved space-time, in the following, I use a general relativistic ray-tracing code by Sebastian Falkner (Falkner 2018). The code calculates an isometric projection of a slowly rotating neutron star onto the observer's plane. It was developed as a geometric model, which allows obtaining the phase-dependent flux in the observer's frame by calculating photon trajectories in the Schwarzschild metric.

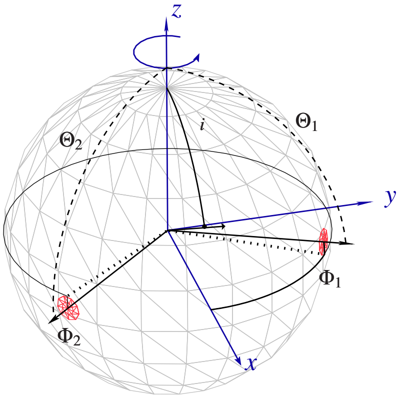

Figure 6.10: Geometry of the light bending object with two emitting poles, as given by the code by Falkner (2018). The sizes of the poles are enlarged for better visibility. This figure is based on Figure 2.4 (left) from Falkner (2018), obtained by modification of the original script written by S. Falkner.

In the following, I assume the accretion onto two poles of a neutron star, whose mass and radius are fixed, as before, to $M_{\mathrm{NS}} = 1.4\,M_{\odot}$ and $R_{\mathrm{NS}} = 10\,\mathrm{km}$. The principal geometrical parameters of the problem are the inclination of the observer's line of sight with respect to the rotational axis i, the polar angles of the magnetic poles Θ_1 and Θ_2, and azimuthal angles of the poles, Φ_1 and Φ_2. The latter are mainly addressed in terms of the azimuthal separation of the poles $\Delta\Phi = |\Phi_1 - \Phi_2|$. Figure 6.10 shows the general geometrical setup with the principle angles and illustrate the sampling of the surface with triangular surface elements. In this study, I consider only the symmetric case for polar angles of the neutron star, that is, $\Theta_2 = 180° - \Theta_1$. For the azimuthal angles, asymmetric configurations, $\Delta\Phi \neq 180°$, will be investigated. In the following, the term "geometry" is often used to denote a specific set of $\{i, \Theta_1, \Phi_1, \Phi_2\}$.

To combine the `polcap` model with the ray tracing code, I prepared a table model which contains an emission angle as one of the parameters and the specific intensity instead of the flux. It is then used as an input for each emitting surface element in the ray-tracing code. This setup, based on a very early version of the `polcap` model, was used by Lucia Härer in her bachelor work to study pulse profiles. The early version of the model used here, however, differs significantly from the published version, not extending, for example, to high optical depths and using the illumination of the black body spectrum from below. This led to significantly different and less physically motivated emission profiles compared to the current version. The following results are obtained only for the sum of two polarization modes. The aspects of the individual mode propagation in the neutron star magnetosphere are outside of the scope of this thesis.

Figure 6.11 shows an example of the projection of a neutron star with two emitting poles, as used in the setup for this work, onto the observer's sky.

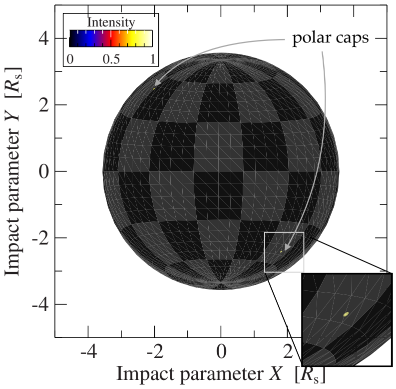

Figure 6.11: Relativistic projection of the neutron star onto the observer's sky. The poles are shown in real size. The corresponding geometry is: $i = 90°$, $\Theta_1 = 40°$, and $\Delta\Phi = 140°$. The energy band for the emission is 1–200 keV. The color bar shows normalized intensity. The axes are given in units of the Schwarzschild radius R_s. Created by the ray-tracing code of Falkner (2018).

6.2.3 *Pulse Profiles*

The complexity of the resulting pulse profiles is mainly driven by two factors: the complexity of the emission profile in the corresponding energy band and the possible range of angles under which the observer can see each pole during the neutron star rotation. The latter is determined by i, Θ_1, and Θ_2. The azimuthal angles of the poles affect pulse profiles in the sense of the phase shift: by changing Φ_1 and Φ_2, while keeping $\Delta\Phi$ constant, one can circularly shift the total profile. The change in $\Delta\Phi$, however, translates into the shift of the individual pole contributions with respect to each other. Here, the pulse profiles are calculated for the same physical parameters as the earlier emission profiles, and the beams shapes for the sum of polarization modes can be used to understand the result (Section 6.2, bottom panel).

Figure 6.12 shows pulse profiles for the geometry with $i = 15^\circ$, $\Theta_1 = 65^\circ$ and azimuthally symmetric poles. In this case, one of the poles (pole 1, displayed in blue on the top panel and by a dash-dotted line on the bottom) is always visible to the observer. As the projection is shown for the energy band 35–45 keV (the red wing of the cyclotron line), given in the rest frame of the neutron star, the underlying emission profile is stretched in the direction perpendicular to the magnetic axis into two petals (see Section 6.2, bottom panel). The pole 1 on the top panel of Figure 6.12 has smaller angular distance to the observer's line of sight and in this phase is seen under the angle, slightly smaller than $\Theta_1 - i = 50^\circ$, where the profile is close to the minimum. The second pole, pole 2, (red) is visible because of the light bending effect, with the emission coming from high angles to the magnetic field. This is the reason, why more distant pole 2 is brighter in this picture (see the colorbar). Its contribution to the pulse profiles (bottom panel) is limited to about a half of the rotational phases. The rest of the time, the pole is eclipsed. The (secondary) minimum at phase 0.5 (face-on location of the poles) in this energy band occurs also originates in the central minimum of the emission profile, as the angular distance to the observer is minimal at this phase. As a result, slightly lower angles (closer to the minimum) are sampled in this configuration. At the highest and lowest energy bands, where the contribution of mode 2 makes emission profiles more stretched along the magnetic axis, pulse profiles also show a minimum at 0.5. All other profiles are characterized by the strong side petals and exhibit a maximum there (except for the already discussed band at the red wing, where on top of the growing component the secondary maximum occurs). At the highest energy band, the global maximum is characterized by a sharper feature, which comes from pole 1 and has its origin in due to the contribution of an "ear" of the "cat"-like emission profile.

The case of near-equatorial pole location, $\Theta_1 = 85^\circ$, $\Theta_2 = 98^\circ$, is shown in Figure 6.14, for the same observer inclination $i = 15^\circ$ and two different azimuthal pole configurations: $\Delta\Phi = 180^\circ$ (left) and $\Delta\Phi = 210^\circ$ (right). Figure 6.13 illustrates the projection corresponding to the left (symmetric) panel. In this case, both poles are visible to the observer at all rotational phases, which translates to the overall much smaller amplitude modulation across the profiles. The same is true for the asymmetric case (right panel). In the energy bands away from the cyclotron resonance, for $\Delta\Phi = 180^\circ$ the structure of the pulse profiles now always has two components. For the azimuthally shifted poles, $\Delta\Phi = 210^\circ$, the contributions of two poles sometimes blend into one asymmetric peak, making the secondary peak disappear. In the bands corresponding to the red wing and the core of the line (35–45 keV and 45–55 keV), the interplay between more complex individual pulse profiles creates multiple additional small peaks. This effect is only enhanced by the poles' asymmetry.

The examples presented in this section show that even relatively small changes in only one of the geometrical parameters, lead to a completely different structure and modulation of pulse profiles, when non-isotropic emission profiles are considered and the light-bending effect is taken into account.

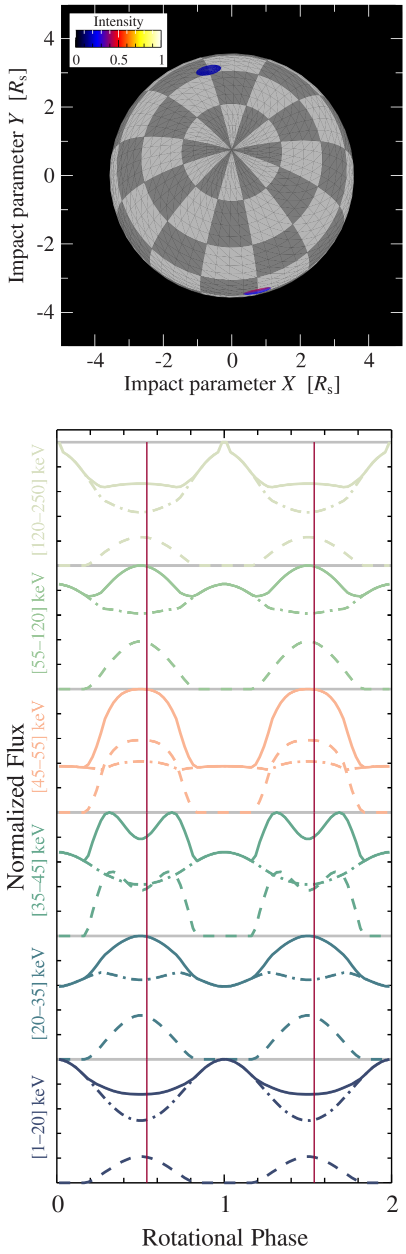

Figure 6.12: *Top:* Projection for $i = 15^\circ$, $\Theta_1 = 65^\circ$, and $\Delta\Phi = 180^\circ$. The sizes of the poles are increased ten times for better visualization. Emission is shown in the band 35–45 keV (before redshift). *Bottom:* Pulse profiles in different energy bands. The energy values are given in the rest frame of the neutron star, corresponding to the emission profiles (Figure 6.9). Individual contributions of the poles are shown by dashed and dash-dotted lines. The solid line represents the sum. Purple vertical lines correspond to the rotational phase displayed at the top panel.

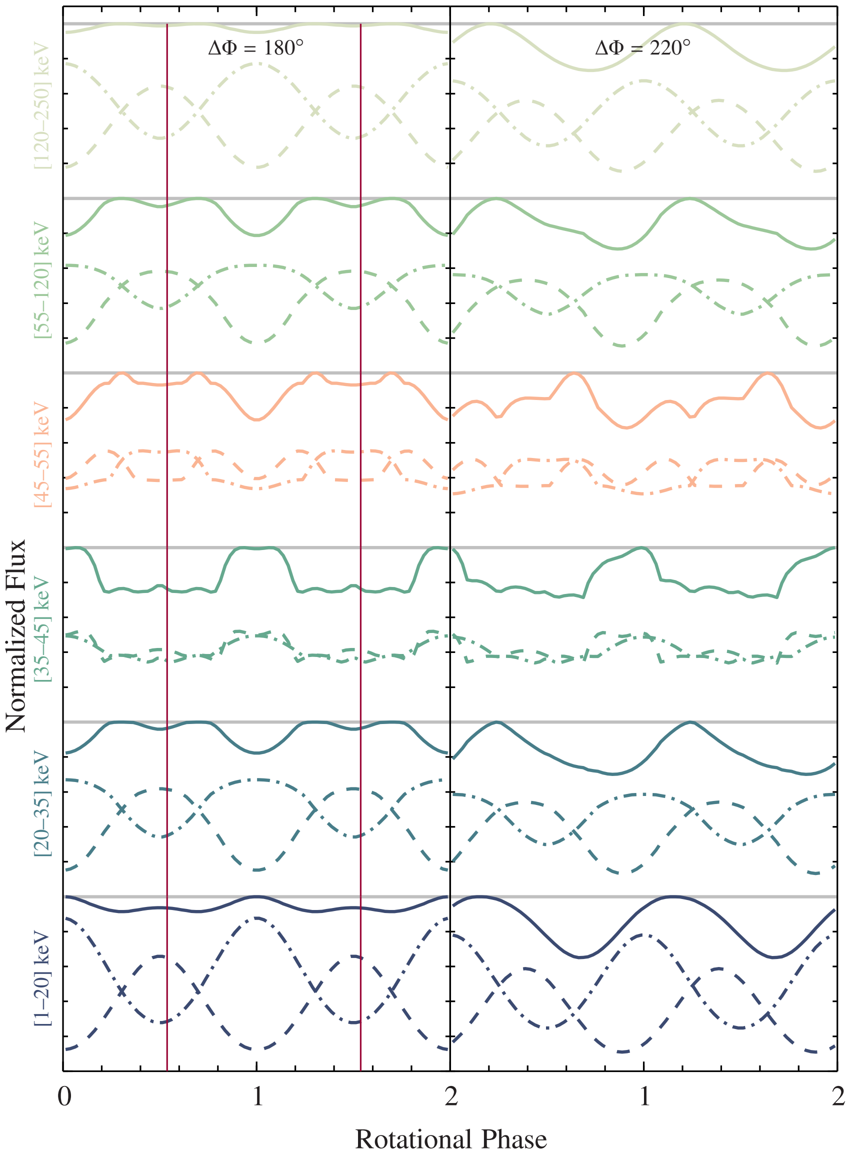

Figure 6.14: Same as in Figure 6.12, but for geometry: $i = 15°$, $\Theta_1 = 85°$, $\Delta\Phi = 180°$ (*left*) and $\Delta\Phi = 210°$ (*right*). The red vertical lines on the left panels correspond to the phase displayed in Figure 6.13.

6.2.4 *Phase-Dependent Spectra*

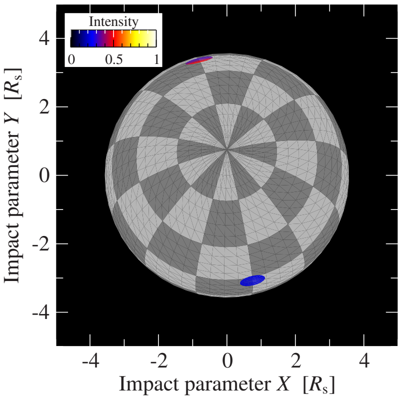

Figure 6.13: Same as in Figure 6.12, but for $i = 15°$, $\Theta_1 = 85°$, and $\Delta\Phi = 180°$.

The discussed shapes of pulse profiles and their variations in the energy bands reflect the change of the observed spectra during the rotation of the neutron star.

Figure 6.15 shows spectra seen by the remote observer at different rotational phases of the neutron star. The geometry is chosen the same as for Figure 6.12: $i = 15°$, $\Theta_1 = 65°$, and $\Delta\Phi = 180°$. In the continuum, the spectrum is always dominated by pole 1 (dash-dotted) line, in agreement with previously discussed pulse profiles. For phase 0, the contribution of pole 2 is completely negligible at all energies. Similarly, for phase 0.8 the spectrum is essentially determined by the emission from the pole 1. At these two phases, the profile of the cyclotron line is the broadest, which means that the pole is seen under an angle that is close to the magnetic field axis. It is clear from Figure 6.15 that contribution of the pole 2 has the most pronounced effect on the cyclotron line shape. As the pole is mainly seen under large angles to the magnetic field, the line profile in its spectra is narrow. From phase 0.3 and phase 0.5, it is seen that summation over contributions of the two poles affects the line shape and, in a number of cases, can make it narrower or more complex. For phase 0.5, the core of the line is dominated by the emission from pole 2, which was previously seen on the pulse profiles for this energy band. At this phase (for this geometry), the narrowest cyclotron line is observed.

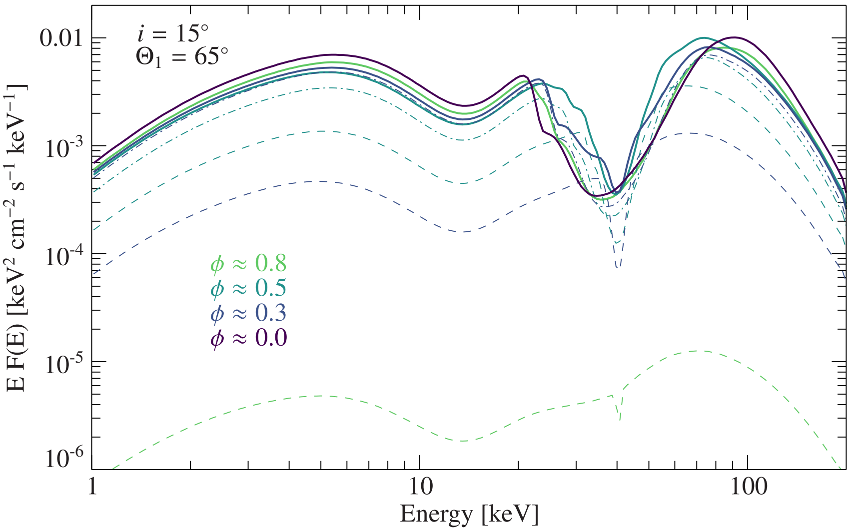

Figure 6.15: Spectra of the emission from the poles of the neutron star at different rotational phases. The geometry is: $i = 15°$, $\Theta_1 = 65°$, $\Delta\Phi = 180°$. Contributions of two poles are shown with dash-dotted (pole 1) and dashed (pole 2) lines. The total spectrum is given by solid lines.

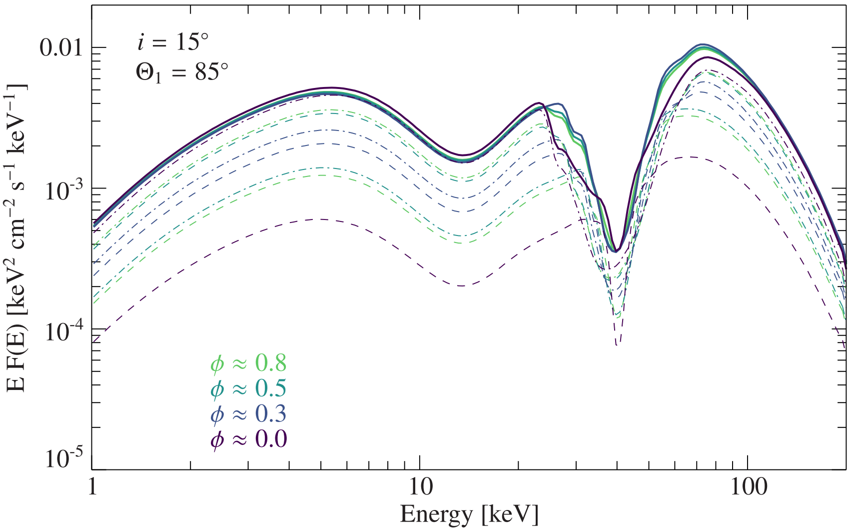

Figure 6.16: Same as in Figure 6.15, but for $i = 15°$, $\Theta_1 = 85°$, $\Delta\Phi = 180°$.

It is important to note that the flux dependency on energy should be compared with the pulse-profile plots with care, keeping in mind that the spectra presented here are gravitationally redshifted.

The spectra for the second previously discussed geometry, $i = 15°$, $\Theta_1 = 85°$, $\Delta\Phi = 180°$, are displayed in Figure 6.16. Here, in agreement with pulse profiles shown in Figure 6.14 (left), the total emission is the mix of the two poles contributions at all phases. Variation of the continuum is not noticeable in this representation (except for phase 0), matching very low modulation of the pulse profiles. The region near the cyclotron line is affected more noticeably than the continuum, but much less pronounced, than for the previous geometry ($\Theta_1 = 65°$). The line profile is narrow for phases 0.3–0.8, and acquire more complex and asymmetric shape for phase 0, due to the second pole contribution.

6.2.5 *Phase-Averaged Spectra*

It is obvious that being averaged over rotational phases, the spectra for the two examples above are not the same for different geometries. In addition, it is interesting to test the phase-averaged `polcap` model, which is based on the assumption of the isotropic emission and does not include the light-bending effect (see Section 6.1.4). Figure 6.17 and Figure 6.18 show the phase-averaged spectra for various geometries. The isotropic model has lower flux than the the full angle-dependent model with relativistic ray tracing for all geometries. This result is hardly surprising, as light

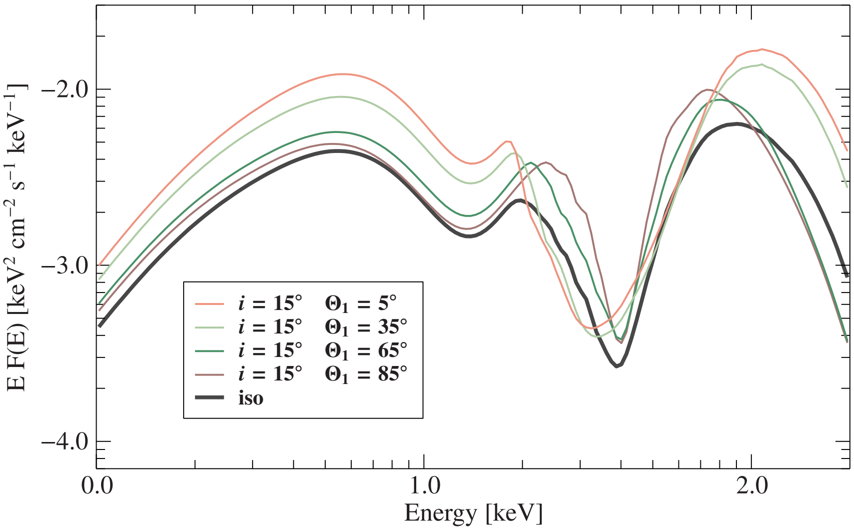

Figure 6.17: Phase-averaged spectra from the two poles of the neutron star, shown for polar angles of the poles. All geometries correspond to $i = 15°$ and $\Delta\Phi = 180°$. The dark thick line presents the phase-averaged model in the assumption of isotropic emission, without the light-bending effect.

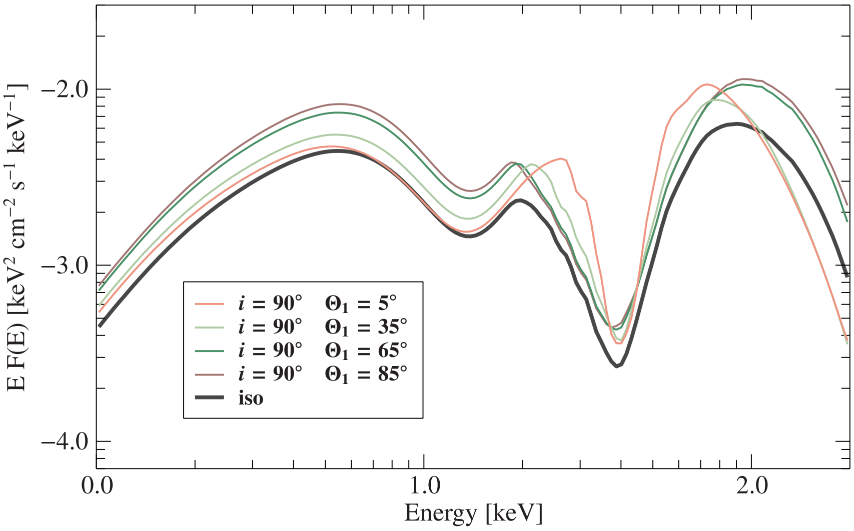

Figure 6.18: Same as in Figure 6.17, but for $i = 90°$.

bending and beaming combined with rotation of the neutron star are only expected to enhance the observed emission. The smaller the angle between i and Θ_1, the higher is the total flux level. If, at the same time, Θ_1 and i are close to the rotational axis, the result is a broad cyclotron line, as only pole 1 is seen under small angles and dominates the flux. In this case, the line centroid energy can be significantly (about 20% from the examples in Figure 6.17) lower than the redshifted cyclotron energy.

6.3 MODEL WITH RAY TRACING: SPECTRAL FITTING

Finally, in order to test the model which now combines the `polcap` emission with relativistic ray-tracing code on the observational data, I create a set of model spectra suitable for spectral fitting. This is not a trivial task, as the straight-forward approach with an interpolation-based table model, which can be simply loaded to the X-ray data analysis package, is not applicable in this case. The main reason for that is the significant extended of parameter space, as now to the original set of physical parameter of `polcap`, $\{\dot{M}, r_0, E_\mathrm{cyc}\}$, the set of geometrical parameters is added, $\{i, \Theta_1, \Delta\Phi\}$ (which is even larger, when one chooses to treat Θ_2 independently from Θ_1). The full table easily excess tenths, and even hundreds, of Gigabyte as geometrical parameters require very fine angular grids to avoid interpolation problems. This severely limits the application of this model for spectral fitting. While there exists ongoing research at the Dr. Karl Remeis Observatory to overcome this problem (Jakob Stierhof, priv. comm.), currently a few useful tricks are adopted, which at least allow to start testing of the model.

The first solution is to freeze physical parameters of the `polcap` model to investigate the effect of geometry. For this reason, in the following the `polcap` parameters are fixed to the best-fit ones given by the isotropic model without the light bending effect in Section 6.1.4. This choice was made based on an attempt to first test the model on the same data set. The second trick is the calculation of an interpolation table, which contains phase-dependent spectra for one-pole geometry, which includes only i and Θ_1 parameters. This table is then used in the main model script to combine the contributions of the two poles and apply their azimuthal offset. Currently, this implementation is specific to the Interactive Spectral Interpretation System (`ISIS`, actively used at the Dr. Karl Remeis Observatory; Houck & Denicola 2000) for the X-ray data analysis. The polar angle of the second pole Θ_2 is an independent parameter, but for the purposes of this research is fixed, as stated before, to $180° - \Theta_1$.

The final model presented here permits the analysis of phase-averaged and phase-resolved spectra and is referred to in the following as `polcap_lb`. Section 6.3.1 presents the results of the phase-averaged spectral analysis for the same observation of GX 304−1, which was discussed in Section 6.1.4. The analysis presented in Section 6.3.2 is performed on the phase-resolved spectra for this observation and provides significant constraints on the geometry of the system. Finally, in Section 6.3.3 I attempt to understand the origin of the obtained results.

6.3.1 *Fitting Phase-Averaged Spectra*

The results of the spectral fitting of `polcap_lb` to the same phase-averaged spectra of GX 304−1 which were discussed in Section 6.1.4 are shown in Figure 6.19 and Table 6.2. The model provides an overall good description of the observed data, with $\Delta C = 1.26$. The best-fit parameters suggest the observer's inclination, $i \approx 13°$ and the polar angle of pole 1, $\Theta_1 \approx 90°$. The azimuthal separation of the poles, $\Delta\Phi$ is, however, not constrained.

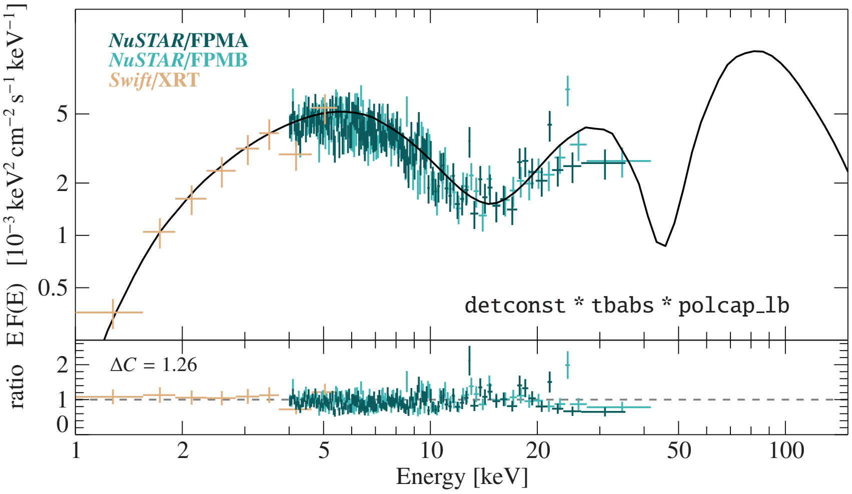

Figure 6.19: Same as in Figure 6.6, but the model now takes into account general relativistic ray tracing.

Table 6.2: Best-fit parameters for the model plotted in Figure 6.19.

PARAMETER	BEST-FIT
N_H [10^{22} cm^{-2}]	1.1 *(fixed)*
$\log_{10}(\dot{M}/[\mathrm{g\,s^{-1}}])$	13.928 *(fixed)*
r_0 [m]	1.386×10^2 *(fixed)*
E_{cyc} [keV]	56.6 *(fixed)*
i [rad]	$0.23^{+0.09}_{-0.23}$
Θ_1 [rad]	1.57 ± 0.19
Θ_2 [rad]	$(\pi - \Theta_1)$
$\Delta\Phi$ [rad]	$5.3^{+1.0}_{-5.4}$
C_FPMA	1 *(fixed)*
C_FPMB	0.974 ± 0.026
C_XRT	$0.88^{+0.11}_{-0.10}$
Cash/d.o.f.	$267.44/213 = 1.26$

To explore the parameter space, I used Marcov-Chain-Monte-Carlo sampling method, precisely, `emcee` (The MCMC Hammer, Foreman-Mackey et al. 2013), with 10 walkers for each free parameter, drawing from the initially uniform distributions. Figure 6.20 shows the final probability distributions for i, Θ_1, and $\Delta\Phi$. Two-dimensional maps confirm the poor constraints for $\Delta\Phi$. This makes sense, as the dependency of the phase-averaged spectra on the azimuthal angle is very weak. Here, all information about phase-dependency was eliminated and thus the probability of the $\Delta\Phi$ value is nearly uniformly distributed from 0° to 360°, with some excess near 0° and 300°. On the contrary, two other angles have clear regions of high probabilities. For a probable value of $i \approx 10°$, the corresponding polar angle is $\Theta_1 \approx 90°$. The second region provides exactly the opposite situation with $\Theta_1 \approx 10°$ and $i \approx 90°$. Here I would like to note that two side regions for $\Theta_1 \approx 10°$ represent in fact the same solution, when each of the poles is located almost on the rotational axis. This symmetry in the obtained probabilities is not accidental and reflects a simple fact that for the observer only the behavior of the angle between Θ_1 and i plays a role. These symmetric solutions give the same variation of this angle during the rotational period and thus are indistinguishable for the observer.

6.3.2 *Fitting Phase-Resolved Spectra*

To study phase-resolved spectra of GX 304−1, I first obtained a pulse period of 275.13 s by performing epoch folding (Leahy et al. 1983) on barycenter-corrected *NuSTAR* light curves. This value is in good agreement with previous findings (see, e.g., Rouco Escorial et al. 2018, for the latest measurement). The obtained pulse profiles are shown in Figure 6.21. To extract the data, the bins were selected as denoted on the left side of the figure. For each phase bin, data were extracted using `NUSTARDAS` pipeline of version 2.1.1 under `HEASoft` V6.29a, with `CalDB` version 20211103. The energy range used for the extraction is 3–35 keV. Circular regions with a radius of 30″ were chosen for both, source and

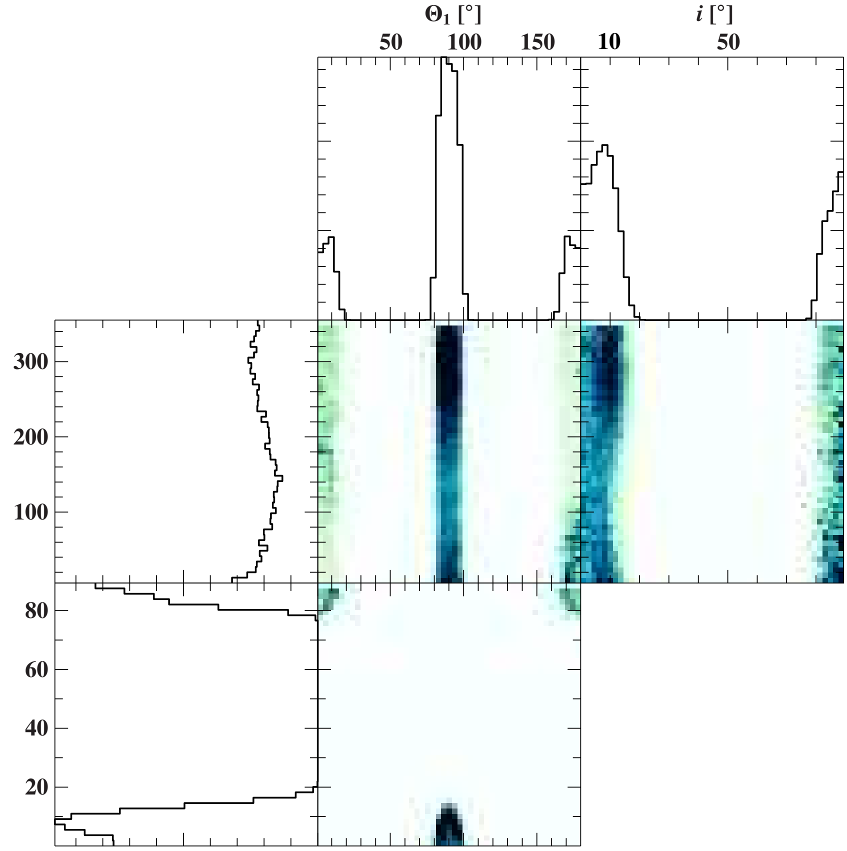

Figure 6.20: Parameter probability distribution from the `emcee` run. The darker part of the colorscheme corresponds to higher probabilities.

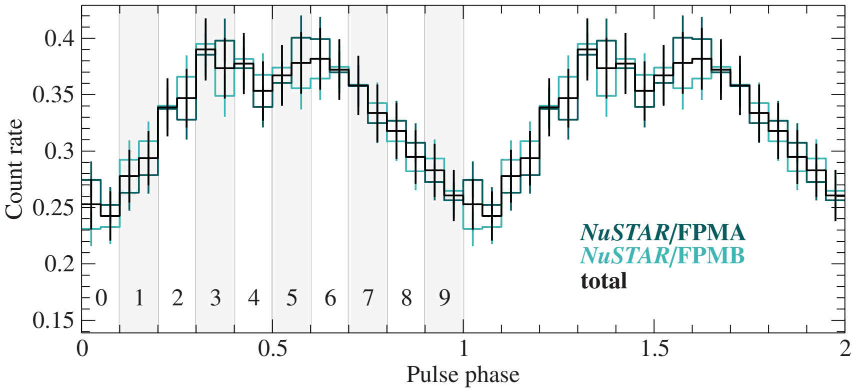

Figure 6.21: Pulse profile of GX 304−1 in quiescence from *NuSTAR* data. Ten bins selected for phase-resolved analysis are shown on the left.

background. In the first case, the region was centered on the source, in the second, it was located outside of the point-spread function.

I performed a simultaneous fit of the `polcap_lb` model to the spectra corresponding to the selected phase bins. The best-fit model and *NuSTAR* data are shown in Figure 6.22 for three selected bins. Table 6.3 contains the best-fit parameters. Interestingly, here one of the previously obtained solutions for the phase-averaged case appears again for the magnetic angle and the observer's inclination: $\Theta_1 \approx 90°$ and $i \approx 13°$. At this geometry, both poles are always visible for the observer and the phase variation of the cyclotron line is rather small (see Figure 6.16, where the phase variation is shown for the geometry, close to the discussed one).

The model application to the phase-resolved spectra, finally constrains the azimuthal offset of the poles, with the best-fit value of $\Delta\Phi \approx 223^\circ$, which translates into about 43° offset compared to the symmetric case.

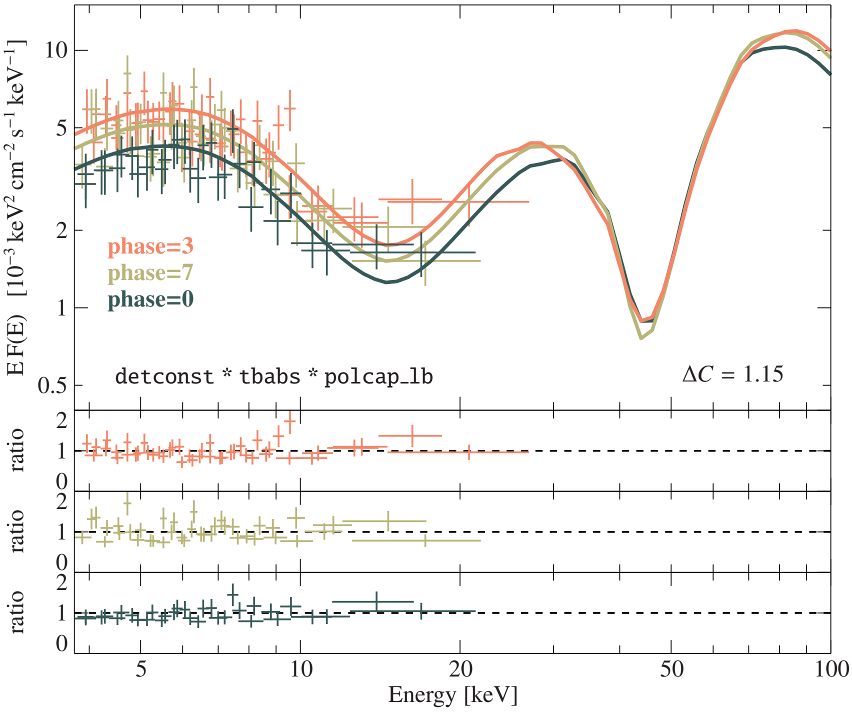

Figure 6.22: Spectra of GX 304−1 in quiescence for three selected phase bins. The bins' numeration is the same as in Figure 6.21. For each bin, the spectra include both, *NuSTAR* FPMA and FPMB.

Table 6.3: Best-fit parameters for the model plotted in Figure 6.22.

PARAMETER	BEST-FIT
N_H [10^{22} cm^{-2}]	1.1 *(fixed)*
$\log_{10}(\dot{M}/[\mathrm{g\,s^{-1}}])$	13.928 *(fixed)*
r_0 [m]	1.386×10^2 *(fixed)*
E_cyc [keV]	56.6 *(fixed)*
i [rad]	0.22 ± 0.06
Θ_1 [rad]	$1.51^{+0.07}_{-0.05}$
Θ_2 [rad]	$(\pi - \Theta_1)$
$\Delta\Phi$ [rad]	$3.89^{+0.26}_{-0.16}$
C_FPMA	1 *(fixed)*
C_FPMB	$0.963^{+0.027}_{-0.025}$
Cash/d.o.f.	$1724.52/1495 = 1.15$

I again explore the parameter space by using `emcee` with 10 walkers for each free parameter and initially uniform distributions. The result is displayed in Figure 6.23. The high-probability regions for for Θ_1 and i are centered to the similar values, as before, in the phase-averaged case, but are much narrower, providing better constrain for these parameters. In addition, the probability distribution for $\Delta\Phi$ now distinctly peak between ~ 220–230°, in agreement with the best fit. In this way, the analysis of the phase-resolved spectra with `polcap_lb` allowed to constrain the azimuthal offset of the poles and provides very restrictive constraints for the polar angle and the observer's inclination.

6.3.3 *Can This Result be Understood and Ruined?*

The narrow regions of high probability obtained in the previous section, look promising. The question remains, however, how much this result is biased by underlying assumptions. The fixed mass accretion rate and polar cap radius are of the biggest concern, as they determine the total flux level of emission in the neutron star rest frame. Currently, the flux used as input for ray tracing code is fixed, and thus geometry is the only way to change the flux level in the observer's rest frame. To investigate the possibility of altering the solution by allowing for a variation of the flux level, I created a version of `polcap_lb` with an additional parameter of flux normalization, which is allowed to vary in the range 0.1–10, i.e., the range of flux variation, typically introduced by geometry.

I again explore the parameter probabilities for `polcap_lb`, this time with normalization parameter, to produce the phase-resolved spectra

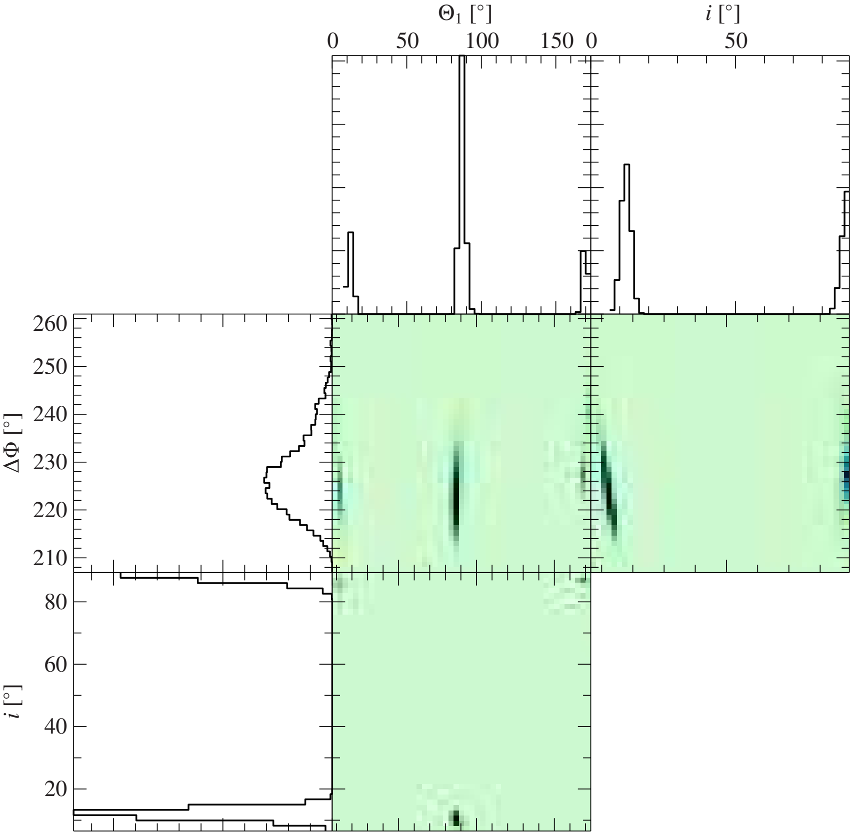

Figure 6.23: Parameter probability distribution obtained with `emcee` for the phase-resolved analysis of GX 304−1. The darker part of the colorscheme corresponds to higher probabilities.

of GX 304−1, by using `emcee` (same setup for the run as in the phase-resolved case before). The column density for photoelectric absorption is also set to $1.1 \times 10^{22}\mathrm{cm}^{-2}$ and the detector constant for *NuSTAR*/FPMB is fixed to the previously obtained best-fit value (see Table 6.3). Figure 6.24 shows the probability distribution for the normalization parameter and the same geometrical parameters as before. The most interesting result here is that the probability for the normalization parameter peaks very close to unity, at ~0.98. This slightly lower flux level shift the highest probability for Θ_1 by a few degrees, slightly above 90°. Similarly, the most probable value for i is at a few degrees higher than in Figure 6.23. The most important is that there are no principally new solutions of the normalization parameter, substantially different from unity.

This result reflects the fact that there are a only a few different factors influencing the solution: the total flux level, its spectral shape (especially at energies below ~15 keV, which dominate the statistics), and its variability with the rotational phase. The variability with rotational phase is what allows to narrow down ranges of high-probability values for Θ_1 and i and to constrain $\Delta\Phi$ when working with phase-resolved, instead of phase-averaged, spectra. The total flux level is allowed to vary within two orders of magnitude in the presented test model with the normalization parameter, and does not affect crucially the obtained solutions. I conclude that it is the spectral shape which principally restricts the geometry. Below 15 keV, it is affected by $\dot{M}$ and r_0. It is then expected that the usage of the full version of the `polcap_lb` model, where the physical parameters of `polcap` are allowed to vary simultaneously with

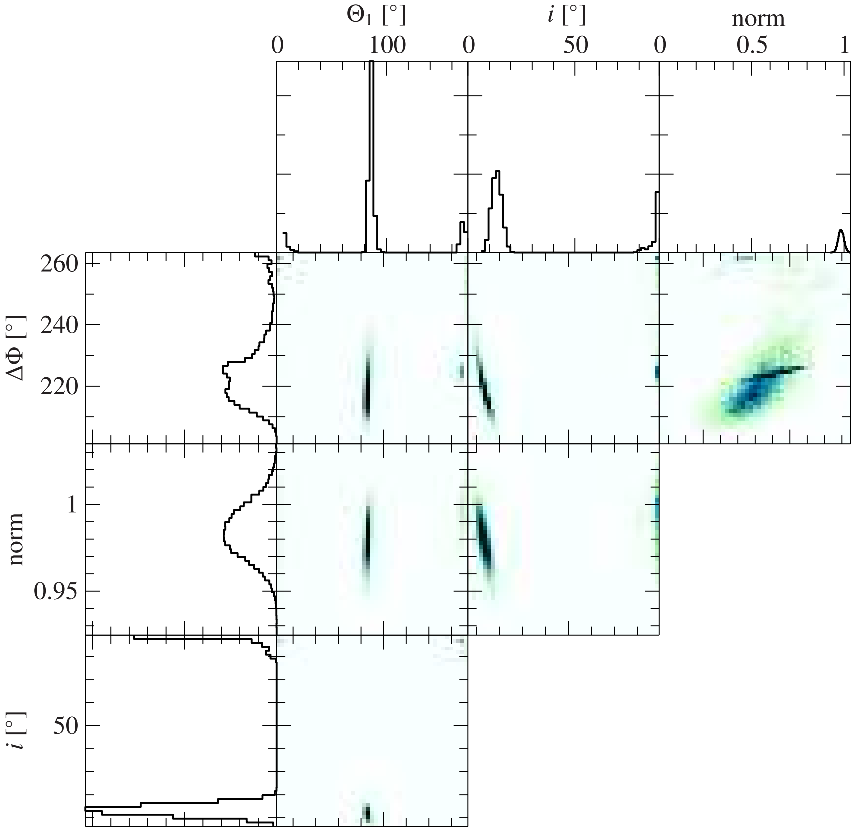

Figure 6.24: Parameter probabilities obtained with `emcee`, for the `polcap_lb` model, which includes the normalization parameters and phase-resolved spectra of GX 304−1.

the geometrical parameters of the ray tracing code, could extend the regions of high-probability values for geometrical parameters. This extent, however, is not expected to be dramatic, nor should it lead to additional degeneracy between the angles. The reason for that is that at low energies variation of the geometry affects predominantly flux level, not its overall spectral shape (see, for example, Figure 6.17 and Figure 6.18) due to a relatively simple shape of the emission profile, compared to high energies. Simultaneously, r_0 and $\dot{M}$, which then have the highest influence on the spectral shape, are not degenerate, as was shown in Figure 6.7.

What can affect this conclusion is the inclusion of the vacuum resonance in the simulations, as it can alter beaming at low energies as well (see, for example, Figure 5.17). This effect has to be investigated with care in future works.

6.4 DISCUSSION AND CONCLUSIONS

In this chapter, I presented a model which describes the emission from accreting highly magnetized neutron stars at low mass-accretion rates. Different aspects of the emission formation, propagation, and projection onto the observer's sky were discussed. Here, I provide a discussion of the model's principal abilities and limitations in Section 6.4.1, mainly addressing the atmospheric structure, the general spectral shape of emission, and the influence of beaming on the geometrical parameters. In Section 6.4.2, I summarize the results and outline some plans for future development of the model.

6.4.1 *Discussion*

A few important limitations of the present model have to be noted with respect to spectral formation. First of all, a simplified way of coupling energy balance in the atmosphere with the radiation field presented above and non-magnetic coefficients used in the energy balance equation result in the atmospheric structure being almost independent of the magnetic field value. This contradicts basic physical considerations, as well as more consistent simulations of the atmospheric structure (see, e.g., Meszaros et al. 1983). Magnetic opacities can play a crucial role in the cooling of highly magnetized plasmas (Suleimanov et al. 2022), and are likely especially relevant for the upper-most optically thin overheated layer. I do not expect these effects to change the basic properties of the obtained solutions, that is, variation of the electron temperature from significantly higher values on top of the atmosphere down to only a few keV at high depths. However, they can alter the exact values and the overall temperature gradient behavior. This would not change a principle spectral shape, but would affect the strength of components and the transition region between the two humps.

Another aspect that can have a similar effect on the solution is the energy deposition profile inside the atmosphere, which in principle should be calculated consistently with the energy balance and radiative transfer in the atmosphere. If the braking process also results in collective plasma effects or collisional excitations of the Landau levels, this energy should be removed from the thermal reservoir, lowering the temperature of the plasma. In the case of a significant contribution of collisional excitations, cyclotron photons, which are produced by radiative decay of collisionally populated levels, also have to be included in the radiative transfer. I, however, argue for more careful treatment of this process than a simple introduction of an additional source of photons, as was done in Sokolova-Lapa et al. (2021) and Mushtukov et al. (2021). The presence of this source can help increasing the high-energy component and reduce the depth and width of the cyclotron line, whose profile is broader due to the non-relativistic cross sections used in the mentioned works, compared to the fully relativistic case (Alexander et al. 1989). In addition, the `FINRAD` code, adopting an approximate treatment of the induced processes via the modified detailed balance condition, knowingly produces slightly lower high-energy flux than in the case of full iterative scheme for induced process (see Alexander et al. 1989, for a comparison of different treatments). These are the reasons why a simple introduction of the source of the cyclotron photons with arbitrary chosen distribution with depth, without careful consideration of the levels population and the knowledge of the depth-dependent probability of collisional excitations, can introduce a significant bias and lead to over-interpretation of the results, while simply compensating for another, not accounted effects.

The last effect worth mentioning in the discussion of the general spectral shape, is vacuum resonance. Undoubtedly, taking this effect into account can have a noticeable influence, based on the results of Chapter 5. The high density gradient in the atmosphere will enforce mode conversion at different depths for different photon energies. High-energy photons are expected to pass the resonant density, where mode conversion occurs, deep down in the atmosphere. After that, their propagation is determined only by the magnetized vacuum, as given by the current version of the model. The low-energy photons will be, however, much more affected. Based on the results of Chapter 5, one could expect that the main effects on the spectra will be a slight suppression of the cyclotron resonance and noticeable depolarization of the spectra, as the lowest energy of the vacuum resonance, corresponding to $n_\mathrm{e} \sim 10^{19}\,\mathrm{cm}^{-3}$, is shifted to $\sim 0.1\,\mathrm{keV}$. But I am not sure that much stronger redistribution effects in the accretion-heated atmosphere will not introduce additional modifications to this picture. This has to be investigated in future works.

Finally, it is important to note that beaming of the radiation is expected to be modified by the vacuum polarization effect, according to emission profiles in Section 5.3. Different emission profiles will result in the different phase dependency of the flux, observed from the poles. This means different pulse profiles for geometries considered here. With a different angular dependency of emission in the neutron star rest frame, introduced by the vacuum resonance, it is likely that the fit to the same dataset will result in a best-fit different geometry.

6.4.2 *Summary*

The main results of this chapter are as following:

- Based on the assumption of a certain energy deposition profile in the neutron star atmosphere, characteristic of Coulomb-heated atmospheres, the plasma density and electron temperature distributions were found. The resulting temperature profile varies strongly from high temperature, $\sim 30\,\mathrm{keV}$, on top of the neutron star atmosphere, down to $\sim 2\,\mathrm{keV}$ in the deep isothermal layers, where thermalization of the radiation is typically achieved. The density values also vary from $10^{19}\,\mathrm{cm}^{-3}$, corresponding to the top overheated layer, down to $10^{25}\,\mathrm{cm}^{-3}$.

- The radiative transfer simulations performed on this inhomogeneous atmospheric layer for various sets of the principal parameters reveal a two-component spectral structure, which differs significantly from the power law with high-energy cutoff seen at higher $\dot{M}$. The low-energy "thermal" hump is strongly enhanced by mode 1, which has lower opacity in the continuum. The high-energy excess is formed by the resonant Comptonization of the soft photons in the intermediate part of the atmosphere, $\tau_\mathrm{T} \sim 10$–0.1 with a high temperature gradient. It is modified by the cyclotron line at the top-most layer of the atmosphere, with $\tau_\mathrm{T} \lesssim 10^{-2}$. This evolution of the photon density in the atmosphere has not been studied in detail before.

- By combining the physical emission model with relativistic ray tracing and taking into account rotation of the neutron star, I presented a methodology for the search for the geometrical parameters of the neutron star based on the phase-resolved spectral fitting. As shown in Section 6.3.3, the model is capable of providing very tight constraints on the geometrical parameters. Improvement of the physical foundations of the model, especially including the effect of mode conversion, will thus make possible to constrain the true geometry by reducing the systematic error.

In addition, I demonstrated that by having an underlying physical angle-dependent model, some general conclusions on the spectra from polar caps can be made:

- The phase-averaged spectra noticeably depend on the geometry. This applies to both, the overall flux level and the shape of the cyclotron line and its wings.
- For both, phase-averaged and phase-resolved spectra, the contribution of the second pole, which is further away from the observer, can make a cyclotron line narrower. In the case when the line profile from the spectrum of the first pole is broad, this contribution can introduce irregularity and complexity to the line shape.
- The variation of the cyclotron line with energy depends on geometry. Typically, large angles between the observer's line of sight and pole 1 result in a minimal variation of the cyclotron line. The geometries with the intermediate separation of the observer and pole 1 ($|\Theta_1 - i| \approx 50^\circ$) already show the significant phase dependency of the line profile.

The latter conclusions are only wrong in the case of the isotropic emission from the pole. None of the effects, which were omitted in this chapter, including the vacuum resonance in the strong magnetic field, are expected to create the isotropic emission.

The presented model is by no means a last word in this research. It, however, paves a path for the future development which should include all relevant effects. The first objectives are inclusion of the effect of the vacuum resonance and implementation of magnetic opacities for the energy balance calculations. Simultaneously, a relatively easy improvement of the self-consistency can be made by introducing an iterative procedure using the calculated flux to find the atmospheric structure.

Independently, the approach to handling the full model, combining physical and geometrical parameters, will be improved in the near future. It is important to perform tests with the full model, to make sure that $\dot{M}$ and r_0, together with geometrical parameters, will not produce degenerate solutions. The result of introducing the model with the flux normalization parameter (Section 6.3.3) looks promising with this respect, but has to be verified. In addition, the combined effect of the magnetic field variation and geometrical parameters has to be studied, as geometry can affect the location of the line wings and core, as well as its general shape.

Part IV

CONCLUSIONS

CONCLUSIONS & OUTLOOK

7

In this thesis, I addressed the problem of the radiative transfer of polarized radiation in a hot, highly magnetized medium, which is expected in the vicinity of accreting highly magnetized neutron stars in High-Mass X-ray Binaries. The main finding of this work is that angular and energy redistribution in the presence of cyclotron resonance and polarization effects have a major influence on the spectral shape, beaming, and polarization of the emission. In order to obtain a realistic picture of the angle-dependent emission from accretion columns and polar caps of accreting X-ray pulsars, these effects have to be taken into account, together with a simultaneous treatment of the continuum and the cyclotron line. Using relativistic ray tracing and taking neutron star rotation into consideration, this approach allows to access fundamental information about the magnetic field of the neutron star and its orientation with respect to the observer. Here I outline the major conclusions of this research and mention possible directions that further development of the presented models could take.

I. Complexity of the Continuum

The continua of the X-ray spectra emitted from hot highly magnetized media ($kT_{\mathrm{e}} \gtrsim 4\,\mathrm{keV}$, $B \gtrsim 10^{12}\,\mathrm{G}$, typical for polar caps and accretion columns of accreting neutron stars in High-Mass X-ray Binaries), naturally have a complex shape. This shape can be described by humps and dips on top of a power law ("10-keV" feature) or a few Comptonized components with different plasma temperatures – both are common choices for spectral data analysis. There are *two major reasons* for this behavior.

The first one is the *natural change of the dominant polarization mode* across the spectrum which results from the vastly different interactions of the modes with the real and virtual plasmas. This effect can be enhanced by the vacuum resonance, which is produced by the cancellation of the responses of the real and virtual charges. The vacuum resonance introduces an additional interplay of polarization modes and can result in a standalone line-like feature at soft and intermediate energies. This serves as a potential explanation of the necessity of the "10-keV" feature (or a standalone cyclotron line at $\sim$10 keV) or the two-component continuum. I suggest that it might be especially relevant in the absence of the confirmed cyclotron line in the continuum with complexity around $\sim$10 keV, as observed, for example, for KS 1947+300 (Fürst et al. 2014a; Doroshenko et al. 2020a), EXO 2030+375 (Klochkov et al. 2007), and 4U 1901+03 (Reig & Milonaki 2016). This would help to isolate the influence of redistribution near the cyclotron resonance from purely continuum behavior of the polarization modes, providing that these sources do not hide a cyclotron line in the X-ray energy band due to, for example, purely geometrical effects.

The second principal mechanism which is responsible for the complex continuum shape is *anisotropic redistribution near the cyclotron resonance*. It can result in a substantial excess of photons in a broad band of energies below the fundamental cyclotron line, which is essentially a red wing of the line. This effect is very likely to be responsible for the occasional necessity of the "10-keV feature" in emission at higher energies below the cyclotron resonance. A possible example of this effect is a $\sim$25-keV Gaussian emission feature required to describe an otherwise power-law-like continuum of A 0535+262, while the fundamental cyclotron line is at $\sim$45 keV (Ballhausen et al. 2017). During the data analysis, depending on the choice of continuum model and access to high energies with the dataset, the wing can be erroneously treated as part of the (power-law-like) continuum, causing a dip to appear at energies below it. This is likely the case for X Persei, where the cyclotron line at $\sim$30 keV was observed (Coburn et al. 2001) together with a strong excess at higher energies. Later observations of Be X-ray Binaries in quiescence revealed, however, that a similar dip also appears at intermediate energies ($\sim$20 keV) of the spectra from sources with known cyclotron lines at energies $\gtrsim$ 45 keV (e.g., A 0535+262 and GX 304$-$1; Tsygankov et al. 2019b,c). It is possible that for X Persei, which has a low-luminosity, the dip at $\sim$30 keV is followed by the strong red wing of the cyclotron line and is a continuum feature (see also notes in Mushtukov et al. 2021; Sokolova-Lapa et al. 2021). As was demonstrated in Chapter 6, this effect is significantly enhanced in the case of low-luminosity accretion where the atmosphere is heated to higher temperatures and the red wing of the cyclotron line is seen as a strong high-energy hump in the spectra.

For sources with intermediate field values ($E_{\rm cyc} \sim$ 20–30 keV) and, possibly, multiple cyclotron lines (e.g., Cep X-4 and Vela X-1; Vybornov et al. 2017; Diez et al. 2022, respectively), it is possible that both effects – continuum mode crossing/vacuum resonance and the redistribution in the red wing of the cyclotron line – are present. A number of spectra presented in Chapter 5 illustrate this case: see, for example, Figure 5.15, where the classical "10-keV" feature is brought up by mode 1 after the crossing and is emphasized by a later growth of the line wing, which enhances the formation of a dip. It is important to note that all these components can exhibit phase dependency as nothing is fully isotropic when the vacuum polarization is taken into account together with the magnetized plasma.

II. Spectral Formation

The immediate result that follows from the previous discussion of the continuum complexity based on the findings of Chapter 5 and Chapter 6 is that the classical approach of separating the problem for the formation of the cyclotron lines and of the Comptonized continuum (see, e.g., Nishimura 2008; Schwarm et al. 2017b) will fail to provide the correct total spectral shape, even though it addresses the specific behavior of the lines. This approach could be justified to describe the total spectral shape only in the case where *the input continuum for cyclotron line simulations was obtained by taking into account resonant energy and angular redistribution and polarization effects*. As I showed in Chapter 6 by studying the evolution of the energy-dependent photon density in the atmosphere (see Figure 6.4), the formation of the red wing of the cyclotron line proceeds in an extended region corresponding to $\tau_{\rm T} \sim$ 10–0.1. At smaller $\tau_{\rm T}$, the complex continuum is already unaffected by the radiative transfer effects and only the cyclotron line is imprinted at $\tau_{\rm T} \lesssim 10^2$. Since in this work I treat the cyclotron processes in a simplified way, the shape of the fundamental line is not reproduced in detail and higher harmonics are not included. I suggest that the obtained result opens an avenue for improvement of the model by combined physical modeling of the Comptonized continuum including necessary effects of resonant redistribution to reproduce a complex spectral shape (as was done here) at $\tau_\mathrm{T} \sim 10^{-2}$ with detailed treatment of the cyclotron resonances at lower τ_T (e.g., with the method of Schwarm et al. 2017b).

III. Polarization Modes. Vacuum Polarization

In Chapter 5, I performed radiative transfer simulations for a few basic choices of polarization modes used in the literature and demonstrated their principal effect on the emergent spectrum. I showed there that for spectral modeling under typical condition, the pure vacuum polarization modes provide a better approximation (especially for the region near the cyclotron line) to the more general case of mixed plasma and vacuum effects, but still can result in a significantly different polarization signal and spectra at intermediate energies. The latter is true for the pure plasma polarization modes. The conclusion is that it is *generally important to take into account the responses of both real and virtual charges*.

In the cases where the vacuum polarization was included together with a magnetized plasma with continuous choice of refractive indices of the modes, I demonstrated that it can result in a depression of the continuum above the vacuum resonance, the suppression of the cyclotron line (compared to the pure vacuum polarization modes), and overall increased complexity of the spectral shape. For the simplified model of the inhomogeneous accretion mound presented in Section 5.4, I showed that these effects on the spectrum are also present. In this case, the vacuum resonance results in a low-energy broad absorption-line-like feature. As was discussed in Chapter 5, similar effects due to vacuum polarization are known for the cold atmospheres of neutron stars with higher magnetic fields, $B \sim 10^{14}\,\mathrm{G}$. For hot inhomogeneous media with strong anisotropic photon redistribution due to resonant Comptonization this effect was demonstrated for the first time.

The polarized radiative transfer simulations for the inhomogeneous accretion mound model showed an overall lower degree of polarization in the neutron star rest frame than the previous models (e.g., Caiazzo & Heyl 2021b) when both plasma and vacuum influences are taken into account. The simulations show that the vacuum polarization generally induces the depolarization at energies above the lowest vacuum resonance (given by the lowest density and the highest magnetic field for a given emission region) It does not necessarily have to be accompanied by the "inverse" temperature distribution in the emission region, that is, with an overheated top layer, as suggested by Doroshenko et al. (2022), but simply requires an inhomogeneous density profile, which is always the case in accretion flows near compact objects. The temperature gradient can, of course, also enhance this effect. Further studies should address a combination of emission in the neutron star rest frame with light bending (as was done for the `polcap` model in Chapter 6) and radiation propagation in the magnetosphere, which might bring the total polarization degree to the low values observed by *IXPE* Tsygankov et al. (2022); Doroshenko et al. (2022). In the future work, the partial mode conversion (similar to van Adelsberg & Lai 2006, , for cold highly magnetized atmospheres) also has to be taken into account, which will require modification of the numerical scheme.

IV. Beaming and Pulse Profiles

As was shown in Chapter 5 and Chapter 6, the beam profiles from a slab of highly magnetized plasma can rarely be described as simple pencil and fan beams. Emission profiles are complex not only near the cyclotron resonance, but also in the low-energy continuum. Although angular dependency of the cross sections can provide one with intuition about the final emission profiles, the latter strongly depends on the total optical depth of the emission region, which depends on the energy and angle of photon propagation. As I discussed in detail in Section 5.3, the transport effects can result in strikingly different emission profiles even for two energy bands which have the same angular behavior of cross sections. For the physical model presented in Chapter 6, pulse profiles were also obtained. Considering that only the pure vacuum normal modes, which show the overall simplest angular dependency, were used, it is interesting how complex the resulting pulse profiles are in a broad range of energies around the cyclotron resonance, $\sim$35–50 keV (see Figure 6.14). The complex beam shapes are expected from highly magnetized plasma, including the energies far below the typical location of the cyclotron resonance, which can be a key factor in explaining the various shapes of the observed pulse profiles. Further research on this specific topic should include the effect of the vacuum resonance on the emission profiles for the `polcap` model and obtain pulse profiles from a simple model of the accretion mound (Section 5.4).

V. Geometry Determination with `polcap_lb`

As already emphasized, two principal physical models with an inhomogeneous emission region were presented in this dissertation. The more complex `polcap` model for low-luminosity accretion onto highly magnetized neutron stars presented in Chapter 6 was developed to be coupled with a ray-tracing code for slowly rotating neutron stars (Falkner 2018). The final model, `polcap_lb`, can be used for phase-averaged and phase-resolved data analysis and is applicable for highly magnetized neutron stars, $B \gtrsim 10^{14}\,\mathrm{G}$, accreting at $\dot{M} \lesssim 10^{15}\,\mathrm{g\,s^{-1}}$ (for example, Be X-ray Binaries in quiescence). This approach allows us determine the location of the magnetic poles and the observer's inclination with respect to the rotation axis of the neutron star.

I showed the applicability of this method using the quiescent observation of GX 304−1, finding the magnetic angle of the pole (pole 1) and the inclination of the observer to be $\Theta_1 \approx 90^\circ$ and $i \approx 13^\circ$ respectively. However, this solution is indistinguishable from the opposite case, when $\Theta_1 \approx 13^\circ$ and $i \approx 90^\circ$). Using the phase-resolved spectra, the azimuthal separation of the poles can also be found. For GX 304−1, the offset $\Delta\Phi \sim 43^\circ$ was found in this work, pointing at a distorted dipole geometry. This result might be influenced by including the effect of a magnetized plasma, which will introduce vacuum resonance. This possibility will be investigated in future work. Once the problem of handling large tables of the model is solved, it can be expanded on to find the physical parameters r_0, $\dot{M}$, E_{cyc} together with the geometrical ones. The geometries that are found with the presented model have to be compared with the results of polarimetric observations. The best candidate is X Persei as it was observed with *IXPE* and is expected to be in the regime described by the `polcap_lb` model. It is interesting to note that so far two Be X-ray Binaries exhibiting the quiescent two-hump spectra which were observed with *IXPE*, are found to be orthogonal rotators, that is, $\theta_1 \sim 90^\circ$ (Mushtukov et al. 2023; Tsygankov et al. 2023). More studies are required to answer the question of whether it is a coincidence, the result of a bias, or the true nature of the sources, where a constant accretion at low rates forces, for example, the alignment of the magnetic axis with the plane of the (possibly present) accretion disk.

After the current limitations of the `polcap_lb` are eliminated, the compactness of the neutron star, $M_{\mathrm{NS}}/R_{\mathrm{NS}}$ can be allowed to be a free parameter. In the current version of the model, this ratio affects the energy deposition in the atmosphere during the accretion, and, most importantly, have a large effect on light bending and phase variability of the emission.

An exciting future for quiescent accretion in slowly rotating Be X-ray Binaries is expected with The High Energy X-ray Probe (HEX-P), a mission concept that will be submitted to NASA in response to its 2023 Probe call. The mission would allow us to access an unprecedentedly broad energy range 0.1–150 keV. As these sources typically have high-energy cyclotron lines with centroid energies $\gtrsim$ 40 keV, observations with exposure of few tens of ks with *NuSTAR* are insufficient to access them (see, e.g., Tsygankov et al. 2019c; Lutovinov et al. 2021). Even higher exposure of more than a hundred ks struggle with the cyclotron line region (Zainab et al., in prep.). HEX-P would allow to access these energies and thus provide a direct measurement of the magnetic field strength in the poles by constraining the cyclotron line. Figure 7.1 shows a simulated observation of HEX-P for the `polcap` model with parameters similar to the best-fit to GX 304−1 quiescent observation.

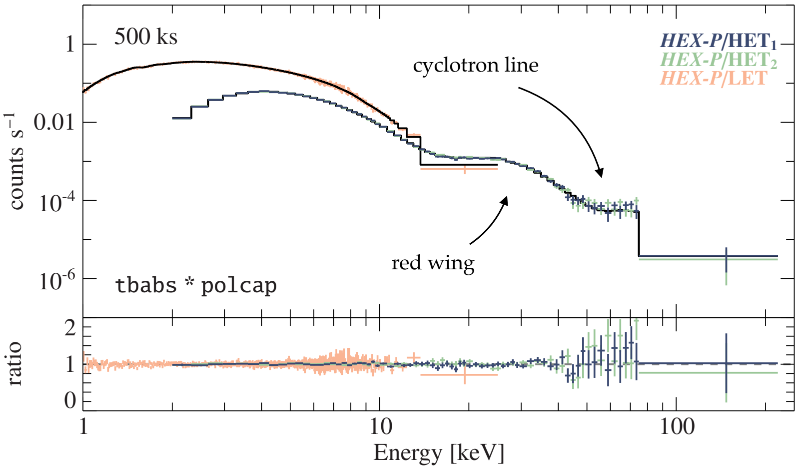

Figure 7.1: Simulated 500 ks observation of HEX-P with the `polcap` model. The source is assumed to have a distance of 2 kpc and the total luminosity of $\sim 10^{34}$ erg s^{-1}, with the parameters, close to the ones presented in Table 6.1.

VI. Accretion Mound

The simplified model of the accretion mound, which was presented in Chapter 5, provides a basic understanding of the formation of the polarized spectra in the bottom dense region of the accretion channel, but is only a first step toward a full description of the physical picture at higher $\dot{M}$. The regions of high velocities of the tenuous accretion flow above the mound and possibly on the sides of the are expected to affect the predicted emission in a few ways. First, processing in a lower density plasma can bring the vacuum resonance down to lower energies, opening the avenue for even stronger depolarization of the mid-X-ray energies. The overall shape of the continuum at lower energies is likely less affected than higher energies, as the optical depth of the tenuous plasma can still remain high for photons in a wide vicinity of the cyclotron resonance. Beaming due to the high velocities of electrons and near-resonant redistribution in a warm inhomogeneous plasma is expected to further smooth the cyclotron resonance and bring components of emission profiles more to the sides and downwards (see Figure 5.17 and Figure 5.18). It is important to note that in the current model, the top boundary condition did not include the photon flux which is expected due to advection. The combination of these effects and gravitational light bending during the rotation of the neutron star can also affect the visibility of the cyclotron line and fine continuum features.

The following improvement of the model can be done in the near future: the radiative transfer simulation should be coupled with the calculation of the hydrodynamic structure of the column in a consistent way. It is crucial that the effects of the strong magnetic field are included in the calculation of the column structure as they can dramatically alter the picture (O. Blaes, L. Zhang, priv. comm.). Due to the two-dimensional nature of the (magneto-)hydrodynamic simulations of the accretion column, the *two-dimensional* angular- and polarization-dependent radiative transfer, which includes proper redistribution treatment in the continuum and resonances, is required. In addition, it should include the possibility of bulk Comptonization, whose influence on the total spectrum has to be carefully estimated. Further more, phase-dependent modeling that includes light bending and assumed location of the accreting poles have to be considered. This is the plan for future work.

To conclude this work, I would like to add a few final remarks. First of all, hard X-ray polarimetry is required to confirm some of the findings of this research. The polarization signal near the continuum irregularities can provide crucial information about their nature, such as the crossing of the polarization mode spectra or redistribution in the broad region around the cyclotron resonance. It will also allow us to search for hidden cyclotron lines, which could be washed out by dynamic effects in the accretion channel in combination with a certain geometrical configuration and suppression of the resonance due to vacuum polarization, still keeping an imprint on the polarization signal. Unfortunately, the energy range of *IXPE* only reaches $\sim$8 keV, not accessing the majority of the continuum irregularities at $\gtrsim 10$ keV. The next flight of the balloon-borne XL-Calibur mission planned for this year, 2023, will hopefully address the effect of the vacuum polarization in the formation of the spectra of accreting X-ray pulsars in High-Mass X-ray Binaries.

Secondly, complex shapes of spectra and pulse profiles are not exclusive to High-Mass X-ray Binaries. As was mentioned in Section 2.4.1, magnetars also exhibit spectra with dips and excesses. In addition, their pulse profiles can be fairly complex (see, e.g., Younes et al. 2022). I would like to note that polarized angular- and energy-dependent radiative transfer with resonant redistribution can be important for several populations of neutron stars, especially in the case of magnetic field $\gtrsim 10^{11}$ G when anisotropic properties of the medium can significantly modify emission beaming, polarization signal, and spectral shape.

My final remark is that the prosperous development of our understanding of neutron stars (and other objects in the Universe), would not be possible without open collaboration and cooperation between various groups in this field that I have experienced during my research, inspiring riveting discussions and leading to the rapid growth of this fascinating branch of astrophysics.

BIBLIOGRAPHY

Abarr, Q., Awaki, H., Baring, M. G., et al. 2021, XL-Calibur - a second-generation balloon-borne hard X-ray polarimetry mission, Astroparticle Physics, 126, 102529

Abarr, Q., Baring, M., Beheshtipour, B., et al. 2020, Observations of a GX 301-2 Apastron Flare with the X-Calibur Hard X-Ray Polarimeter Supported by NICER, the Swift XRT and BAT, and Fermi GBM, ApJ, 891, 70

Abbott, R., Abbott, T. D., Abraham, S., et al. 2020, GW190814: Gravitational Waves from the Coalescence of a 23 Solar Mass Black Hole with a 2.6 Solar Mass Compact Object, ApJ, 896, L44

Abdo, A. A., Ackermann, M., Ajello, M., et al. 2010, Discovery of Pulsed γ-Rays from PSR J0034-0534 with the Fermi Large Area Telescope: A Case for Co-Located Radio and γ-Ray Emission Regions, ApJ, 712, 957

Abdo, A. A., Ackermann, M., Ajello, M., et al. 2011, The First Fermi Multifrequency Campaign on BL Lacertae: Characterizing the Low-activity State of the Eponymous Blazar, ApJ, 730, 101

Abdo, A. A., Ajello, M., Allafort, A., et al. 2013, The Second Fermi Large Area Telescope Catalog of Gamma-Ray Pulsars, ApJS, 208, 17

Abeysekara, A. U., Benbow, W., Bird, R., et al. 2018, Periastron Observations of TeV Gamma-Ray Emission from a Binary System with a 50-year Period, ApJ, 867, L19

Abolmasov, P. & Lipunova, G. 2022, Simulating the shock dynamics of a neutron star accretion column, MNRAS, submitted, (arxiv:2207.12312)

Adams, C. B., Benbow, W., Brill, A., et al. 2021, Observation of the Gamma-Ray Binary HESS J0632+057 with the H.E.S.S., MAGIC, and VERITAS Telescopes, ApJ, 923, 241

Adams, T. F., Hummer, D. G., & Rybicki, G. B. 1971, Numerical evaluation of the redistribution function R_{II-A}(x, xÿ) and of the associated scattering integral., J. Quant. Spectr. Rad. Transf., 11, 1365

Adler, S. L. 1971, Photon splitting and photon dispersion in a strong magnetic field., Ann. Phys., 67, 599

Aguilera, D. N., Pons, J. A., & Miralles, J. A. 2008, 2D Cooling of magnetized neutron stars, A&A, 486, 255

Ahnert, P., van Schewick, H., & Hoffmeister, C. 1941, Die Veraenderlichen Sterne der noerdlichen Milchstrasse. Teil II, Kleine Veroeffentlichungen der Universitaetssternwarte zu Berlin Babelsberg, 6, 4.1

Akgün, T., Cerdá-Durán, P., Miralles, J. A., & Pons, J. A. 2017, Long-term evolution of the force-free twisted magnetosphere of a magnetar, MNRAS, 472, 3914

Alexander, S. G. & Meszaros, P. 1991, Cyclotron Harmonics in Accreting Pulsars and Gamma-Ray Bursters: Effect of Two-Photon Processes, ApJ, 372, 565

Alexander, S. G., Meszaros, P., & Bussard, R. W. 1989, The nonlinear transfer problem in accreting pulsars - Stimulated scattering effects, ApJ, 342, 928

Alme, M. L. & Wilson, J. R. 1973, X-Ray Emission from a Neutron Star Accreting Material, ApJ, 186, 1015

Alpar, M. A. 2001, On Young Neutron Stars as Propellers and Accretors with Conventional Magnetic Fields, ApJ, 554, 1245

Alpar, M. A., Cheng, A. F., Ruderman, M. A., & Shaham, J. 1982, A new class of radio pulsars, Nature, 300, 728

Araya, R. A. & Harding, A. K. 1999, Cyclotron Line Features from Near-critical Magnetic Fields: The Effect of Optical Depth and Plasma Geometry, ApJ, 517, 334

Arons, J., Klein, R. I., & Lea, S. M. 1987, Radiation Gas Dynamics of Polar CAP Accretion onto Magnetized Neutron Stars: Basic Theory, ApJ, 312, 666

Auer, L. 1967, Improved Boundary Conditions for the Feautrier Method, ApJ, 150, L53

Baade, W. & Zwicky, F. 1934, On Super-novae, PNAS, 20, 254

Bachetti, M., Harrison, F. A., Walton, D. J., et al. 2014, An ultraluminous X-ray source powered by an accreting neutron star, Nature, 514, 202

Backer, D. C. 1970, Pulsar Nulling Phenomena, Nature, 228, 42

Backer, D. C., Kulkarni, S. R., Heiles, C., Davis, M. M., & Goss, W. M. 1982, A millisecond pulsar, Nature, 300, 615

Bahramian, A. & Degenaar, N. 2022, Low-Mass X-ray Binaries, Invited chapter for Handbook of X-ray and Gamma-ray Astrophysics, eds. C. Bambi and A. Santangelo, Springer Singapore (arXiv:2206.10053)

Ballhausen, R. 2021, X-ray spectroscopy of X-ray binaries, PhD thesis, Friedrich-Alexander-Universität Erlangen-Nürnberg, Germany

Ballhausen, R., Pottschmidt, K., Fürst, F., et al. 2017, Looking at A 0535+26 at low luminosities with NuSTAR, A&A, 608, A105

Baring, M. G. & Harding, A. K. 2007, Resonant Compton upscattering in anomalous X-ray pulsars, Ap&SS, 308, 109

Basko, M. M. & Sunyaev, R. A. 1975, Radiative transfer in a strong magnetic field and accreting X-ray pulsars., A&A, 42, 311

Basko, M. M. & Sunyaev, R. A. 1976, The limiting luminosity of accreting neutron stars with magnetic fields, MNRAS, 175, 395

Becker, P. A., Klochkov, D., Schönherr, G., et al. 2012, Spectral formation in accreting X-ray pulsars: bimodal variation of the cyclotron energy with luminosity, A&A, 544, A123

Becker, P. A. & Wolff, M. T. 2005, Spectral Formation in X-Ray Pulsar Accretion Columns, ApJ, 621, L45

Becker, P. A. & Wolff, M. T. 2007, Thermal and Bulk Comptonization in Accretion-powered X-Ray Pulsars, ApJ, 654, 435

Becker, P. A. & Wolff, M. T. 2022, A Generalized Analytical Model for Thermal and Bulk Comptonization in Accretion-powered X-Ray Pulsars, ApJ, 939, 67

Becker, W. 2009, in Astrophysics and Space Science Library, Vol. 357, Astrophysics and Space Science Library, ed. W. Becker, X-Ray Emission from Pulsars and Neutron Stars, 91

Bekefi, G. 1966, Radiation Processes in Plasmas (New York, London, Sydney: New York, London, Sydney: John Wiley Inc.)

Bell, S. J. & Hewish, A. 1967, Angular Size and Flux Density of the Small Source in the Crab Nebula at 81.5 Mc/s, Nature, 213, 1214

Beloborodov, A. M. 2009, Untwisting Magnetospheres of Neutron Stars, ApJ, 703, 1044

Beloborodov, A. M. & Li, X. 2016, Magnetar Heating, ApJ, 833, 261

Benacquista, M. J. & Downing, J. M. B. 2013, Relativistic Binaries in Globular Clusters, Living Rev. Relativity, 16, 4

Bethe, H. A. 1990, Supernova mechanisms, Reviews of Modern Physics, 62, 801

Bhattacharya, D. & van den Heuvel, E. P. J. 1991, Formation and evolution of binary and millisecond radio pulsars, Phys. Rep., 203, 1

Bignami, G. F., Caraveo, P. A., De Luca, A., & Mereghetti, S. 2003, The magnetic field of an isolated neutron star from X-ray cyclotron absorption lines, Nature, 423, 725

Bisnovatyi-Kogan, G. S. & Ruzmaikin, A. A. 1976, The Accretion of Matter by a Collapsing Star in the Presence of a Magnetic Field. II: Self-consistent Stationary Picture, Ap&SS, 42, 401

Bissinger, M. 2016, Observations of Be X-ray Binaries: Spin Period and Spectral Evolution, PhD thesis, Friedrich-Alexander-Universität Erlangen-Nürnberg, Germany

Bissinger né Kühnel, M., Kreykenbohm, I., Ferrigno, C., et al. 2020, The giant outburst of 4U 0115+634 in 2011 with Suzaku and RXTE. Minimizing cyclotron line biases, A&A, 634, A99

Blandford, R. & Eichler, D. 1987, Particle acceleration at astrophysical shocks: A theory of cosmic ray origin, Phys. Rep., 154, 1

Blandford, R. D. & Payne, D. G. 1981, Compton scattering in a converging fluid flow. I - The transfer equation. II - Radiation-dominated shock, MNRAS, 194, 1033

Bogdanov, S., Dittmann, A. J., Ho, W. C. G., et al. 2021, Constraining the Neutron Star Mass-Radius Relation and Dense Matter Equation of State with NICER. III. Model Description and Verification of Parameter Estimation Codes, ApJ, 914, L15

Bondi, H. 1952, On spherically symmetrical accretion, MNRAS, 112, 195

Bondi, H. & Hoyle, F. 1944, On the mechanism of accretion by stars, MNRAS, 104, 273

Bozzo, E., Falanga, M., & Stella, L. 2008, Are There Magnetars in High-Mass X-Ray Binaries? The Case of Supergiant Fast X-Ray Transients, ApJ, 683, 1031

Bozzo, E., Oskinova, L., Feldmeier, A., & Falanga, M. 2016, Clumpy wind accretion in supergiant neutron star high mass X-ray binaries, A&A, 589, A102

Braithwaite, J. 2009, Axisymmetric magnetic fields in stars: relative strengths of poloidal and toroidal components, MNRAS, 397, 763

Bulik, T. & Miller, M. C. 1997, Spectral effects of the vacuum resonance in soft gamma-ray repeaters, MNRAS, 288, 596

Bulik, T. & Pavlov, G. G. 1996, Polarization Modes in a Strongly Magnetized Hydrogen Gas, ApJ, 469, 373

Bulik, T., Riffert, H., Meszaros, P., et al. 1995, Geometry and Pulse Profiles of X-Ray Pulsars: Asymmetric Relativistic FITS to 4U 1538-52 and VELA X-1, ApJ, 444, 405

Burbidge, E. M., Burbidge, G. R., Fowler, W. A., & Hoyle, F. 1957, Synthesis of the Elements in Stars, Reviews of Modern Physics, 29, 547

Burke-Spolaor, S. 2013, in Neutron Stars and Pulsars: Challenges and Opportunities after 80 years, ed. J. van Leeuwen, Vol. 291, Rotating Radio Transients and their place among pulsars (Cambridge, UK, Cambridge University Press), 95–100

Burnard, D. J., Arons, J., & Klein, R. I. 1991, Accretion Powered Pulsars: Continuum Spectra and Light Curves of Settling Accretion Mounds, ApJ, 367, 575

Bussard, R. W., Alexander, S. B., & Meszaros, P. 1986, One- and two-photon Compton scattering in strong magnetic fields, Phys. Rev. D, 34, 440

Bykov, A. M. & Krasil'Shchikov, A. M. 2004, Dynamics of the Flows Accreting onto a Magnetized Neutron Star, Astron. Let., 30, 309

Caditz, D. M. & Tsuruta, S. 1998, Adiabatic Shocks in Accretion Flows, ApJ, 501, 242

Caiazzo, I. & Heyl, J. 2021a, Polarization of accreting X-ray pulsars - II.

Hercules X-1, MNRAS, 501, 129

Caiazzo, I. & Heyl, J. 2021b, Polarization of accreting X-ray pulsars. I. A new model, MNRAS, 501, 109

Campana, S., Stella, L., Mereghetti, S., & de Martino, D. 2018, A universal relation for the propeller mechanisms in magnetic rotating stars at different scales, A&A, 610, A46

Canuto, V. 1970, Radiative Opacities and Compton Scattering in Strong Magnetic Fields, ApJ, 160, L153

Canuto, V., Lodenquai, J., & Ruderman, M. 1971, Thomson Scattering in a Strong Magnetic Field, Phys. Rev. D, 3, 2303

Caplan, M. E. & Horowitz, C. J. 2017, Colloquium: Astromaterial science and nuclear pasta, Reviews of Modern Physics, 89, 041002

Cappallo, R., Laycock, S. G. T., & Christodoulou, D. M. 2017, On the Geometry of the X-Ray Emission from Pulsars. I. Model Formulation and Tests, PASP, 129, 124201

Cappallo, R., Laycock, S. G. T., Christodoulou, D. M., Coe, M. J., & Zezas, A. 2019, On the geometry of the X-ray emission from pulsars: the changing aspect of the Be/X-ray pulsar SXP348, MNRAS, 486, 3248

Carpano, S., Haberl, F., Maitra, C., & Vasilopoulos, G. 2018, Discovery of pulsations from NGC 300 ULX1 and its fast period evolution, MNRAS, 476, L45

Cash, W. 1979, Parameter estimation in astronomy through application of the likelihood ratio., ApJ, 228, 939

Ceccobello, C., Farinelli, R., & Titarchuk, L. 2014, Comptonization in ultra-strong magnetic fields: numerical solution to the radiative transfer problem, A&A, 562, A99

Chadwick, J. 1932, Possible Existence of a Neutron, Nature, 129, 312

Chamel, N. & Haensel, P. 2008, Physics of Neutron Star Crusts, Living Rev. Relativity, 11, 10

Chandrasekhar, S. 1931, The highly collapsed configurations of a stellar mass, MNRAS, 91, 456

Chandrasekhar, S. 1939, An introduction to the study of stellar structure (Chicago: Univ. Chicago Press)

Chashkina, A., Lipunova, G., Abolmasov, P., & Poutanen, J. 2019, Super-Eddington accretion discs with advection and outflows around magnetized neutron stars, A&A, 626, A18

Chen, H.-L., Chen, X., Tauris, T. M., & Han, Z. 2013, Formation of Black Widows and Redbacks—Two Distinct Populations of Eclipsing Binary Millisecond Pulsars, ApJ, 775, 27

Cheng, K. S., Ho, C., & Ruderman, M. 1986, Energetic Radiation from Rapidly Spinning Pulsars. I. Outer Magnetosphere Gaps, ApJ, 300, 500

Cheng, Z. Q., Shao, Y., & Li, X. D. 2014, On the Spin Period Distribution in Be/X-Ray Binaries, ApJ, 786, 128

Chevalier, R. A. 1989, Neutron Star Accretion in a Supernova, ApJ, 346, 847

Chu, C.-Y., Ng, C. Y., Kong, A. K. H., & Chang, H.-K. 2021, High-frequency radio observations of two magnetars, PSR J1622 - 4950 and 1E 1547.0 - 5408, MNRAS, 503, 1214

Clark, J. S., Ritchie, B. W., Najarro, F., Langer, N., & Negueruela, I. 2014, A VLT/FLAMES survey for massive binaries in Westerlund 1. IV. Wd1-5 - binary product and a pre-supernova companion for the magnetar CXOU J1647-45?, A&A, 565, A90

Cline, T. L., Desai, U. D., Pizzichini, G., et al. 1980, Detection of a fast, intense and unusual gamma-ray transient., ApJ, 237, L1

Coburn, W., Heindl, W. A., Gruber, D. E., et al. 2001, Discovery of a Cyclotron Resonant Scattering Feature in the Rossi X-Ray Timing Explorer Spectrum of 4U 0352+309 (X Persei), ApJ, 552, 738

Coburn, W., Heindl, W. A., Rothschild, R. E., et al. 2002, Magnetic Fields of Accreting X-Ray Pulsars with the Rossi X-Ray Timing Explorer, ApJ, 580, 394

Colgate, S. A. 1989, Hot bubbles drive explosions, Nature, 341, 489

Comella, J. M., Craft, H. D., Lovelace, R. V. E., & Sutton, J. M. 1969, Crab Nebula Pulsar NP 0532, Nature, 221, 453

Condon, J. J. & Ransom, S. M. 2016, Essential Radio Astronomy (Princeton, NJ: Princeton University Press)

Corbet, R. H. D. 1984, Be/neutron star binaries : a relationship between orbital period and neutron star spin period., A&A, 141, 91

Corbet, R. H. D., Coley, J. B., & Krimm, H. A. 2017, Diverse Long-term Variability of Five Candidate High-mass X-Ray Binaries from Swift Burst Alert Telescope Observations, ApJ, 846, 161

Cordes, J. M. 1979, Coherent Radio Emission from Pulsars, Space Sci. Rev., 24, 567

Crusius-Waetzel, A. R. & Lesch, H. 2002, in Neutron Stars, Pulsars, and Supernova Remnants, ed. W. Becker, H. Lesch, & J. Trümper, Emission Mechanisms in High Energy Pulsars: From Gamma Rays to Infrared (Garching bei München: Max-Plank-Institut für extraterrestrische Physik), 162

Daugherty, J. K. & Harding, A. K. 1986, Compton Scattering in Strong Magnetic Fields, ApJ, 309, 362

Davidson, K. 1973, Accretion at a Magnetic Pole of a Neutron Star, Nature Phys. Sci., 246, 1

Davidson, K. & Ostriker, J. P. 1973, Neutron-Star Accretion in a Stellar Wind: Model for a Pulsed X-Ray Source, ApJ, 179, 585

Davies, R. E., Fabian, A. C., & Pringle, J. E. 1979, Spindown of neutron stars in close binary systems., MNRAS, 186, 779

Davies, R. E. & Pringle, J. E. 1981, Spindown of neutron stars in close binary systems - II., MNRAS, 196, 209

De Grandis, D., Turolla, R., Wood, T. S., et al. 2020, Three-dimensional Modeling of the Magnetothermal Evolution of Neutron Stars: Method and Test Cases, ApJ, 903, 40

De Luca, A. 2017, in Journal of Physics Conference Series, Vol. 932, Journal of Physics Conference Series, ed. G. G. Pavlov, J. A. Pons, P. S. Shternin, & D. G. Yakovlev, Central compact objects in supernova remnants (St. Petersburg), 012006

De Luca, A., Caraveo, P. A., Mereghetti, S., Negroni, M., & Bignami, G. F. 2005, On the Polar Caps of the Three Musketeers, ApJ, 623, 1051

DeCesar, M. E., Boyd, P. T., Pottschmidt, K., et al. 2013, The Be/X-Ray Binary Swift J1626.6-5156 as a Variable Cyclotron Line Source, ApJ, 762, 61

Dessert, C., Foster, J. W., & Safdi, B. R. 2020, Hard X-Ray Excess from the Magnificent Seven Neutron Stars, ApJ, 904, 42

Deufel, B., Dullemond, C. P., & Spruit, H. C. 2001, X-ray spectra from protons illuminating a neutron star, A&A, 377, 955

Diez, C. M., Grinberg, V., Fürst, F., et al. 2022, Continuum, cyclotron line, and absorption variability in the high-mass X-ray binary Vela X-1, A&A, 660, A19

Dodson, R. G., McCulloch, P. M., & Lewis, D. R. 2002, High Time Resolution Observations of the January 2000 Glitch in the Vela Pulsar, ApJ, 564, L85

Dong, B. & Yeh, K. C. 2002, Three-dimensional electromagnetic wave polarizations in a plasma, Radio Science, 37, 1100

Doroshenko, R. 2017, A systematic study of the X-ray cyclotron-line sources observed by BeppoSAX, PhD thesis, Eberhard Karls University of Tübingen, Germany

Doroshenko, R., Piraino, S., Doroshenko, V., & Santangelo, A. 2020a, Revisiting BeppoSAX and NuSTAR observations of KS 1947+300 and the missing cyclotron line, MNRAS, 493, 3442

Doroshenko, V., Poutanen, J., Tsygankov, S. S., et al. 2022, Determination of X-ray pulsar geometry with IXPE polarimetry, Nature Astron., 6, 1433

Doroshenko, V., Santangelo, A., Doroshenko, R., et al. 2014, XMM-Newton observations of <ASTROBJ>1A 0535+262</ASTROBJ> in quiescence, A&A, 561, A96

Doroshenko, V., Santangelo, A., Kreykenbohm, I., & Doroshenko, R. 2012, The hard X-ray emission of X Persei, A&A, 540, L1

Doroshenko, V., Santangelo, A., Suleimanov, V. F., & Tsygankov, S. S. 2020b, An observational argument against accretion in magnetars, A&A, 643, A173

Doroshenko, V., Suleimanov, V., & Santangelo, A. 2018, CXOU J160103.1-513353: another central compact object with a carbon atmosphere?, A&A, 618, A76

Doroshenko, V., Tsygankov, S. S., Mushtukov, A. A., et al. 2017, Luminosity dependence of the cyclotron line and evidence for the accretion regime transition in V 0332+53, MNRAS, 466, 2143

Douchin, F. & Haensel, P. 2000, Inner edge of neutron-star crust with SLy effective nucleon-nucleon interactions, Physics Letters B, 485, 107

Dubus, G. 2015, Gamma-ray emission from binaries in context, Comptes Rendus Physique, 16, 661

Dubus, G., Guillard, N., Petrucci, P.-O., & Martin, P. 2017, Sizing up the population of gamma-ray binaries, A&A, 608, A59

Duncan, R. C. & Thompson, C. 1992, Formation of Very Strongly Magnetized Neutron Stars: Implications for Gamma-Ray Bursts, ApJ, 392, L9

Eddington, A. S. 1916, On the radiative equilibrium of the stars, MNRAS, 77, 16

Edgar, R. 2004, A review of Bondi-Hoyle-Lyttleton accretion, New Astron. Rev., 48, 843

Eksi, K. Y., Andac, I. C., Cikintoglu, S., et al. 2015, The ultraluminous X-ray source NuSTAR J095551+6940.8: a magnetar in a high-mass X-ray binary., MNRAS, 448, L40

El Mellah, I., Sander, A. A. C., Sundqvist, J. O., & Keppens, R. 2019, Formation of wind-captured disks in supergiant X-ray binaries. Consequences for Vela X-1 and Cygnus X-1, A&A, 622, A189

El Mellah, I., Sundqvist, J. O., & Keppens, R. 2018, Accretion from a clumpy massive-star wind in supergiant X-ray binaries, MNRAS, 475, 3240

Elsner, R. F. & Lamb, F. K. 1976, Accretion flows in the magnetospheres of Vela X-1, AO535 + 26 and Her X-1, Nature, 262, 356

Enoto, T., Sasano, M., Yamada, S., et al. 2014, Spectral and Timing Nature of the Symbiotic X-Ray Binary 4U 1954+319: The Slowest Rotating Neutron Star in an X-Ray Binary System, ApJ, 786, 127

Epili, P., Naik, S., Jaisawal, G. K., & Gupta, S. 2017, Decade long RXTE monitoring observations of Be/X-ray binary pulsar EXO 2030+375, MNRAS, 472, 3455

Erkut, M. H., Türkoğlu, M. M., Ekşi, K. Y., & Alpar, M. A. 2020, On the Magnetic Fields, Beaming Fractions, and Fastness Parameters of Pulsating Ultraluminous X-Ray Sources, ApJ, 899, 97

Espinoza, C. M., Lyne, A. G., Stappers, B. W., & Kramer, M. 2011, A study of 315 glitches in the rotation of 102 pulsars, MNRAS, 414, 1679

Fabian, A. C., Pringle, J. E., Verbunt, F., & Wade, R. A. 1983, Do galactic bulge X-ray sources evolve into millisecond pulsars?, Nature, 301, 222

Falkner, S. 2018, Modeling X-ray pulsars in curved space-time, PhD thesis, Friedrich-Alexander-Universität Erlangen-Nürnberg, Germany

Farinelli, R., Ceccobello, C., Romano, P., & Titarchuk, L. 2012, Numerical solution of the radiative transfer equation: X-ray spectral formation from cylindrical accretion onto a magnetized neutron star, A&A, 538, A67

Farinelli, R., Ferrigno, C., Bozzo, E., & Becker, P. A. 2016, A new model for the X-ray continuum of the magnetized accreting pulsars, A&A, 591, A29

Feautrier, P. 1964, A Procedure for computing the Mean Intensity and the Flux, SAO Special Report, 167, 80

Ferrigno, C., Becker, P. A., Segreto, A., Mineo, T., & Santangelo, A. 2009, Study of the accreting pulsar 4U 0115+63 using a bulk and thermal Comptonization model, A&A, 498, 825

Ferrigno, C., Falanga, M., Bozzo, E., et al. 2011, <ASTROBJ>4U 0115 + 63</ASTROBJ>: phase lags and cyclotron resonant scattering, A&A, 532, A76

Flowers, E., Ruderman, M., & Sutherland, P. 1976, Neutrino pair emission from finite-temperature neutron superfluid and the cooling of young neutron stars., ApJ, 205, 541

Foreman-Mackey, D., Hogg, D. W., Lang, D., & Goodman, J. 2013, emcee: The MCMC Hammer, PASP, 125, 306

Fowler, R. H. 1926, On dense matter, MNRAS, 87, 114

Frank, J., King, A., & Raine, D. J. 2002, Accretion Power in Astrophysics: Third Edition (Cambridge, UK: Cambridge University Press)

Freedman, D. Z. 1974, Coherent effects of a weak neutral current, Phys. Rev. D, 9, 1389

Fried, B. D. & Conte, S. D. 1961, The Plasma Dispersion Function (New York: Academic Press)

Fürst, F., Falkner, S., Marcu-Cheatham, D., et al. 2018, Multiple cyclotron line-forming regions in GX 301-2, A&A, 620, A153

Fürst, F., Pottschmidt, K., Wilms, J., et al. 2014a, NuSTAR Discovery of a Cyclotron Line in KS 1947+300, ApJ, 784, L40

Fürst, F., Pottschmidt, K., Wilms, J., et al. 2014b, NuSTAR Discovery of a Luminosity Dependent Cyclotron Line Energy in Vela X-1, ApJ, 780, 133

Fürst, F., Walton, D. J., Harrison, F. A., et al. 2016, Discovery of Coherent Pulsations from the Ultraluminous X-Ray Source NGC 7793 P13, ApJ, 831, L14

Galloway, D. K., Muno, M. P., Hartman, J. M., Psaltis, D., & Chakrabarty, D. 2008, Thermonuclear (Type I) X-Ray Bursts Observed by the Rossi X-Ray Timing Explorer, ApJS, 179, 360

Gamow, G. & Schoenberg, M. 1941, Neutrino Theory of Stellar Collapse, Phys. Rev., 59, 539

Gangadhara, R. T., Han, J. L., & Wang, P. F. 2021, Coherent Curvature Radio Emission and Polarization from Pulsars, ApJ, 911, 152

Gao, Z. F., Wang, N., & Shan, H. 2017, Could the low-braking-index pulsar PSR J1734-3333 evolve into a magnetar?, Astron. Nachr., 338, 1060

Garasev, M. A., Derishev, E. V., Kocharovsky, V. V., & Kocharovsky, V. V. 2016, Cyclotron line formation in the magnetized atmospheres of compact stars - I. The transfer equations for polarized radiation, MNRAS, 459, 1847

García, J., Dauser, T., Reynolds, C. S., et al. 2013, X-Ray Reflected Spectra from Accretion Disk Models. III. A Complete Grid of Ionized Reflection Calculations, ApJ, 768, 146

García, J. & Kallman, T. R. 2010, X-ray Reflected Spectra from Accretion Disk Models. I. Constant Density Atmospheres, ApJ, 718, 695

Gaunt, J. A. 1930, Continuous Absorption, Phil. Trans. R. Soc. London, Ser. A, 229, 163

Gautschi, W. 1970, Efficient Computation of the Complex Error Function, SIAM J. Numer. Anal., 7, 187

Gençali, A. A. & Ertan, Ü. 2021, On the long-term evolution of rotating radio transients, MNRAS, 500, 3281

Ghosh, P. & Lamb, F. K. 1978, Disk accretion by magnetic neutron stars., ApJ, 223, L83

Ghosh, P., Lamb, F. K., & Pethick, C. J. 1977, Accretion by rotating magnetic neutron stars. I. Flow of matter inside the magnetosphere and its implications for spin-up and spin-down of the star., ApJ, 217, 578

Giacconi, R., Gursky, H., Paolini, F. R., & Rossi, B. B. 1962, Evidence for x Rays From Sources Outside the Solar System, Phys. Rev. Lett., 9, 439

Gil, J., Melikidze, G. I., & Geppert, U. 2003, Drifting subpulses and inner accelerationregions in radio pulsars, A&A, 407, 315

Giménez-García, A., Shenar, T., Torrejón, J. M., et al. 2016, Measuring the stellar wind parameters in IGR J17544-2619 and Vela X-1 constrains the accretion physics in supergiant fast X-ray transient and classical supergiant X-ray binaries, A&A, 591, A26

Glampedakis, K., Jones, D. I., & Samuelsson, L. 2011, Ambipolar diffusion in superfluid neutron stars, MNRAS, 413, 2021

Gnedin, Y. N. & Pavlov, G. G. 1974, The transfer equations for normal waves and radiation polarization in an anisotropic medium, JETP, 38, 903

Gnedin, Y. N., Pavlov, G. G., & Shibanov, Y. A. 1978, The effect of vacuum birefringence in a magnetic field on the polarization and beaming of X-ray pulsars, Sov. Astron. Let., 4, 117

Godzieba, D. A., Radice, D., & Bernuzzi, S. 2021, On the Maximum Mass of Neutron Stars and GW190814, ApJ, 908, 122

Goldreich, P. & Julian, W. H. 1969, Pulsar Electrodynamics, ApJ, 157, 869

Gonthier, P. L., Baring, M. G., Eiles, M. T., et al. 2014, Compton scattering in strong magnetic fields: Spin-dependent influences at the cyclotron resonance, Phys. Rev. D, 90, 043014

González-Caniulef, D., Zane, S., Turolla, R., & Wu, K. 2019, Atmosphere of strongly magnetized neutron stars heated by particle bombardment, MNRAS, 483, 599

Gorban, A. S., Molkov, S. V., Tsygankov, S. S., & Lutovinov, A. A. 2021, Study of the X-ray Pulsar XTE J1946+274 with NuSTAR, Astron. Let., 47, 390, Springer Nature

Gornostaev, M. I. 2021, Three-dimensional modelling of accretion columns: spatial asymmetry and self-consistent simulations, MNRAS, 501, 564

Gourgouliatos, K. N., Wood, T. S., & Hollerbach, R. 2016, Magnetic field evolution in magnetar crusts through three-dimensional simulations, PNAS, 113, 3944

Grinberg, V. 2014, Investigations of the long term variability of black hole binaries, PhD thesis, Friedrich-Alexander-Universität Erlangen-Nürnberg, Germany

Grinberg, V., Hell, N., El Mellah, I., et al. 2017, The clumpy absorber in the high-mass X-ray binary Vela X-1, A&A, 608, A143

Güngör, C., Ekşi, K. Y., Göğüş, E., & Güver, T. 2017, Partial Accretion in the Propeller Stage of Low-mass X-Ray Binary Aql X-1, ApJ, 848, 13

Gvaramadze, V. V., Kniazev, A. Y., & Oskinova, L. M. 2019, Discovery of a putative supernova remnant around the long-period X-ray pulsar SXP 1323 in the Small Magellanic Cloud, MNRAS, 485, L6

Haberl, F. 2007, The magnificent seven: magnetic fields and surface temperature distributions, Ap&SS, 308, 181

Haberl, F. & Sturm, R. 2016, High-mass X-ray binaries in the Small Magellanic Cloud, A&A, 586, A81

Haensel, P., Potekhin, A. Y., & Yakovlev, D. G. 2007, Neutron Stars 1 : Equation of State and Structure, Vol. 326 (New York: Springer)

Haensel, P. & Zdunik, J. L. 2008, Models of crustal heating in accreting neutron stars, A&A, 480, 459

Halpern, J. P. & Gotthelf, E. V. 2010, Spin-Down Measurement of PSR J1852+0040 in Kesteven 79: Central Compact Objects as Anti-Magnetars, ApJ, 709, 436

Harding, A. K. 2013, The neutron star zoo, Frontiers of Physics, 8, 679

Harding, A. K. 2022, in Astrophysics and Space Science Library, Vol. 465, Astrophysics and Space Science Library, ed. S. Bhattacharyya, A. Papitto, & D. Bhattacharya, The Emission Physics of Millisecond Pulsars (Springer), 57–85

Harding, A. K. & Daugherty, J. K. 1991, Cyclotron Resonant Scattering and Absorption, ApJ, 374, 687

Harding, A. K. & Leventhal, M. 1992, Can accretion onto isolated neutron stars produce γ-ray bursts?, Nature, 357, 388

Harding, A. K., Meszaros, P., Kirk, J. G., & Galloway, D. J. 1984, Self-consistent models for Coulomb-heated X-ray pulsar atmospheres, ApJ, 278, 369

Haskell, B., Antonopoulou, D., & Barenghi, C. 2020, Turbulent, pinned superfluids in neutron stars and pulsar glitch recoveries, MNRAS, 499, 161

Haskell, B. & Sedrakian, A. 2018, in Astrophysics and Space Science Library, Vol. 457, Astrophysics and Space Science Library, ed. L. Rezzolla, P. Pizzochero, D. I. Jones, N. Rea, & I. Vidaña, Superfluidity and Superconductivity in Neutron Stars (Springer Nature Switzerland), 401

Haxton, W. C. 1995, The Solar Neutrino Problem, ARA&A, 33, 459

Heindl, W. A., Coburn, W., Gruber, D. E., et al. 2000, in AAS/High Energy Astrophysics Division, Vol. 5, AAS/High Energy Astrophysics Division #5, Multiple Cyclotron Lines in the Spectrum of 4U 0115+63, 29.06

Heinz, S., Sell, P., Fender, R. P., et al. 2013, The Youngest Known X-Ray Binary: Circinus X-1 and Its Natal Supernova Remnant, ApJ, 779, 171

Herold, H. 1979, Compton and Thomson scattering in strong magnetic fields, Phys. Rev. D, 19, 2868

Hewish, A., Bell, S. J., Pilkington, J. D. H., Scott, P. F., & Collins, R. A. 1968, Observation of a Rapidly Pulsating Radio Source, Nature, 217, 709

Ho, W. C. G. 2013, in Neutron Stars and Pulsars: Challenges and Opportunities after 80 years, ed. J. van Leeuwen, Vol. 291, Central compact objects and their magnetic fields (Cambridge University Press), 101–106

Ho, W. C. G. & Heinke, C. O. 2009, A neutron star with a carbon atmosphere in the Cassiopeia A supernova remnant, Nature, 462, 71

Ho, W. C. G., Kaplan, D. L., Chang, P., van Adelsberg, M., & Potekhin, A. Y. 2007, Magnetic hydrogen atmosphere models and the neutron star RX J1856.5-3754, MNRAS, 375, 821

Ho, W. C. G. & Lai, D. 2003, Atmospheres and spectra of strongly magnetized neutron stars - II. The effect of vacuum polarization, MNRAS, 338, 233

Ho, W. C. G. & Lai, D. 2004, Spectral Features in the Thermal Emission from Isolated Neutron Stars: Dependence on Magnetic Field Strengths, ApJ, 607, 420

Hoffmeister, C. 1936, 604 neue Veräderliche, Astron. Nachr., 259, 37

Houck, J. C. & Denicola, L. A. 2000, in Astron. Soc. Pacific Conf. Ser., Vol. 216, Astronomical Data Analysis Software and Systems IX, ed. N. Manset, C. Veillet, & D. Crabtree, ISIS: An Interactive Spectral Interpretation System for High Resolution X-Ray Spectroscopy, 591

Hoyle, F. 1954, On Nuclear Reactions Occuring in Very Hot STARS.I. the Synthesis of Elements from Carbon to Nickel., ApJS, 1, 121

Hoyle, F. & Lyttleton, R. A. 1941, On the accretion theory of stellar evolution, MNRAS, 101, 227

Hu, C.-P., Ng, C. Y., & Ho, W. C. G. 2019, A systematic study of soft X-ray pulse profiles of magnetars in quiescence, MNRAS, 485, 4274

Hubeny, I. & Mihalas, D. 2014, Theory of Stellar Atmospheres (Princeton, NJ, Princeton University Press)

Hui, C. Y., Lee, J., Takata, J., Ng, C. W., & Cheng, K. S. 2017, Differences between Radio-loud and Radio-quiet Gamma-ray Pulsars as Revealed by Fermi, ApJ, 834, 120

Hulse, R. A. & Taylor, J. H. 1975, Discovery of a pulsar in a binary system., ApJ, 195, L51

Igoshev, A. P., Gourgouliatos, K. N., Hollerbach, R., & Wood, T. S. 2021a, 3D Magnetothermal Simulations of Tangled Crustal Magnetic Field in Central Compact Objects, ApJ, 909, 101

Igoshev, A. P., Popov, S. B., & Hollerbach, R. 2021b, Evolution of Neutron Star Magnetic Fields, Universe, 7, 351

Igumenshchev, I. V., Narayan, R., & Abramowicz, M. A. 2003, Three-dimensional Magnetohydrodynamic Simulations of Radiatively Inefficient Accretion Flows, ApJ, 592, 1042

Ikhsanov, N. R. 2001, On the state of low luminous accreting neutron stars, A&A, 375, 944

Ikhsanov, N. R. 2007, Accretion by isolated neutron stars, Ap&SS, 308, 137

Ikhsanov, N. R. 2012, Signs of magnetic accretion in the young Be/X-ray pulsar SXP 1062, MNRAS, 424, L39

Illarionov, A. F. & Sunyaev, R. A. 1975, Why the Number of Galactic X-ray Stars Is so Small?, A&A, 39, 185

Israel, G. L., Belfiore, A., Stella, L., et al. 2017a, An accreting pulsar with extreme properties drives an ultraluminous x-ray source in NGC 5907, Science, 355, 817

Israel, G. L., Papitto, A., Esposito, P., et al. 2017b, Discovery of a 0.42-s pulsar in the ultraluminous X-ray source NGC 7793 P13, MNRAS, 466, L48

Iwakiri, W. B., Pottschmidt, K., Falkner, S., et al. 2019, Spectral and Timing Analysis of the Accretion-powered Pulsar 4U 1626-67 Observed with Suzaku and NuSTAR, ApJ, 878, 121

Iyer, N., Mukherjee, D., Dewangan, G. C., Bhattacharya, D., & Seetha, S. 2015, Variations in the cyclotron resonant scattering features during 2011 outburst of 4U 0115+63, MNRAS, 454, 741

Jaisawal, G. K. & Naik, S. 2016, Detection of cyclotron resonance scattering feature in high-mass X-ray binary pulsar SMC X-2, MNRAS, 461, L97

Jaisawal, G. K., Naik, S., & Epili, P. 2016, Suzaku view of the Be/X-ray binary pulsar GX 304-1 during Type I X-ray outbursts, MNRAS, 457, 2749

Janka, H. T., Langanke, K., Marek, A., Martínez-Pinedo, G., & Müller, B. 2007, Theory of core-collapse supernovae, Phys. Rep., 442, 38

Kaaret, P., Feng, H., & Roberts, T. P. 2017, Ultraluminous X-Ray Sources, ARA&A, 55, 303

Kaastra, J. S. & Bleeker, J. A. M. 2016, Optimal binning of X-ray spectra and response matrix design, A&A, 587, A151

Kalemci, E., Boggs, S. E., Kouveliotou, C., Finger, M., & Baring, M. G. 2007, Search for Polarization from the Prompt Gamma-Ray Emission of GRB 041219a with SPI on INTEGRAL, ApJS, 169, 75

Kalogera, V. & Baym, G. 1996, The Maximum Mass of a Neutron Star, ApJ, 470, L61

Kaminker, A. D., Pavlov, G. G., & Shibanov, I. A. 1982, Radiation from a Strongly Magnetized Plasma - the Case of Predominant Scattering, Ap&SS, 86, 249

Kaspi, V. M. 2010, Grand unification of neutron stars, PNAS, 107, 7147

Kaspi, V. M. & Beloborodov, A. M. 2017, Magnetars, ARA&A, 55, 261

Katz, J. I. 1976, Nonrelativistic Compton scattering and models of quasars., ApJ, 206, 910

Keane, E. F. & Kramer, M. 2008, On the birthrates of Galactic neutron stars, MNRAS, 391, 2009

Khokhriakova, A. D. & Popov, S. B. 2022, Origin of young accreting neutron stars in high-mass X-ray binaries in supernova remnants, MNRAS, 511, 4447

Khomenko, V. & Haskell, B. 2018, Modelling Pulsar Glitches: The Hydrodynamics of Superfluid Vortex Avalanches in Neutron Stars, PASA, 35, e020

King, A. & Lasota, J.-P. 2019, No magnetars in ULXs, MNRAS, 485, 3588

King, A. R., Davies, M. B., Ward, M. J., Fabbiano, G., & Elvis, M. 2001, Ultraluminous X-Ray Sources in External Galaxies, ApJ, 552, L109

Kippenhahn, R., Weigert, A., & Weiss, A. 2013, Stellar Structure and Evolution

Kirk, J. G. 1980, The propagation of high frequency waves in a strongly magnetized plasma, Plasma Physics, 22, 639

Kirk, J. G. & Galloway, D. J. 1982, The evolution of a test particle distribution in a strongly magnetized plasma, Plasma Physics, 24, 339

Kirk, J. G. & Meszaros, P. 1980, Thermal effects on the cyclotron line formation process in X-ray pulsars, ApJ, 241, 1153

Klein, R. I. & Arons, J. 1989, in ESA Special Publication, Vol. 1, Two Topics in X-Ray Astronomy, Volume 1: X Ray Binaries. Volume 2: AGN and the X Ray Background, ed. J. Hunt & B. Battrick, Time-Dependent Two Dimensional Radiation Hydrodynamics of Accreting Matter onto Highly Magnetised Neutron Stars, 89

Klein, R. I., Arons, J., Jernigan, G., & Hsu, J. J. L. 1996, Photon Bubble Oscillations in Accretion-powered Pulsars, ApJ, 457, L85

Klochkov, D., Horns, D., Santangelo, A., et al. 2007, INTEGRAL and Swift observations of EXO 2030+375 during a giant outburst, A&A, 464, L45

Klochkov, D., Staubert, R., Santangelo, A., Rothschild, R. E., & Ferrigno, C. 2011, Pulse-amplitude-resolved spectroscopy of bright accreting pulsars: indication of two accretion regimes, A&A, 532, A126

Knigge, C., Coe, M. J., & Podsiadlowski, P. 2011, Two populations of X-ray pulsars produced by two types of supernova, Nature, 479, 372

Kojo, T., Baym, G., & Hatsuda, T. 2022, Implications of NICER for Neutron Star Matter: The QHC21 Equation of State, ApJ, 934, 46

Kompaneets, A. S. 1957, The Establishment of Thermal Equilibrium between Quanta and Electrons, JETP, 4, 730

Kong, L.-D., Zhang, S., Ji, L., et al. 2022a, Phase-dependent Evolution within the Large Luminosity Range of 1A 0535+262 Observed by Insight-HXMT during 2020 Giant Outburst, ApJ, 932, 106

Kong, L. D., Zhang, S., Ji, L., et al. 2021, Luminosity Dependence of the Cyclotron Line Energy in 1A 0535+262 Observed by Insight-HXMT during the 2020 Giant Outburst, ApJ, 917, L38

Kong, L.-D., Zhang, S., Zhang, S.-N., et al. 2022b, Insight-HXMT Discovery of the Highest-energy CRSF from the First Galactic Ultraluminous X-Ray Pulsar Swift J0243.6+6124, ApJ, 933, L3

Kornilov, V. G. & Lipunov, V. M. 1983, Neutron Stars in Massive Binary Systems - Part One - Classification and Evolution, Soviet Ast., 27, 163

Kramer, M., Lyne, A. G., O'Brien, J. T., Jordan, C. A., & Lorimer, D. R. 2006, A Periodically Active Pulsar Giving Insight into Magnetospheric Physics, Science, 312, 549

Kraus, U., Nollert, H. P., Ruder, H., & Riffert, H. 1995, Analyzing X-Ray Pulsar Profiles: Asymmetry as a Key to Geometry and Beam Pattern, ApJ, 450, 763

Kretschmar, P., El Mellah, I., Martínez-Núñez, S., et al. 2021, Revisiting the archetypical wind accretor Vela X-1 in depth. Case study of a well-known X-ray binary and the limits of our knowledge, A&A, 652, A95

Kretschmar, P., Fürst, F., Sidoli, L., et al. 2019, Advances in Understanding High-Mass X-ray Binaries with INTEGRALand Future Directions, New Astron. Rev., 86, 101546

Kuiper, L., Hermsen, W., Urama, J. O., et al. 2010, Hard X-ray timing and spectral characteristics of the energetic pulsar PSR J0205+6449 in supernova remnant 3C 58. An RXTE PCA/HEXTE and XMM-Newton view on the 0.5-250 keV band, A&A, 515, A34

Kumar, S., Bala, S., & Bhattacharya, D. 2022, A new Monte Carlo radiative transfer simulation of cyclotron resonant scattering features, MNRAS, 515, 914

Kylafis, N. D., Trümper, J. E., & Loudas, N. A. 2021, Cyclotron line formation by reflection on the surface of a magnetic neutron star, A&A, 655, A39

Lai, D., Chernoff, D. F., & Cordes, J. M. 2001, Pulsar Jets: Implications for Neutron Star Kicks and Initial Spins, ApJ, 549, 1111

Lai, D. & Ho, W. C. 2003a, Polarized X-Ray Emission from Magnetized Neutron Stars: Signature of Strong-Field Vacuum Polarization, Phys. Rev. Lett., 91, 071101

Lai, D. & Ho, W. C. G. 2002, Resonant Conversion of Photon Modes Due to Vacuum Polarization in a Magnetized Plasma: Implications for X-Ray Emission from Magnetars, ApJ, 566, 373

Lai, D. & Ho, W. C. G. 2003b, Transfer of Polarized Radiation in Strongly Magnetized Plasmas and Thermal Emission from Magnetars: Effect of Vacuum Polarization, ApJ, 588, 962

Lamb, F. K., Pethick, C. J., & Pines, D. 1973, A Model for Compact X-Ray Sources: Accretion by Rotating Magnetic Stars, ApJ, 184, 271

Landau, L. 1930, Diamagnetismus der Metalle, Zeitschrift fur Physik, 64, 629

Landau, L. D. 1932, To the Stars theory, Phys. Zs. Sowjet, 1, 285

Lander, S. K., Andersson, N., Antonopoulou, D., & Watts, A. L. 2015, Magnetically driven crustquakes in neutron stars, MNRAS, 449, 2047

Lander, S. K. & Gourgouliatos, K. N. 2019, Magnetic-field evolution in a plastically failing neutron-star crust, MNRAS, 486, 4130

Langer, N. 2012, Presupernova Evolution of Massive Single and Binary Stars, ARA&A, 50, 107

Langer, N., Wellstein, S., & Petrovic, J. 2003, in A Massive Star Odyssey: From Main Sequence to Supernova, ed. K. van der Hucht, A. Herrero, & C. Esteban, Vol. 212, On the evolution of massive close binaries (San Francisco: Astronomical Society of the Pacific), 275

Langer, S. H. & Rappaport, S. 1982, Low-luminosity accretion onto magnetized neutron stars, ApJ, 257, 733

Langmuir, I. 1928, Oscillations in Ionized Gases, PNAS, 14, 627

Lattimer, J. M. 2021, Neutron Stars and the Nuclear Matter Equation of State, Annual Review of Nuclear and Particle Science, 71, 433

Lattimer, J. M. & Prakash, M. 2004, The Physics of Neutron Stars, Science, 304, 536

Lattimer, J. M. & Swesty, D. F. 1991, A generalized equation of state for hot, dense matter, Nucl. Phys. A, 535, 331

Laurent, P., Rodriguez, J., Wilms, J., et al. 2011, Polarized Gamma-Ray Emission from the Galactic Black Hole Cygnus X-1, Science, 332, 438

Leahy, D. A. 2004, Mass-Radius Constraints from a Pulse Shape Model for Hercules X-1, ApJ, 613, 517

Leahy, D. A. 2005, in 22nd Texas Symposium on Relativistic Astrophysics, ed. P. Chen, E. Bloom, G. Madejski, & P. V., Effects of Accretion Column Structure on Beam Shapes (Stanford, California,), 619–622

Leahy, D. A., Elsner, R. F., & Weisskopf, M. C. 1983, On searches for periodic pulsed emission - The Rayleigh test compared to epoch folding, ApJ, 272, 256

Lewin, W. H. G., van Paradijs, J., & Taam, R. E. 1993, X-Ray Bursts, Space Sci. Rev., 62, 223

Lin, L. C. C., Huang, R. H. H., Takata, J., et al. 2010, Detection of an X-ray Pulsation for the Gamma-Ray Pulsar Centered in CTA 1, ApJ, 725, L1

Lipunov, V. M. 1982, The Universal Diagram for Magnetized Neutron Stars in the Galaxy, Ap&SS, 85, 451

Lipunov, V. M. 1987, The Ecology of Rotators, Ap&SS, 132, 1

Lipunov, V. M. 1992, Astrophysics of Neutron Stars (Berlin, Heidelberg, New York: Springer-Verlag)

Liu, B.-S., Tao, L., Zhang, S.-N., et al. 2020, A Peculiar Cyclotron Line near 16 keV Detected in the 2015 Outburst of 4U 0115+63?, ApJ, 900, 41

Long, K. S. & van Speybroeck, L. P. 1983, in Accretion-Driven Stellar X-ray Sources, ed. W. H. G. Lewin & E. P. J. van den Heuvel, Very Bright Non-Nuclear Sources (Cambridge, New York: Cambridge University Press), 141

Lorimer, D. R. 2008, Binary and Millisecond Pulsars, Living Rev. Relativity, 11, 8

Lovchinsky, I., Slane, P., Gaensler, B. M., et al. 2011, A Chandra Observation of Supernova Remnant G350.1-0.3 and Its Central Compact Object, ApJ, 731, 70

Lutovinov, A., Tsygankov, S., Molkov, S., et al. 2021, SRG/ART-XC and NuSTAR Observations of the X-Ray pulsar GRO J1008-57 in the Lowest Luminosity State, ApJ, 912, 17

Lyne, A. G., McLaughlin, M. A., Keane, E. F., et al. 2009, Unusual glitch activity in the RRAT J1819-1458: an exhausted magnetar?, MNRAS, 400, 1439

Lyne, A. G., Shemar, S. L., & Smith, F. G. 2000, Statistical studies of pulsar glitches, MNRAS, 315, 534

Lyubarskii, Y. É. 1988, Comptonization in a superstrong magnetic field. II, Astrophysics, 28, 253

Lyubarskii, Y. E. & Syunyaev, R. A. 1982, Comptonization in a Radiation Dominated Shock and the Spectra of X-Ray Pulsars, Soviet Astron. Let., 8, 330

Maccarone, T. J., Girard, T. M., & Casetti-Dinescu, D. I. 2014, High proper motion X-ray binaries from the Yale Southern Proper Motion Survey, MNRAS, 440, 1626

Mahy, L., Rauw, G., De Becker, M., Eenens, P., & Flores, C. A. 2013, A spectroscopic investigation of the O-type star population in four Cygnus OB associations. I. Determination of the binary fraction, A&A, 550, A27

Maitra, C., Haberl, F., Filipović, M. D., et al. 2019, Discovery of a very young high-mass X-ray binary associated with the supernova remnant MCSNR J0513-6724 in the LMC, MNRAS, 490, 5494

Maitra, C., Paul, B., Haberl, F., & Vasilopoulos, G. 2018, Detection of a cyclotron line in SXP 15.3 during its 2017 outburst, MNRAS, 480, L136

Makarenko, E. I., Igoshev, A. P., & Kholtygin, A. F. 2021, Testing the fossil field hypothesis: could strongly magnetized OB stars produce all known magnetars?, MNRAS, 504, 5813

Makishima, K., Mihara, T., Ishida, M., et al. 1990, Discovery of a Prominent Cyclotron Absorption Feature from the Transient X-Ray Pulsar X0331+53, ApJ, 365, L59

Makishima, K., Mihara, T., Nagase, F., & Tanaka, Y. 1999, Cyclotron Resonance Effects in Two Binary X-Ray Pulsars and the Evolution of Neutron Star Magnetic Fields, ApJ, 525, 978

Malacaria, C., Bogdanov, S., Ho, W. C. G., et al. 2019, A Joint NICER and XMM-Newton View of the “Magnificent” Thermally Emitting X-Ray Isolated Neutron Star RX J1605.3+3249, ApJ, 880, 74

Malacaria, C., Klochkov, D., Santangelo, A., & Staubert, R. 2015, Luminosity-dependent spectral and timing properties of the accreting pulsar GX 304-1 measured with INTEGRAL, A&A, 581, A121

Manchester, R. N. 2017, Millisecond Pulsars, their Evolution and Applications, J. Astrophys. Astron., 38, 42

Manchester, R. N., Hobbs, G. B., Teoh, A., & Hobbs, M. 2005, The Australia Telescope National Facility Pulsar Catalogue, AJ, 129, 1993

Manousakis, A., Walter, R., & Blondin, J. M. 2012, Neutron star masses from hydrodynamical effects in obscured supergiant high mass X-ray binaries, A&A, 547, A20

Marchant, P., Langer, N., Podsiadlowski, P., et al. 2017, Ultra-luminous X-ray sources and neutron-star-black-hole mergers from very massive close binaries at low metallicity, A&A, 604, A55

Martínez-Núñez, S., Kretschmar, P., Bozzo, E., et al. 2017, Towards a Unified View of Inhomogeneous Stellar Winds in Isolated Supergiant Stars and Supergiant High Mass X-Ray Binaries, Space Sci. Rev., 212, 59

Mason, B. D., Hartkopf, W. I., Gies, D. R., Henry, T. J., & Helsel, J. W. 2009, The High Angular Resolution Multiplicity of Massive Stars, AJ, 137, 3358

Mayer, M. G. F. & Becker, W. 2021, A kinematic study of central compact objects and their host supernova remnants, A&A, 651, A40

McClintock, J. E., Rappaport, S. A., Nugent, J. J., & Li, F. K. 1977, Discovery of a 272 second periodic variation in the X-ray source GX 304-1., ApJ, 216, L15

McLaughlin, M. A., Lyne, A. G., Lorimer, D. R., et al. 2006, Transient radio bursts from rotating neutron stars, Nature, 439, 817

Meisel, Z., Deibel, A., Keek, L., Shternin, P., & Elfritz, J. 2018, Nuclear physics of the outer layers of accreting neutron stars, Journal of Physics G Nuclear Physics, 45, 093001

Melrose, D. B. 1980, Plasma Astrophysics, Vol. 1 (New York: Gordon and Breach)

Menzel, D. H. & Milne, E. A. 1966, Selected papers on the transfer of radiation (New York: Dover Publications)

Mereghetti, S. 2011, in Astrophysics and Space Science Proceedings, Vol. 21, High-Energy Emission from Pulsars and their Systems, ed. D. Torres & N. Rea, X-ray emission from isolated neutron stars (Springer, Berlin, Heidelberg), 345

Mészáros, P. 1992, High-energy radiation from magnetized neutron stars. (Chicago: Univ. Chicago Press)

Meszaros, P., Harding, A. K., Kirk, J. G., & Galloway, D. J. 1983, Accreting X-ray pulsar atmospheres heated by Coulomb deceleration of protons, ApJ, 266, L33

Meszaros, P. & Nagel, W. 1985a, X-ray pulsar models. I - Angle-dependent cyclotron line formation and comptonization, ApJ, 298, 147

Meszaros, P. & Nagel, W. 1985b, X-ray pulsar models. II. Comptonized spectra and pulse shapes., ApJ, 299, 138

Meszaros, P., Pavlov, G. G., & Shibanov, I. A. 1989, The Effect of Stimulated Scattering in Compact Sources, ApJ, 337, 426

Meszaros, P. & Riffert, H. 1988, Gravitational Light Bending near Neutron Stars. II. Accreting Pulsar Spectra as a Function of Phase, ApJ, 327, 712

Mészáros, P. & Ventura, J. 1978, Vacuum-Polarization Effects on Thomson Cross Sections in a Magnetized Plasma, Phys. Rev. Lett., 41, 1544

Meszaros, P. & Ventura, J. 1979, Vacuum polarization effects on radiative opacities in a strong magnetic field, Phys. Rev. D, 19, 3565

Mignani, R. P., De Luca, A., Zharikov, S., et al. 2019, The nature of the infrared counterpart and of the optical nebula associated with the Central Compact Object in Vela Jr., MNRAS, 486, 5716

Mihalas, D. 1978, Stellar atmospheres (San Francisco: W.H. Freeman)

Mihara, T. 1995, Observational study of X-ray spectra of binary pulsars with Ginga, PhD thesis, University of Tokyo

Milkey, R. W., Shine, R. A., & Mihalas, D. 1975, Resonance-line transfer with partial redistribution. VII. Angle-dependent redistribution., ApJ, 202, 250

Miller, G., Wasserman, I., & Salpeter, E. E. 1989, The Deceleration of Infalling Plasma in Magnetized Neutron Star Atmospheres: Nonisothermal Atmospheres, ApJ, 346, 405

Miller, G. S., Salpeter, E. E., & Wasserman, I. 1987, Deceleration of Infalling Plasma in the Atmospheres of Accreting Neutron Stars. I. Isothermal Atmospheres, ApJ, 314, 215

Milne, E. A. 1930a, The analysis of stellar structure, MNRAS, 91, 4

Milne, E. A. 1930b, Thermodynamics of the Stars, Handbuch der Astrophysik, 3, 65

Miralles, J. A., Urpin, V., & Konenkov, D. 1998, Joule Heating and the Thermal Evolution of Old Neutron Stars, ApJ, 503, 368

Miyasaka, H., Bachetti, M., Harrison, F. A., et al. 2013, NuSTAR Detection of Hard X-Ray Phase Lags from the Accreting Pulsar GS 0834-430, ApJ, 775, 65

Molkov, S., Doroshenko, V., Lutovinov, A., et al. 2021, Discovery of the 5 keV Cyclotron Line Followed by Three Harmonics in Swift J1626.6-5156, ApJ, 915, L27

Mori, K. & Ruderman, M. A. 2003, Isolated Magnetar Spin-Down, Soft X-Ray Emission, and RX J1856.5-3754, ApJ, 592, L75

Mukherjee, D., Bhattacharya, D., & Mignone, A. 2013, MHD instabilities in accretion mounds - II. 3D simulations, MNRAS, 435, 718

Müller, D., Klochkov, D., Santangelo, A., Mihara, T., & Sugizaki, M. 2011, No apparent accretion mode changes detected in Centaurus X-3, A&A, 535, A102

Müller, S., Ferrigno, C., Kühnel, M., et al. 2013, No anticorrelation between cyclotron line energy and X-ray flux in 4U 0115+634, A&A, 551, A6

Mushtukov, A. & Tsygankov, S. 2022, Accreting strongly magnetised neutron stars: X-ray Pulsars, Invited chapter for the "Handbook of X-ray and Gamma-ray Astrophysics", eds. C. Bambi and A. Santangelo, Springer Singapore (arXiv:2204.14185)

Mushtukov, A. A., Nagirner, D. I., & Poutanen, J. 2016, Compton scattering S matrix and cross section in strong magnetic field, Phys. Rev. D, 93, 105003

Mushtukov, A. A., Suleimanov, V. F., Tsygankov, S. S., & Portegies Zwart, S. 2021, Spectrum formation in X-ray pulsars at very low mass accretion rate: Monte Carlo approach, MNRAS, 503, 5193

Mushtukov, A. A., Suleimanov, V. F., Tsygankov, S. S., & Poutanen, J. 2015a, On the maximum accretion luminosity of magnetized neutron stars: connecting X-ray pulsars and ultraluminous X-ray sources, MNRAS, 454, 2539

Mushtukov, A. A., Suleimanov, V. F., Tsygankov, S. S., & Poutanen, J. 2015b, The critical accretion luminosity for magnetized neutron stars, MNRAS, 447, 1847

Mushtukov, A. A., Tsygankov, S. S., Poutanen, J., et al. 2023, X-ray polarimetry of X-ray pulsar X Persei: another orthogonal rotator?, MNRAS, submitted (arXiv:2303.17325)

Mushtukov, A. A., Tsygankov, S. S., Serber, A. V., Suleimanov, V. F., & Poutanen, J. 2015c, Positive correlation between the cyclotron line energy and luminosity in sub-critical X-ray pulsars: Doppler effect in the accretion channel, MNRAS, 454, 2714

Nagase, F., Dotani, T., Tanaka, Y., et al. 1991, Cyclotron Line Features in the Spectrum of the Transient X-Ray Pulsar X0115+634, ApJ, 375, L49

Nagel, W. 1980, Cyclotron line formation in the accretion column of an X-ray pulsar, ApJ, 236, 904

Nagel, W. 1981a, Radiative Transfer in a Strongly Magnetized Plasma - Part Two - Effects of Comptonization, ApJ, 251, 288

Nagel, W. 1981b, Radiative transfer in a strongly magnetized plasma. I - Effects of anisotropy. II - Effects of Comptonization, ApJ, 251, 278

Nagel, W. 1982, Radiation transport in a strongly magnetized plasma, PhD thesis, Tech. Univ., Münich Max-Planck-Inst. für Physik und Astrophysik, Garching, Germany

Nagel, W. & Ventura, J. 1983, Coulomb bremsstrahlung and cyclotron emissivity in hot magnetized plasmas, A&A, 118, 66

Naik, S. & Jaisawal, G. K. 2015, Suzaku observation of Be/X-ray binary pulsar EXO 2030+375, Research in Astronomy and Astrophysics, 15, 537

Nelson, R. W., Salpeter, E. E., & Wasserman, I. 1993, Nonthermal Cyclotron Emission from Low-Luminosity Accretion onto Magnetic Neutron Stars, ApJ, 418, 874

Nelson, R. W., Wang, J. C. L., Salpeter, E. E., & Wasserman, I. 1995, A Potential Cyclotron Line Signature in Low-Luminosity X-Ray Sources, ApJ, 438, L99

Neumann, M., Avakyan, A., Doroshenko, V., & Santangelo, A. 2023, XRBcats: Galactic High Mass X-ray Binary Catalogue, A&A, submitted (arXiv:2303.16137)

Ng, C. Y., Ho, W. C. G., Gotthelf, E. V., et al. 2019, X-Ray and Radio Variabilities of PSR J2032+4127 near Periastron, ApJ, 880, 147

Nishimura, O. 2008, Formation Mechanism for Broad and Shallow Profiles of Cyclotron Lines in Accreting X-Ray Pulsars, ApJ, 672, 1127

Nishimura, O. 2014, Variations of Cyclotron Line Energy with Luminosity in Accreting X-Ray Pulsars, ApJ, 781, 30

Okazaki, A. T., Hayasaki, K., & Moritani, Y. 2013, Origin of Two Types of X-Ray Outbursts in Be/X-Ray Binaries. I. Accretion Scenarios, PASJ, 65, 41

Okazaki, A. T. & Negueruela, I. 2001, A natural explanation for periodic X-ray outbursts in Be/X-ray binaries, A&A, 377, 161

Olausen, S. A. & Kaspi, V. M. 2014, The McGill Magnetar Catalog, ApJS, 212, 6

Oppenheimer, J. R. & Volkoff, G. M. 1939, On Massive Neutron Cores, Phys. Rev., 55, 374

Ostriker, J. P., Rees, M. J., & Silk, J. 1970, Some Observable Consequences of Accretion by Defunct Pulsars, Astrophys. Lett., 6, 179

Owocki, S. 2013, in Planets, Stars and Stellar Systems. Volume 4: Stellar Structure and Evolution, ed. T. D. Oswalt & M. A. Barstow, Vol. 4 (Springer Dordrecht), 735

Özel, F. 2003, The Effect of Vacuum Polarization and Proton Cyclotron Resonances on Photon Propagation in Strongly Magnetized Plasmas, ApJ, 583, 402

Özel, F. & Psaltis, D. 2009, Reconstructing the neutron-star equation of state from astrophysical measurements, Phys. Rev. D, 80, 103003

Pacini, F. 1968, Rotating Neutron Stars, Pulsars and Supernova Remnants, Nature, 219, 145

Page, D., Geppert, U., & Weber, F. 2006, The cooling of compact stars, Nucl. Phys. A, 777, 497

Page, D., Lattimer, J. M., Prakash, M., & Steiner, A. W. 2004, Minimal Cooling of Neutron Stars: A New Paradigm, ApJS, 155, 623

Page, D., Lattimer, J. M., Prakash, M., & Steiner, A. W. 2009, Neutrino Emission from Cooper Pairs and Minimal Cooling of Neutron Stars, ApJ, 707, 1131

Palmer, D. M., Barthelmy, S., Gehrels, N., et al. 2005, A giant γ-ray flare from the magnetar SGR 1806 - 20, Nature, 434, 1107, Springer Nature

Parkes, G. E., Murdin, P. G., & Mason, K. O. 1980, The shell spectrum of the optical counterpart of GX 304-1 (4U 1258-61)., MNRAS, 190, 537

Patruno, A. & Watts, A. L. 2021, in Astrophysics and Space Science Library, Vol. 461, Astrophysics and Space Science Library, ed. T. M. Belloni, M. Méndez, & C. Zhang, Accreting Millisecond X-ray Pulsars

(Springer Berlin Heidelberg), 143–208

Paul, B., Raichur, H., & Mukherjee, U. 2005, Accretion mode changes in Centaurus X-3, A&A, 442, L15

Pavlov, G. G. & Shibanov, I. A. 1979, Influence of vacuum polarization by a magnetic field on the propagation of electromagnetic waves in plasmas, Zh. Eksp. Teor. Fiz., 76, 1457

Pavlov, G. G., Shibanov, I. A., & Iakovlev, D. G. 1980, Quantum effects in cyclotron plasma absorption, Ap&SS, 73, 33

Payne, D. G. 1980, Time-dependent comptonization : X-ray reverberations., ApJ, 237, 951

Peraiah, A. 2001, An Introduction to Radiative Transfer (Cambridge, UK: Cambridge University Pres)

Peraiah, A. & Srinivasa Rao, M. 2013, Compton broadening effect on spectral line formation, Ap&SS, 343, 195

Pethick, C. J. 1992, Cooling of neutron stars, Reviews of Modern Physics, 64, 1133

Pétri, J. 2020, Magnetic quadri-dipolar stars rotating in vacuum, MNRAS, 499, 4445

Pilia, M., Hessels, J. W. T., Stappers, B. W., et al. 2016, Wide-band, low-frequency pulse profiles of 100 radio pulsars with LOFAR, A&A, 586, A92

Pires, A. M. 2018, in Pulsar Astrophysics the Next Fifty Years, ed. P. Weltevrede, B. B. P. Perera, L. L. Preston, & S. Sanidas, Vol. 337, What will eROSITA reveal among X-ray faint isolated neutron stars? (Cambridge University Press, online), 112–115

Pires, A. M., Haberl, F., Zavlin, V. E., et al. 2014, XMM-Newton reveals a candidate period for the spin of the “Magnificent Seven” neutron star RX J1605.3+3249, A&A, 563, A50

Pires, A. M., Schwope, A., & Kurpas, J. 2022, in ..., Deep eROSITA observations of the "magnificent seven" isolated neutron stars

Pires, A. M., Schwope, A. D., Haberl, F., et al. 2019, A deep XMM-Newton look on the thermally emitting isolated neutron star RX J1605.3+3249, A&A, 623, A73

Pitkin, M. 2018, psrqpy: a python interface for querying the ATNF pulsar catalogue, Journal of Open Source Software, 3, 538

Pomraning, G. C. 1973, The equations of radiation hydrodynamics (Oxford: Pergamon Press)

Pons, J. A. & Geppert, U. 2007, Magnetic field dissipation in neutron star crusts: from magnetars to isolated neutron stars, A&A, 470, 303

Pons, J. A. & Perna, R. 2011, Magnetars versus High Magnetic Field Pulsars: A Theoretical Interpretation of the Apparent Dichotomy, ApJ, 741, 123

Pons, J. A. & Rea, N. 2012, Modeling Magnetar Outbursts: Flux Enhancements and the Connection with Short Bursts and Glitches, ApJ, 750, L6

Pons, J. A. & Viganò, D. 2019, Magnetic, thermal and rotational evolution of isolated neutron stars, Living Rev. Comput. Astrophys., 5, 3

Ponti, G., De, K., Muñoz-Darias, T., Stella, L., & Nandra, K. 2017, The puzzling orbital period evolution of the LMXB AX J1745.6-2901, MNRAS, 464, 840

Popov, S. B. 2016, Origins of magnetars in binary systems, Astron. Astrophys. Trans., 29, 183

Popov, S. B., Postnov, K. A., & Shakura, N. I. 2015, Settling accretion on to isolated neutron stars from interstellar medium, MNRAS, 447, 2817

Popov, S. B. & Prokhorov, M. E. 2006, Progenitors with enhanced rotation and the origin of magnetars, MNRAS, 367, 732

Popov, S. B. & Prokhorov, M. E. 2007, REVIEWS OF TOPICAL PROBLEMS: Population synthesis in astrophysics, Physics Uspekhi, 50, 1123

Popov, S. B., Turolla, R., & Possenti, A. 2006, A tale of two populations: rotating radio transients and X-ray dim isolated neutron stars, MNRAS, 369, L23

Postnov, K. A., Gornostaev, M. I., Klochkov, D., et al. 2015, On the dependence of the X-ray continuum variations with luminosity in accreting X-ray pulsars, MNRAS, 452, 1601

Postnov, K. A., Shakura, N. I., Kochetkova, A. Y., & Hjalmarsdotter, L. 2014, in European Physical Journal Web of Conferences, Vol. 64, European Physical Journal Web of Conferences, ed. E. Bozzo, P. Kretschmar, M. Audard, M. Falanga, & C. Ferrigno, Do we see accreting magnetars in X-ray pulsars? (Geneva, Switzerland: EDP Sciences), 02002

Postnov, K. A. & Yungelson, L. R. 2014, The Evolution of Compact Binary Star Systems, Living Rev. Relativity, 17, 3

Potekhin, A. Y., Pons, J. A., & Page, D. 2015, Neutron Stars—Cooling and Transport, Space Sci. Rev., 191, 239, Springer Nature

Potekhin, A. Y., Zyuzin, D. A., Yakovlev, D. G., Beznogov, M. V., & Shibanov, Y. A. 2020, Thermal luminosities of cooling neutron stars, MNRAS, 496, 5052

Poutanen, J., Mushtukov, A. A., Suleimanov, V. F., et al. 2013, A Reflection Model for the Cyclotron Lines in the Spectra of X-Ray Pulsars, ApJ, 777, 115

Pradhan, P., Bozzo, E., & Paul, B. 2018, Supergiant fast X-ray transients versus classical supergiant high mass X-ray binaries: Does the difference lie in the companion wind?, A&A, 610, A50

Prendergast, K. H. & Burbidge, G. R. 1968, On the Nature of Some Galactic X-Ray Sources, ApJ, 151, L83

Pringle, J. E. & Rees, M. J. 1972, Accretion Disc Models for Compact X-Ray Sources, A&A, 21, 1

Pustylnik, I. 1998, The Early History of Resolving the Algol Paradox, Astron. Astrophys. Trans., 15, 357

Raaijmakers, G., Greif, S. K., Hebeler, K., et al. 2021, Constraints on the Dense Matter Equation of State and Neutron Star Properties from NICER's Mass-Radius Estimate of PSR J0740+6620 and Multimessenger Observations, ApJ, 918, L29

Radhakrishnan, V. & Srinivasan, G. 1982, On the origin of the recently discovered ultra-rapid pulsar, Current Science, 51, 1096

Ravi, V., Manchester, R. N., & Hobbs, G. 2010, Wide Radio Beams from γ-ray Pulsars, ApJ, 716, L85

Rea, N. & Esposito, P. 2011, in Astrophysics and Space Science Proceedings, Vol. 21, High-Energy Emission from Pulsars and their Systems, ed. D. Torres & N. Rea, Magnetar outbursts: an observational review (Berlin Heidelberg: Springer-Verlag), 247

Rea, N., Esposito, P., Turolla, R., et al. 2010, A Low-Magnetic-Field Soft Gamma Repeater, Science, 330, 944

Rea, N., Israel, G. L., Esposito, P., et al. 2012, A New Low Magnetic Field Magnetar: The 2011 Outburst of Swift J1822.3-1606, ApJ, 754, 27

Reig, P. & Milonaki, F. 2016, Accretion regimes in the X-ray pulsar 4U 1901+03, A&A, 594, A45

Reig, P. & Roche, P. 1999, Discovery of two new persistent Be/X-ray pulsar systems, MNRAS, 306, 100

Reig, P. & Zezas, A. 2018, Discovery of X-ray pulsations in the Be/X-ray binary IGR J06074+2205, A&A, 613, A52

Rhoades, C. E. & Ruffini, R. 1974, Maximum Mass of a Neutron Star, Phys. Rev. Lett., 32, 324

Rigoselli, M., Mereghetti, S., Taverna, R., Turolla, R., & De Grandis, D. 2021, Strongly pulsed thermal X-rays from a single extended hot spot on PSR J2021+4026, A&A, 646, A117

Romanova, M. M., Toropina, O. D., Toropin, Y. M., & Lovelace, R. V. E. 2003, Magnetohydrodynamic Simulations of Accretion onto a Star in the "Propeller" Regime, ApJ, 588, 400

Rothschild, R. E., Kühnel, M., Pottschmidt, K., et al. 2017, Discovery and modelling of a flattening of the positive cyclotron line/luminosity relation in GX 304-1 with RXTE, MNRAS, 466, 2752

Rouco Escorial, A., van den Eijnden, J., & Wijnands, R. 2018, Discovery of accretion-driven pulsations in the prolonged low X-ray luminosity state of the Be/X-ray transient GX 304-1, A&A, 620, L13

Rouco Escorial, A., Wijnands, R., van den Eijnden, J., et al. 2020, Recurrent low-level luminosity behaviour after a giant outburst in the Be/X-ray transient 4U 0115+63, A&A, 638, A152

Ruderman, M. A. & Sutherland, P. G. 1975, Theory of pulsars: polar gaps, sparks, and coherent microwave radiation., ApJ, 196, 51

Russell, H. R., Fabian, A. C., McNamara, B. R., & Broderick, A. E. 2015, Inside the Bondi radius of M87, MNRAS, 451, 588

Rutledge, R. E. 2001, Magnetically Accreting Isolated Old Neutron Stars, ApJ, 553, 796

Rybicki, G. B. & Lightman, A. P. 1986, Radiative Processes in Astrophysics (Wiley-VCH)

Salganik, A., Tsygankov, S. S., Djupvik, A. A., et al. 2022, On the nature of the X-ray pulsar XTE J1859+083 and its broad-band properties, MNRAS, 509, 5955

Salpeter, E. E. 1964, Accretion of Interstellar Matter by Massive Objects., ApJ, 140, 796

Sasaki, M., Klochkov, D., Kraus, U., Caballero, I., & Santangelo, A. 2010, Analyzing X-ray pulsar profiles: geometry and beam pattern of EXO 2030+375, A&A, 517, A8

Sasaki, M., Müller, D., Kraus, U., Ferrigno, C., & Santangelo, A. 2012, Analysing X-ray pulsar profiles. Geometry and beam pattern of 4U 0115+63 and V 0332+53, A&A, 540, A35

Schönherr, G., Wilms, J., Kretschmar, P., et al. 2007a, A model for cyclotron resonance scattering features, A&A, 472, 353

Schönherr, G., Wilms, J., Kretschmar, P., et al. 2007b, A model for cyclotron resonance scattering features, A&A, 472, 353

Schuster, A. 1905, Radiation Through a Foggy Atmosphere, ApJ, 21, 1

Schwarm, F.-W., Ballhausen, R., Falkner, S., et al. 2017a, Cyclotron resonant scattering feature simulations. II. Description of the CRSF simulation process, A&A, 601, A99

Schwarm, F. W., Schönherr, G., Falkner, S., et al. 2017b, Cyclotron resonant scattering feature simulations. I. Thermally averaged cyclotron scattering cross sections, mean free photon-path tables, and electron momentum sampling, A&A, 597, A3

Schwarm, F.-W. M. 2017, Monte Carlo simulation of cyclotron lines in strong magnetic fields : Theory and application, PhD thesis, Friedrich-Alexander-Universität Erlangen-Nürnberg, Germany

Schwarzschild, K. 1906, On the equilibrium of the Sun's atmosphere, Nachrichten von der Königlichen Gesellschaft der Wissenschaften zu

Göttingen. Math.-phys. Klasse, 195, 41

Schwarzschild, K. 1914, Über Diffusion und Absorption in der Sonnenatmosphäre (Berlin)

Shafranov, V. D. 1967, Electromagnetic Waves in a Plasma, Rev. Plasma Phys., 3, 1

Shakura, N., Postnov, K., & Hjalmarsdotter, L. 2013a, On the nature of 'off' states in slowly rotating low-luminosity X-ray pulsars, MNRAS, 428, 670

Shakura, N., Postnov, K., Kochetkova, A., & Hjalmarsdotter, L. 2012, Theory of quasi-spherical accretion in X-ray pulsars, MNRAS, 420, 216

Shakura, N., Postnov, K., Sidoli, L., & Paizis, A. 2014, Bright flares in supergiant fast X-ray transients, MNRAS, 442, 2325

Shakura, N. I., Postnov, K. A., Kochetkova, A. Y., & Hjalmarsdotter, L. 2013b, Quasispherical subsonic accretion in X-ray pulsars, Physics Uspekhi, 56, 321

Shakura, N. I., Postnov, K. A., Kochetkova, A. Y., et al. 2015, Wind accretion: Theory and observations, Astron. Rep., 59, 645

Shakura, N. I. & Sunyaev, R. A. 1973, Black holes in binary systems. Observational appearance., A&A, 24, 337

Shapiro, S. L. & Salpeter, E. E. 1975, Accretion onto neutron stars under adiabatic shock conditions., ApJ, 198, 671

Shapiro-Albert, B. J., McLaughlin, M. A., & Keane, E. F. 2018, Radio Properties of Rotating Radio Transients: Single-pulse Spectral and Wait-time Analyses, ApJ, 866, 152

Shaviv, N. J. 1998, The Eddington Luminosity Limit for Multiphased Media, ApJ, 494, L193

Shibazaki, N., Murakami, T., Shaham, J., & Nomoto, K. 1989, Does mass accretion lead to field decay in neutron stars?, Nature, 342, 656

Shima, E., Matsuda, T., Takeda, H., & Sawada, K. 1985, Hydrodynamic calculations of axisymmetric accretion flow, MNRAS, 217, 367

Shklovskii, I. S. 1967, The Nature of the X-Ray Source Sco X-1., AZh, 44, 930

Shvartsman, V. F. 1970, The Influence of Stellar Wind on Accretion., Soviet Ast., 14, 527

Shvartsman, V. F. 1971a, Halos around "Black Holes"., Soviet Ast., 15, 377

Shvartsman, V. F. 1971b, Neutron Stars in Binary Systems Should Not Be Pulsars., Soviet Ast., 15, 342

Shvartsman, V. G. 1971c, Ionization Zones around Neutron Stars: Hα Emission, Heating of the Interstellar Medium, and the Influence on Accretion., Soviet Ast., 14, 662

Sidoli, L. 2017, in XII Multifrequency Behaviour of High Energy Cosmic Sources Workshop (MULTIF2017), ed. F. Giovannelli & L. Sabau-Graziati, Supergiant Fast X-ray Transients - A short review (Palermo, Italy), 52

Sidoli, L., Tiengo, A., Paizis, A., et al. 2017, XMM-Newton and NuSTAR Simultaneous X-Ray Observations of IGR J11215-5952, ApJ, 838, 133

Silver, E. H., Weisskopf, M. C., Kestenbaum, H. L., et al. 1979, The first search for X-ray polarization in the Centaurus X-3 and Hercules X-1 pulsars., ApJ, 232, 248

Sina, R. 1996, Bhabha scattering and trident production in strong uniform magnetic fields, PhD thesis, University of Maryland

Soffel, M., Herold, H., Ruder, H., & Ventura, J. 1985, Radiative transfer in the accretion column of X-ray pulsars : effectsfrom the hot spot., A&A, 144, 485

Soffel, M., Ventura, J., Herold, H., Ruder, H., & Nagel, W. 1983, Propagation of high frequency waves in strongly magnetized plasmas - Mode ambiguities due to vacuum polarization., A&A, 126, 251

Sokolova-Lapa, E., Gornostaev, M., Wilms, J., et al. 2021, X-ray emission from magnetized neutron star atmospheres at low mass-accretion rates. I. Phase-averaged spectrum, A&A, 651, A12

Sokolova-Lapa, E., Stierhof, J., Dauser, T., & Wilms, J. 2023, Vacuum polarization alters the spectra of accreting X-ray pulsars, A&A, 674, L2

Spruit, H. & Phinney, E. S. 1998, Birth kicks as the origin of pulsar rotation, Nature, 393, 139

Spruit, H. C. 2008, in American Institute of Physics Conference Series, Vol. 983, 40 Years of Pulsars: Millisecond Pulsars, Magnetars and More, ed. C. Bassa, Z. Wang, A. Cumming, & V. M. Kaspi, Origin of neutron star magnetic fields (American Institute of Physics), 391–398

Srinivasan, G. & van den Heuvel, E. P. J. 1982, Some constraints on the evolutionary history of the binary pulsar PSR1913+16., A&A, 108, 143

Staelin, D. H. & Reifenstein, Edward C., I. 1968, Pulsating Radio Sources near the Crab Nebula, Science, 162, 1481

Stappers, B. W., Hessels, J. W. T., Alexov, A., et al. 2011, Observing pulsars and fast transients with LOFAR, A&A, 530, A80

Staubert, R., Shakura, N. I., Postnov, K., et al. 2007, Discovery of a flux-related change of the cyclotron line energy in Hercules X-1, A&A, 465, L25

Staubert, R., Trümper, J., Kendziorra, E., et al. 2019, Cyclotron lines in highly magnetized neutron stars, A&A, 622, A61

Stella, L., White, N. E., & Rosner, R. 1986, Intermittent Stellar Wind Acceleration and the Long-Term Activity of Population I Binary Systems Containing an X-Ray Pulsar, ApJ, 308, 669

Suleimanov, V. F., Mushtukov, A. A., Ognev, I., Doroshenko, V. A., & Werner, K. 2022, Mean opacities of a strongly magnetized high-temperature plasma, MNRAS, 517, 4022

Suleimanov, V. F., Poutanen, J., & Werner, K. 2018, Accretion heated atmospheres of X-ray bursting neutron stars, A&A, 619, A114

Sykes, J. B. 1951, Approximate integration of the equation of transger, MNRAS, 111, 377

Tanaka, Y. 1986, in Lecture Notes in Physics, ed. D. Mihalas & K.-H. A. Winkler, Vol. 255 (Springer), 198

Tavani, M. 1991, Orbital evolution of low-mass X-ray binaries due to radiation driven mass transfer, Nature, 351, 39

Tavella, D. & Randall, C. 2000, Pricing Financial Instruments: The Finite Difference Method (New York: Wiley)

Taylor, J. H. & Weisberg, J. M. 1982, A new test of general relativity - Gravitational radiation and the binary pulsar PSR 1913+16, ApJ, 253, 908

Thalhammer, P., Bissinger, M., Ballhausen, R., et al. 2021, Fitting strategies of accretion column models and application to the broadband spectrum of Cen X-3, A&A, 656, A105

Thomas, L. H. 1949, Elliptic problems in linear difference equations over a network (New York: Columbia University)

Thompson, C. & Duncan, R. C. 1993, Neutron Star Dynamos and the Origins of Pulsar Magnetism, ApJ, 408, 194

Thorne, K. S. & Zytkow, A. N. 1977, Stars with degenerate neutron cores. I. Structure of equilibrium models., ApJ, 212, 832

Timokhin, A. N. 2010, A model for nulling and mode changing in pulsars, MNRAS, 408, L41

Titarchuk, L. 1994, Generalized Comptonization Models and Application to the Recent High-Energy Observations, ApJ, 434, 570

Tokayer, Y. M., An, H., Halpern, J. P., et al. 2021, Multiwavelength Observation Campaign of the TeV Gamma-Ray Binary HESS J0632 + 057 with NuSTAR, VERITAS, MDM, and Swift, ApJ, 923, 17

Tong, H. 2015, Ultraluminous X-ray pulsar: Accreting magnetar?, Astron. Nachr., 336, 835

Tonks, L. & Langmuir, I. 1929, A General Theory of the Plasma of an Arc, Phys. Rev., 34, 876

Toropina, O. D., Romanova, M. M., & Lovelace, R. V. E. 2006, Spinning-down of moving magnetars in the propeller regime, MNRAS, 371, 569

Toropina, O. D., Romanova, M. M., & Lovelace, R. V. E. 2008, MHD Simulations of Accretion onto a Magnetized Neutron Star in the "propeller" Regime, International Journal of Modern Physics D, 17, 1723

Toropina, O. D., Romanova, M. M., & Lovelace, R. V. E. 2012, Bondi-Hoyle accretion on to a magnetized neutron star, MNRAS, 420, 810

Toropina, O. D., Romanova, M. M., Toropin, Y. M., & Lovelace, R. V. E. 2001, Propagation of Magnetized Neutron Stars through the Interstellar Medium, ApJ, 561, 964

Toropina, O. D., Romanova, M. M., Toropin, Y. M., & Lovelace, R. V. E. 2003, Magnetic Inhibition of Accretion and Observability of Isolated Old Neutron Stars, ApJ, 593, 472

Treves, A., Turolla, R., Zane, S., & Colpi, M. 2000, Isolated Neutron Stars: Accretors and Coolers, PASP, 112, 297

Truemper, J., Pietsch, W., Reppin, C., et al. 1978, Evidence for strong cyclotron line emission in the hard X-ray spectrum of Hercules X-1., ApJ, 219, L105

Trümper, J., Pietsch, W., Reppin, C., & Sacco, B. 1977, in Eighth Texas Symposium on Relativistic Astrophysics, ed. M. D. Papagiannis, Vol. 302, Evidence for Strong Cyclotron Emission in the Hard X-Ray Spectrum of Her X-1 (New York: The New York Academy of Sciences), 538

Tsygankov, S. S., Doroshenko, V., Mushtukov, A. A., Lutovinov, A. A., & Poutanen, J. 2019a, Study of the X-ray pulsar IGR J19294+1816 with NuSTAR: Detection of cyclotron line and transition to accretion from the cold disk, A&A, 621, A134

Tsygankov, S. S., Doroshenko, V., Mushtukov, A. A., et al. 2023, X-ray pulsar GRO J1008−57 as an orthogonal rotator, A&A, submitted (arXiv:2302.06680)

Tsygankov, S. S., Doroshenko, V., Mushtukov, A. A., et al. 2019b, Cyclotron emission, absorption, and the two faces of X-ray pulsar A 0535+262, MNRAS, 487, L30

Tsygankov, S. S., Doroshenko, V., Poutanen, J., et al. 2022, The X-Ray Polarimetry View of the Accreting Pulsar Cen X-3, ApJ, 941, L14

Tsygankov, S. S., Lutovinov, A. A., Churazov, E. M., & Sunyaev, R. A. 2006, V0332+53 in the outburst of 2004-2005: luminosity dependence of the cyclotron line and pulse profile, MNRAS, 371, 19

Tsygankov, S. S., Lutovinov, A. A., Doroshenko, V., et al. 2016, Propeller effect in two brightest transient X-ray pulsars: 4U 0115+63 and V 0332+53, A&A, 593, A16

Tsygankov, S. S., Rouco Escorial, A., Suleimanov, V. F., et al. 2019c, Dramatic spectral transition of X-ray pulsar GX 304-1 in low luminous state, MNRAS, 483, L144

Tsygankov, S. S., Wijnands, R., Lutovinov, A. A., Degenaar, N., & Poutanen, J. 2017, The X-ray properties of Be/X-ray pulsars in quiescence, MNRAS, 470, 126

Tubbs, D. L. & Schramm, D. N. 1975, Neutrino Opacities at High Temperatures and Densities, ApJ, 201, 467

Turolla, R. 2009, in Astrophysics and Space Science Library, Vol. 357, Astrophysics and Space Science Library, ed. W. Becker, Isolated Neutron Stars: The Challenge of Simplicity (Springer, Berlin, Heidelberg), 141

Turolla, R., Zampieri, L., Colpi, M., & Treves, A. 1994, Spherical Accretion onto Neutron Stars Revisited: Are Hot Solutions Possible?, ApJ, 426, L35

Turolla, R., Zane, S., & Watts, A. L. 2015, Magnetars: the physics behind observations. A review, Reports on Progress in Physics, 78, 116901

Tutukov, A. & Yungelson, L. 1973, Evolution of massive close binaries, Nauchnye Informatsii, 27, 70

van Adelsberg, M. & Lai, D. 2006, Atmosphere models of magnetized neutron stars: QED effects, radiation spectra and polarization signals, MNRAS, 373, 1495

van den Heuvel, E. P. J. 2017, Formation of Double Neutron Stars, Millisecond Pulsars and Double Black Holes, J. Astrophys. Astron., 38, 45

van den Heuvel, E. P. J. & De Loore, C. 1973, The nature of X-ray binaries III. Evolution of massive close binaries with one collapsed component - with a possible application to Cygnus X-3., A&A, 25, 387

Vasilopoulos, G., Haberl, F., Carpano, S., & Maitra, C. 2018, NGC 300 ULX1: A test case for accretion torque theory, A&A, 620, L12

Vasilopoulos, G., Petropoulou, M., Koliopanos, F., et al. 2019, NGC 300 ULX1: spin evolution, super-Eddington accretion, and outflows, MNRAS, 488, 5225

Ventura, J. 1979, Scattering of light in a strongly magnetized plasma, Phys. Rev. D, 19, 1684

Ventura, J., Nagel, W., & Meszaros, P. 1979, Possible vacuum signature in the spectra of X-ray pulsars, ApJL, 233, L125

Verner, D. A., Ferland, G. J., Korista, K. T., & Yakovlev, D. G. 1996, Atomic Data for Astrophysics. II. New Analytic FITS for Photoionization Cross Sections of Atoms and Ions, ApJ, 465, 487

Viganò, D., Garcia-Garcia, A., Pons, J. A., Dehman, C., & Graber, V. 2021, Magneto-thermal evolution of neutron stars with coupled Ohmic, Hall and ambipolar effects via accurate finite-volume simulations, Computer Physics Comm., 265, 108001

Viganò, D., Rea, N., Pons, J. A., et al. 2013, Unifying the observational diversity of isolated neutron stars via magneto-thermal evolution models, MNRAS, 434, 123

Vinciguerra, S., Neijssel, C. J., Vigna-Gómez, A., et al. 2020, Be X-ray binaries in the SMC as indicators of mass-transfer efficiency, MNRAS, 498, 4705

Virtamo, J. & Jauho, P. 1975, Bremsstrahlung in a plasma under the influence of a strong magnetic field., Nuovo Cimento Ser. B, 26, 537

Vybornov, V., Klochkov, D., Gornostaev, M., et al. 2017, Luminosity-dependent changes of the cyclotron line energy and spectral hardness in Cep X-4, A&A, 601, A126

Walder, R., Folini, D., & Meynet, G. 2012, Magnetic Fields in Massive Stars, Their Winds, and Their Nebulae, Space Sci. Rev., 166, 145

Walter, F. M., Wolk, S. J., & Neuhäuser, R. 1996, Discovery of a nearby isolated neutron star, Nature, 379, 233

Walter, R., Lutovinov, A. A., Bozzo, E., & Tsygankov, S. S. 2015, High-mass X-ray binaries in the Milky Way. A closer look with INTEGRAL, A&A Rev., 23, 2

Walton, D. J., Mackenzie, A. D. A., Gully, H., et al. 2022, A multimission catalogue of ultraluminous X-ray source candidates, MNRAS, 509, 1587

Wang, C. & Lai, D. 2009, Polarization evolution in a strongly magnetized vacuum: QED effect and polarized X-ray emission from magnetized neutron stars, MNRAS, 398, 515

Wang, J. 2016, Physical Environment of Accreting Neutron Stars, Adv. Astronomy, 2016, 3434565

Wang, J. C. L., Wasserman, I. M., & Salpeter, E. E. 1988, Cyclotron line resonant transfer through neutron star atmospheres, ApJS, 68, 735

Wang, N., Manchester, R. N., & Johnston, S. 2007, Pulsar nulling and mode changing, MNRAS, 377, 1383

Wang, P. F., Han, J. L., Han, L., et al. 2020, Jiamusi pulsar observations. III. Nulling of 20 pulsars, A&A, 644, A73

Wang, P. J., Kong, L. D., Zhang, S., et al. 2022, Timing Properties of the X-Ray Accreting Pulsar 1A 0535+262 Studied with Insight-HXMT, ApJ, 935, 125

Wang, W. 2013, in Neutron Stars and Pulsars: Challenges and Opportunities after 80 years, ed. J. van Leeuwen, Vol. 291, The superslow pulsation X-ray pulsars in high mass X-ray binaries, 203–206

Wang, Y. M. & Frank, J. 1981, Plasma infall and X-ray production in the magnetic funnel of an accretning neutron star., A&A, 93, 255

Wasserman, I. & Salpeter, E. 1980, Resonance radiative transfer for cyclotron line emission with recoil, ApJ, 241, 1107

Watts, A. L., Andersson, N., Chakrabarty, D., et al. 2016, Colloquium: Measuring the neutron star equation of state using x-ray timing, Reviews of Modern Physics, 88, 021001

Weisskopf, M. 2018, An Overview of X-Ray Polarimetry of Astronomical Sources, Galaxies, 6, 33

Weisskopf, M. C., Elsner, R. F., Hanna, D., et al. 2006, The prospects for X-ray polarimetry and its potential use for understanding neutron stars, Springer Lecture Notes, submitted, (arxiv:0611483)

Weng, S.-S., Qian, L., Wang, B.-J., et al. 2022, Radio pulsations from a neutron star within the gamma-ray binary LS I +61° 303, Nature Astron., 6, 698

West, B. F., Wolfram, K. D., & Becker, P. A. 2017a, A New Two-fluid Radiation-hydrodynamical Model for X-Ray Pulsar Accretion Columns, ApJ, 835, 129

West, B. F., Wolfram, K. D., & Becker, P. A. 2017b, Dynamical and Radiative Properties of X-Ray Pulsar Accretion Columns: Phase-averaged Spectra, ApJ, 835, 130

Wilms, J., Allen, A., & McCray, R. 2000, On the Absorption of X-Rays in the Interstellar Medium, ApJ, 542, 914

Wilson-Hodge, C. A., Malacaria, C., Jenke, P. A., et al. 2018, NICER and Fermi GBM Observations of the First Galactic Ultraluminous X-Ray Pulsar Swift J0243.6+6124, ApJ, 863, 9

Wolff, M. T., Becker, P. A., Gottlieb, A. M., et al. 2016, The NuSTAR X-Ray Spectrum of Hercules X-1: A Radiation-dominated Radiative Shock, ApJ, 831, 194

Yahel, R. Z. 1979, Cyclotron line formation in the atmosphere of a magnetized neutron star., ApJ, 229, L73

Yahel, R. Z. 1980a, Spectra and pulse formation mechanism in X-ray pulsars : application to HER X-1., A&A, 90, 26

Yahel, R. Z. 1980b, X-ray spectra from accreting, magnetized neutron stars - Inclusion of the optically thick region, ApJ, 236, 911

Yakovlev, D. G., Gnedin, O. Y., Kaminker, A. D., Levenfish, K. P., & Potekhin, A. Y. 2004, Neutron star cooling: theoretical aspects and observational constraints, Adv. Space Res., 33, 523

Yakovlev, D. G., Haensel, P., Baym, G., & Pethick, C. 2013, Lev Landau and the concept of neutron stars, Physics Uspekhi, 56, 289

Yakovlev, D. G., Kaminker, A. D., Gnedin, O. Y., & Haensel, P. 2001, Neutrino emission from neutron stars, Phys. Rep., 354, 1

Yakovlev, D. G. & Pethick, C. J. 2004, Neutron Star Cooling, ARA&A, 42, 169

Yamamoto, T., Sugizaki, M., Mihara, T., et al. 2011, Discovery of a Cyclotron Resonance Feature in the X-Ray Spectrum of GX 304-1 with RXTE and Suzaku during Outbursts Detected by MAXI in 2010, PASJ, 63, S751

Ye, C.-Q., Wang, D.-H., Zhang, C.-M., & Diao, Z.-Q. 2019, Evolution implications of neutron star magnetic fields: inferred from pulsars and cyclotron lines of HMXBs, Ap&SS, 364, 198

Younes, G., Archibald, R., Kouveliotou, C., et al. 2016, Fermi-LAT TOO observations of PSR J1119-6127 following its 2016 magnetar-like outburst, ATEL, 9378

Younes, G., Lander, S. K., Baring, M. G., et al. 2022, Pulse Peak Migration during the Outburst Decay of the Magnetar SGR 1830-0645: Crustal Motion and Magnetospheric Untwisting, ApJ, 924, L27

Yungelson, L. R., Kuranov, A. G., & Postnov, K. A. 2019, Wind-accreting symbiotic X-ray binaries, MNRAS, 485, 851

Zampieri, L., Campana, S., Turolla, R., et al. 2001, 1RXS J214303.7+065419/RBS 1774: A new Isolated Neutron Star candidate, A&A, 378, L5

Zane, S., Turolla, R., & Treves, A. 2000, Magnetized Atmospheres around Neutron Stars Accreting at Low Rates, ApJ, 537, 387

Zavlin, V. E. 2007, Thermal emission from isolated neutron stars: theoretical and observational aspects, Springer Lecture Notes, to be published (arxiv:0702426)

Zavlin, V. E. & Pavlov, G. G. 2002, in Neutron Stars, Pulsars, and Supernova Remnants, ed. W. Becker, H. Lesch, & J. Trümper, Modeling Neutron Star Atmospheres, 263

Zdunik, J. L., Fortin, M., & Haensel, P. 2017, Neutron star properties and the equation of state for the core, A&A, 599, A119

Zdziarski, A. A., Neronov, A., & Chernyakova, M. 2010, A compact pulsar wind nebula model of the γ-ray-loud binary LS I +61$\circ$303, MNRAS, 403, 1873

Zel'dovich, Y. B. 1964, The Fate of a Star and the Evolution of Gravitational Energy Upon Accretion, Soviet Physics Doklady, 9, 195

Zel'dovich, Y. B. & Shakura, N. I. 1969, X-Ray Emission Accompanying the Accretion of Gas by a Neutron Star, Soviet Ast., 13, 175

Zhang, L., Blaes, O., & Jiang, Y.-F. 2022, Radiative relativistic magnetohydrodynamic simulations of neutron star column accretion in Cartesian geometry, MNRAS, 515, 4371

Zheleznyakov, V. V., Kocharovskii, V. V., & Kocharovskii, V. V. 1983, Linear coupling of electromagnetic waves in inhomogeneous weakly-ionized media, Uspekhi Fizicheskikh Nauk, 141, 257

ACKNOWLEDGMENTS

"There is no justice in the laws of nature, . . . no term for fairness in the equations of motion. The universe is neither evil, nor good, it simply does not care. The stars don't care, or the Sun, or the sky. But they don't have to. We care. There is light in the world, and it is us."

"Harry Potter and the Methods of Rationality" by Eliezer Yudkowsky

I hope the reader forgives me for starting my acknowledgments with a few general sentences which are intended to show what I am truly grateful for. The logic-based system of reasoning, which allows arranging (observational) information, accessing its veracity, and inferring beyond it, is the foundation of the scientific method. It is also one of the greatest joys to use, in my opinion. Recently, the value of this system of reasoning, together with the virtue of dignity and ethic, became strikingly important far outside the frames of academic scientific research. The events of the outer world swirl around us without our consent, and sometimes we are just lucky to be where were are. I am *lucky* to be where I am, to learn what I learned, and to be able to conduct this research. For the opportunity to find myself at this stage of my life, I am grateful to many people.

First of all, I would like to express heartfelt gratitude to Jörn Wilms. For giving me this opportunity to join the Dr. Karl Remeis Observatory, for the most interesting discussions, for many valuable lessons, for the support, care about his students, and just for being an amazing "scientific father". I learned from him that even in the rapidly developing world of X-ray astrophysics, the high quality of research and scientific ethics come first, no matter the time pressure. Yes, that is why this thesis took so long! Kidding. Jörn, thank you for everything.

I am also very grateful to Katja Pottschmidt who, together with Jörn, made our X-ray gang a real family. Katja, thank you very much for the fascinating discussions, the most thoughtful questions, and your care about us. Our coffee-exchange tradition became very precious to me. I tried some great beans thanks to you and Jörn! Not to mention how it lifted my mood during some desperate times of writing when the optical depth of this thesis was too large for me.

I would like to sincerely thank Konstantin Postnov, who was my supervisor for the diploma at SAI MSU. He introduced me to the puzzling world of neutron stars and radiative transfer in stellar atmospheres. Konstantin Aleksandrovich, thank you for the inspiration and also for your support and understanding, especially in the grimmest days. I am also very grateful for the time when I worked in the Relativistic Astrophysics Department, and especially to Nikolai Ivanovich Shakura for the discussions of the neutron star atmospheres, Mikhail Gornostaev for a few years of fruitful collaboration and some philosophical discussions, Galina Lipunova and Konstantin Malanchev for the light mood in the office, and Sergey Popov for his popular lectures, which contributed to the spark of my interest in astrophysics before I entered the university. I would like to thank my teachers from SAI MSU, who introduced me not only to astronomy and astrophysics, but also to the historical school of the Russian astrophysics and cosmology: Genadiy Shirmin, Anatoly Zasov, Konstantin Postnov, Sergey Lamzin, Konstantin Bychkov, Vladimir Lipunov, Vladimir Surdin, and many others. Also, sadly departed: Boris Somov, Mikhail Sazhin, Victor Kornilov, and Valeriy Panteleev. I appreciate "growing up" in SAI, especially in my "Kapitza-Zustand".

I received the greatest inspiration and support from the XMAG collaboration during our traditional Monday meetings. I would like to thank my "scientific grandfather" Rüdiger Staubert for the discussions of cyclotron lines and works of Immanuel Kant, Richard Rothschild for the most insightful comments and our shared admiration of A 0535+262 (it is a remarkable source!), Peter Kretschmar for making pulse profiles even more exciting and for the kind support, Kent Wood for the sharpest questions and for bringing up the topic of falsifiability of the currently used models for accreting X-ray pulsars, Michael Wolff and Peter Becker for keeping up the in-depth theory discussions, Christian Malacaria for insightful observational information, and all the other members. I am also grateful to Bärbel and Peter Kretschmar for the warmest stay in Madrid with them during my visit to ESAC.

A special thank goes to Javier Garcia. Javier, I was so happy to discover that we can freely speak the radiative transfer language during my first year at the observatory. I thank you for many years of exciting collaboration and friendship, and also for introducing me to the "black hole" community.

Among many people who provided the inspiring discussions about accretion onto compact objects and high-energy astrophysics, I would like to especially thank Ileyk el Mellah for his endless enthusiasm, musical exchange, and deep knowledge of accretion phenomena (and local speakeasies!), Victoria Grinberg for her (definitely high!) energy and for teaching me how to challenge Jörn, Alicia Ruoco Escorial for the shared love for low-luminosity sources and the warmest atmosphere, Matthew Middleton for the greatest discussions of his "crazy" photons and magnetic fields, George Younes for motivating me to learn more about isolated neutron stars, Omer Blaes who, together with Liang Zhang, revealed some very exciting features of accretion columns, Anna Watts and Pushpita Das for our discussions of the physics of accretion and enthusiasm in combining our models, Inga Saathoff for bravely challenging pulse profiles, and Elena Ambrosi for our long chats about accreting X-ray pulsars.

The recent workshop "X-ray Tracking of Magnetic Field Geometries in Accreting X-ray Pulsars" at ESAC provided the most insightful discussions of neutron star magnetic fields. I would like to sincerely thank the organizers – Peter Kretschmar, Katja Pottschmidt, and Jörn Wilms – and the other participants: Felix Fürst, Georgios Vasilopoulos, George Younes, Anna Watts, Carlo Ferrigno, Daniele Viganò, Omer Blaes, Liang Zhang, Jeremy Heyl, Amruta Jaodand, Jakob Stierhof, Philipp Thalhammer, Aafia Zainab, and Katrin Berger.

I am grateful to the HEX-P team, who work hard to make this great mission happen. The special thank goes to the accreting neutron stars group for inspiring brainstorms, and to Renee Ludlam, for her enthusiasm and for keeping us on track.

Telecons on modeling polarized emission from accretion disks with Javier Garcia and Henric Krawczynski have also been a great pleasure over the last few years. I thank Javier for keeping this project going, Henric for all the fascinating discussions about scattering and polarization, and also other former (Arman Hossan) and new (Kun Hu, Edward Nathan) members for their work.

There are so many things to be grateful for to the Dr. Karl Remeis Observatory. I would like to thank Manami Sasaki and Ulrich Heber, who together with Jörn Wilms made the observatory this special, home-like place, Edith Day for holding all of us on the pillars of infinite paperwork (we cannot survive without you), Ingo Kreykenbohm and the other people who keep our cluster away from the abyss of chaos: Philipp Weber, Jakob Stierhof, Caroline Collischon, Maximillian Lorenz, and Jonathan Knies.

During the years of my doctoral studies, I found many friends at the observatory. Ralf Ballhausen, thank you for introducing me to the X-ray data analysis, for our "Italian" evenings, and for relaxing cooking together. Simon Kreuzer, I really appreciate all our beer discussions and your cheerful life attitude. Maximillian Lorenz, thank you for always being there for your friends, for our exchange of gourmet experiences, and for a joint search for new wine discoveries. Thomas Dauser, you are the greatest office mate, and I am grateful for your support, our discussions of ray tracing, and long evenings in the Galerie am Stephansberg. Fritz-Walter Schwarm, thank you for the "CRSF post", long chats about cyclotron processes, and for your guitar, which sometimes brightens up my late evenings at the observatory. Sebastian Falkner, thank you for our long discussion of general relativity and your ray-tracing code and for being always so supportive when I was desperate with `ISIS` and `lbscripts`. Katrin Berger, thank you for your amazing work with the observatory library and for always being ready to help. Ole König, thank you for the cheerful mood of the top floor and your sincere care. Lucia Härer, Alexander Salganik, and Nicolas Zalot, you all are bright young minds, and I was/am happy to take some part in advising your projects. The future is yours. Amy Joyce and Aafia Zainab, thank you both so much for your support, amazing baking skills, and our "girl's nights in". Amy, there is no other person I would trust to judge the correctness of a Guinness foam. Aafia, your berry blondies without a doubt became my favorite dessert. Philipp Thalhammer, I am grateful for our in-depth discussions of neutron stars, your ability to read Jörn's handwriting, and the Rorschach experience in Prague. Jonathan Knies, thank you very much for the shared admiration of the Lovecraft stories and the greatest recommendations regarding coffee beans and coffee making.

Amy, Aafia, Jakob, Jona, Philipp, and Bastien, thank you so much for our game gang. I very much appreciate that you allowed me to drag you into the shadows and green lights of the Call of Cthulhu RPG. I am afraid that the sanity points lost by you during our sessions helped me to restore my mental health! Bastien Gorret, a special thanks go to you for leading the Mouse Guard RPG and for inspiring game-master chats.

I am very grateful to the people who had to suffer through proofreading of various parts of my thesis: Jakob Stierhof, Philipp Thalhammer, Amy Joyce, Aafia Zainab, Ileyk el Mellah, Peter Kretschmar, Thomas Dauser, Ole König, Maximillian Lorenz, and Katrin Berger! I also would like to thank Seven Hills Coffee Roasters for providing the best possible coffee for long writing sessions.

Jakob Stierhof, thank you so much for always having the most inspiring questions about physics, for long discussions of neutron stars and accretion phenomena, for your support, especially during the last year, and for our "morning puzzles" tradition, which deserves to be revived. I am very grateful to the Stierhof's family for a great time together and for gently making me practice my German.

I would like to sincerely thank Petr Sokolov for many years of friendship and care, for teaching me a lot about software development, for our philosophical disputes, and for taking best care about Russian Snowball! The Sokolov's family deserves a special thanks for their support and understanding.

I thank one of my oldest friends, Ivan Vititnev (2×V, 2×T), for this friendship and shared love for Tolkien's books and British literature.

I am grateful to the LessWrong community, who made me think much harder about cognitive biases. "Harry Potter and the Methods of Ratio-

nality” was one of the most exciting fiction books I came across during the years of my doctoral research.

Finally, I want to thank my family, without whom I simply would not be where and who I am. I am so grateful for your love, support, and understanding. I am grateful to my mother for being such an amazing, complex woman, who always inspires me. I sincerely thank my sister for all long evenings playing Call of Cthulhu and Arkham Horror together, for fascinating discussions of behavioral analysis, and all the support. I thank my uncle for challenging me with the most puzzling questions when I was a kid and introducing me to “Heroes III” (I play now not only for the elves!), my grandmother for the greatest collection of books with which I grew up, my grandfather for the most exciting games of chess, Sasha for his kind jokes, Stas for his positive life attitude and curiosity, and all the other members. Last but not least, I am grateful to my departed father, thanks to whom I learned some wonderful pieces of fiction literature, including works of J. R. R. Tolkien, H. P. Lovecraft, and R. Zelazny.